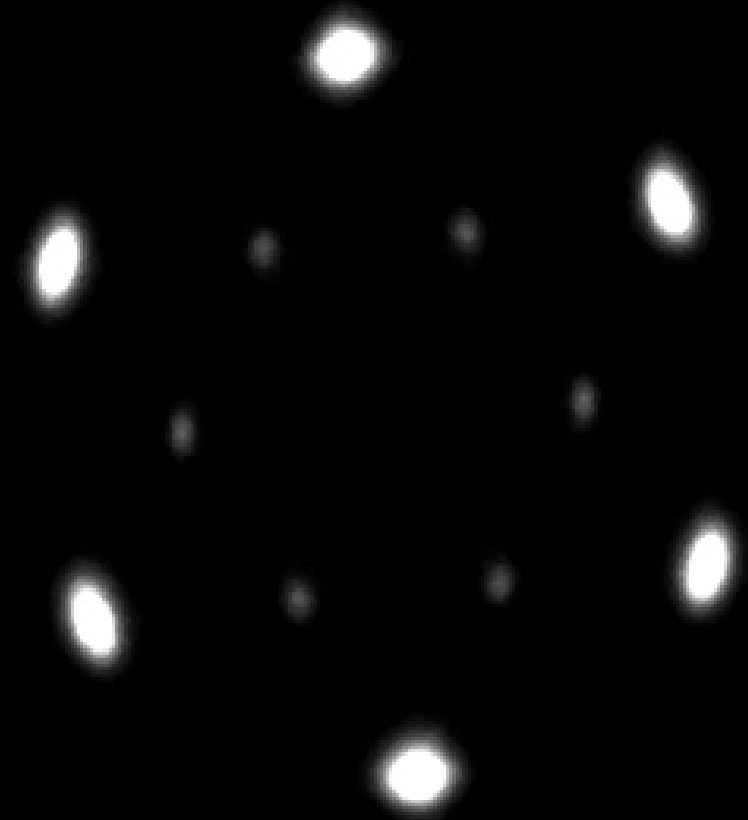


Characterization of photonic colloidal crystals
in
real and reciprocal space



Job Thijssen

Characterization of photonic colloidal crystals in real and reciprocal space

Job Thijssen

2007

Characterization of photonic colloidal crystals
in
real and reciprocal space

Cover Normal-incidence, X-ray diffraction pattern (edited) of a colloidal crystal consisting of approximately 350 nm diameter silica spheres in air.

Cover design the author

PhD thesis, Utrecht University, the Netherlands, May 2007.

ISBN: 978-90-393-4527-6

A digital version of this thesis is available at <http://www.colloid.nl/>

Supplemental information can also be downloaded from <http://www.colloid.nl/>

Characterization of photonic colloidal crystals in real and reciprocal space

Karakterisering van fotonische colloïdale kristallen in de reële en
in de reciproke ruimte

(met een samenvatting in het Nederlands)

Proefschrift

ter verkrijging van de graad van doctor aan de Universiteit Utrecht op gezag van de rector
magnificus, prof. dr. W. H. Gispen, ingevolge het besluit van het college voor promoties in het
openbaar te verdedigen op maandag 21 mei 2007 des middags te 2.30 uur

door

Job Hendrikus Jacobus Thijssen

geboren op 19 april 1980 te Wamel.

Promotor Prof. Dr. A. van Blaaderen
Co-promotor Dr. A. Imhof

Dit werk maakt deel uit van het onderzoekprogramma van de Stichting voor Fundamenteel Onderzoek der Materie (FOM), die financieel wordt gesteund door de Nederlandse Organisatie voor Wetenschappelijk Onderzoek (NWO).

This work is part of the research programme of the 'Stichting voor Fundamenteel Onderzoek der Materie (FOM)', which is financially supported by the 'Nederlandse Organisatie voor Wetenschappelijk Onderzoek (NWO)'.

The history of science teaches only too plainly the lesson that no single method is absolutely to be relied upon.

Lord Rayleigh

From *Accurate Measurement Is an English Science*,
by Simon Schaffer,
Chapter six in *The Values of Precision*,
edited by M. Norton Wise (1995).

Contents

1	Introduction	1
1.1	Photonic crystals – semiconductors for light	2
1.1.1	Photonic band gaps – a model	3
1.1.2	Photonic crystals – fabrication	6
1.2	Colloids	7
1.3	Photonic colloidal crystals	9
1.4	Reciprocal space	11
1.5	This thesis	16
2	Photonic band-structure calculations	17
2.1	Introduction	18
2.2	Theoretical background	20
2.2.1	The Maxwell equations in photonic crystals	20
2.2.2	The irreducible Brillouin zone	23
2.2.3	Irreducible Brillouin zones and crystal bases	25
2.2.4	Photonic band diagrams	26
2.2.5	Summary	26
2.3	Methods	27
2.4	Photonic band structure of Laves-phase colloidal crystals	28
2.4.1	Photonic band structure of MgCu ₂	30
2.4.2	Convergence in band-structure calculations	34
2.4.3	Summary	36
2.5	Photonic band structure of BCT crystals	37
2.5.1	KKR transmission spectra of body-centered tetragonal crystals	39
2.5.2	Surface modes in KKR transmission spectra	40
2.5.3	Summary	40
2.6	Photonic band-structure calculations & optical spectra	41
2.7	General conclusions and outlook	45
3	Microradian X-ray diffraction from photonic colloidal crystals	49
3.1	Introduction	50
3.2	Disorder in colloidal crystals	51
3.3	Resolution and coherence	52
3.4	Experimental methods	53
3.5	Wall crystallization of PMMA spheres	54
3.6	Photonic crystals with a periodicity larger than a micron	56

3.7	Disorder in a crystal of silica spheres	58
3.8	Measurements with X-ray films	61
3.9	Concluding remarks	61
4	Orientation, packing and stacking in convective assembly	65
4.1	Introduction	66
4.2	Theoretical model	68
4.2.1	Real space	68
4.2.2	Reciprocal space	70
4.3	Experimental methods	75
4.3.1	Sample fabrication	75
4.3.2	Characterization	76
4.4	Results and discussion	77
4.4.1	Orientation	77
4.4.2	Packing	82
4.4.3	Stacking	84
4.5	Conclusions and outlook	88
5	Towards binary colloidal crystals for photonic applications	91
5.1	Introduction	92
5.2	Experimental methods	95
5.2.1	Sample fabrication	95
5.2.2	Atomic layer deposition and silicon infiltration	96
5.2.3	Silica etching	96
5.2.4	Sample characterization	97
5.3	Results and discussion	97
5.3.1	Infiltrating crystals of organic colloids	97
5.3.2	Future challenges	104
5.3.3	Etching crystals of silica colloids	105
5.4	Conclusions and outlook	108
6	Electric-field-induced photonic colloidal crystals	111
6.1	Introduction	112
6.2	Experimental methods	113
6.2.1	Sample fabrication involving diffusion-polymerization	113
6.2.2	Sample fabrication involving photo-induced polymerization	115
6.2.3	Infiltrating crystals with silicon	116
6.2.4	Sample characterization	116
6.3	Results and discussion – diffusion-polymerization	117
6.4	Results and discussion – photo-induced polymerization	122
6.4.1	Characterization by confocal microscopy	123
6.4.2	Inverting BCT crystals	128
6.5	Results and discussion – diffraction and switching	132
6.6	Conclusions and outlook	136

7	Characterization of photonic colloidal crystals by microradian X-ray diffraction	139
7.1	Introduction	140
7.2	Experimental methods	140
7.2.1	Sample preparation	140
7.2.2	Sample characterization	141
7.3	Results and discussion	142
7.4	Conclusions	148
	Summary	151
	Samenvatting	155
	Acknowledgements	159
	Curriculum vitae	161
	Publications	163
	References	165

Introduction

In this introductory chapter, we attempt to explain the most important concepts of this thesis in an intuitive manner. First, the notion and the possible applications of photonic crystals are introduced in an analogy with electronic semiconductors. One of the most important properties of photonic crystals is the possibility of their having a photonic band gap. In a simple model, the basic physics behind photonic band gaps is clarified.

Although the concept of photonic band-gap materials is well-established, their fabrication remains challenging. Fabricating structures at submicrometer length scales using materials that have a high refractive index has turned out to be difficult. After a short overview of possible fabrication methods, self-assembly of colloidal particles is introduced as a possible fabrication method. The study of colloids is not limited to their self-assembly for photonic applications. What colloids are and the potential of colloidal dispersions to act as model systems for the phase behavior of atomic and molecular systems is discussed, after which their use as templates for the fabrication of photonic crystals is elaborated upon.

Characterization of crystalline structures consisting of submicrometer particles is discussed. Although far from trivial, real-space imaging is only touched upon briefly, as the notion of real space is intuitively clear. A large part of this thesis, however, is about characterization by scattering or diffraction, both of which are most easily described in reciprocal space. The concept of reciprocal space is more abstract than that of real space. Near the end of this introductory chapter, we ‘derive’ reciprocal space intuitively from the general real-space structure of crystals. Finally, the last section of the introduction contains a short outline of this thesis.

1.1 Photonic crystals – semiconductors for light

In 1947 William Shockley, John Bardeen and Walter Brattain built the first practical point-contact transistor at Bell Labs [1]. Nine years later, the three of them received the Nobel Prize in physics “for their researches on semiconductors and their discovery of the transistor effect” [2]. The importance of the transistor in today’s society can hardly be exaggerated. For example, present-day computers contain billions of transistors on chips that are the size of a finger tip! Actually, the transistor is the key component in nearly all modern electronics, ranging from cellular phones and MP3 players to digital cameras and DVD players.

Transistors are made of materials called ‘semiconductors’, examples of which are silicon and gallium arsenide. The ‘transistor effect’ itself relies on the electronic properties of semiconductors, the latter allowing accurate control over the flow of electric currents [3–5]. In a computer, for example, this ability to switch electric currents is used to transfer and store data. However, for long-distance data transfer between computers, like downloading websites, the data is usually converted to an optical signal and transferred via glass fibres. It would be faster and more reliable if the computer itself could handle optical instead of electronic signals. This would require the optical analogue of a transistor. Optical transistors, in turn, could possibly be realized using semiconductors for light in combination with non-linear optical effects.

The optical analogues of semiconductors are called photonic crystals [6]. These are structures in which the refractive index varies periodically in space in one, two or three dimensions (3-D) [7–9]. The refractive index n_m of a material is a measure of how strongly the material interacts with light. More specifically, it is the ratio of the speed of light c in vacuum and the speed of light c_m in the material [10, 11].

$$n_m = \frac{c}{c_m} \quad (1.1)$$

Differences in refractive index between materials cause phenomena such as refraction. It is straightforward to demonstrate refraction, just put a chopstick in a glass of water - when viewed from the outside in, the stick suddenly appears to be kinked (see Figure 2.1a). The kink is actually an optical illusion that is caused by refraction [12]. In a photonic crystal, the variation in refractive index forms a varying potential for light. In a way, this is similar to mountains and valleys forming a varying potential for cyclists. The periodicity in a photonic crystal is typically on the order of the wavelength of light. Matching the wavelength λ to the lattice spacing a results in Bragg diffraction. In photonic crystals, Bragg diffraction is the basic principle underlying important optical properties, including photonic band gaps. This is similar to electronic semiconductors, where Bragg diffraction of electrons can lead to electronic band gaps.

Electronic semiconductors consist of atoms, which have a typical size of 0.1 nm, about $100,000,000\times$ smaller than a typical marble, the latter having a diameter of approximately 1 cm. Electrons flowing through such a semiconductor interact with the atoms of which the material consists, a process that is analogous to water waves interacting with floats bobbing up and down the water. According to quantum mechanics, every particle also has a wave-like nature. The equation for the wavelength λ_{DB} that is associated with a particle was formulated by De Broglie [13].

$$\lambda_{\text{DB}} = \frac{h}{mv} \quad (1.2)$$

Here m is the mass of the particle, v is its speed and $h \approx 6.6 \cdot 10^{-34}$ Js [14] is a physical constant that is known as Planck's constant. To give an idea of associated length scales, a human being walking at a speed of $v = 4$ km/h ≈ 1 m/s has a De Broglie wavelength on the order of 10^{-35} m. As typical length scales in their environment are on the order of a meter, humans never notice their wave-like nature in daily life. Electrons in a semiconductor, however, have a typical wavelength of $\lambda_{\text{DB}} \sim 0.1$ nm [15], which is similar to the size of and the spacing between surrounding atoms. In a photonic crystal, one would like to manipulate the flow of (visible) light, which has a typical wavelength of 500 nm. Therefore, photonic-crystal building blocks should have a size that is comparable to 500 nm, which brings them into the realm of colloids (see Section 1.2).

Provided the refractive-index contrast between the photonic-crystal building blocks and their host medium is large enough, and a suitable crystal structure is chosen, three-dimensional (3-D) photonic crystals can exhibit a photonic band gap. This means that light of a certain frequency range ('color range') cannot propagate within the crystal in any direction, regardless of its polarization [16–18]. Thus, a photonic band gap is the optical analogue of an electronic band gap in semiconductors. Photonic band-gap materials interact strongly with light and can provide unprecedented control over both the emission and the propagation of light [19–25], allowing important applications in, for example, optical integrated circuits and infrared telecommunications [26–28].

1.1.1 Photonic band gaps – a model

To get an intuitive idea of what a photonic band gap is, consider a linear chain of very thin, semi-transparent, two-sided mirrors (see Figure 1.1a). This configuration forms a 1-D crystal in which the mirrors have a lattice spacing a . An electromagnetic wave is incident from the left and travels towards the right (see Figure 1.1a), which can be described mathematically by a cosine function [10, 11].

$$\mathbf{E}_+(z, t) = \mathbf{E}_0 \cos(kz - \omega t) . \quad (1.3)$$

Here $\mathbf{E}_+(z, t)$ is the electric field of the light wave, \mathbf{E}_0 is its amplitude, including the direction of polarization, $k = (2\pi/\lambda)$ is the wave vector, with λ the wavelength, ω is the (angular) frequency of the wave, z is the position coordinate along the z -axis and t is time. Maxima of the wave are reached when its phase

$$\varphi(z, t) = kz - \omega t \quad (1.4)$$

is equal to $2\pi \cdot m$ for integer m . If we consider the maximum for which the phase is 0 (see Figure 1.1a), it is clear that its z -coordinate z_0 increases with increasing t , as $kz_0 = \omega t$ in that case. In other words, the wave is indeed travelling towards the right, which is why its electric field \mathbf{E}_+ has a subscript $+$.

The semi-transparent mirrors allow part of the light to pass, while the other part is reflected. Because of reflections from the mirrors, several waves in the 1-D crystal travel towards the right (\mathbf{E}_+), while other waves travel towards the left (\mathbf{E}_-). Being an elastic process, the wavelength λ and the angular frequency ω of the wave do not change upon reflection, only the sign of k .

$$\mathbf{E}_-(z, t) = \mathbf{E}_0 \cos(-kz - \omega t) . \quad (1.5)$$

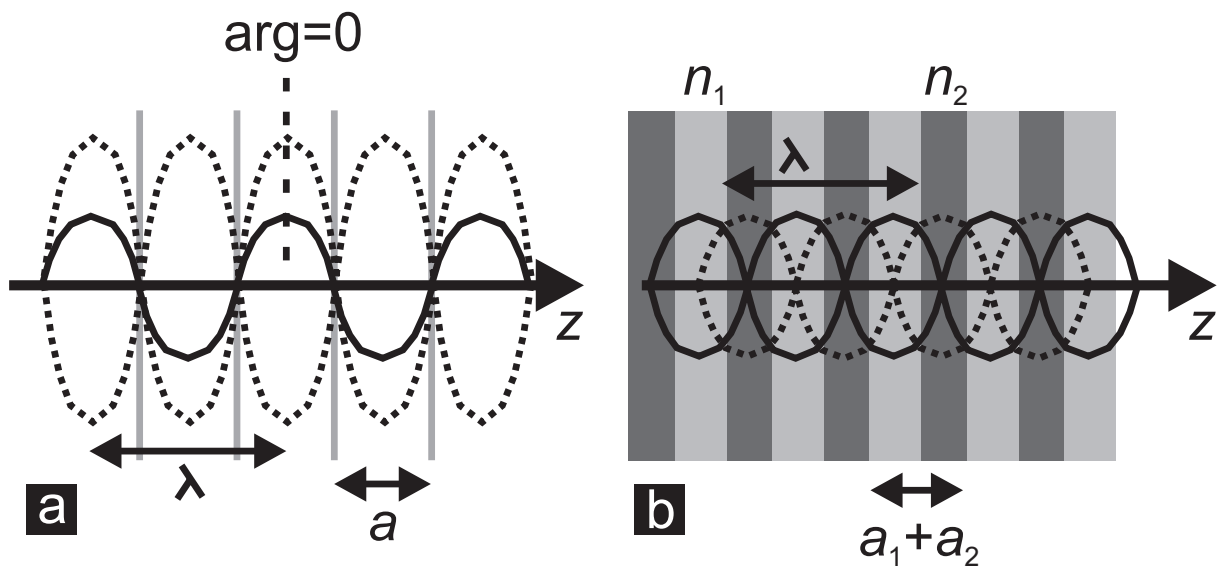


Figure 1.1: Panel (a) is a schematic representation of a 1-D crystal of very thin, semi-transparent, two-sided mirrors with lattice spacing a . An electromagnetic wave propagating to the right (solid line) and the profile of a standing wave caused by Bragg diffraction (dotted line) have been drawn as well. The dashed vertical line intersects the maximum of the wave that we have, arbitrarily, chosen as the maximum for which the absolute value of the argument of the cosine function is 0. Panel (b) shows the same system after insertion of dielectric slabs with refractive indices n_1, n_2 and subsequent removal of the mirrors. The optical thickness of the slabs is a_1 and a_2 , respectively. Both the solid line and the dotted line represent standing-wave profiles. For clarity, the amplitude of the standing waves has been rescaled compared to panel (a).

Electromagnetic waves obey the superposition principle, which means the electric field $\mathbf{E}(z, t)$ at any position z and any time t is equal to the sum of the individual electric fields. For simplicity, consider one wave \mathbf{E}_+ that is travelling through the 1-D crystal towards the right and one wave \mathbf{E}_- that is travelling towards the left. The total electric field is then

$$\mathbf{E} = \mathbf{E}_0 \cdot (\cos(kz - \omega t) + \cos(-kz - \omega t)) . \quad (1.6)$$

Using trigonometry [29],

$$\cos \alpha + \cos \beta = 2 \cos \left(\frac{1}{2} (\alpha + \beta) \right) \cos \left(\frac{1}{2} (\alpha - \beta) \right) , \quad (1.7)$$

the total electric field can be written as

$$\mathbf{E} = 2\mathbf{E}_0 \cdot \cos(kz) \cdot \cos(\omega t) . \quad (1.8)$$

Note that we have not attributed an additional phase shift to the argument of the wave travelling towards the left in Equation 1.6. This is only possible if transmitted and reflected waves are in phase, i.e. the positions z where the electric fields are 0 overlap for all t . In this case, the waves ‘fit’ the lattice:

$$p \cdot \left(\frac{\lambda}{2} \right) = a \quad \text{with } p \in \mathbb{Z} . \quad (1.9)$$

If Equation 1.9 is combined with the definitions of k and ω

$$\omega = 2\pi\nu = \frac{2\pi c}{\lambda} , \quad (1.10)$$

after which these expressions for k and ω are inserted into Equation 1.8, the final result is

$$\mathbf{E} = 2\mathbf{E}_0 \cos \left(\left(\frac{\pi}{a} \right) pz \right) \cos \left(\left(\frac{\pi c}{a} \right) pt \right) \quad \text{with } p \in \mathbb{Z} . \quad (1.11)$$

In Equations 1.8 and 1.11, the position z_{\max} of a maximum no longer depends on the time t . At any moment in time, the total electromagnetic field $\mathbf{E}(z, t)$ has a spatial distribution that is described by a cosine function. The amplitude of this sinusoidal profile varies in time with an angular frequency ω . This means the total wave is not travelling anymore, it is a standing wave. Thus, if the wavelength matches the lattice parameter, our 1-D crystal of mirrors does not support propagating modes, i.e. it has a stop gap along the z -axis at the corresponding (angular) frequency ω . It is basically the result of coherent, or in-phase, reflections from the mirrors.

Real 1-D photonic crystals do not consist of mirrors on a lattice. To make a transition to a more realistic model, the space in between two mirrors is filled with two slabs of dielectric material, having a refractive index of n_1 and n_2 , respectively (Figure 1.1b). If $n_1 \neq n_2$, the wavelength of light travelling through the crystal is different in different slabs, which complicates our discussion. Fortunately, we can introduce a useful concept from optics, the so-called optical distance, which is the distance Δx_{op} that light travels in vacuum in the same amount of time that it requires to travel a distance Δx in the material under consideration. From Equation 1.1, it is clear that real and optical distances are proportional and that the proportionality constant is the material refractive index n_m .

$$\Delta x_{\text{op}} = n_m \cdot \Delta x \quad (1.12)$$

The major advantage of using optical thicknesses is that the wavelength of light in the dielectric slab of optical thickness a_1, a_2 is the same as its wavelength in vacuum. After all, the decrease of the speed of light in the material has been incorporated in the optical thickness. Note that the (angular) frequency ν, ω of an electromagnetic wave is independent of the material refractive index - blue light that travels from air into a piece of glass will stay blue.

If $n_1 = n_2$, nothing really changes in our model, except for the frequency at which standing waves are generated, for that depends on the optical thickness of the slab (Equation 1.11). If $n_1 \neq n_2$, thus obtaining the well-known Bragg stack [7], we can actually remove the mirrors (see Figure 1.1b). After all, any dielectric interface between two substances with non-equal refractive indices n_1, n_2 acts as a partially transparent mirror with a transmission and a reflection coefficient that can be derived from the boundary conditions of the Maxwell equations [10]. Being analogous to the previously discussed crystal of mirrors, it is not hard to see that standing waves can also be generated in Bragg stacks. Two possible standing waves are shown in Figure 1.1b. The energy that is stored in such a standing wave is mainly concentrated at the positions of the maxima. One of the standing waves concentrates its energy in the low-dielectric phase, n_1 for example (solid line), while the other concentrates its energy in the high-dielectric phase n_2 (dotted line). Modes that store their energy in the high-dielectric phases have a lower energy than modes that store their energy in the low-dielectric phase [7]. Modes that have a lower energy also have a lower frequency ($U_{\text{photon}} = \hbar\omega$). In other words, the difference in refractive index of the slabs causes two non-propagating modes that have the same wavelength, and thus the same absolute value for the wave vector, but different angular frequencies ω_1 and ω_2 . If $n_1 \approx n_2$, the difference between ω_1 and ω_2 will be small. Increasing the refractive-index contrast (n_2/n_1) will cause ω_1 and ω_2 to move further apart along the frequency axis, thus opening up a range of forbidden frequencies ('colors') for propagating modes along the z -axis, i.e. a stop gap along z . For a more rigorous treatment of the (1-D) Bragg stack, we refer to Reference [30].

In a 3-D photonic crystal, crystal planes act as dielectric slabs, effectively forming Bragg stacks along directions in the crystal that are perpendicular to the different sets of planes. For specific frequency ranges, Bragg diffraction along such a crystal direction can open up stop gaps. If stop gaps along all crystal directions (partly) overlap, there is a frequency range for which electromagnetic-wave propagation within the crystal is forbidden in any direction, regardless of polarization [16–18]. That frequency range is referred to as a photonic band gap. To find photonic band gaps for 3-D structures, the dispersion relation $\omega(\mathbf{k})$ is plotted along carefully selected directions in reciprocal space, the latter being the collection of all possible wave vectors \mathbf{k} . The gaps are recognized as frequency ranges for which corresponding wave vectors do not exist. Such band diagrams are discussed in more detail in Chapter 2.

1.1.2 Photonic crystals – fabrication

Although the photonic properties of periodic dielectric media were already theoretically investigated in the 70s of the 20th century [16], the concept of a photonic crystal really took flight with the publications of Yablonovitch and John in 1987 [17, 18]. Early calculations showed that face-centered cubic structures of low-dielectric spheres in a background medium with a higher dielectric constant, a so-called inverse FCC structure, should have a gap between bands 8 and 9 if the dielectric contrast exceeds ~ 7 [31]. Diamond has always been a strong candidate for photonic band-gap materials as well, though early calculations for the diamond structure

were plagued by convergence issues [31–34]. One of the first proposals for the fabrication of photonic crystals was the so-called Yablonovite-structure [35]. Drilling cylindrical holes along specific directions in a block of material would create a connected network with a symmetry that resembles that of diamond [36, 37]. The latter is, together with pyrochlore, the presently known clear champion structure, both for opening up a band gap at the lowest refractive-index-contrast ratio (~ 2) and the largest band-gap width to center-frequency ratio [32, 38]. A few years after the introduction of its concept, Yablonovite was actually fabricated at the micron scale by chemically assisted ion-beam etching [39].

Since Yablonovite, several other schemes and fabrication methods have been developed for the fabrication of 3-D photonic crystals. One of the first was lithography [40–42], which relies on techniques that were borrowed from the semiconductor industry. The major advantage of lithography is that it allows great flexibility in the shape of the features that are written into a 2-D slab of material. Although the periodicity with which structures can be written is quite accurate, the size-dispersion of the features themselves is rather large. Moreover, lithography is essentially a 2-D technique, making it less suitable for the fabrication of truly 3-D structures. In a layer-by-layer fashion, lithography can be used to build, for example, a 3-D woodpile structure [41–43]. The symmetry of the woodpile structure is similar to that of diamond. It is no surprise then that it has a relatively wide band gap [44]. Unfortunately, the 2-D nature of lithography causes lateral alignment problems when the number of layers gets larger than approximately 7. This means that, for example, the 5th layer is not always exactly above the 1st layer, as it should.

Recently, concentrated polyelectrolyte inks were developed to directly ‘write’ microperiodic structures without using masks [45]. The inks flow readily through fine deposition nozzles, but solidify quickly upon deposition. In this way, structures can be literally written in 2-D, seemingly not unlike writing your name on a cake with whipped cream. Layer-by-layer writing subsequently results in truly 3-D structures. Methods to obtain 3-D photonic crystals without layer-by-layer processing include multibeam holography and two-photon lithography [46–48]. An interference pattern that mimics the crystals symmetry of the desired structure is set up in a 3-D block of photo-resist (usually SU-8 [46, 49]). At the positions where the laser beams interfere constructively, the intensity gets high enough for polymerization of the photo-resist to take place. After illumination with laser light, the unexposed parts of the resist can be washed away, resulting in a 3-D photonic crystal. Mechanical stability limits the possible structures to bicontinuous ones. More importantly, the polymerized photo-resist is not heat-resistant, which means raising the refractive-index contrast within such a crystal above the threshold is difficult, though major progress has recently been made [50]. Finally, a promising route towards 3-D photonic crystals having areas on the order of mm^2 and a large number of layers ($\gtrsim 25$) is self-assembly of colloidal particles.

1.2 Colloids

Though many people may not realize it, we eat and use colloids almost daily. Milk, paint, ink, toothpaste, shampoo and sunblock are but a few examples of colloidal systems in everyday life. More than that, a large fraction of the material of which our own body consists, our blood namely, is colloidal in nature. The term ‘colloidal’ refers to a state of matter in which the material is finely distributed in a suspending medium. With that in mind, one could define colloids

as mesoscopic particles of which at least one dimension has a size between a few nanometers (~ 0.000001 mm) and a few micrometers (~ 0.001 mm) [51]. Asbestos, for example, is a colloidal rod that typically has a length of $3\ \mu\text{m}$ to $20\ \mu\text{m}$, the latter exceeding the colloidal size range, but it can be as thin as $0.01\ \mu\text{m}$ [1]. For comparison, a human hair is typically $17\ \mu\text{m}$ to $181\ \mu\text{m}$ in width [1]. Another example of a colloidal system is clay, for it consists of colloidal platelets in water. It is no surprise then that colloids are also important to farmers, though they may not be conscious of it, as colloidal processes can have a major impact on the structure of soil [52].

The word ‘colloid’ was derived from the Greek word ‘ $\kappa\omicron\lambda\lambda\alpha$ ’, meaning ‘glue’. It was introduced by Thomas Graham in his 1861 paper *Liquid Diffusion Applied to Analysis* [53], where he describes two classes of matter, ‘crystalloids’ and ‘colloids’. In his experiments, crystalloids diffused through a membrane separating pure water from an aqueous solution of such crystalloids (like salt). Other substances, including gum arabic and gelatin, did not diffuse through the membrane. Because of the gluey nature of these substances, he called them colloids [51]. Nowadays, the material of which a particle consists no longer determines whether it is a colloid or not, it is the size of the particle that matters. Colloids, and the suspending medium, can consist of various materials in various phases. Fog, for instance, consists of finely distributed water droplets in air. Emulsions, like vinaigrette, consist of colloidal droplets of one liquid that are suspended in another liquid. In the case of vinaigrette, small droplets of water (vinegar) are suspended in oil (typically olive oil). As water is polar and oil is apolar, the two liquids do not like to mix. If we mix water and oil, they will separate into a system with a water-phase and an oil-phase. Everyone who prepares vinaigrette occasionally knows this - you have to add mustard to prevent the separation. The mustard acts as an emulsifier that stabilizes the emulsion against phase separation. In the research that is described in this thesis, we fabricated photonic crystals from colloidal dispersions - systems in which solid particles are suspended in a solvent. Paint and ink are common examples of dispersions. We used chemically synthesized colloidal silica (‘glass’) spheres in organic solvents, including ethanol (‘alcohol’) and dimethyl sulfoxide (DMSO).

The colloidal size range of several nanometers (nm) up to several micrometers (μm) may seem arbitrary. There are, however, good reasons for the lower and upper limits on the size of colloidal particles. Consider, for example, a dispersion of silica spheres in ethanol. We wish to describe this system as a collection of solid spheres in a homogeneous, smooth background medium. If our colloids are very small, about the size of the ethanol molecules themselves, the background cannot be treated as a homogeneous medium, for the colloids will be hard to distinguish from the ethanol molecules by size. Ethanol molecules have a size on the order of 0.5 nm. If the silica colloids are a couple of nm in diameter, we can integrate out the degrees of freedom of the solvent molecules. The integration procedure yields a homogeneous background medium in which the colloids then have acquired a mutual, effective interaction [54]. In short, the lower limit on the size of colloids is set by the size of the solvent molecules.

The upper limit on the length scale of colloids is related to the phenomenon of Brownian motion. The name is derived from the 19th century botanist Robert Brown, who observed a jittery motion of plant spores while studying plant pollen floating in water [55]. The explanation for the random walk of small (solid) particles suspended in a liquid was provided by Albert Einstein [56], who claimed that the motion was due to unbalanced momentum, at any time t , from collisions with solvent molecules. Not only did the paper explain the origin of Brownian

motion, in combination with the experimental verification by Jean Baptiste Perrin, it also convinced many scientists of the existence of molecules, a concept that was not generally accepted in the 19th century. Colloids are still small enough to experience Brownian motion due to collisions with solvent molecules. A grain of sand in water on the other hand, with a typical size of about 1 mm, does not perform Brownian motion on the length scale of a mm, for it is too large and too heavy to ‘feel’ the water molecules - it will just sink to the bottom of the container. The fact that colloids perform Brownian motion enables them to redistribute (kinetic) energy via the thermal motion of the solvent molecules. Therefore, they can explore many different configurations, moving along a trajectory in phase space. In other words, a colloidal system can reach thermodynamic equilibrium.

Their ability to reach thermodynamic equilibrium is one of the key properties of colloidal systems. It basically means that colloidal systems exhibit analogous phase behavior as atoms and molecules. For example, a dispersion of colloids with a hard-sphere interaction potential, which means they only interact when they physically collide, can form a liquid phase, a crystalline phase and even a glassy phase [57]. Which phase is formed, depends on the concentration of colloids. In other words, colloidal dispersions are a model system for atomic and molecular processes [58], including melting and crystallization.

One might wonder why processes such as melting and crystallization are studied in colloidal systems in addition to the actual atomic and molecular systems. The reason is straightforward - atoms and molecules are so small that it is very hard to observe them individually. Even if they can be visualized, using high-resolution transmission electron microscopy (TEM) or atomic force microscopy (AFM) for example, it is still impossible to probe their trajectories. As colloids are much larger than a typical molecule, and severely overdamped due to friction with the solvent, they are much more accessible experimentally. Jean Baptiste Perrin used ordinary light microscopy to observe the sedimentation profile of colloids in a dispersion, from which he could extract Avogadro’s number, i.e. the number of particles in one mole of substance ($N_A \approx 6 \cdot 10^{23} \text{ mol}^{-1}$). His work was basically an experimental verification of Einstein’s theory of Brownian motion. In 1926, Perrin received the Nobel Prize in Physics “for his work on the discontinuous structure of matter, and especially for his discovery of sedimentation equilibrium” [59], which is one of the few Nobel Prizes that have been awarded to colloid research since its introduction in 1901. Nowadays, the more advanced technique of confocal microscopy can be used to image dispersed colloids in 3-D and in real time, thus allowing quantitative real-space characterization using image-analysis software. Another advantage of studying phase behavior in colloidal systems is that the interactions between colloidal particles can be tuned using chemical synthesis or external fields (see Chapter 6).

1.3 Photonic colloidal crystals

Colloids are not only interesting from a fundamental point of view, they are also used for various applications, including smart shock absorbers and electronic paper (e-paper) [60, 61]. Moreover, due to their ability to reach thermodynamic equilibrium, monodisperse colloids are able to self-assemble into regular arrays, which are known as colloidal crystals [57]. If the refractive index of the colloids is different from that of the surrounding medium, they form a 3-D structure in which the refractive index varies periodically in space, i.e. they form a photonic crystal. In

other words, if $n_{\text{colloid}} \neq n_{\text{medium}}$, colloidal crystals are photonic crystals by definition. Even colloids that only have a hard-sphere interaction can form colloidal crystals. The only prerequisite is that the polydispersity of the particles, i.e. the relative width of their size distribution, is small enough ($\lesssim 0.07$) [62].

The driving mechanism behind crystallization of hard-sphere colloids is maximization of entropy. A system reaches thermodynamic equilibrium when it minimizes its free energy F [63].

$$F = U - TS \quad (1.13)$$

Here, U is the total (interaction) energy of the system, T is its temperature and S is the entropy of the system. In the case of hard spheres, the energy U plays no role in minimizing the free energy F , for the interaction energy of two spheres is either 0 (no overlap) or infinitely large (overlap). Thus, the hard-sphere interaction only reduces the volume that is available to the colloids. Entropy is a measure of the number of possible microscopic configurations, a single configuration being a set of values for all particle coordinates and momenta, that the system can assume for given values of some macroscopic observables, such as temperature and pressure. Even in textbooks on thermodynamics, entropy is sometimes related to *chaos* or *disorder*. The idea is that there are more ways for a system to be disordered than there are ways to be ordered. However, entropy is actually a measure of the volume that is available to the system in phase space, a volume that we cannot ‘see’ in real space. Colloids in a crystal are, of course, ‘trapped’ in the unit cell surrounding their lattice position. However, at high concentrations of colloids, the particles can have more freedom of movement within their cell than they would have had in a liquid at the same concentration. In a way, this is similar to a crowded disco. If everyone in the disco would be assigned an equally large area on which they should dance, many more party people would fit in the same disco without feeling crowded. In this way, we can understand intuitively why an ordered system may have a larger number of possible microscopic configurations than a disordered system having the same values for some macroscopic observables, i.e. why an ordered system can have a higher entropy than a disordered system [64].

As was already mentioned, colloidal crystals are photonic crystals by definition. Unfortunately, in the case of silica colloids in ethanol, the refractive-index contrast between silica and ethanol is too small to open up a band gap [31, 65, 66]. Even if we allow the ethanol to evaporate, leaving behind a crystal of silica spheres in air, the index contrast would be no larger than approximately 1.5, which is still too low to open up a band gap. Even worse, increasing the refractive index of the spheres is of no avail in this case. At best, the colloids self-assemble into face-centered cubic (FCC) structures, which only have a band gap if the index contrast ($n_{\text{max}}/n_{\text{min}} \gtrsim 3$ and the refractive index of the spheres must be smaller than that of the surrounding medium ($n_{\text{colloid}} < n_{\text{medium}}$). It is possible, however, to use the colloidal crystal as a template for infiltration with high-index materials, such as silicon or germanium [67–69]. The space in between the spheres can be filled with such materials by, for example, chemical vapor deposition (CVD) and atomic layer deposition (ALD) [70, 71]. In such processes, no material can be deposited at the contact point of two spheres. If the spheres could be removed, the contact point would be a connecting hole between two air spheres. Hydrofluoric acid (HF) can be used to etch the silica template. Through the connecting holes, the HF can reach all of the spheres in the crystal, thus allowing complete removal of the silica template. The resulting crystal consists of air spheres in a background of, for example, silicon (Figure 1.2a). Calculations have shown that such an inverse FCC crystal of air spheres in silicon has a photonic band gap [31, 65, 66].

Optimization of the gap width is possible by tuning the thickness of the deposited silicon layer.

Several ways of fabricating colloidal-crystal templates by self-assembly have been explored over the past few years. One of the most straightforward ones is sedimentation - allow colloids with a density that is higher than that of the solvent to settle under the influence of gravity. At the bottom of the container, the volume fraction of spheres will increase (locally), thus causing crystallization. The 1st layer of the crystal, which rests on the bottom of the container, is hexagonally packed. Particles in the 2nd layer, which is also hexagonal, will rest on 3 particles of the 1st layer. In a way, this is similar to stacking oranges in a crate. However, there are 2 possible, lateral positions for the 2nd layer, denoted by B and C, the 1st layer being denoted by A (see Figure 4.1b). If the stacking sequence of subsequent layers is ABAB, the resulting crystal is hexagonal close-packed (HCP). If the stacking sequence is ABCABC, the final crystal structure is face-centered cubic (FCC). Unfortunately, the free-energy difference between HCP and FCC is small ($\sim 10^{-3}k_{\text{B}}T$) [72, 73], resulting in uncontrolled mixtures of FCC and HCP, which is referred to as random hexagonal close-packed (RHCP). Calculations have shown that (stacking) disorder in these crystals deteriorates their photonic properties [74, 75]. In addition, for entropic reasons, sedimented colloidal crystals have a layer of colloidal fluid on top. For 1.4 μm diameter silica particles, a layer of colloidal fluid as thick as 8 interlayer spacings is required to build up enough pressure to keep the crystal below from melting. As it leads to isotropic scattering, such a fluid layer is undesirable.

To circumvent problems encountered in sedimentation, several other self-assembly schemes have been explored. Controlled drying, also known as convective assembly, yields close-packed crystals that are uniform in orientation and thickness over areas on the order of cm^2 [76]. These crystals do not have a layer of colloidal fluid on top. Tuning the particle volume fraction even allows control over the number of layers in the resulting crystals [77]. The 3-D structure of the crystals is generally considered to be face-centered cubic (FCC, see also Chapter 4). Unfortunately, controlled drying is difficult for larger particles ($\gtrsim 400 \text{ nm}$), as their weight causes them to sediment too fast. Methods have been developed to counteract sedimentation in controlled drying of larger particles, but it has proven to be difficult to tune experimental parameters such that these methods work reproducibly. Other self-assembly techniques include colloidal epitaxy [78, 79], spin coating [80] and the application of shear flows [81, 82].

Compared to other PC fabrication methods, colloidal self-assembly is rather inexpensive. An additional advantage is that structure, size and composition of the individual building blocks can be modified in order to tune their optical properties. Advances in chemical synthesis have resulted in, for example, anisotropic particles [83–86], core-shell morphologies [87–89], metalodielectric colloids [90], and the incorporation of luminescent materials, such as fluorescent dyes [91, 92], rare-earth ions [93] and even quantum dots [94]. Furthermore, the interparticle potential can be affected by external fields [95], including electric fields (Chapter 6) and optical fields [96, 97].

1.4 Reciprocal space

As was explained in the previous section, colloidal crystals can be used as templates for the fabrication of photonic crystals. However, the multistep fabrication procedure can significantly affect the final 3-D structure of the resulting photonic crystals. For example, the force that

is exerted on particles in a colloidal crystal upon drying can be compared, after scaling, with the force that is exerted on a crystal of oranges when a truck drives over it [98]. Therefore, it is important to characterize the photonic colloidal crystals in 3-D at the various stages of their fabrication. Initial characterization is usually performed in real space. Although sound, quantitative analysis of real-space data is far from trivial, the concept of real-space imaging is easy. Real-space imaging is WYSIWYG (what-you-see-is-what-you-get) - if you want to have a real-space image of a crystal of marbles, just take a digital camera and make a photograph of the structure.

As colloids are approximately $10,000\times$ smaller than marbles, techniques to image them in real space are more advanced than the average digital camera. A popular imaging technique for colloidal systems is scanning electron microscopy (SEM). Although SEM yields beautiful images, thus yielding important information on mostly qualitative sample characteristics, it only provides topological information on a small part of the accessible 2-D surface. To obtain truly 3-D information, optical techniques are more suitable, as the penetration depth of electrons is only on the order of 10 nm. Over the past few years, it has been recognized that fluorescence confocal microscopy is a very useful technique to characterize photonic crystals at several stages of their fabrication [78, 99, 100]. The 3-D coordinates of all particles in the measurement volume can be extracted from 3-D stacks, thus allowing quantitative, real-space analysis using bond-order parameters [101, 102]. Unfortunately, it requires refractive-index matching, which is impossible for structures with a high dielectric contrast, such as colloidal crystals of air spheres in silicon.

Apart from the necessity of index matching, confocal microscopy has two additional disadvantages. First of all, it has limited resolution, because of which it is mainly useful for particles with a diameter larger than 600 nm. Secondly, its field of view is rather small, on the order of $150\ \mu\text{m} \times 150\ \mu\text{m}$ for sub-micron resolutions, which is a typical problem for most real-space characterization techniques. However, using convolution algorithms, several real-space images of adjacent sample areas can be stitched into a 'panorama' view. Scattering techniques, on the other hand, are able to provide detailed macroscopically-averaged information and are superior in quantitative determination of the order parameters over large distances, as long as the coherence length is not a limiting factor. In Chapter 7, we demonstrate that X-ray scattering is an excellent way to characterize photonic crystals, even if refractive-index matching is no longer an option.

As photonic crystals are spatially regular structures, scattering from different particles is coherent, leading to constructive interference in some directions and destructive interference in other directions, i.e. diffraction. Interference manifests itself in many phenomena in everyday life. If one drops two stones in a pond of water, the pattern that is formed on the surface is caused by interference of the water waves emanating from the positions where the stones hit the water. Colors in rain droplets on your glasses, rainbows, colors in soap bubbles or oil films, these are all examples of interference of light [12]. Even nature itself employs interference to produce colors, e.g. in the tail feathers of peacocks and the wings of butterflies [103]. Because they rely on interference, such colors are more vibrant, less diffuse, than colors caused by scattering & absorption, such as colors in paints.

The basic idea behind diffraction as a characterization technique for colloidal crystals is to look at the directions in which an incident wave is scattered by the sample and to derive from that the 3-D structure of the crystal. In the case of light scattering or X-ray diffraction, the incident wave is an electromagnetic wave. As any wave can be described as a superposition of

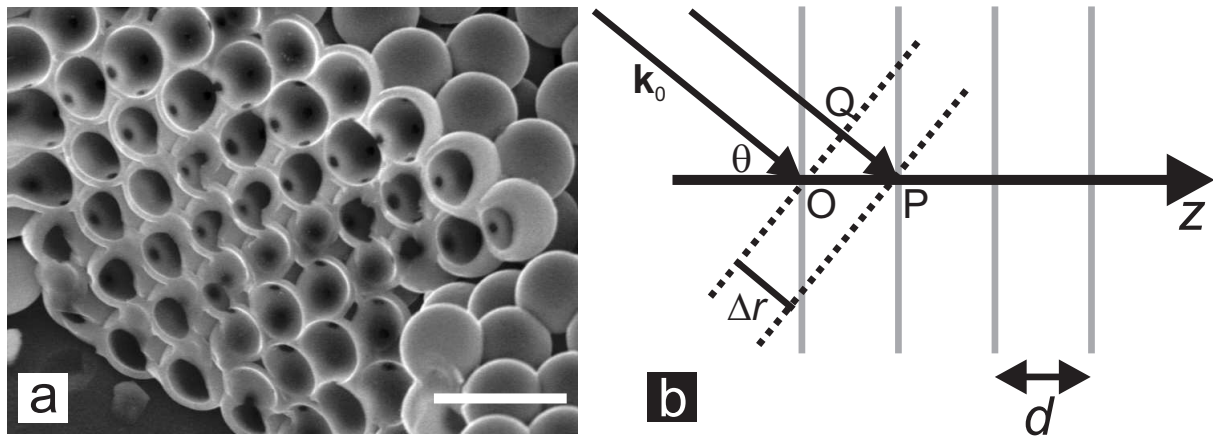


Figure 1.2: Panel (a) is a side-view of a photonic crystal of air spheres in silicon. After fabrication, the crystal was cleaved, allowing images of the bulk of the crystal to be taken in a scanning electron microscope (SEM). The ‘holes’ in the silicon used to be the contact points of the spheres in the colloidal-crystal template consisting of silica spheres. The white scale bar is $2 \mu\text{m}$, image courtesy of Dannis 't Hart. Panel (b) is a schematic image of a 1-D crystal. The crystal planes, indicated by the gray lines, are separated by an interplanar distance d . An electromagnetic (light) wave with wave vector \mathbf{k}_0 is incident under an angle θ .

plane waves, we can restrict our attention to plane waves.

$$\mathbf{E}(\mathbf{r}, t) = \mathbf{E}_0 \cos(\varphi(\mathbf{r}, t)) \quad (1.14)$$

Here $\mathbf{E}(\mathbf{r}, t)$ is the electric field of the wave, \mathbf{E}_0 is its amplitude, including the polarization, and $\varphi(\mathbf{r}, t)$ is the phase of the wave at position \mathbf{r} and time t

$$\varphi(\mathbf{r}, t) = \mathbf{k}_0 \cdot \mathbf{r} - \omega t . \quad (1.15)$$

The amplitude of the wave in Equation 1.14 is constant in space, which means it is not a good probe of spatial periodicity in crystals. As the phase $\varphi(\mathbf{r}, t)$ depends on \mathbf{r} , it can be used to probe the spatial coherence within the sample. Since we are not interested in temporal coherence, we will neglect the time-dependence of the phase here.

Consider a 1-D crystal on which an electromagnetic wave with wave vector \mathbf{k}_0 is incident (see Figure 1.2b). The distance between the crystal layers is d . As the wave propagates through the crystal, its phase changes with the distance travelled by the wave front.

$$\Delta\varphi = k_0\Delta r \quad (1.16)$$

Using the triangle OPQ, it is straightforward to show that $\Delta r = \Delta z \cos(\theta)$, yielding

$$\Delta\varphi = k_0\Delta z \cos(\theta) . \quad (1.17)$$

Taking the limit for $\Delta z \rightarrow 0$, we can derive an expression for the partial phase derivative $\varphi'(z)$.

$$\varphi'(z) = \frac{\partial\varphi}{\partial z} = \lim_{\Delta z \rightarrow 0} \left(\frac{\Delta\varphi}{\Delta z} \right) = k_0 \cos(\theta) \quad (1.18)$$

It follows directly from Equation 1.18 that the phase derivative $\phi'(z)$ is maximal, and the crystal planes are surfaces of constant phase, for normal incidence ($\theta = 0$). From vector calculus [104], it is known that the direction in which a function changes its value fastest is the direction of its gradient. So, in our example, the phase gradient $\nabla\phi$ points in the z -direction and has a length of k_0 .

One could say that the direction of the phase gradient probes the periodicity of the crystal most effectively, as it is the direction along which phase changes as a function of displacement are maximal. Moreover, as was already mentioned, crystal planes are also surfaces of constant phase along the direction of the phase gradient. Since plane waves \mathbf{k}_0 have a planar wave front that is perpendicular to their direction of propagation, it seems only natural to describe wave vectors as linear combinations of basis vectors (\mathbf{b}_i) that point in directions that are perpendicular to sets of crystal planes. The vector space that is spanned by such a set of basis vectors $\{\mathbf{b}_i\}$ is called *reciprocal space*. The set of all points in reciprocal space that are a linear combination of the reciprocal-space basis vectors $\{\mathbf{b}_i\}$ for integer coordinates is called *the reciprocal lattice*. In a 1-D crystal, there is only one set of crystal planes, so there is only one reciprocal-space basis vector \mathbf{b} . It points in the same direction and it has the same unit as the phase gradient.

So far, we have only considered the direction of the reciprocal-space basis vector \mathbf{b} in our 1-D model. The length of \mathbf{b} is determined by the condition for constructive interference at normal incidence. As we are only interested in how the crystal under considerations *changes* the direction of the incident wave \mathbf{k}_0 , we introduce the scattering vector \mathbf{q} as the vector difference between the outgoing wave \mathbf{k} and the incoming wave \mathbf{k}_0

$$\mathbf{q} = \mathbf{k} - \mathbf{k}_0 . \quad (1.19)$$

Furthermore, instead of the wave vectors themselves, we write \mathbf{q} as a linear combination of \mathbf{b} .

$$\mathbf{q} = \ell\mathbf{b} \quad (1.20)$$

At normal incidence, in the case of constructive interference, the standing wave that is set up in the crystal (Section 1.1) causes the incoming wave $\mathbf{k}_0 = k_0\hat{z}$ to be reflected into the outgoing wave $\mathbf{k} = -k_0\hat{z}$.

$$\begin{aligned} \mathbf{q} &= -k_0\hat{z} - k_0\hat{z} = \ell b_3\hat{z} \\ &= -2k_0\hat{z} = \ell b_3\hat{z} \end{aligned} \quad (1.21)$$

$$\Rightarrow b_3 = \left\| \left(\frac{2k_0}{\ell} \right) \right\| = \left(\frac{4\pi}{\ell\lambda} \right)$$

Constructive interference occurs if waves ‘fit’ the lattice (see Equation 1.9),

$$\begin{aligned} p \cdot \left(\frac{\lambda}{2} \right) &= d \quad \text{with } p \in \mathbb{Z} \\ b_3 &= \left(\frac{4\pi}{\ell\lambda} \right) = \left(\frac{4\pi}{2d} \cdot \frac{p}{\ell} \right) \\ \Rightarrow b_3 &= \left(\frac{2\pi}{d} \right) , \end{aligned} \quad (1.22)$$

where (p/ℓ) has been set to 1, to ensure that the phase difference that a scattered wave picks up in between planes is a multiple of 2π .

In the previous paragraph, the notion of reciprocal-space basis vectors was introduced and it was shown that they are useful in describing diffraction. We can extend this intuitive idea to 3-D. Any point of a 3-D lattice in real space can be reached by a lattice vector \mathbf{t} . A lattice vector \mathbf{t} in 3-D is a linear combination of 3 real-space basis vectors ($\mathbf{a}_1, \mathbf{a}_2, \mathbf{a}_3$) with integer coordinates (l_1, l_2, l_3).

$$\mathbf{t} = l_1 \mathbf{a}_1 + l_2 \mathbf{a}_2 + l_3 \mathbf{a}_3 \quad (1.23)$$

Each set of two lattice basis vectors spans a crystal plane, of course. Directions along which we should probe periodicity are the directions perpendicular to these planes, as these are the directions of phase gradients.

Without loss of generality, consider the crystal plane W that is spanned by the lattice vectors ($\mathbf{a}_1, \mathbf{a}_2$).

$$W = \text{sp}(\mathbf{a}_1, \mathbf{a}_2) \quad (1.24)$$

The reciprocal-space basis vector \mathbf{b}_3 , which should be perpendicular to the plane W , has a direction that is parallel to the cross product of \mathbf{a}_1 and \mathbf{a}_2 .

$$\mathbf{b}_3 \propto \mathbf{a}_1 \times \mathbf{a}_2 \quad (1.25)$$

$$b_3 = A \|\mathbf{a}_1 \times \mathbf{a}_2\|$$

As in the 1-D example, the length b_3 of the reciprocal-space basis vector \mathbf{b}_3 is determined by the interplanar spacing d .

$$b_3 = \frac{2\pi}{d} = \frac{2\pi}{a_3 \cos(\vartheta)} \quad (1.26)$$

$$\begin{aligned} \text{where } \vartheta &= \angle(\mathbf{a}_3, \mathbf{b}_3) \\ &= \angle(\mathbf{a}_3, (\mathbf{a}_1 \times \mathbf{a}_2)) \end{aligned}$$

Combining Equations 1.25 and 1.26 yields an expression for the factor A ,

$$\begin{aligned} A &= \frac{2\pi}{\|\mathbf{a}_3\| \cdot \|\mathbf{a}_1 \times \mathbf{a}_2\| \cdot \cos(\vartheta)} \\ &= \frac{2\pi}{\mathbf{a}_3 \cdot (\mathbf{a}_1 \times \mathbf{a}_2)}, \end{aligned} \quad (1.27)$$

finally resulting in an expression for the vector \mathbf{b}_3 .

$$\begin{aligned} \mathbf{b}_3 &= \frac{2\pi}{\mathbf{a}_3 \cdot (\mathbf{a}_1 \times \mathbf{a}_2)} \cdot (\mathbf{a}_1 \times \mathbf{a}_2) \\ &= 2\pi \cdot \frac{\mathbf{a}_1 \times \mathbf{a}_2}{\mathbf{a}_1 \cdot (\mathbf{a}_2 \times \mathbf{a}_3)} \end{aligned} \quad (1.28)$$

In a similar way, we obtain two additional reciprocal-space basis vectors \mathbf{b}_1 and \mathbf{b}_2 . Together with \mathbf{b}_3 , they form the so-called reciprocal triad $\{\mathbf{b}_i\}$.

$$\begin{aligned} \mathbf{b}_1 &= 2\pi \cdot \frac{\mathbf{a}_2 \times \mathbf{a}_3}{\mathbf{a}_1 \cdot (\mathbf{a}_2 \times \mathbf{a}_3)} \\ \mathbf{b}_2 &= 2\pi \cdot \frac{\mathbf{a}_3 \times \mathbf{a}_1}{\mathbf{a}_1 \cdot (\mathbf{a}_2 \times \mathbf{a}_3)} \\ \mathbf{b}_3 &= 2\pi \cdot \frac{\mathbf{a}_1 \times \mathbf{a}_2}{\mathbf{a}_1 \cdot (\mathbf{a}_2 \times \mathbf{a}_3)} \end{aligned} \quad (1.29)$$

As was mentioned before, the reciprocal triad $\{\mathbf{b}_i\}$ forms a set of basis vectors for a lattice that corresponds to the real-space lattice - it is known as the reciprocal lattice. Diffraction is usually described in reciprocal space, which is not surprising, for its basis vectors $\{\mathbf{b}_i\}$ can be considered as phase gradients of the corresponding real-space structure.*

1.5 This thesis

This thesis is mainly about the characterization of photonic crystals, which were fabricated by self-assembly of colloidal particles, in real and reciprocal space. In Chapter 2, we start with a review of how to deal with photonic crystals within the framework of classical electrodynamics. It allows the calculation of photonic band diagrams, which effectively summarize the optical properties of photonic crystals. To demonstrate their use, we present calculations that assisted the development of a self-assembly route towards photonic crystals with a band gap in the visible. Furthermore, band diagrams are calculated for body-centered tetragonal (BCT) crystals. Their fabrication using colloids in external, high-frequency electric fields is presented in Chapter 6. At the end of Chapter 2, we describe the use of photonic band-structure calculations for data analysis in optical spectroscopy.

One of the main reciprocal-space characterization techniques that we used is small-angle X-ray diffraction. As our colloids are about $10,000\times$ larger than the typical X-ray wavelength, the diffraction angles are tiny. It required the development of a microradian X-ray diffraction setup, which we describe in Chapter 3, together with some examples of its application to colloidal systems. The setup was also used to quantitatively characterize the orientation and 3-D structure of colloidal crystals that were fabricated by convective assembly, also known as controlled drying (Chapter 4). As controlled drying is a popular method for growing colloidal-crystal templates, the latter acting as scaffolds for the fabrication of photonic crystals, our results are relevant for this community. In Chapter 7, we demonstrate that X-ray diffraction is an excellent probe of the internal 3-D structure of photonic colloidal crystals at various stages of their fabrication. Throughout all of these chapters, results from reciprocal space are compared with data sets that were obtained using real-space techniques, including confocal microscopy and electron microscopy.

In Chapter 5, to conclude this overview with, *binary* colloidal crystals of organic spheres (polystyrene, PMMA) and/or inorganic spheres (silica) are introduced as promising templates for the fabrication of strongly photonic crystals via the infiltration of high-index materials. Organic templates cannot be infiltrated with standard techniques like chemical vapor deposition (CVD), but we demonstrate that atomic layer deposition (ALD) is a promising alternative. Binary crystals of silica spheres are often plagued by layers of colloidal fluid on top, which have to be removed before further processing. We experimentally investigated the applicability of plasma etching and removal of crystal layers using adhesive tape. Both real-space and reciprocal-space techniques were used to characterize the colloidal crystals at various stages of processing.

*Note that the intuitive notion of reciprocal space that is derived in this section assumes a crystalline real-space structure. Bear in mind that reciprocal space is also a sensible concept in the case of non-crystalline samples [105].

Photonic band-structure calculations

As the fabrication of 3-D photonic band-gap materials remains a major challenge, calculations that predict their optical properties play a very important, guiding role. This chapter starts with a review of how to deal with photonic crystals within the framework of classical electrodynamics. Next, it is shown that band diagrams can effectively describe the optical properties of photonic band-gap materials. For this thesis, such band diagrams were calculated using an expansion of the electromagnetic fields in plane waves (MPB). Now and then, we compare our results to calculations in which an expansion in spherical waves (KKR) is used instead.

In subsequent sections, the power and versatility of photonic band-structure calculations is demonstrated in various examples. We start with calculations for binary Laves phases, especially MgCu_2 . By removal of one of the two species of colloids from the MgCu_2 structure, either diamond or pyrochlore structures can be fabricated. Our calculations confirm that both of these structures have a relatively wide photonic band gap between low-lying bands for modest refractive-index contrasts. The issue of convergence of MPB plane-wave calculations in such strongly photonic crystals is also discussed. Combined with thermodynamic stability simulations by Antti-Pekka Hynninen, our results have led to a proposed route towards photonic colloidal crystals with a band gap in the visible region. Next, we present photonic band diagrams of (inverse) body-centered tetragonal (BCT) crystals. In contradiction to results in literature, we found that there is no photonic band gap for inverse BCT crystals. Finally, we demonstrate that photonic band-structure calculations can be used in the analysis of optical spectra of photonic colloidal crystals, probing quantities that were difficult to measure before, including the average refractive index of a colloidal crystal and the diameter of colloidal spheres in such a crystal.

2.1 Introduction

From a theoretical point of view, photonic crystals are nothing more and nothing less than structures in which the refractive index varies periodically in space in one, two or three dimensions. The periodicity is typically on the order of the wavelength of light [7, 8]. Provided the refractive-index contrast between the building blocks and their host medium is large enough, and a suitable crystal structure is chosen, three-dimensional (3-D) photonic crystals can have a full photonic band gap. This means that light of a certain frequency range cannot propagate inside the crystal in any direction, regardless of its polarization [16–18]. Because of their strong interaction with light, photonic band-gap materials may provide unprecedented control over both the emission and the propagation of light [19], giving way to important applications in, for example, optical integrated circuits and infrared telecommunications [7, 8].

Several methods have been proposed for the fabrication of photonic crystals, including lithography [47, 106], colloidal self-assembly [107–110], direct-writing assembly [45], multi-beam holography [46, 48, 111] and even nanorobotic manipulation [112]. Despite the enormous efforts in photonic-crystal fabrication, it is still challenging to make a material with a photonic band gap. Ironically enough, it is not that difficult to make a structure in which the refractive index varies periodically in 3-D. For example, face-centered cubic (FCC) colloidal crystals can be grown by convective-assembly [67]. Inverse FCC crystals have a band gap for dielectric contrasts larger than ~ 8.3 [65]. Chemical vapor deposition (CVD) can be used to infiltrate FCC colloidal crystal templates with silicon, the latter having a dielectric constant of approximately 12. After removal of the colloidal crystal template by a wet-chemical etch, the contrast is large enough to open up a band gap. However, silicon strongly absorbs light with a wavelength below $1 \mu\text{m}$, which makes it unsuitable for the fabrication of materials with a band gap in the visible. Other crystal structures, such as diamond and pyrochlore, would allow the use of non-absorbing materials with a high refractive index, like titania [113] or zinc sulfide [87], but these structures have not yet been explored experimentally [114].

Numerical calculations play a very important role in guiding the fabrication of photonic crystals. First of all, if it is known in advance that a structure does not have a band gap, no effort has to be directed into its fabrication unnecessarily. Current technology is able to fabricate a host of photonic crystals, but only a small fraction of those actually have a photonic band gap, so some form of pre-selection is definitely desirable. For example, in Section 2.4, we present a route towards materials with a photonic band gap in the visible via binary Laves phases. Though the fabrication of such crystals is challenging, it may yield self-assembled diamond and pyrochlore structures by selective removal of one of the two components. Both of these structures are strongly photonic. Secondly, calculations can predict the effects on an existing photonic band gap of specific sample treatments such as sintering [115] and (partial) infiltration with materials having a high refractive index [67, 68, 116]. The guiding, or rather steering, role of calculations is even more obvious in so-called ‘reverse engineering’. For example, genetic algorithms have been used to optimize the design of photonic materials within given boundary conditions [117–119]. Finally, several optical properties of photonic crystals have been found for the first time in simulations. New properties, such as the non-relativistic Doppler shift [120], may allow new characterization techniques or applications that were previously unthought of.

The importance of photonic calculations has been established by now. The question remains, however, How should the optical properties of photonic crystals be represented? For

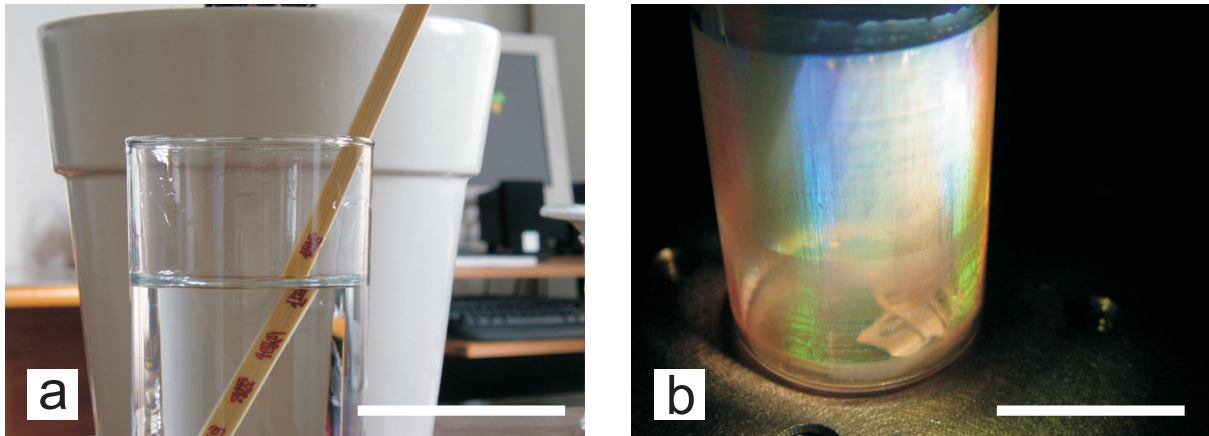


Figure 2.1: (a) Wooden chopstick in a glass of tap water. Both the kink and the magnification of the markings are due to the difference in refractive index between water and air. (b) Bragg colors coming from a photonic crystal, which is on the inside of a glass bottle, under white-light illumination. The white scale bar in panel (a) is 5 cm, the one in panel (b) is 2 cm.

atomic and molecular substances, like water, the optical response is summarized by its refractive index n . It is basically a number, or a second-rank tensor, which describes the interaction of electromagnetic radiation with the atoms or molecules of which the substance consists, leading to phenomena such as refraction (Figure 2.1a). The interaction is averaged over a volume that is large compared to the size of the constituent entities. Averaging the optical response of a molecular substance is permitted, because the wavelength of visible light is typically $5000\times$ larger than the average molecule. This enormous size difference is also the reason why Bragg diffraction of visible light does not occur in atomic and molecular substances. In such materials, the typical length scale is on the order of 0.1 nm, as is demonstrated in X-ray diffraction [121].

For Bragg diffraction of visible or infrared electromagnetic radiation to occur in a material, thus allowing greater control over the propagation of light in such a substance, the size of its constituents needs to be matched to the wavelength of light, which is approximately 500 nm. This is why colloids are excellent building blocks for photonic crystals, as they have a size of approximately $1\ \mu\text{m}$. Crystals consisting of colloids, so-called colloidal crystals, interact strongly with light, as demonstrated in Figure 2.1b. The periodicity of the crystal, and the length-scale of the lattice spacings, cause beautiful Bragg colors under white-light illumination. However, as the size of the particles is on the same order as the wavelength of the light they interact with, the material can no longer be considered as isotropic. Moreover, spatial averaging of the *local* optical response of the material no longer yields an average refractive index that correctly describes the interaction of the material with light. Thus, a different way to summarize the optical properties of such a material is required.

The ‘refractive index’ of a photonic crystal is its photonic band diagram. It contains the photonic band structure of the crystal, which is basically the dispersion relation of electromagnetic radiation inside the crystal. In other words, it is a plot of the energy of propagating modes versus their wave vector, plotted along correctly selected crystal directions. The dispersion relation has several, separate bands due to translational symmetry of the crystal. If the crystal directions are indeed carefully selected, symmetry ensures that the diagram is a complete representation

of the optical properties of the photonic crystal. How to select the correct crystal directions and how to actually calculate such a diagram will be discussed in Sections 2.2 and 2.3.

In this chapter, we will first review the theoretical concepts that underly photonic band diagrams (Section 2.2). Starting from the Maxwell equations, a master equation for purely dielectric photonic crystals will be derived. Group theory will be applied to explain why the dispersion relation for electromagnetic waves in photonic crystals need only be calculated from the master equation along a piecewise-linear trajectory in reciprocal space. Numerical simulations are required to actually solve the master equation, which will be described in Section 2.3. Once the necessary tools have been discussed, we will continue with an example of how photonic band structure calculations can guide the fabrication of photonic crystals with a band gap in the visible region (Section 2.4). Here, we present a route towards photonic band-gap materials with the diamond or pyrochlore structure via the self-assembly of binary Laves phases using colloidal particles. Next, we consider the photonic band diagram of body-centered tetragonal (BCT) crystals and find results that contradict results with literature data (Section 2.5). Finally, the use of photonic band-structure calculations in the analysis of spectroscopic measurements on colloidal crystals is presented (Section 2.6). In this way, we probed the size of colloidal spheres in a colloidal crystal, a quantity that was previously difficult to determine.

2.2 Theoretical background

2.2.1 The Maxwell equations in photonic crystals

At the start of the 20th century, scientists realized that classical physics cannot correctly describe the behavior of very small particles, such as electrons and atoms. It took the community a couple of decades to develop the required theoretical framework, which is known nowadays as quantum mechanics [13]. Although photonic crystals strongly interact with one of the elementary particles, the photon, no quantum description of light is necessary to calculate the photonic band structure of a photonic crystal, which describes their interaction with light. Typical photonic crystal building blocks have a size on the order of a micron, which is approximately $10,000\times$ larger than the typical size of an atom. The De Broglie wavelength of an electron in an atom is on the order of 0.1 nm as well [15]. As the characteristic length scale of atoms and electrons is much smaller than the wavelength of visible light (~ 500 nm), the latter will not be diffracted by individual atoms and electrons in photonic crystals. Therefore, the optical response of photonic band gap materials can be described theoretically using classical electrodynamics [10].

Phenomena in classical electrodynamics are governed by the Maxwell equations (2.1).

$$\begin{aligned}
 \nabla \cdot \mathbf{D} &= \rho_{\text{free}} \\
 \nabla \cdot \mathbf{B} &= 0 \\
 \nabla \times \mathbf{E} + \frac{\partial \mathbf{B}}{\partial t} &= \mathbf{0} \\
 \nabla \times \mathbf{H} - \frac{\partial \mathbf{D}}{\partial t} &= \mathbf{J}_{\text{free}}
 \end{aligned} \tag{2.1}$$

The free-charge density ρ_{free} and the free-current density \mathbf{J}_{free} are the basic sources of, respectively, electrostatic and magnetostatic fields. In this thesis, we will mostly consider purely

dielectric photonic crystals, which are mixed dielectric media [7]. They consist of regions of homogeneous, dielectric material without any free charges or currents.

$$\begin{aligned}\rho_{\text{free}} &= 0 \\ \mathbf{J}_{\text{free}} &= \mathbf{0}\end{aligned}\tag{2.2}$$

This assumption turns the two inhomogeneous Maxwell equations into homogeneous equations, making it significantly easier to solve the resulting set of Maxwell equations (2.3), though that may still be quite vexing.

$$\begin{aligned}\nabla \cdot \mathbf{D} &= 0 \\ \nabla \cdot \mathbf{B} &= 0 \\ \nabla \times \mathbf{E} + \frac{\partial \mathbf{B}}{\partial t} &= \mathbf{0} \\ \nabla \times \mathbf{H} - \frac{\partial \mathbf{D}}{\partial t} &= \mathbf{0}\end{aligned}\tag{2.3}$$

In order to solve the Maxwell equations, the displacement field \mathbf{D} and the magnetic induction \mathbf{B} have to be written in terms of the electric field \mathbf{E} and the magnetic field \mathbf{H} . The equations describing these relations are called the constitutive relations. In vacuum, the electric displacement \mathbf{D} and the electric field \mathbf{E} are proportional, the proportionality constant being the permittivity of free space $\epsilon_0 \approx 8.854 \cdot 10^{-12}$ F/m [14]. The magnetic field \mathbf{H} and the magnetic induction \mathbf{B} are also proportional in vacuum - they are connected by the permeability of free space $\mu_0 = 4\pi \cdot 10^{-7}$ H/m [14].

To treat dielectric media, the constitutive relations must first be written in their general form.

$$\begin{aligned}\mathbf{D} &= \epsilon_0 \mathbf{E} + \mathbf{P} \\ \mathbf{B} &= \mu_0 \mathbf{H} + \mathbf{M}\end{aligned}\tag{2.4}$$

The relation between the polarization \mathbf{P} and the electric field \mathbf{E} depends on the material under consideration, just as the relation between the magnetization \mathbf{M} and the magnetic field \mathbf{H} . For simplicity, we assume that our photonic crystals only consist of non-magnetic materials (Equation 2.5), which is usually a valid assumption in pure dielectrics, as they carry no macroscopic electric currents.

$$\mathbf{M} = \mathbf{0}\tag{2.5}$$

For simplicity, we also assume that the field strengths are so small that the response of materials to electric fields is linear. Not only is the response linear, we also assume the dielectric materials are isotropic, such that the displacement field \mathbf{D} and the electric field \mathbf{E} are related by a scalar* dielectric function $\epsilon(\mathbf{r})$.

$$\begin{aligned}\mathbf{D} &= \epsilon_0 \epsilon(\mathbf{r}) \mathbf{E} \\ \mathbf{B} &= \mu_0 \mathbf{H}\end{aligned}\tag{2.6}$$

*The formalism that is described in this section can be generalized to anisotropic media in a straightforward manner. However, the more general formalism will require the use of a dielectric tensor $\epsilon_{ij}(\mathbf{r})$ instead of a dielectric scalar function $\epsilon(\mathbf{r})$, which complicates subsequent calculations.

The scalar dielectric function $\varepsilon(\mathbf{r})$ only depends on the position vector \mathbf{r} , not on the frequency ω of the electromagnetic waves. In other words, the dispersion of the dielectric material is ignored. The value of the dielectric constant is chosen such that it is appropriate to the frequency range of interest for the physical system under consideration.

Using the constitutive relations for linear and isotropic media (Equation 2.6), the displacement field \mathbf{D} and the magnetic induction \mathbf{B} can be eliminated from the homogeneous Maxwell equations (2.3), yielding

$$\begin{aligned}\nabla \cdot (\varepsilon(\mathbf{r})\mathbf{E}) &= 0 \\ \nabla \cdot \mathbf{H} &= 0 \\ \nabla \times \mathbf{E} + \mu_0 \frac{\partial \mathbf{H}}{\partial t} &= \mathbf{0} \\ \nabla \times \mathbf{H} - \varepsilon_0 \varepsilon(\mathbf{r}) \frac{\partial \mathbf{E}}{\partial t} &= \mathbf{0} .\end{aligned}\tag{2.7}$$

In principle, the electric field \mathbf{E} and the magnetic field \mathbf{H} are complicated functions of time and space. Although interesting in themselves, we do not concern ourselves with time-dependent optical phenomena in this thesis. If only time-independent optical phenomena are considered, only the dispersion relation of light in photonic materials needs to be calculated. In addition, it is useful to determine the spatial distribution of the electric and magnetic fields, as the distribution may explain the existence or absence of gaps and it reveals where the field is strongly enhanced or reduced. The latter is especially useful if fluorescent dyes or quantum dots are to be incorporated. Because of the restriction to time-independent phenomena, we will separate out the time-dependence of the fields by imposing a harmonic time-dependence of the fields (Equation 2.8). This is allowed because the Maxwell equations are linear in time.

$$\begin{aligned}\mathbf{H}(\mathbf{r}, t) &= \mathbf{H}(\mathbf{r})e^{i\omega t} \\ \mathbf{E}(\mathbf{r}, t) &= \mathbf{E}(\mathbf{r})e^{i\omega t}\end{aligned}\tag{2.8}$$

Please note that assuming a harmonic time-dependence is no great limitation. According to Fourier theory, any solution can be written as an appropriate combination of harmonic modes. However, in most cases, the general solution will not be constructed from the Fourier components, they will just be referred to as different modes.

In order to calculate the frequency ω of propagating modes, and the corresponding mode profiles, the above equations are substituted into Equation 2.7, resulting in

$$\begin{aligned}\nabla \cdot (\varepsilon(\mathbf{r})\mathbf{E}) &= 0 \\ \nabla \cdot \mathbf{H} &= 0 \\ \nabla \times \mathbf{E} &= -\mu_0 i \omega \mathbf{H} \\ \nabla \times \mathbf{H} &= \varepsilon_0 \varepsilon(\mathbf{r}) i \omega \mathbf{E} .\end{aligned}\tag{2.9}$$

The two divergence equations require the fields to be built up of transverse electromagnetic waves. As long as this transversality is carefully enforced upon the field solutions, only the curl

equations have to be solved. Unfortunately, the two curl equations are coupled. They can be decoupled by dividing the fourth Maxwell equation (see Equation 2.9) by $\varepsilon(\mathbf{r})$ and then taking the curl, after which the third Maxwell equation can be inserted to eliminate the electric field \mathbf{E} . The result is an equation (2.10), which has been named a “master equation” [7], in which only the magnetic field \mathbf{H} occurs.

$$\Theta\mathbf{H}(\mathbf{r}) = \left(\frac{\omega}{c}\right)^2 \mathbf{H}(\mathbf{r}) \quad (2.10)$$

$$\text{where } \Theta\mathbf{H}(\mathbf{r}) \equiv \nabla \times \left(\frac{1}{\varepsilon(\mathbf{r})} \nabla \times \mathbf{H}(\mathbf{r}) \right)$$

The master equation (2.10), together with the transversality condition for \mathbf{H} and the functional form of the dielectric constant $\varepsilon(\mathbf{r})$, completely determine the magnetic field \mathbf{H} . Once the magnetic field is determined, the fourth Maxwell equation (see Equation 2.9) can be used to calculate the electric field \mathbf{E} . Most people prefer to write the master equation (2.10) in terms of the magnetic field \mathbf{H} , because the operator Θ is Hermitian, whereas the corresponding operator for the electric field \mathbf{E} is not. Please note that the dielectric function $\varepsilon(\mathbf{r})$ need not be a scalar for the operator Θ to be Hermitian. If the dielectric function $\varepsilon(\mathbf{r})$ itself is Hermitian, the operator Θ will be Hermitian as well.

The master equation is a so-called eigenvalue equation: applying the operator Θ to the magnetic field \mathbf{H} yields a scalar $(\omega/c)^2$ times the same magnetic field \mathbf{H} . It is very similar to the time-independent Schrödinger equation [7, 122]. Just as the Hamiltonian operator H in quantum mechanics, the operator Θ is linear and Hermitian. In quantum mechanics, a translational symmetry of the electronic potential V_e causes the dispersion relation of the electron to split into separate energy bands. Similarly, the translational symmetry of a photonic crystal will cause the dispersion relation of electromagnetic radiation to split into photonic bands. However, the vector nature of the electromagnetic field complicates calculations, for the operator Θ couples different directions, even if the dielectric function $\varepsilon(\mathbf{r})$ is separable. Another difference is that there is usually a typical length scale in quantum mechanical problems, an estimate of which can be given using Heisenberg’s uncertainty relation, while the Maxwell equations are scaleless. The latter means that photonic band structure calculations that are valid for a crystal of marbles are still valid for a crystal of colloids, as long as wavelengths are scaled accordingly and dispersion of the constituent materials is negligible! Thus, photonic band diagrams for specific crystal structures, such as body-centered tetragonal (Section 2.5) or MgCu_2 (Section 2.4), only have to be calculated once. For example, if the diameter of the spheres is changed in experiments, the position of a stop gap in units of (c/a) will not change! As was already mentioned, scaling only applies if dispersion of the constituent dielectric materials can be neglected. Thus, if the size of the constituents changes drastically, the frequency range of interest shifts significantly, which means different values for the dielectric constants of several composite materials may be required. In that case, the photonic band diagram will have to be calculated again, this time with the dielectric constants that are appropriate to the frequency range of interest.

2.2.2 The irreducible Brillouin zone

An important goal in photonics is the fabrication of materials with a photonic band gap in the visible or near-infrared. As explained in Section 2.1, their fabrication process is guided by

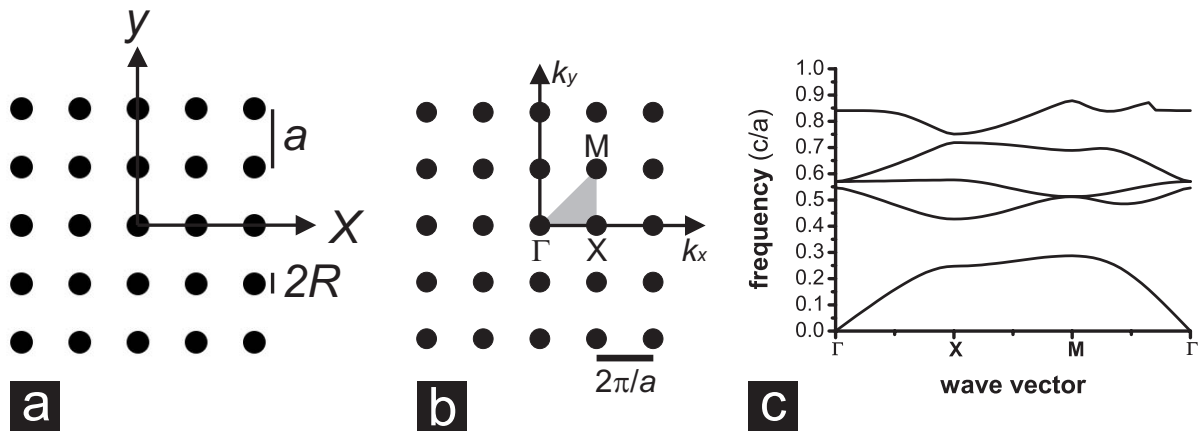


Figure 2.2: (a) Real-space structure, (b) reciprocal-space lattice with the irreducible Brillouin zone in gray and (c) the corresponding band diagram of a 2-D, square lattice of silicon cylinders in air. The band diagram was calculated for TM-modes, which have their magnetic field \mathbf{H} in the plane that is perpendicular to the long axis of the cylinders.

calculated photonic band structures. Such calculations are used to trace frequency gaps in the dispersion relation $\omega(\mathbf{k})$ of light, called photonic band gaps, which means that light cannot propagate in the material in any direction, regardless of polarization. Such gaps open up if the maximum of band n has a lower frequency than the minimum of band $(n + 1)$. However, how can the minima and maxima of a band be located? Usually, the derivative of a function is set equal to 0 in order to find its extrema. However, this requires a functional form for the dispersion relation $\omega(\mathbf{k})$. Such a functional form, in turn, requires an analytical solution for the master equation (2.10). Unfortunately, except for some very special cases, the master equation cannot be solved analytically.

If the master equation typically needs to be solved numerically, the most obvious way to find the extrema of bands is by calculating the frequencies ω for all possible wave vectors \mathbf{k} . Binning frequencies belonging to the same wave vector \mathbf{k} , the extrema of bands can be located. However, this scheme requires the calculation of frequencies belonging to an infinite number of wave vectors. In other words, frequencies need to be calculated for each point in reciprocal space, which is generally 3-D and infinite. Fortunately, symmetries of the crystal can be used to reduce the volume of reciprocal space that has to be probed in order to find band extrema.

Using Bloch's theorem [3], we can restrict ourselves to the Wigner-Seitz cell of reciprocal space: the first Brillouin zone (BZ). Bloch's theorem fully exploits the translational symmetry of the crystal lattice. However, the other symmetry properties of the crystal (the point group) have not been exploited yet. These remaining symmetries can be used to construct a set of wave vectors within the BZ that do not transform into themselves under any of the symmetry operations of the space group G , except for the identity element I of G . This set is called the irreducible Brillouin zone (IBZ) and can be considered as the smallest possible set of non-equivalent wave vectors that can still generate the entire reciprocal space of the crystal (see Figure 2.2 for a 2-D example) [4].

Up till now, the argument has been quite easy to understand intuitively. However, why do we only need to plot the band diagram along the edges of the IBZ? It follows from group

theory that all wave vectors \mathbf{k}' in the neighborhood of an arbitrary wave vector \mathbf{k} have an energy eigenvalue E' close to the energy eigenvalue E of \mathbf{k} [123]. For a wave vector in the interior of the IBZ, the only associated symmetry element is the identity I . This means that symmetry does not force neighboring wave vectors to all have lower/higher energy eigenvalues; we only know that their energy eigenvalues are close to E . In other words, the dispersion relation is a continuous function of the wave vector \mathbf{k} . However, wave vectors on the edges of the IBZ do have symmetry operations other than the identity associated with them. It follows from group theory that only if a wave vector \mathbf{k} is on an edge of the IBZ can symmetry force other wave vectors in the neighborhood of \mathbf{k} , that are not on the same edge, to all have a higher energy eigenvalue or to all have a lower energy eigenvalue [123]. It is a consequence of the fact that symmetry forces this eigenvalue to be degenerate. Thus, the extrema of bands can only occur on the edges of the IBZ, not in its interior. Of course, it could be that a wave vector in the interior of the IBZ belongs to a degenerate energy eigenvalue, but this is not due to symmetry. These degeneracies are referred to as accidental degeneracies. They depend critically on the specific functional form of the Hamiltonian and are lifted if the Hamiltonian is slightly changed (e.g. changing the dielectric contrast) [123].

2.2.3 Irreducible Brillouin zones and crystal bases

As was explained in Section 2.2.2, photonic band diagrams only have to be calculated along the edges of the irreducible Brillouin zone of the crystal under consideration. If a crystal has only one particle in its basis, the symmetry group of the crystal is a sub-group of the symmetry group of the corresponding lattice.[†] After all, if the particle is invariant under a symmetry operation that is not part of the symmetry group of the lattice, application of that symmetry operation will not transform the lattice into itself. The latter amounts to the positions of the particles being changed, which means the crystal has not been transformed into itself either. Thus, the particle in the basis of a Bravais crystal can only remove symmetry elements from the symmetry group of the Bravais lattice.

If the symmetry group of the crystal is a sub-group of the symmetry group of the lattice, plotting photonic band diagrams along the irreducible Brillouin zone of the lattice is safe. After all, the true edges of the irreducible Brillouin zone of the crystal are still probed, possibly together with some additional edges, which are actually inside the true zone. As band extrema are always on the true edges of the irreducible Brillouin zone, the true minima and maxima of each band will still be found. If there is no gap between bands n and $(n + 1)$, the diagram along the additional edges cannot open up such a gap, as it has already been closed along one of the true edges. If there *is* a gap between these two bands, it cannot be closed by plotting along the additional edges. The true maximum/minimum of band $n/(n + 1)$ has already been found along the true edges, so no frequencies in the gap will be found along the additional edges.

However, if the structure cannot be described as a Bravais crystal with one particle in its basis, care has to be taken in the selection of the underlying lattice. In this case, one has to make sure that the symmetry group of the crystal is still a sub-group of the symmetry group of the lattice. If not, plotting band diagrams along the edges of the irreducible Brillouin zone of the lattice, as is common practice, means that not all symmetry directions of the crystal are probed.

[†]In solid state physics, a crystal is considered to be the ‘sum’ of an underlying, mathematical lattice and a basis, the latter containing one or more particles. Thus, a crystal can be built up by placing one basis on each lattice site.

In other words, not all true edges of the irreducible Brillouin zone are probed. For example, the FCC structure can be described as an FCC lattice with a single particle on each lattice site. However, it can also be described as a simple cubic lattice with four particles attached to each lattice site. If the band diagram of an FCC structure would be plotted along the irreducible Brillouin zone of the simple cubic lattice, the edge of the irreducible Brillouin zone of the structure along the hexagonal symmetry axis would not be probed. If the true maximum or minimum of band n is on one of the forgotten edges, it will not be found. This might incorrectly open up a gap between bands $(n - 1)$ and n or between bands n and $(n + 1)$, thus leading to false conclusions regarding the existence of band gaps.

2.2.4 Photonic band diagrams

Plotting the dispersion relation along a characteristic path along the edges of the irreducible Brillouin zone results in the so-called photonic band diagram [123]. Corners and symmetry axes of the irreducible Brillouin zone are conventionally labelled with letters such as Γ , X, M and so on [124]. Thus, the letters on the horizontal axis of a photonic band diagram correspond to a piecewise-linear trajectory through reciprocal space. As explained in the introduction of this chapter (Section 2.1), the band diagram is a summary of the optical properties of a photonic crystal, its ‘refractive index’. There is a lot of information in such a diagram. If there is a frequency range for which no modes exist along one specific direction, this range is called a stop gap. Such stop gaps correspond to standing waves in the photonic crystal, which are basically the extension of Bragg reflections. If there is a frequency range for which stop gaps along all directions (partly) overlap, that frequency range is called a photonic band gap. Finally, if a band runs (nearly) horizontal, the derivative of the frequency ω with respect to the length of the wave vector along that direction k is nearly zero. This derivative is identical to the group velocity v_g . Thus, flat bands along specific crystal directions correspond to light propagating at a very low speeds along those directions.

2.2.5 Summary

Starting from the Maxwell equations (2.1), we derived the master equation (2.10) for electromagnetic waves in photonic crystals. Several assumptions have been used in the derivation.

- The photonic crystals under consideration are mixed dielectric media, without any free charges or free currents.
- All materials are non-magnetic.
- The polarization of all materials is proportional to the electric field \mathbf{E} , the proportionality constant between the electric field \mathbf{E} and the displacement field \mathbf{D} being $\epsilon_0\epsilon(\mathbf{r})$.
- The dielectric function $\epsilon(\mathbf{r})$ is isotropic. Although this is not a necessary requirement, it does significantly simplify calculations.
- The dielectric function $\epsilon(\mathbf{r})$ is a function of position \mathbf{r} only, not of the frequency ω . Neglecting the dispersion of materials is not a serious restriction, but it does affect scaling properties indirectly.

- Harmonic time-dependence of the electric and magnetic fields. This is no serious restriction, as any field pattern can be decomposed into such Fourier modes.

Together with the transversality condition, the master equation completely determines the magnetic field \mathbf{H} , from which the electric field \mathbf{E} can be calculated using the Maxwell equations. From the master equation, the dispersion relation $\omega(\mathbf{k})$ of electromagnetic waves in photonic crystals can be calculated. Using group theory, it can be shown that, in order to find the gaps of a photonic crystal, the dispersion relation only needs to be plotted along a specific trajectory in reciprocal space, in a so-called photonic band diagram.

2.3 Methods

In the previous section (2.2), classical electrodynamics [7, 10], solid-state theory [3, 4] and group theory [29] were applied to prove that photonic band gaps can be found by plotting appropriate photonic band diagrams [123]. However, it was not discussed how to actually calculate such a diagram numerically. For this thesis, photonic band diagrams were calculated using the MIT Photonic Bands (MPB) software package [125], version 1.4.2. Calculations were typically performed up to band 10 and for dielectric contrasts ranging from 2 to 20 using $32 \times 32 \times 32$ grid points to discretize the unit cell. MPB computes fully-vectorial eigenmodes of Maxwell's equations with periodic boundary conditions by preconditioned conjugate-gradient minimization of the block Rayleigh quotient in a plane-wave basis [126].

In most cases presented here, we used MPB 1.4.2 extended with Mischa Megens' patch file [127] for calculating the effective dielectric constant over Wigner-Seitz real-space unit cells instead of the parallelepiped unit cells spanned by the lattice vectors. Moreover, the patch ensures proper weighting of the dielectric constant at the edges of the unit cells, thus avoiding double-counting. We note here that we have not noticed any major differences between calculations that were performed with or without this patch, though differences in relative gap width of 0.2%-points have been observed.

MPB itself calls several packages, including libctl 3.0.1, Guile 1.6.4 and lapack 1.1. Most plane-wave calculations were performed on VENUS [128], which is a UNIX server of the department of Physics & Astronomy at Utrecht University. VENUS is an SMP server with 4 AMD Opteron 848 processors and 16 Gb of memory. The Opteron is a 64 bit CPU with 32 bit capabilities. Its operating system is RedHat Enterprise 4 AS.

Parameters of the physical system under considerations are passed to MPB via Scheme code in an input control file (.ctl). The user has to specify the lattice geometry, the crystal basis, the dielectric constants of the composite materials and the trajectory along which to plot the band diagram. As part of its output, MPB returns the dielectric function to the user. We used an IDL (Interactive Data Language) procedure to plot isosurfaces of this dielectric function to double-check the input against the real-space structure. In addition, we compared the filling fraction of our structure, as calculated by MPB, with the analytical value.

MPB also requires the user to provide the values of some calculational parameters, including resolution, mesh-size, number of bands and tolerance ($1 \cdot 10^{-7}$). The resolution determines the number of plane waves that are used in the calculation. The real-space unit-cell is discretized using $(\text{resolution})^3$ grid points, the number of grid points being equal to the number of plane waves [126]. The value of the dielectric function at a specific grid point is determined by

averaging the dielectric function over a sub-grid. Each resolution grid point is surrounded by a sub-grid consisting of (mesh-size)³ sub-grid points. Typical values for the resolution and the mesh-size were, respectively, 32 and 25.

The calculations for nearly all structures with a photonic band gap were checked for convergence by plotting the relative gap width against the resolution used. For many of these calculations, the mesh-size was also scanned to check for convergence. Moreover, we checked the convergence of the MPB calculations for diamond and pyrochlore using the photonic analogue of the Koringa-Kohn-Rostoker (KKR) method [32, 129, 130] and found that MPB and KKR agree on the midgap frequency of the gap between bands 2 and 3, and on the dielectric contrast at which the gap opens, but not always on the gap width.

Reflection and transmission spectra of colloidal crystals with a finite number of layers were calculated using the photonic analogue of the layered Koringa-Kohn-Rostoker (LKKR) method [32, 129, 130]. We used an approximately 5-year-old code that was written by Alexander Moroz. A more recent version of this LKKR code is or will be freely available [131]. The code was compiled using an F77 compiler and run on RUUNAT, which is the predecessor of VENUS. RUUNAT is a UNIX server with a couple of Compaq Tru64 processors. The operating system is Unix v5.1A.

2.4 Photonic band structure of Laves-phase colloidal crystals

In Section 2.1, we have explained that photonic band-structure calculations can be used to guide the fabrication of photonic crystals. This is important, because the fabrication of periodic structures with a high index contrast on the sub-micron scale is challenging. For example, photonic crystals with a band gap in the visible have not been realized yet. Assembling 3-D periodic structures with feature sizes of the right length scale is not the main problem. However, most of these materials have the face-centered cubic (FCC) structure, at best. Inverse FCC crystals are predicted to have a photonic band gap between bands 8 and 9, but only if the index contrast exceeds ~ 2.9 [31, 65, 66]. Unfortunately, there are hardly any non-absorbing materials available that have such a high refractive index in the visible region.

Calculations have been performed which predict that there are structures with a photonic band gap at lower index contrasts. The presently known clear champion structures, both for opening up a band gap at the lowest refractive-index-contrast ratio (around 2) and the largest band-gap width to center-frequency ratio, are dielectric diamond [32, 36] and pyrochlore [38] structures. Both these structures also give rise to gaps at low lying bands which makes them more stable against disorder [74, 75]. Conventional methods like lithography have not realized these structures for a band gap in the visible, as this requires 3-D feature sizes of just a few hundred nanometers. This size range is easily achieved with colloidal particles. Therefore, recently, several methods to realize structures with diamond symmetry by self-organization of colloids have been proposed. However, they require inter-particle potentials that are not spherically symmetric [132] or that are even more complicated [133], both of which have yet to be realized experimentally. Although it is proposed in [134] to use four spheres combined in the form of tetrahedrons to arrive at diamond and pyrochlore structures, the fabrication process is not described. Garcia-Adeva [38] proposed making pyrochlore lattices by a layer-by-layer growth procedure, as shown by Velikov *et al.* [135], which is a laborious route.

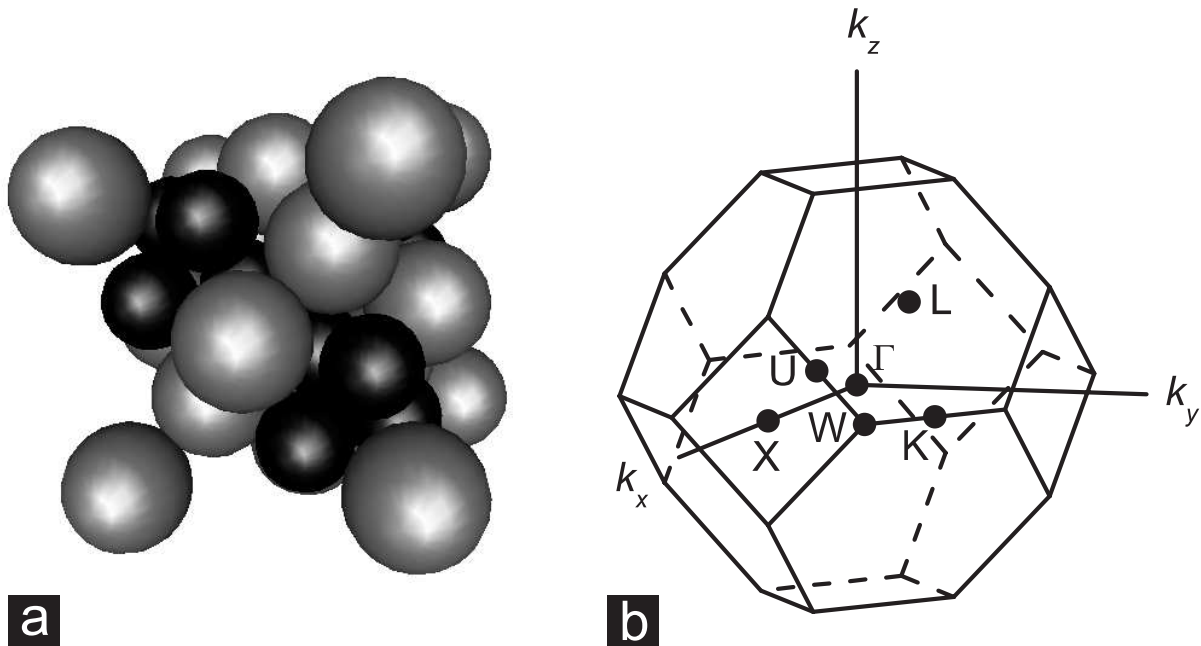


Figure 2.3: Figure (a) is the conventional, real-space unit cell of the MgCu₂ structure. The large spheres (gray) are on the sites of a diamond structure, whereas the small spheres (black) are on the sites of a pyrochlore structure. At maximum sphere packing, the large spheres are touching each other, the small spheres are touching each other, but the large spheres do not touch the small spheres. The maximum sphere packing fraction is approximately 71.0%, at which the ratio of the sphere diameters $\sigma_S/\sigma_L = (\sqrt{2}/\sqrt{3}) \approx 0.816$. The underlying Bravais lattice of the MgCu₂ structure is face-centered cubic (FCC). The first Brillouin zone for FCC is depicted in panel (b), together with its irreducible part: $\Gamma X U W K L \Gamma$. In FCC photonic band-structure calculations, the dispersion relation is usually plotted along the characteristic path: XUL Γ XWK.

In a recent paper, we have shown how both the pyrochlore and diamond structures can be obtained from a binary mixture of colloidal spheres with easily realizable interaction potentials [114]. The removal of the large or small spheres from the so-called binary Laves phase [136] MgCu₂ can be done using already well-established procedures such as dissolution [67] or burning [135]. The paper focuses mostly on Monte-Carlo simulations that demonstrate the possibility of fabricating binary Laves phases by colloidal self-assembly. The MgCu₂ structure, which is the most favorable of the binary Laves phases from a photonic point of view, can be selected using a specific template as the sample substrate. Although the optical properties of the binary Laves phases are considered in the article, it does not go into the details of the photonic calculations. Therefore, we will now elaborate on photonic band-structure calculations for the MgCu₂ structure and its derivatives. These investigations have led, amongst other things, to a clearer understanding of why diamond is one of the two champion structures for photonic band-gap materials.

2.4.1 Photonic band structure of MgCu₂

We consider a MgCu₂ structure consisting of large spheres L and small spheres S with diameters of σ_L and σ_S , respectively. Figure 2.3a is a schematic representation of the conventional unit cell of such a MgCu₂ structure. The large spheres form a diamond structure, which is itself equivalent to two interpenetrating face-centered cubic (FCC) lattices, one being displaced along $(1/4)$ of the body diagonal of the conventional, cubic unit cell. The small spheres form tetrahedrons that fill up the voids of the diamond structure, thus forming a pyrochlore structure. In the case of optimal packing, the large spheres are mutually touching and have a diameter $\sigma_L = a \cdot (\sqrt{3}/4)$, in which a is the length of the cube edge (Figure 2.3a). The small spheres are also touching, having a diameter of $\sigma_S = a \cdot (\sqrt{2}/4)$. However, the distance between a large sphere and a neighboring small sphere is $a \cdot (\sqrt{11}/8)$, which is larger than the sum of σ_L and σ_S , so the large and the small spheres are not touching one another. At closest-packing, the size ratio ζ of large and small spheres in the MgCu₂ structure is $(\sqrt{2}/\sqrt{3}) \approx 0.816$, yielding a sphere volume fraction φ_{\max} of approximately 71.0% (Equation 2.11).

$$\begin{aligned} \text{at max. packing } \left(\frac{\sigma_S}{\sigma_L} \right) &= \frac{\sqrt{6}}{3} \approx 0.816 \\ \varphi_{\max} &= \left(\frac{4\pi}{3} \right) \cdot \left(\left(\frac{\sigma_L}{a} \right)^3 + 2 \left(\frac{\sigma_S}{a} \right)^3 \right) \approx 0.710 \end{aligned} \quad (2.11)$$

As was explained in Section 2.2.2, the photonic band diagram only has to be plotted along a characteristic path in reciprocal space. In addition, the case of crystals with more than one particle in the crystal basis was discussed. The MgCu₂ structure has at least six particles in its basis, so care should be taken in selecting the underlying lattice. The lattice of a certain crystal structure should always be selected such that the symmetry group of the structure is a sub-group of the symmetry group of the lattice. This can be accomplished by selecting the underlying lattice having the largest possible number of elements in its symmetry group. In that case, the corresponding basis of the crystal can only remove elements from the lattice symmetry group, which means plotting band diagrams along the edges of the irreducible Brillouin zone of the lattice is always safe. For MgCu₂, the lattice with the highest possible symmetry is an FCC lattice, the first Brillouin zone of which is depicted in Figure 2.3b. The irreducible part of this zone is $\Gamma X U W K L \Gamma$ - photonic band diagrams are conventionally plotted along the characteristic path $X U L \Gamma X W K$.

Figure 2.4a displays the photonic band structure of a MgCu₂ structure of silicon spheres ($\epsilon = 12$) in air at optimal packing. Dielectric spheres in air were selected instead of an inverse structure, because both pyrochlore and diamond have a large gap between bands 2 and 3 for silicon spheres in air. However, it is clear from Figure 2.4 that the MgCu₂ structure does not have a band gap in this geometry. To explain why the diamond/pyrochlore gap between bands 2 and 3 closes for MgCu₂, a series of calculations have been performed in which the diameter of the small spheres σ_S was varied. At the start, the diameter of the small spheres was set to zero, which yielded a diamond structure at its maximum sphere packing fraction of approximately 34%. Increasing the diameter of the small spheres in small steps, the width of the gap between bands 2 and 3 was determined for each diameter, negative gap widths corresponding to the absence of a gap. The graph in Figure 2.4b starts at a relative gap width of approximately 7%, which is indeed the width of that gap for the diamond structure, at least according to plane-wave calculations [33]. The graph clearly proves that introducing the small spheres deteriorates and finally closes the gap completely.

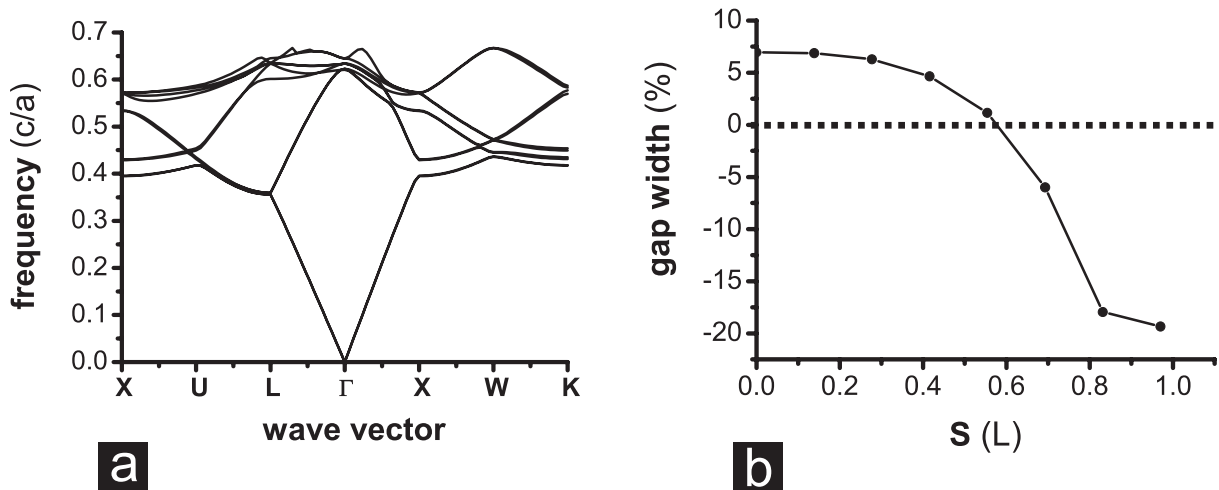


Figure 2.4: Figure (a) is the calculated photonic band diagram for a close-packed, MgCu_2 structure of silicon spheres ($\epsilon = 12$) in air. Panel (b) shows the relative width of the gap between bands 2 and 3 for a MgCu_2 structure in which the large spheres are touching and in which the small spheres have a radius $\sigma_S = S \cdot \sigma_L$. The small spheres start overlapping at $\sigma_S \approx 0.816 \cdot \sigma_L$. Negative gap widths correspond to the absence of a gap. It is clear that introducing small spheres deteriorates the gap width.

Strangely enough, the small spheres themselves form a structure that also has a large gap between bands 2 and 3 at optimal packing. How is it possible that a structure that consists of the sum of two strongly photonic crystals is itself hardly photonic at all? In order to get a grip on this problem, the origin of the gap needs to be found, for which energy-density maps are very useful. Figure 2.5 compares the dielectric functions of a diamond and a MgCu_2 structure of silicon spheres in air at optimal packing with energy density plots of bands 2 and 3. In diamond, the energy densities of bands 2 and 3 are clearly arranged in bands. One band concentrates its field energy in the low-dielectric phase, while the other band concentrates the energy in the high-dielectric phase. According to the variational principle [7], this enables the bands to separate their frequencies, thus causing a stop gap to open up. The local tetrahedral symmetry of diamond ensures that stop gaps along different directions overlap [36], leading to a frequency range with an omnidirectional stop gap - a photonic band gap. Introducing the small spheres into the voids of diamond causes the energy densities of bands 2 and 3 to be much more scattered. Field lines of the \mathbf{D} field, which have to be continuous, now have to cross dielectric interfaces between sphere and host media, simply because there is no longer enough space in the air phase to contain all the field lines of an entire frequency band. The result is that the two successive bands can no longer concentrate their field energy in different dielectric phases. Thus, they cannot separate their frequencies, which means that no gap will open up. Though qualitative and in hindsight, such a reasoning based on the variational principle can provide some insight into why gaps open or close upon changes in the geometry of a structure.

Removing one of the components of MgCu_2 , leaves either diamond (large spheres) or pyrochlore (small spheres). Both of these structures are strongly photonic, especially in their inverse geometry (to be discussed more below) with the low-dielectric spheres heavily overlapping. To start with, we have only investigated diamond and pyrochlore geometries with non-overlapping spheres at optimal packing, as these are easiest to realize experimentally. Note

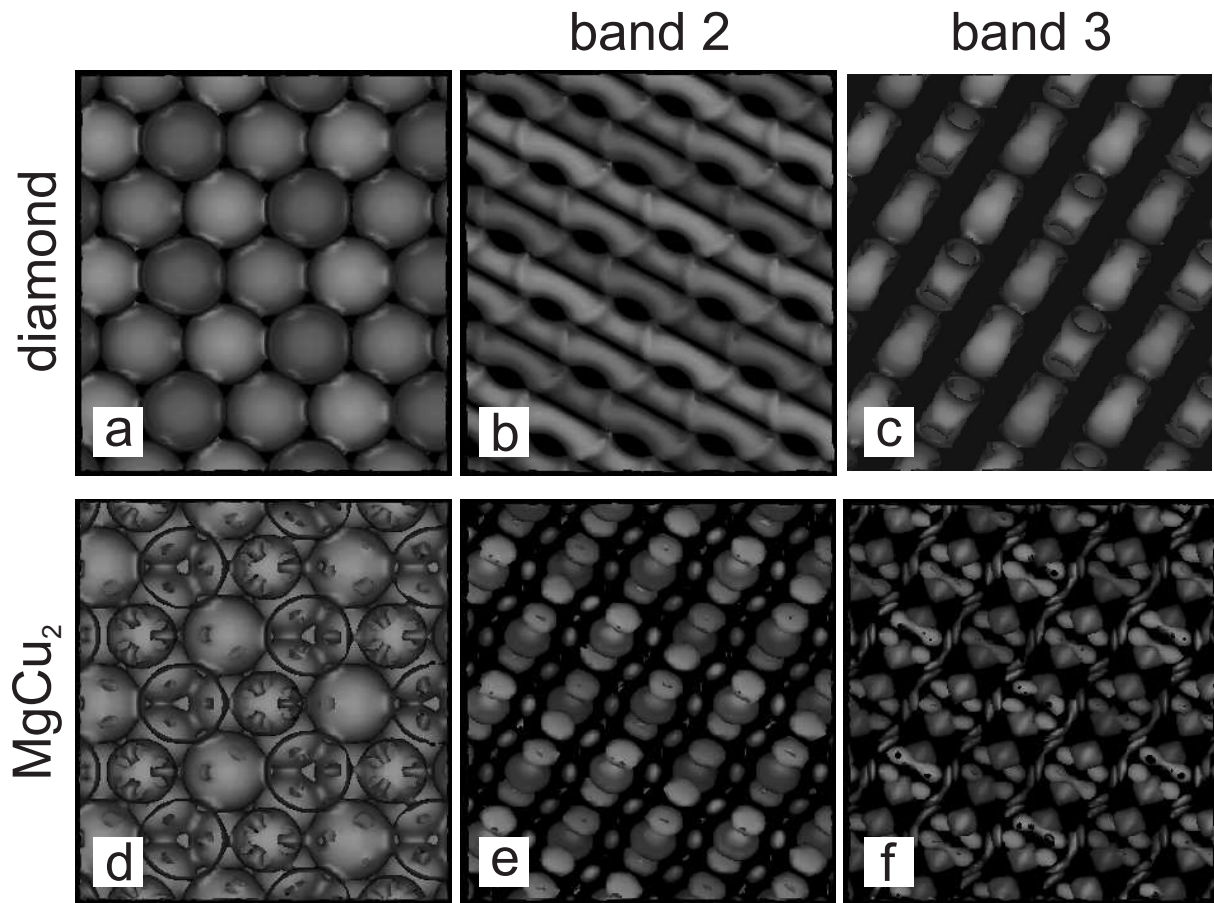


Figure 2.5: Panels (a,d) show iso-surface representations of the dielectric function of (a) a diamond and (d) a MgCu₂ structure of silicon spheres ($\epsilon = 12$) in air at maximum sphere packing. This representation shows the projection along the $[111]$ direction in the conventional unit cell of the dielectric function, the latter being part of the MPB output. Iso-surface representations of the energy densities of the displacement field \mathbf{D} at the L-point (see Figure 2.3b) of the (b,e) 2nd and (c,f) 3rd bands in the (b,c) diamond and (e,f) MgCu₂ structure, as calculated by MPB, are plotted over the same area as panels (a,c).

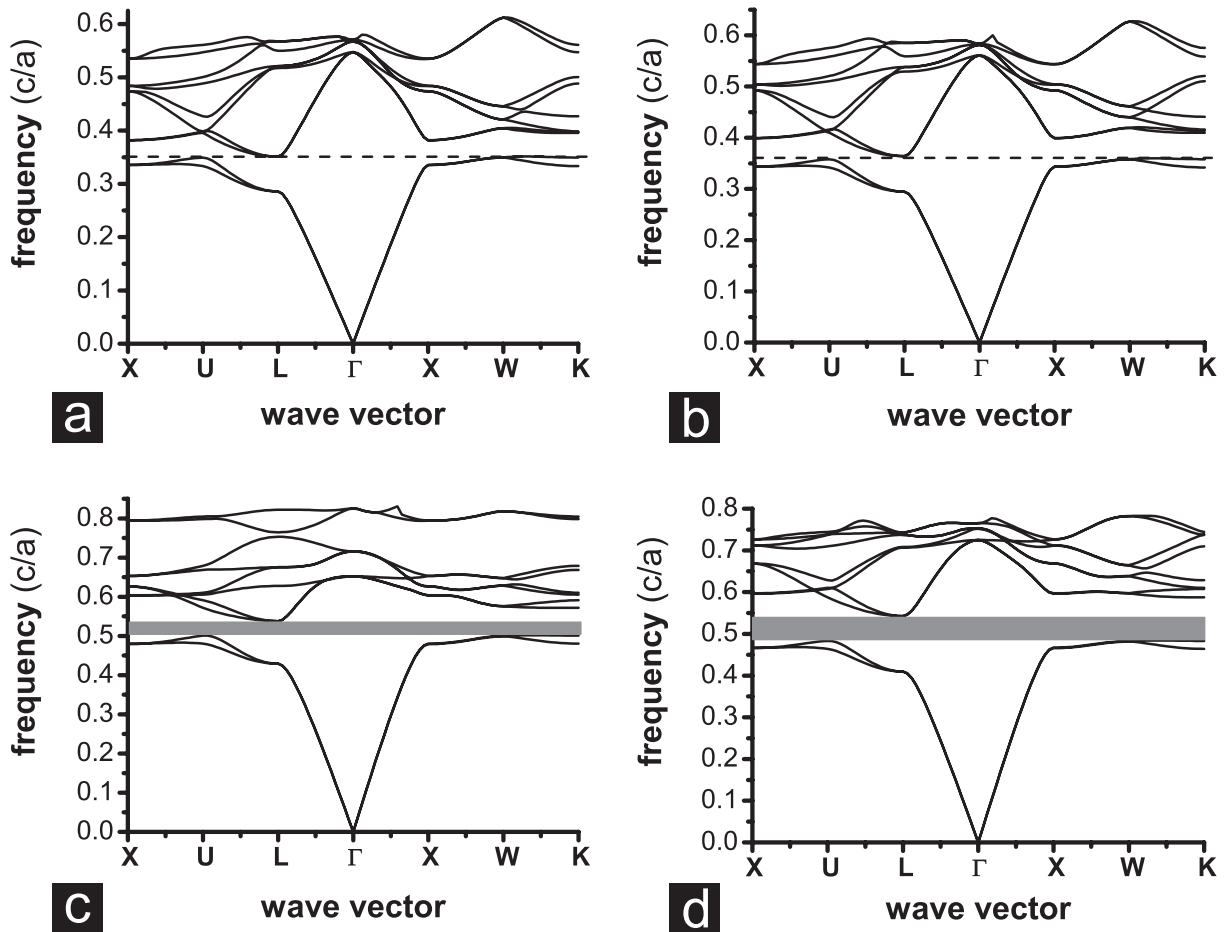


Figure 2.6: Calculated photonic band diagrams of four different structures: (a) inverse diamond, (b) inverse pyrochlore (air spheres in silicon) and (c) direct diamond, (d) direct pyrochlore. For all structures, MPB band diagrams were calculated at maximum sphere packing fraction. The dashed lines and gray boxes indicate the position of the gap between bands 2 and 3.

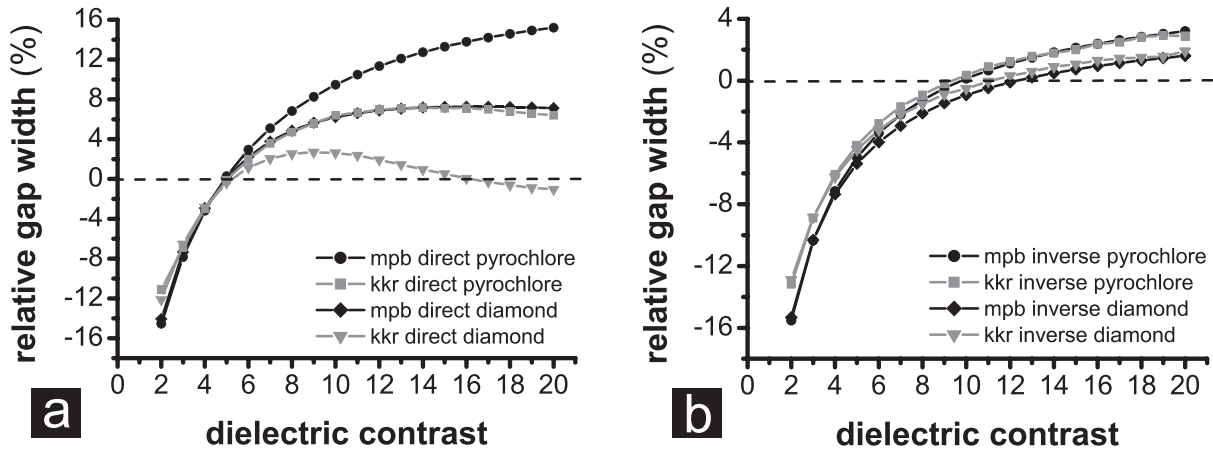


Figure 2.7: Calculated relative width of the gap between bands 2 and 3, as a function of the dielectric contrast, for four different structures: direct pyrochlore ($\phi = 0.37$), direct diamond ($\phi = 0.34$) (dielectric spheres in air) and inverse pyrochlore, inverse diamond (air spheres in a dielectric background). Both MPB plane-wave and KKR calculations are shown. It is clear that MPB and KKR agree with each other for the inverse structures, but not for the direct ones. The relative gap width is defined as the gap width divided by the midgap frequency. The solid lines are a guide to the eye.

that the underlying lattice of the diamond and pyrochlore structures is still FCC, so the same characteristic path through reciprocal space can be taken for band-structure calculations. At a dielectric contrast of 12, which is close to the contrast of silicon and air, both inverse diamond/pyrochlore and direct diamond/pyrochlore have a gap between bands 2 and 3, though the photonic band gap of the direct structures is larger than that of the inverse ones (Figure 2.6). A gap between such low-lying bands is advantageous, because it makes them more stable against disorder [74].

Figure 2.7 shows the relative width of the photonic band gap between bands 2 and 3, as a function of the dielectric contrast, for (a) the direct diamond and pyrochlore structures (dielectric spheres in air), and (b) their inverse structures (air spheres in a dielectric background), at maximum sphere packing fraction. Results of both MPB and KKR calculations are shown for easy comparison. The direct structures (Figure 2.7a) in particular possess large photonic band gaps for moderate dielectric contrasts. Their gap opens up at a dielectric contrast of 5, which is much lower than the required contrast of 8.4 for an inverse FCC structure [31, 65]. At a contrast of 12 (silicon spheres in air), the gap width has increased to approximately 7% and 11% for the direct diamond and direct pyrochlore structure, respectively. These gaps are much larger and open up at lower contrasts than for the inverse structures. We did not find any band gaps for the other two binary Laves structures. Neither did we find any significant gaps for the small/large particle components of the MgZn_2 and MgNi_2 structures.

2.4.2 Convergence in band-structure calculations

Photonic band diagrams for diamond are notoriously difficult to calculate using plane-wave expansions [32]. KKR calculations have shown, for example, that plane-wave calculations severely overestimate the relative width of the gap between bands 2 and 3 for diamond structures

of silicon spheres in air [32]. One explanation could be that KKR employs an expansion in spherical instead of plane waves and that spherical waves fit the boundary condition at the edge of the sphere better than plane waves. However, in that case, it is difficult to understand why plane-wave calculations for FCC structures do converge very rapidly. Another explanation could be that plane-wave calculations get into trouble if the crystal basis contains more than one particle. This seems unlikely as well, as MPB calculations for the sodium-chloride (NaCl) structure seem to converge just fine (see Chapter 5). All the same, a combination of the above-mentioned arguments is likely to play a role. If the structure has a basis with spherical particles, and the sphere volume fraction is low or the number of particles in the basis is large, then the number of grid points that is available in or near the edge of a particular sphere is low, which may result in moderate convergence.

To check the convergence of MPB plane-wave calculations, we plot the relative width of the gap under consideration as a function of the resolution (res). In MPB, $(\text{resolution})^3$ is the number of grid points that is used to discretize the real-space unit cell, which is equal to the number of plane waves that is used in the band-structure calculation. In the case of a diamond structure of close-packed silicon spheres in air, this convergence plot displays a peculiar, oscillatory behavior (Figure 2.8a). The oscillations reach local maxima for values of the resolution that are a multiple of 8, while they reach local minima for values that are a multiple of 4 but not of 8. This peculiar behavior may be a numerical artefact of the discretization of the diamond unit cell. The vector connecting the two spheres in the diamond crystal basis runs along the body diagonal of the conventional, cubic diamond real-space unit cell and has a length of $(a/4) \cdot \sqrt{3}$, in which a is the length of the cube edge. The body diagonal of a grid cell is parallel to the vector connecting the spheres and has a length of $(a/\text{res}) \cdot \sqrt{3}$. Thus, the length of the vector connecting the spheres has a length of $(\text{res}/4)$ body-diagonal grid units. This means that its length, in units of grid body diagonals, is odd if the resolution is a multiple of 4 but not of 8 and that it is even if the resolution is a multiple of 8. The question remains how the distance between the two spheres in the diamond crystal basis being even or odd can have an effect on the relative width of the gap between bands 2 and 3.

The center of one of the spheres in the diamond crystal basis is on the origin grid point. As the displacement vector between the two spheres in this basis has a length of $(\text{res}/4)$ body-diagonal grid units, the center of the second sphere is also on a grid point if the resolution is a multiple of 4. Then, at maximum packing, the contact point of the two spheres in the diamond crystal basis is on an edge at which two grid cells touch if the resolution is a multiple of 4 but not of 8. One of the touching grid cells is in one sphere, the other one is in the other sphere. In other words, one grid point is situated in one of the spheres, the other grid point is situated in the other sphere. In this case, the spheres are clearly not overlapping. Alternatively, if the resolution is a multiple of 8, the contact point of two spheres will be inside a grid cell. The grid point of this grid cell is actually the contact point. This means that this grid point is shared by the two spheres. In a way, this situation is similar to a situation in which the spheres are overlapping. In both cases, one or more grid points are shared by adjacent spheres.

Figure 2.8b shows that the relative width of the gap between bands 2 and 3 for a diamond structure of silicon spheres in air is significantly larger if the spheres slightly overlap than if they touch. We have not found an explanation yet for the sensitivity of this gap to overlap of the spheres. In KKR calculations, spherical coordinates are used, which means that the boundary of the spheres does not have to be discretized. Thus, independent of the calculational

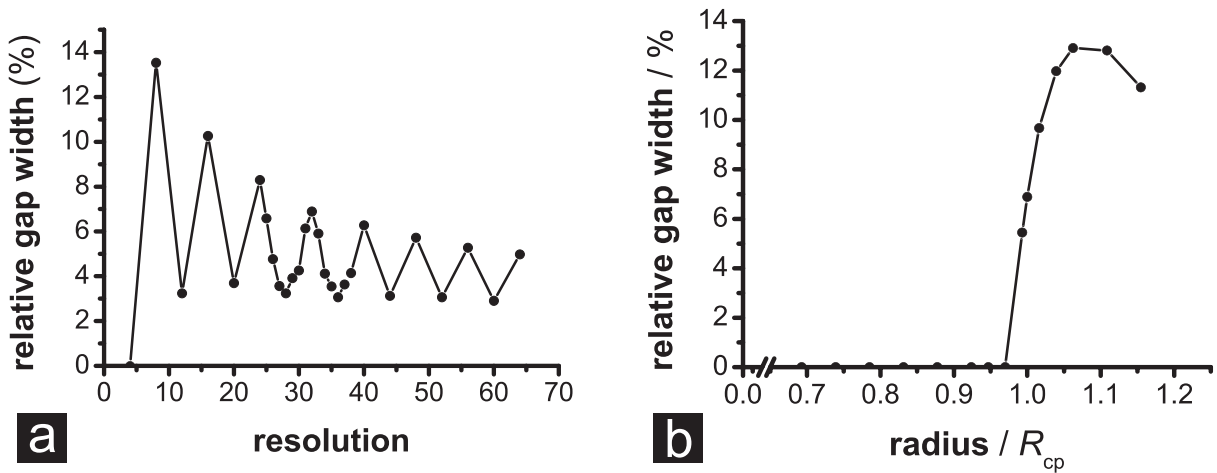


Figure 2.8: (a) Calculated relative width of the gap between bands 2 and 3 for a close-packed ($\phi = 0.34$) diamond structure of silicon spheres ($\epsilon = 12$) in air as a function of the resolution. The $(\text{resolution})^3$ is the number of grid points with which the unit cell is discretized, which is equal to the number of planes waves that is used in the field expansion. It is clear that the calculations do not converge very well for diamond structures. (b) Calculated relative width, at resolution 32, of the gap between bands 2 and 3 for a diamond structure of silicon spheres in air as a function of the radius of the silicon spheres. Note that the radius of the silicon spheres in panel (b) is given in units of the close-packed radius of spheres in a diamond structure. The relative gap width is defined as the gap width divided by the midgap frequency. The solid lines are a guide to the eye.

resolution in KKR, which is the number of spherical waves that are used for the expansion of the electromagnetic fields, touching spheres are not overlapping. Thus, if we wish to compare our plane-wave calculations to KKR calculations, we should compare calculations for touching spheres, which means only resolutions that are a multiple of 4 but not of 8 should be used. For those resolutions, MPB predicts a relative gap width of approximately 3% instead of 7%, the former being in reasonable agreement with KKR results [32]. Note that the convergence plot for diamond structures of silicon spheres in air (Figure 2.8a) is nearly flat if only resolutions that are a multiple of 4 but not of 8 are considered.

2.4.3 Summary

Concluding, our photonic band-structure calculations indicate that one of the binary Laves phases, the MgCu_2 structure, holds great potential for the fabrication of photonic crystals with a band gap in the visible. Although it does not seem to have a band gap itself, removing the small spheres yields diamond and removing the large spheres yields pyrochlore, both of which are strongly photonic. We have shown that, starting with diamond, introducing the small spheres to form MgCu_2 actually closes the diamond gap between bands 2 and 3. The structure gets too crowded, because of which different bands can no longer completely store their energy in different dielectric phases. According to the variational principle, the latter prohibits the bands from separating their frequencies, thus closing a possible gap. Furthermore, comparing MPB with KKR calculations, we found that MPB calculations for direct diamond and direct

pyrochlore converge badly. For diamond, this bad convergence seems to be a numerical artefact of the discretization of the real-space unit cell. Finally, we emphasize that the structures for which the large gaps are calculated have not been optimized in any way. This optimization might be achieved for instance by using incomplete filling, which increases gaps for inverse FCC structures [116], or by sintering the structures [115]. Nevertheless, as shown in Figure 2.7, several materials that do not absorb in the visible region, such as titania and zinc sulfide, could open a gap in the visible for close-packed diamond and pyrochlore structures. Although we have focused in this chapter on purely dielectric materials, interesting possibilities also exist for structures consisting of metallodielectric spheres [32].

2.5 Photonic band structure of BCT crystals

In Chapter 6, we present a procedure for fabricating large-area, electric-field-induced colloidal single crystals for photonic applications [109]. The dipole-dipole interaction between the colloidal spheres, which is induced by the external electric field, favors the formation of body-centered tetragonal (BCT) crystals over close-packed (CP) crystals [137, 138]. Figure 2.9a is a schematic picture of the conventional unit cell for BCT crystals in real-space. The primitive, BCT unit cell is spanned by the primitive, real-space lattice vectors $\{\mathbf{t}_i\}$. If $b/a = (\sqrt{6}/2)$, as is the case at maximum packing, the diagonal $(110)_{\text{conv}}$ plane, indicated by the dark-gray spheres, has hexagonal symmetry.[‡] In that case, BCT crystals consist of hexagonal layers that are bridge-site stacked and have an ABAB stacking sequence (Chapter 6).

As can be expected from the analogy with BCC and FCC lattices, the reciprocal space of BCT is face-centered tetragonal (FCT). However, the FCT lattice is identical to the BCT lattice after a rotation by 45° , so BCT reciprocal space is actually BCT. Figure 2.9b shows the first Brillouin zone for BCT for $b/a = (\sqrt{6}/2)$, spanned by the primitive, reciprocal-space lattice vectors $\{\mathbf{g}_i\}$ [124]. The irreducible part of the Brillouin zone, which is important for calculating photonic band diagrams (Section 2.2.2), has been labelled with ΓLNVZXP . Although shorter paths along the edges of the irreducible part of the Brillouin zone are possible, we plot band diagrams along XZVNLFXPNL in order to include directions that can be easily probed in experiments. Please note that the ΓX direction in BCT reciprocal space corresponds to the direction perpendicular to the hexagonal $(110)_{\text{conv}}$ planes in real space.

To our knowledge, there is only one article in literature that discusses the photonic band structure of colloidal BCT crystals consisting of spheres [139]. Tao *et al.* consider inverse BCT crystals of air spheres in a dielectric host at the maximum sphere packing fraction of $(2\pi/9) \approx 0.698$. They claim that such structures have a photonic band gap between bands 5 and 6 if the dielectric contrast is larger than 15.7. As many of the samples that are considered in Chapters 6 and 7 are BCT crystals, we decided to perform similar calculations ourselves using the MIT Photonic Bands (MPB) package (Section 2.3). Figure 2.10a shows the photonic band diagram for a BCT crystal of air spheres in a host with dielectric constant $\epsilon_h = 20$ at the maximum sphere packing fraction. Though the diagram looks similar to the one by Tao *et al.*, especially for the low-frequency bands, our calculations do not yield a photonic band gap at all! Unfortunately, we have no explanation for the results by Tao *et al.* [139].

[‡]The subscript “conv” refers to the conventional real-space unit cell of the crystal structure under consideration.

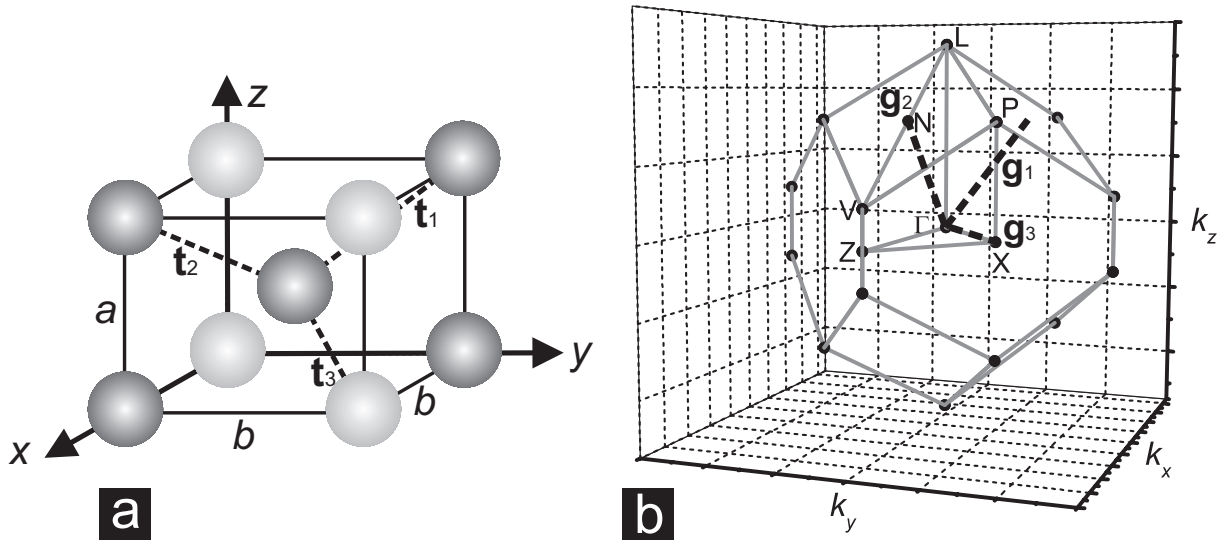


Figure 2.9: Panel (a) is a schematic picture of the conventional unit cell for the BCT structure in real space. For $a/b = (2/\sqrt{6})$, the $(110)_{\text{conv}}$ plane, which is indicated by the dark-gray spheres, has hexagonal symmetry. The dashed lines in panel (a) represent the primitive, real-space basis vectors $\{\mathbf{t}_i\}$. The spheres have not been drawn to scale for clarity. Panel (b) is a schematic image of the first Brillouin zone for the BCT lattice. The reciprocal-space lattice vectors $\{\mathbf{g}_i\}$ have been drawn in, at half their length, as dashed lines. The irreducible part of the Brillouin zone has been labelled $\Gamma\text{LN}\text{V}\text{Z}\text{X}\text{P}$. In the $\{\mathbf{g}_i\}$ basis, the coordinates of these labelled points are: $\Gamma(000)$, $\text{N}(0\frac{1}{2}0)$, $\text{Z}(\frac{1}{2}\frac{1}{2}\frac{1}{2})$, $\text{X}(00\frac{1}{2})$ and $\text{P}(\frac{1}{4}\frac{1}{4}\frac{1}{4})$. For $b/a = (\sqrt{6}/2)$, the coordinates of the other two points are: $\text{L}(\frac{5}{12}\frac{5}{12}\frac{5}{12})$ and $\text{V}(\frac{5}{12}\frac{7}{12}\frac{5}{12})$. Although shorter paths along the edges of the irreducible part of the Brillouin zone are possible, we plot band diagrams along $\text{XZ}\text{V}\text{N}\text{L}\text{I}\text{X}\text{P}\text{N}\text{L}$. In real space, the direction perpendicular to the hexagonal $(110)_{\text{conv}}$ plane is $[110]_{\text{conv}}$, which corresponds to the ΓX direction.

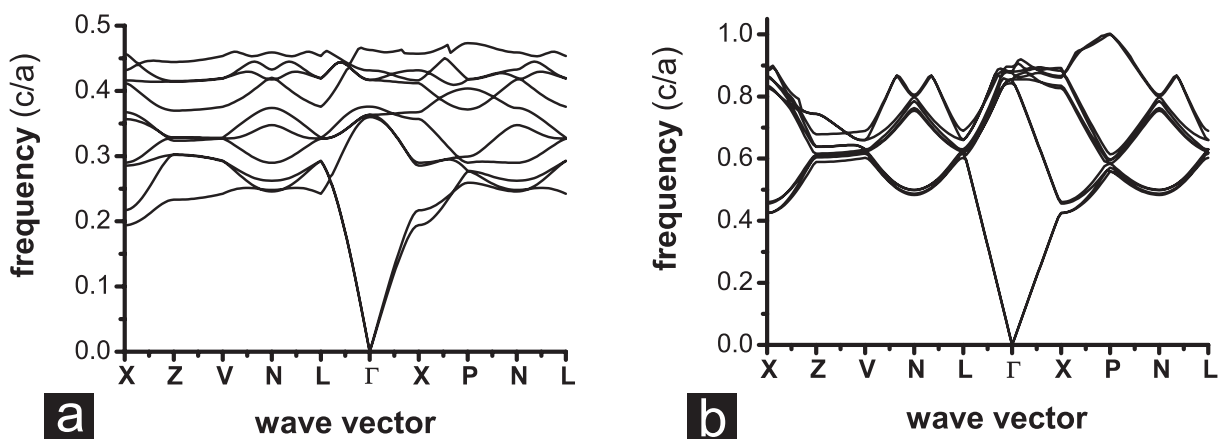


Figure 2.10: Calculated photonic band diagrams for body-centered tetragonal (BCT) crystal structures at maximum sphere packing fraction for (a) air spheres in a background with a dielectric constant $\epsilon_h = 20$ and (b) for silica spheres with a dielectric constant $\epsilon_s = 2.1025$ in air.

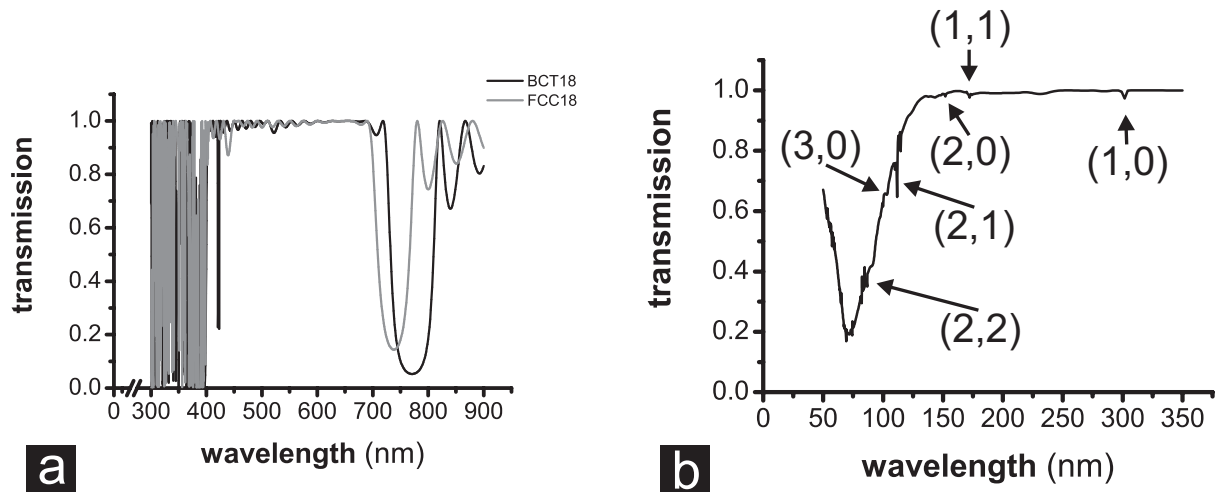


Figure 2.11: Panel (a) shows calculated (KKR) transmission spectra of an FCC and a BCT crystal of 338 nm diameter silica spheres in air at maximum packing. Both crystals consist of 18 hexagonal layers in simulation. Panel (b) is the calculated (KKR) transmission spectrum of a single hexagonal layer of close-packed, 338 nm diameter spheres of refractive index 1.05 in air. All these spectra were calculated for the direction perpendicular to the hexagonal layers.

Even though BCT may not have a photonic band gap at all, it might still be a very interesting structure for photonic applications. For example, Figure 2.10b shows the photonic band diagram for a BCT structure of close-packed silica spheres in air. Along the $[110]_{\text{conv}}$ (or ΓX) direction, the BCT crystal ($\varphi_{\text{crys}} = (2\pi/9) \approx 0.698$) has a stop gap between bands 2 and 3 at a frequency of $0.440 \cdot (c/a)$ with a relative width of 6.85%. A close-packed, FCC crystal ($\varphi_{\text{crys}} = (\pi\sqrt{2}/6) \approx 0.740$) of silica spheres in air also has a stop gap along the direction perpendicular to the hexagonal planes, the $[111]_{\text{conv}}$ direction. This stop gap is also situated between bands 2 and 3, but it only has a relative width of 5.26%. Thus, at the same refractive-index contrast, BCT crystals of dielectric spheres in air have a stop gap that is wider than for FCC crystals. In the next section, KKR calculations that support the latter observation are presented.

2.5.1 KKR transmission spectra of body-centered tetragonal crystals

To check the results of our plane-wave calculations, we extended Alexander Moroz' code for the photonic analogue of the layered Koringa-Kohn-Rostoker (KKR) method [32, 129, 130], such that it could handle BCT crystals along the ΓX direction as well. KKR transmission spectra of BCT and FCC crystals, both consisting of 18 hexagonal layers of close-packed, 338 nm diameter silica particles in air, confirm that BCT crystals indeed have a stop gap that is wider than the stop gap in FCC crystals, for the first-order $(110)/(111)_{\text{conv}}$ Bragg dip is deeper and wider in the case of BCT (Figure 2.11a). For crystals of silica spheres in air having approximately 20 layers or more, we expect that the number of layers hardly affects the depth or the width of the Bragg dip (Figure 2.14b).

The wavelength of the maximum of the Bragg diffraction can also be calculated from the

center frequency of the stop gap in the MPB band diagram (Figure 2.10b).

$$\lambda_{(110)}^{(1)} = \frac{c}{\nu} = \frac{c \cdot a}{\hat{\nu} \cdot c} = \frac{a}{\hat{\nu}} = \frac{\sigma}{\hat{\nu}} = \frac{338 \text{ nm}}{0.440} = 768 \text{ nm} \quad (2.12)$$

Here, c is the speed of light in vacuum, ν is the frequency, $\hat{\nu}$ is the same frequency in units of (c/a) , a is the lattice parameter (Figure 2.9)a and σ is the particle diameter. Thus, the MPB calculations predict that the Bragg peak should be at a wavelength of 768 nm. The KKR transmission spectrum indicates a wavelength of 770 nm, which is in reasonable agreement with the MPB result.

2.5.2 Surface modes in KKR transmission spectra

Another common feature of the calculated KKR spectra is the ‘forest’ of spikes below 400 nm. These spikes may be caused by coupling of the incoming light to surface modes. In this case, the diffracted light grazes the 2-D surface of the colloidal crystal. This scattering process, which is assumed to be elastic, must obey in-plane conservation of momentum. As the 2-D surface of the crystals is hexagonal in the KKR calculations, one can prove that coupling to these surface modes can only occur at specific wavelengths λ_{surf} ,

$$\begin{aligned} \mathbf{k}_{\text{out},\parallel} &= \mathbf{k}_{\text{in},\parallel} + m \cdot \mathbf{b}_1 + n \cdot \mathbf{b}_2 \\ \lambda_{\text{surf}} &= \left(\frac{a \cdot \bar{n}_{2D} \cdot \sqrt{3}}{2} \right) \cdot \left(\frac{1}{\sqrt{m^2 + m \cdot n + n^2}} \right), \end{aligned} \quad (2.13)$$

in which $\mathbf{k}_{\text{out},\text{in},\parallel}$ are the components of the outgoing and incoming waves parallel to the crystal surface, $\mathbf{b}_{1,2}$ are the reciprocal-space basis vectors of the hexagonal surface, a is the lattice constant of the crystal surface, \bar{n}_{2D} is the 2-D average refractive index and (m, n) are integers. Equation 2.13 assumes single-scattering and, therefore, it should be applied to a single hexagonal layer of spheres with a small dielectric contrast only. Figure 2.11b presents the calculated transmission spectrum of a single hexagonal layer of 338 nm diameter spheres of refractive index 1.05 in air. Although the spikes are quite small due to the low refractive-index contrast, it is clear that every spike in the spectrum in Figure 2.11b can be attributed to a surface mode. It is not yet understood why the surface modes appear as a ‘forest’ of spikes in 3-D calculations, but it may have something to do with the larger index contrast. Anyway, Equation 2.13 can still be used to predict the wavelength λ_{max} above which coupling to surface modes should no longer occur, by using the lowest-order surface mode $(m, n) = (1, 0)$. This gives a maximum wavelength for coupling of surface modes of approximately 412 nm for Figure 2.11a and 306 nm for Figure 2.11b.

2.5.3 Summary

To summarize, our photonic band-structure calculations do not predict a band gap between band 5 and 6 for inverse BCT crystals at high dielectric contrast, contrary to what was predicted by Tao *et al.* [139]. Though BCT crystals may not have a band gap, they are still interesting for photonic applications, as plane-wave calculations show that they have a larger stop gap than FCC crystals at the same dielectric contrast. KKR calculations of transmission spectra confirmed the MPB calculations and additional low-wavelength features seen in these spectra have been explained as surface modes.

2.6 Photonic band-structure calculations & optical spectra

In Section 2.4, photonic band diagrams have been used to steer the development of a promising self-assembly route towards photonic crystals with a band gap in the visible. As the fabrication of these materials on the submicron scale remains challenging, band diagrams are typically calculated to predict the optical properties of photonic crystals *before* a lot of time and effort is invested in their actual fabrication. However, we demonstrate in this section that band-structure calculations can also be of great value in the analysis of spectroscopic data. Even better, we will show here that they can be used to probe, via optical spectroscopy, the average diameter of spheres within colloidal crystals in air, a quantity that was hardly accessible before! Electron microscopy, for example, can be used to accurately determine the size of colloidal particles, but the particles are heated up by the electron beam and they have to be in vacuum during the measurement. In the case of silica, for example, it is known that this can cause the particles to shrink up to 9% in electron microscopy measurements [140]. Furthermore, only particles at the surface of the crystal can be probed, as the penetration length of electrons in dielectric materials is only on the order of 10 nm.

Optical spectroscopy is a popular method for characterizing the quality of colloidal crystals [76]. However, it is a well-known problem that obtaining absolute values from experimental spectra is difficult, for what is actually measured, are optical distances Δx_{op} .

$$\Delta x_{\text{op}} = \bar{n} \Delta x \quad (2.14)$$

In order to convert such optical distances to real distances, a value for the average refractive index \bar{n} of the colloidal crystal slab must be known. For this, several schemes are being used: averaging the refractive index or the dielectric constant by volume, or using the Bruggeman approximation. Another approximation that is often used to average refractive indices is the Maxwell-Garnet approximation [141].

$$\bar{\epsilon}_{\text{MG}} = \frac{(1 - \varphi_{\text{crys}}) \epsilon_{\text{m}} + \varphi_{\text{crys}} \beta \epsilon_{\text{p}}}{1 - \varphi_{\text{crys}} + \varphi_{\text{crys}} \beta} \quad (2.15)$$

$$\text{with } \beta = \frac{3\epsilon_{\text{m}}}{\epsilon_{\text{p}} + 2\epsilon_{\text{m}}} \text{ for spheres}$$

Here, φ_{crys} is the filling fraction of spheres in the crystal (~ 0.74 for close-packed FCC), ϵ_{m} is the dielectric constant of the background medium (air in our case) and ϵ_{p} is the dielectric constant of the particles. However, there is no rigorous derivation available that supports the use of any of these schemes.

A value for the average refractive index of a colloidal crystal can be extracted from experimental spectroscopy data, but it requires an accurate value for the size of the colloidal spheres as well as knowledge of the 3-D structure of the sample. In the case of convective assembly of colloidal crystals of silica spheres, a close-packed structure is usually assumed[§], but the particle diameter is not accurately known. Silica particles that have been synthesized using the Stöber method are ultramicroporous [142, 143], leading to different sizes in static light scattering (SLS) and transmission electron microscopy (TEM) due to shrinkage upon drying [140].

[§]In Chapter 4, we show that colloidal crystals grown by convective assembly are not exactly close-packed. However, the observed deformation of the hexagonal layers hardly affects the interlayer spacing, so we can safely assume close-packing as far as the interlayer spacing is concerned.

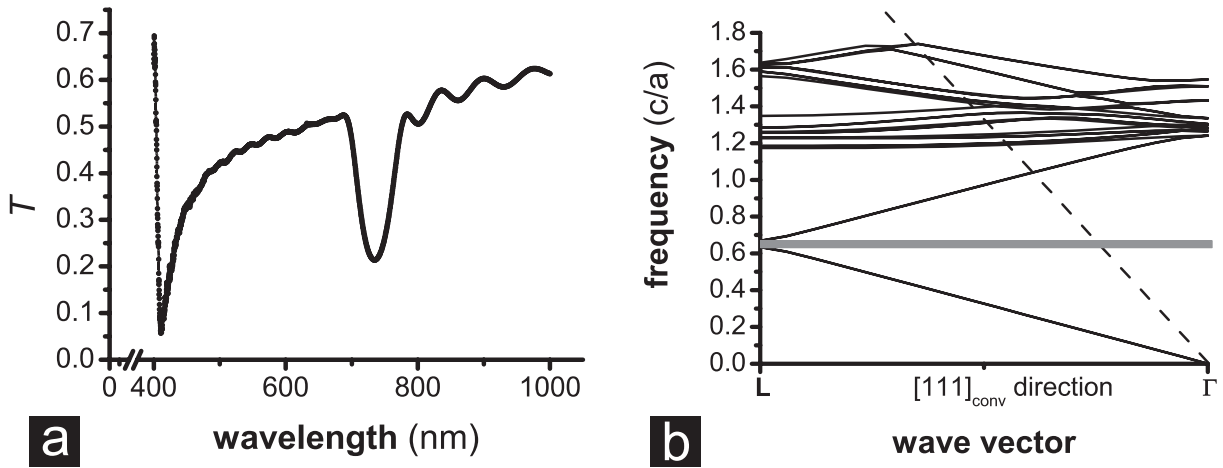


Figure 2.12: Figure (a) is the FTIR transmission spectrum of an approximately 17-layer colloidal crystal of $\sigma_{\text{TEM}} = 337$ nm diameter silica spheres in air (see also Figure 4.11a). The Bragg peak at 734 nm corresponds to the stop gap (gray), along the ΓL direction in the band diagram shown in panel (b). The dashed line represents the light line in vacuum.

However, transmission spectra of such colloidal crystals (Figure 2.12a) can be used to obtain an upper limit on the value for their average refractive index \bar{n} .

First of all, we will rewrite Bragg's law and use it as the definition of the average refractive index \bar{n} . For normal incidence onto the set of planes (hkl)

$$2\bar{n}d_{(hkl)} = m \cdot \lambda_{(hkl)}^{(m)} \Rightarrow \bar{n} = \frac{m \cdot \lambda_{(hkl)}^{(m)}}{2d_{(hkl)}}. \quad (2.16)$$

Typically, spectra are obtained along the $[111]_{\text{conv}}$ direction. If close-packing is assumed, the interlayer spacing $d_{(111)}$ along this direction can be written in terms of the particle diameter σ .

$$d_{(111)} = \frac{\sigma\sqrt{6}}{3} \geq \frac{\sigma_{\text{TEM}}\sqrt{6}}{3} \quad (2.17)$$

Unfortunately, as mentioned before, the particle diameter of our silica particles in the colloidal crystals is not accurately known. However, due to shrinkage in the TEM, we can safely assume that those spheres have a diameter of which the value is at least as large as the one determined by TEM (Equation 2.17). For a close-packed colloidal crystal, consisting of approximately 17 layers of 336.6 nm diameter silica spheres in air, the Fourier transform infrared (FTIR) spectrum shown in Figure 2.12a results in an upper limit for \bar{n} of (1.335 ± 0.008) .

The upper limit on \bar{n} that was just obtained from spectroscopy measurements is a useful quantity to know, but as it is an upper limit, it does not allow the determination of absolute values for interlayer spacings in colloidal crystals. MPB is able to *calculate* the average refractive index \bar{n} of a photonic crystal at the wavelength of a Bragg diffraction, if the refractive indices of the constituent components are known, thus allowing extraction of absolute distances from experimental spectra. In the following, we assume that our colloidal silica spheres are homogeneous in their refractive index, though this need not necessarily be the case [144]. The

first-order $(111)_{\text{conv}}$ Bragg peak corresponds to the stop gap, along the ΓL or $[111]_{\text{conv}}$ direction, between bands 2 and 3 (Figure 2.12b). Using Equations 2.16 and 2.17, we calculate \bar{n} from the center frequency of the corresponding gap according to,

$$\bar{n} = \frac{m \cdot \lambda_{(hkl)}^m}{2d_{(hkl)}} = \left(\frac{\sqrt{6}}{4} \right) \cdot \left(\frac{\sqrt{2}}{\hat{\nu}} \right), \quad (2.18)$$

in which $\hat{\nu}$ is again the center frequency of the gap in units of (c/a) . In the case of colloidal silica, its refractive index varies between syntheses, so a graph of \bar{n} versus the refractive index of silica around 1.45 is very useful. Figure 2.13 shows a comparison of four of such graphs obtained by averaging in different ways. KKR calculations also provide values for \bar{n} , for the wavelength $\lambda_{(111)}^{(1)}$ can be taken directly from the calculated transmission spectra. They can subsequently be inserted into Equation 2.16. Two of such values are also plotted in Figure 2.13 and they agree with the MPB result quite reasonably. For easy comparison, the experimental upper limit for the average refractive index has been incorporated in Figure 2.13 as well. It can be compared to the theoretical value from MPB, assuming a refractive index of 1.45 for silica: $\bar{n} = (1.328 \pm 0.007)$. As expected, the value of the upper limit for \bar{n} that was extracted from the FTIR spectrum is slightly larger than the value calculated via MPB.

We used MPB averaging to extract from optical spectroscopy measurements the size of the silica spheres in one of our colloidal crystals (Section 4.3). The average diameter of these spheres was determined to be (336.6 ± 2.0) nm by TEM after drying a droplet of dispersion on a grid. Due to the ultra-micro-porosity of Stöber silica, SLS and TEM results can differ up to 9% for such particles [140]. However, experiments involving index-matching with solvent mixtures showed that our Stöber particles typically have a refractive index of $n = (1.45 \pm 0.02)$ at a wavelength of $\lambda = 546$ nm [145, 146]. Reading off the value for \bar{n} from the graph in Figure 2.13, inserting that number into Bragg's law (Equation 2.16), the experimental transmission spectrum in Figure 2.12a yields a value for the interlayer spacing. Assuming close-packing, the diameter of the spheres in the crystal was determined to be (338.5 ± 3.8) nm, which is reasonably close to the TEM diameter. Note that the accuracy with which the diameter of the colloidal spheres can be extracted from spectroscopic data is comparable to the accuracy of results from TEM and SLS measurements!

It may come as a surprise that the 'spectroscopic' diameter of the colloids in the crystal is so close to their TEM diameter. The sample of which a spectrum is shown in Figure 2.12a had been in an SEM, but that was at least several months before the spectroscopic measurements presented here. Because of the severe conditions in an SEM, a pressure that is approximately $10^7 \times$ lower than 1 atmosphere to name one, our ultramicroporous Stöber silica particles lose most of the water that they absorbed during synthesis in an SEM measurement. In a TEM, conditions are even more severe than in an SEM, for the energy of the electron beam is typically on the order of 100 keV instead of 5 keV. This causes silica particles to shrink even more! We observed, however, that silica particles that were dried under a lamp gained approximately 10% in weight after switching off the light, which is probably due to adsorption of water from the air. Therefore, it is no surprise that the 'spectroscopic' diameter of silica spheres is close to, but slightly larger than, the TEM diameter.

Although it is a bit more involved, KKR spectra were also fitted to experimental data (Figure 2.14a). These normal-incidence spectra were calculated for a free-standing, colloidal crystal of

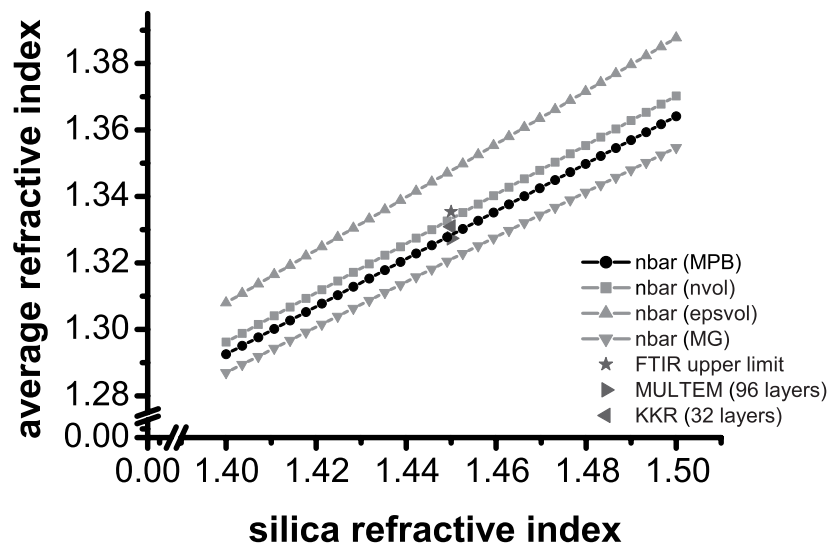


Figure 2.13: Calculated average refractive index of an infinite, FCC crystal of colloidal silica spheres in air as a function of the refractive index of silica. The black dots correspond to MPB plane-wave calculations, the gray squares to averaging the refractive index by volume, the gray triangles pointing upwards to averaging the dielectric constant by volume and the gray triangles pointing downwards to averaging the dielectric constant using Maxwell-Garnet. In addition, KKR calculations were performed for a 96-layer FCC crystal using MULTEM (dark gray triangle pointing to the right) and for 32 layers using a KKR code by Alexander Moroz (dark gray triangle pointing to the left). Finally, an upper limit for the average refractive index of the crystal was obtained from FTIR spectroscopy in combination with TEM measurements, which is plotted as a dark-gray star.

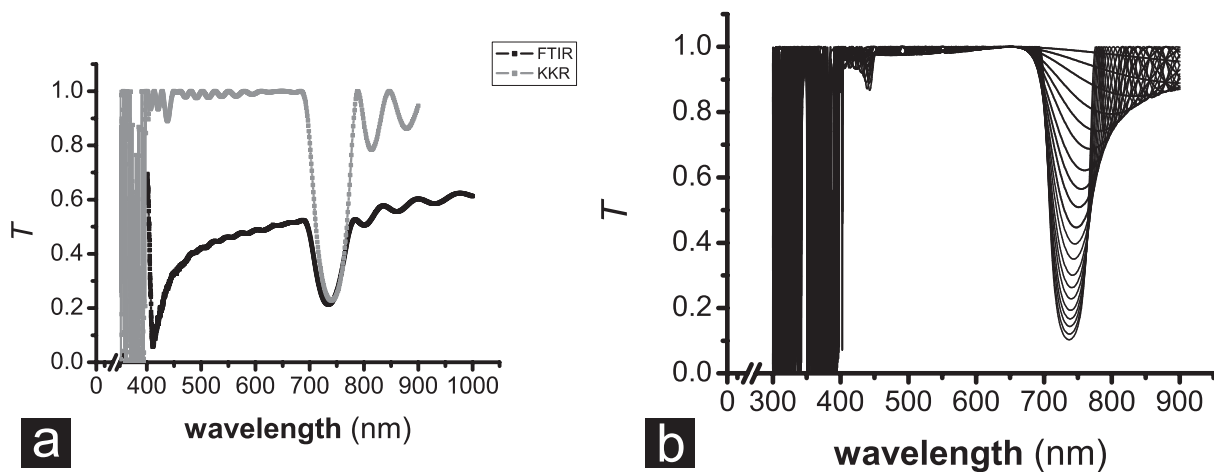


Figure 2.14: Figure (a) is the FTIR transmission spectrum of an approximately 17-layer colloidal crystal of $\sigma_{\text{TEM}} = 336.6$ nm silica spheres in air (see Figure 2.12a). The gray line is a fit using a KKR code by Alexander Moroz for a free-standing, colloidal crystal of 338 nm silica ($n = 1.45$) spheres in air, having 15 layers. The same code was used to calculate transmission spectra for a similar crystal in which the number of layers was varied (panel b). Spectra are shown for 2 layers (upper graph) to 20 layers (lower graph).

338 nm diameter silica ($n = 1.45$) spheres in air, having 15 layers. The position of the Bragg peak can be fitted quite well, just as the fringe spacing. However, the average transmission of the real crystal was quite small compared to the theoretical prediction, which might be due to scattering from the sample substrate and from crystal defects. KKR calculations are also useful to determine the effect of finite size of colloidal crystals on their optical properties. As the refractive-index contrast between silica and air is relatively small, interference needs to build up over several layers. Figure 2.14b clearly proves that the Bragg diffraction shifts to smaller wavelengths and becomes deeper if the number of layers increases. However, it is quite clear from the same figure that the peak will hardly shift anymore if the number of layers is larger than 20.

In short, we have shown that photonic band-structure calculations are not only able to guide the fabrication of photonic band-gap materials, they can also be used in the analysis of experimental data. Combining optical spectroscopy with MPB plane-wave calculations, we have been able to obtain a value for the average refractive index of a colloidal crystal of silica spheres in air. Using that value, we have probed the size of the spheres in the crystal, a quantity that was hardly accessible before.

2.7 General conclusions and outlook

In this chapter, we have first explained what a photonic crystal is and why it is important to be able to calculate its optical properties. Next, the concept of a photonic band diagram was introduced. Starting from the Maxwell equations, we derived the master equation for electromagnetic waves in photonic crystals. From the master equation, enforcing transversality of the magnetic and displacement fields, the dispersion relation $\omega(\mathbf{k})$ of electromagnetic waves in

photonic crystals can be calculated. Using group theory, it can be shown that, in order to find the gaps of a photonic crystal, the dispersion relation only needs to be plotted along a specific trajectory in reciprocal space, resulting in a photonic band diagram.

Subsequently, it was shown that such photonic band-structure calculations can be used to guide the fabrication of photonic band-gap materials. Our calculations confirmed that both diamond and pyrochlore are strongly photonic crystals, i.e. they have low-lying gaps, possibly in the visible region, that are relatively wide at low refractive-index contrasts. They can be fabricated via the self-assembly of one of the binary Laves phases, as they are the large and small-sphere components, respectively, of the MgCu_2 structure.

Furthermore, we have calculated the photonic band diagram of inverse body-centered tetragonal (BCT) crystals. In contradiction to results in literature [139], we found that there is no photonic band gap for inverse BCT crystals. Finally, we have demonstrated that photonic band-gap calculations can be used in the data-analysis of spectroscopic measurements. As an example, we have been able to obtain a value for the average refractive index of a colloidal crystal of silica spheres in air. Using that value, we have probed the size of the spheres in the crystal, a quantity that was very hard to probe before. In the near future, the proposed scheme for calculating average refractive indices of colloidal crystals, thus allowing accurate determination of interlayer spacings, can be used to correct distances measured along the optical axis of a confocal-microscope objective for spherical aberrations [147].

Although we think it is due to a numerical artefact of the discretization of the real-space unit cell, the slow convergence of plane-wave calculations for direct diamond and pyrochlore structures should be looked into more carefully. In general, convergence in photonic band-structure calculations, be it MPB plane-wave or KKR calculations, should be studied more extensively, as experimentalists start to rely on numerical results more and more. Another important issue in photonic calculations is the incorporation of metals in photonic crystals. Recent simulations have demonstrated that metallodielectric photonic crystals may have very interesting optical properties [32, 148]. KKR codes can deal with the strong dispersion in metals, more or less, but it would be of great value if a plane-wave code would be developed that can deal with the negative real part of the dielectric constant and the absorption in metals. Finally, once the optical properties of ideal photonic crystals can be calculated, the effect of (dielectric) doping on these optical properties should be investigated from a theoretical point of view. As such defects break the translational symmetry of their host crystal, finite-difference time-domain (FDTD) simulations may be more suitable to deal with defects. Still, plane-wave band-structure calculations for supercell geometries will be a valuable addition to the FDTD results.

Acknowledgements

First and foremost, I would like to express my sincere gratitude towards Esther Vermolen for many pleasant and useful discussions on photonic band-structure calculations and for critical reading of this chapter. Furthermore, the MULTEM and KKR results that have been presented in Figures 2.7 and 2.13 were calculated by her.

In addition, I would like to thank Mischa Megens for providing the MPB patch file [127]. Dannis 't Hart is gratefully acknowledged for helping me out whenever I got stuck in UNIX,

Henk Mos for installing MPB and the additional patch file on RUUNAT and VENUS. Finally, I would like to thank Alexander Moroz for useful discussions on photonic band diagrams and for providing the KKR code to calculate reflection and transmission spectra of photonic crystals with a finite number of layers.

Part of the work that is described in Section 2.4 has been published as Reference [114] - A.-P. Hynninen, J. H. J. Thijssen, E. C. M. Vermolen, M. Dijkstra and A. van Blaaderen, *Self-assembly route for photonic crystals with a bandgap in the visible region*, Nature Materials **6**(3), 202 (2007). A.-P.H. did the MC simulations under the supervision of M.D., J.H.J.T. and E.C.M.V. did the photonic band-structure calculations and A.v.B. initiated and supervised the project.

Microradian X-ray diffraction from photonic colloidal crystals

Ultra-high resolution, small-angle X-ray scattering (SAXS) in various photonic colloidal crystals is reported. It is demonstrated that an angular resolution of about 2 microradians is readily achievable at a third-generation synchrotron source using compound refractive optics. The scheme allows for fast acquisition of two-dimensional X-ray diffraction data and can be realized at sample-detector separations of only a few meters. As a result, diffraction measurements in colloidal crystals with interplanar spacings larger than a micron, as well as determination of the range of various order parameters from the width of the Bragg peaks are made possible.

3.1 Introduction

As was discussed in Chapter 2, photonic crystals are structures in which the refractive index varies periodically in space in one, two or three dimensions. The periodicity is typically on the order of the wavelength of light [7]. Because of their strong interaction with light, photonic crystals may lead to important applications in infrared telecommunications [8, 67]. A promising route towards relatively cheap photonic crystals with many crystal layers is colloidal self-assembly [95, 107, 108]. Colloids are excellent building blocks for photonic band-gap materials, as they have a size comparable to the wavelength of light. Monodisperse colloidal particles can self-assemble into 3-D periodic arrangements, analogous to thermodynamic crystal phases [57]. These so-called colloidal crystals are then used as templates for infiltration with a high-index material, such as silicon, to enhance the refractive-index contrast [67, 68]. After infiltration, the original template is removed by a wet-chemical etch, resulting in a strongly photonic crystal.

Microscopic techniques, including confocal microscopy and electron microscopy, have been successfully applied in order to probe the structure of the resulting colloidal crystals [78, 88, 99, 149]. These real-space techniques, however, suffer from a couple of disadvantages. First of all, they provide structural data only on a microscopic scale. Typically, only a small part of the sample volume is imaged, making it difficult to probe long-range order. In addition, electron microscopy only provides topological data on the surface of the sample. Samples have to be cleaved, causing structural damage, to get an idea of the 3-D structure in the bulk of the crystal. Confocal microscopy has the ability to obtain true 3-D structural information from the bulk of a sample, but it requires refractive-index matching of the particles and the surrounding medium, which is impossible in the case of, for example, a crystal of air spheres in silicon.

Small-angle X-ray scattering (SAXS) has proven to be a powerful technique to study the structure of colloidal crystals made of submicron particles [150–153]. In comparison to light scattering [154–157], X-rays have an extremely small refractive-index contrast (typically on the order of 10^{-6}) and do not require index matching in most cases. SAXS can thus be applied to crystals that are strongly scattering or absorbing in the visible region. Moreover, scattering of X-rays can be measured in a wide range of scattering vector values q and can therefore be applied to colloidal crystals with periodicities that are too small to be accessed with visible light (see Chapter 4).^{*} Finally, diffraction techniques, which are able to provide detailed macroscopically-averaged information, are superior in quantitative determination of the order parameters over large distances, as long as coherence length is not the limiting factor.

The challenge of the application of SAXS for structural characterization of self-assembled photonic colloidal crystals stems from the 3 to 4 orders of magnitude difference between the typical size of colloidal particles ($\sim 1 \mu\text{m}$) and typical X-ray wavelengths ($\sim 0.1 \text{ nm}$). To resolve the diffraction pattern, one often needs an angular resolution well beyond 10^{-4} rad. Even higher resolution, on the order of 10^{-6} rad, is needed to determine the intrinsic width of the diffraction peaks, which would allow for detailed characterization of long-range order. Moreover, in some cases [158], the distinction between different thermodynamic phases can only be made on the basis of the difference in the intrinsic width of the reflections [158].

The so-called ultra-small-angle X-ray scattering (USAXS) technique is commonly believed

^{*}Throughout this chapter, the scattering vector $\mathbf{q} = \mathbf{k}_s - \mathbf{k}_i$ is defined as the vector difference between the wave vectors of the scattered \mathbf{k}_s and the incident \mathbf{k}_i waves with $k_s = k_i = (2\pi/\lambda)$, where λ denotes the wavelength.

to facilitate the highest angular resolution possible [159, 160]. It uses a point detector and a set of so-called Bonse-Hart cameras [161], each consisting of a pair of Bragg-reflecting crystals. USAXS allows one to resolve the angular spectrum of scattered radiation with a resolution determined by the angular width of the rocking curve of the Bragg reflection. The presently used Si-(111) and Si-(220) reflections have an angular width on the order of 10^{-5} rad, which is often not sufficient to resolve the intrinsic width of the reflections in colloidal crystals. The resolution of the Bonse-Hart camera can be further enhanced by choosing higher-order reflections [162], but such a possibility has not been realized yet for USAXS applications. More importantly, the USAXS scheme requires a long acquisition time due to its point-by-point data collection. It has been used for samples consisting of colloidal-crystal powders [163], but in the case of single crystals, yielding essentially two-dimensional (2-D) patterns, the USAXS scheme is impractical.

Much shorter acquisition times (from minutes down to milliseconds) can be achieved in an ordinary SAXS scheme with a 2-D detector. Most of the reported studies of colloidal crystals using a SAXS setup [150–153] were performed with an angular resolution on the order of 10^{-4} rad. A few examples of studies at resolutions of $1 \cdot 10^{-5}$ rad to $5 \cdot 10^{-5}$ rad were also reported for sample-detector distances on the order of 10 m [164–166] and more than 100 m [167]. For colloidal crystals with submicron lattice spacings this resolution is sufficient to resolve the Bragg reflections, but the information on the intrinsic width of the reflections can hardly be obtained from the apparent size of the reflections on the detector. Moreover, the resolution of an ordinary SAXS setup is often insufficient for photonic crystals with spacings larger than a micron.

A significant increase in terms of the angular resolution well into the 10^{-6} rad range can be achieved at third-generation synchrotron sources using refractive optics [168]. In this chapter, we further demonstrate that this gives access to information on long-range order in colloidal crystals, which was not achievable before, and which opens up new avenues for future fundamental and applied research. The rest of the chapter is organized as follows. First, in Section 3.2, the different types of disorder in (colloidal) crystals are discussed. Next, in Section 3.3 we briefly review the conditions needed to achieve high angular resolution. Experimental details are summarized in Section 3.4. We then present several examples of our results obtained in various self-organized colloidal crystals. Section 3.5 describes the results on a wall-induced crystal of PMMA spheres. In Section 3.6, application of the technique to photonic crystals with interplanar spacings as large as $1.35 \mu\text{m}$ is demonstrated. A study of disorder in random hexagonal close-packed (RHCP) crystals of hard silica spheres is briefly described in Section 3.7. The ultimate limit of the angular resolution which can be achieved by the optical setup was measured with high-resolution X-ray films, as described in Section 3.8. Finally, the results are summarized in Section 3.9.

3.2 Disorder in colloidal crystals

For atomic crystals there are two main types of disorder [105]. In so-called *perfect* crystals one finds only disorder of the first type, such as the thermal motion of atoms around the lattice points. It does not disturb the average, ideal lattice of the crystal and the positional correlations between the atoms extend over the whole crystal. In *real* crystals, however, one can also find

disorder of the second type, which disturbs the average lattice so that the positional correlations have only a finite spatial extent, which is smaller than the crystal size. In real colloidal crystals one can expect that different types of disorder play an important role. In addition to various growth defects, which are also typical for atomic crystals, colloids possess inherent size polydispersity, which can contribute to the disorder of the first type in a colloidal crystal. It can also induce various internal stress fields, which can deform the average lattice and thus can lead to disorder of the second type. The long-range order can be of fundamental importance since it can greatly affect the crystallization rate and it can influence the size of the grown crystallites. Moreover, the various types of disorder can also lead to a significant degradation of the performance of the photonic materials fabricated from such self-organized colloidal crystals [149, 169].

Disorder of various types manifests itself in different ways in a diffraction pattern. For small crystals, finite size effects lead to broadening of the diffraction peaks, which is independent of the diffraction order. In a so-called mosaic, consisting of small crystallites which are orientationally correlated but positionally independent, the peak width in the *azimuthal* direction apparently increases with the diffraction order due to small fluctuations in the orientation of different crystallites. However, the *radial* width is still independent of the diffraction order. Disorder of the first type does not broaden the Bragg peaks but manifests itself in the Debye-Waller factor, which can be accurately measured by SAXS [170]. Disorder of the second type leads to additional peak broadening, which increases with diffraction order [105].

3.3 Resolution and coherence

An X-ray diffraction pattern originates from interference of waves scattered coherently by colloidal particles. To resolve it, the conditions for constructive interference of coherent waves scattered from particles separated by a few structure periods must be met. To resolve the intrinsic width of Bragg reflections, one needs coherence over distances that are comparable to the positional correlation length of the structure [171].

In the longitudinal, direction this condition can be easily fulfilled over macroscopic ($> 100 \mu\text{m}$) distances for small diffraction angles [152, 166]. By tilting the crystal from a certain crystallographic direction and observing the variation of the integrated intensity of reflections, one can achieve a reciprocal-space resolution on the order of $10^{-6} \cdot k_i$. This technique, however, is only applicable to single crystals and only allows one to measure intrinsic widths of Bragg reflections along the X-ray beam, *i.e.* orthogonal to the scattering vector \mathbf{q} for small diffraction angles 2θ . Moreover, one often needs to collect diffraction data for many crystal orientations in order to reconstruct rocking curves, which requires longer data-acquisition times.

Of much more importance is the width of reflections in the radial direction, along \mathbf{q} . It can only be probed if a very high angular resolution is achieved. The latter is also much more challenging, since it requires the random fluctuations of the phase front to be much smaller than the tiny X-ray wavelength λ on macroscopic distances. For a freely propagating X-ray wave, this condition is fulfilled over the so-called transverse coherence length l_{trans} , which is equal to

$$l_{\text{trans}} = \frac{L\lambda}{\sigma}, \quad (3.1)$$

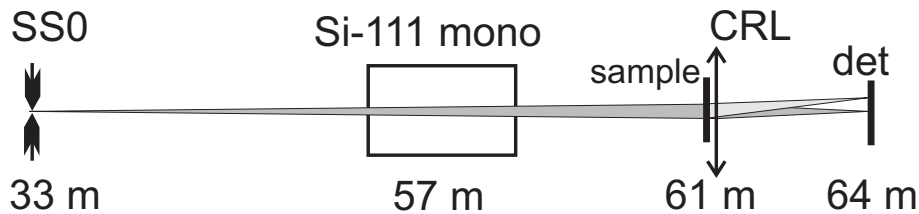


Figure 3.1: Sketch of the setup. Only the principal components (the primary slits SS0, the Si-(111) monochromator, the sample, the lens (CRL) and the detector) are shown. The numbers indicate distances from the undulator source.

where σ is the source size and L is the distance travelled by the beam. Furthermore, beamline optics can affect beam coherence. Apart from imperfections in optical elements, which can introduce additional distortions of the phase front, beam focusing can significantly reduce l_{trans} [166]. A simple solution to this problem is to avoid beam focusing before the sample and to let the X-ray beam propagate freely to the sample. With a typical source size $\sigma \sim 100 \mu\text{m}$ and a source-sample distance $L \sim 50$ meters at a synchrotron X-ray source, a transverse coherence length on the order of $l_{\text{trans}} \sim 50 \mu\text{m}$ to $100 \mu\text{m}$ can be reached, *i.e.* the transmitted X-ray beam will contain information on the positional correlations of the colloidal particles over a distance of about 100 lattice periods. To extract this information, we used a compound refractive lens (CRL) [172], which can recover the Fourier spectrum of the transmitted beam [173] by performing beam focusing onto the detector within a relatively short sample-detector distance (usually limited to several meters by the length of the experimental hutch).

3.4 Experimental methods

The experiments were performed at beamline ID10A “TROÏKA” of the European Synchrotron Radiation Facility (ESRF) in Grenoble, France. The fifth harmonic of the undulator source with a photon energy of 13.4 keV (wavelength $\lambda = 0.0925$ nm) was selected by a flat, channel-cut Si-(111) monochromator. Due to the particular properties of the electron β -function of the ESRF storage ring, the X-ray source of ID10 has dimensions of about $25 \mu\text{m} \times 1000 \mu\text{m}$, *i.e.* it is too large in the horizontal direction to obtain a sufficient coherence length at the sample position. We therefore used a rather small opening of the primary slits (SS0) of $30 \mu\text{m}$ in both the horizontal and the vertical direction, as illustrated in Figure 3.1. This scheme leads to a significant loss of beam intensity. Fortunately, most of our samples scatter X-rays strongly enough to allow collection of sufficient signal within short exposure times τ (typically on the order of a few seconds).

The $30 \mu\text{m} \times 30 \mu\text{m}$ slit size was on the order of the transverse coherence length at the position of the SS0 slits in the vertical direction, but about one order of magnitude larger than the transverse coherence length in the horizontal direction. Considering the primary slits as a secondary X-ray source for the rest of the setup, we estimated the transverse coherence length at the sample position to be on the order of $l_{\text{trans}} = 100 \mu\text{m}$ and the beam size of a few hundreds of μm . Thus, we intentionally did not create conditions for fully coherent X-ray illumination to avoid the appearance of speckle patterns [174].

The transmitted and diffracted X-ray beams were focused by a CRL [168, 172] that was positioned just behind the sample. The lens position and its focal length were adjusted such that it created an image of the secondary X-ray source (SS0) at the position of the detector. For the given SS0-lens and lens-detector distances, the magnification of the imaging system was about 1:8.5, such that the CRL should have produced an image of about $3.5 \mu\text{m}$ of the $30 \mu\text{m}$ wide SS0 slits. With a lens-detector distance of $L_{ld} = 3.25$ meters, one can therefore expect an angular resolution of the setup on the order of $1 \mu\text{rad}$.

The vast majority of the results (Sections 3.5 to 3.7) were recorded with a 12-bit CCD camera (Sensicam) with a pixel size of $6.7 \mu\text{m} \times 6.7 \mu\text{m}$ and a field size of $8.6 \text{ mm} \times 6.9 \text{ mm}$. The camera was supplemented by an X-ray sensitive phosphor screen and a 1:1 projecting objective. Since CCD detectors have a rather limited dynamic range (*i.e.* the ratio of maximum to minimum intensity that can be measured reliably at the same instant), every diffraction pattern was recorded several times with different exposure times τ . The shortest exposure was used to quantify the strongest reflections, while the longer exposures were used for analysis of weaker, higher-order reflections. Furthermore, X-ray sensitive films (Kodak) with a spatial resolution better than 1 micron were used to probe the angular-resolution limit provided by the optical setup as described in Section 3.8.

3.5 Wall crystallization of PMMA spheres

Cylindrical glass capillaries (diameter 1.5 mm, wall thickness $10 \mu\text{m}$) were filled with suspensions of poly(methyl methacrylate) (PMMA) colloidal hard spheres in cis-decalin at an initial volume fraction of 30%. The particles (diameter 230 nm) are sterically stabilized with 10 nm chemically-grafted polyhydrostearic acid. The capillaries were stored vertically to establish a sedimentation-diffusion equilibrium. Visual inspection revealed that the top part of the capillary contained a turbid colloidal fluid. Colloidal crystals yielding strong Bragg reflections of visible light formed in the sediment at the bottom of the capillary. Figure 3.2a presents a pattern measured a few millimeters above the crystalline sediment. The broad rings in the scattering field originate from the fluid phase in the bulk of the suspension. In addition, sharp Bragg peaks in the pattern reveal that a colloidal crystal had grown at the capillary wall.

The diffraction pattern is typical for a random hexagonal close-packed (RHCP) crystal. The reciprocal lattice of the RHCP structure consists of Bragg spots and Bragg rods [151, 153]. The stacking-independent Bragg spots are found at the (hkl) reflections with $(h-k)$ divisible by 3 and integer values of ℓ . The stacking-disorder-induced Bragg rods with a smooth intensity variation along ℓ are observed for $(h-k)$ not divisible by 3. For the crystal orientation in Figure 3.2a, the X-ray beam is orthogonal to the hexagonal planes and thus $\ell = 0$. One can clearly see the (110) and (300) reflections originating from the true Bragg spots. Here the contributions from all the hexagonal layers have the same phase leading to a large structure factor. For $(h-k)$ not divisible by 3, the contributions of the hexagonal layers possess an additional stacking-dependent phase of 0° or $\pm 120^\circ$ leading to significant cancellation between them and therefore a much smaller structure factor. This explains the significantly weaker diffraction intensity of the (100) reflection relative to the (110) reflection, despite the much larger form factor of the former. Similarly, the (300) reflection is much stronger than the (200) reflection, which has a much higher value for the form factor. The (220) reflection with a strong structure factor is,

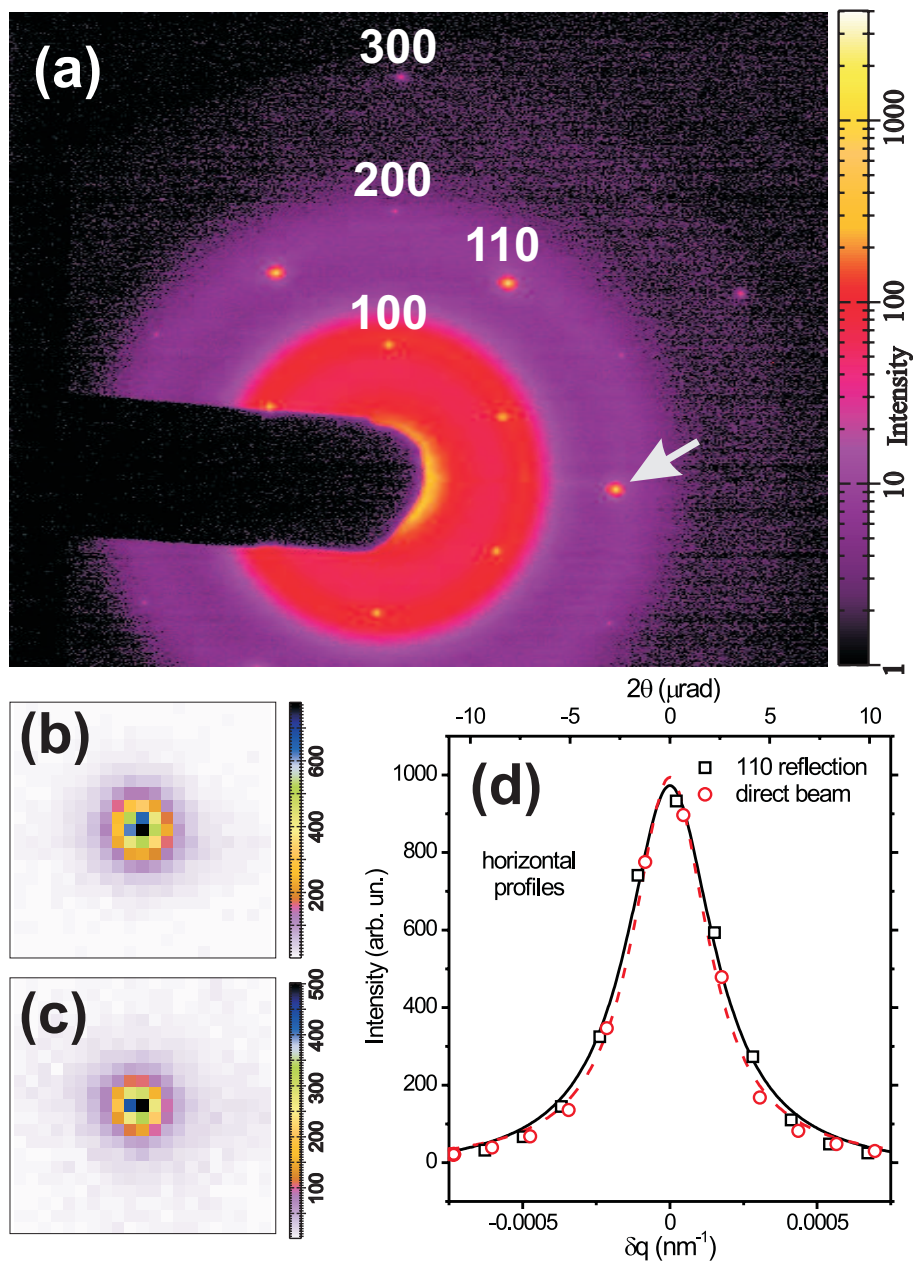


Figure 3.2: (a) Diffraction pattern ($1280 \text{ pixels} \times 1024 \text{ pixels}$) of wall-induced crystals, in coexistence with a colloidal fluid, in a cylindrical capillary with a PMMA hard-sphere colloidal suspension. Exposure time $\tau = 10 \text{ s}$. Note that the strong (110)-class reflections saturate the detector here. Panel (b) presents a zoom ($21 \text{ pixels} \times 21 \text{ pixels}$) into the (110)-class reflection marked in (a) by a white arrow. It was taken from a similar pattern, but measured with an exposure time of $\tau = 1 \text{ s}$. For comparison, panel (c) shows a magnified view of the direct beam after removing the beam stop ($\tau = 1 \text{ ms}$). Note that a linear intensity scale is used in panels (b) and (c) and a logarithmic scale in panel (a). In panel (d), the squares and circles represent pixel readings in horizontal slices through the peaks in panels (b) and (c), respectively. The lines are Lorentzian fits to the data. The vertical scale for both data sets is slightly readjusted.

however, hardly visible since it appears very close to a zero of the sphere form factor.

Figure 3.2b presents a magnified ($\times 20$) view of one of the (110)-class reflections. For comparison, an image of the direct beam is also given in Figure 3.2c. By adjusting the exposure time τ , we made sure that the intensity scale was similar in the data presented in Figures 3.2b and 3.2c. It is seen that both peaks have practically the same width, *i.e.* the (110) reflection from the colloidal crystal is practically instrument-limited. This is further illustrated in Figure 3.2d, where the horizontal profiles through both peaks are presented. The pixel intensities were fitted with Lorentzian line profiles. For the profile of the direct beam, which can be considered as the instrument resolution function, the fit yields a full-width-at-half-maximum (FWHM) of $\Delta_{\text{ver}} = 3.12 \cdot 10^{-4} \text{ nm}^{-1}$ and $\Delta_{\text{hor}} = 3.09 \cdot 10^{-4} \text{ nm}^{-1}$ in the vertical and horizontal directions, respectively. This means that, in angular terms, the digital data recorded with the CCD detector have a resolution of about $4.6 \mu\text{rad}$. We will show in Section 3.8 that this value is mainly limited by the resolution of the detector itself.

For the (110) reflection in Figure 3.2b, the Lorentzian fits yield a FWHM of $3.87 \cdot 10^{-4} \text{ nm}^{-1}$ and $3.62 \cdot 10^{-4} \text{ nm}^{-1}$ in the vertical and horizontal directions, respectively. These values are slightly higher than those for the instrument resolution. Since the intrinsic width of the sample reflection δq_{intr} and the width of the instrument resolution Δ yield statistically independent contributions to the apparent reflection width δq_{app} , we may assume that

$$\delta q_{\text{app}}^2 = \Delta^2 + \delta q_{\text{intr}}^2 . \quad (3.2)$$

Substituting the obtained widths of the Lorentzian fits, one gets $\delta q_{\text{intr}} = 2.3 \cdot 10^{-4} \text{ nm}^{-1}$ and $1.9 \cdot 10^{-4} \text{ nm}^{-1}$ in the vertical and horizontal directions, respectively. For comparison, the magnitude of the diffraction vector of the (110) reflection is $q_{(110)} = 4.70 \cdot 10^{-2} \text{ nm}^{-1}$. It is worth stressing that these values of δq_{intr} can only be used as an order-of-magnitude indication for the upper limit of the width of the crystal reflections. Peak profiles of the direct beam and the crystal reflections are very close to each other (Figure 3.2d) and a small inaccuracy in the determination of their widths can lead to a significant change of δq_{intr} due to the relation assumed in Equation 3.2.

3.6 Photonic crystals with a periodicity larger than a micron

In order to open up a photonic band gap, photonic crystals require a large refractive-index contrast for visible and near infrared light. This complicates characterization of their structure using optical techniques. As X-rays interact relatively weakly with matter, they form an excellent probe for the internal 3-D structure of and the long-range order in photonic crystals (see Chapter 7). Photonic materials for near-infrared-telecommunication applications, with spacings on the order of $1 \mu\text{m}$, are especially challenging for X-ray scattering techniques, because the diffraction angles are extremely small. Here we demonstrate the application of microradian SAXS to such a crystal with lattice spacings larger than a micron.

Colloidal crystals were fabricated using a method described by Yethiraj *et al.* [109], which allows the growth of large colloidal single crystals (see Chapter 6). Silica colloidal spheres (diameter $d = 1.4 \mu\text{m}$) in a refractive-index-matching solvent mixture of water and dimethyl sulfoxide (DMSO) were allowed to sediment in an AC electric field perpendicular to gravity.

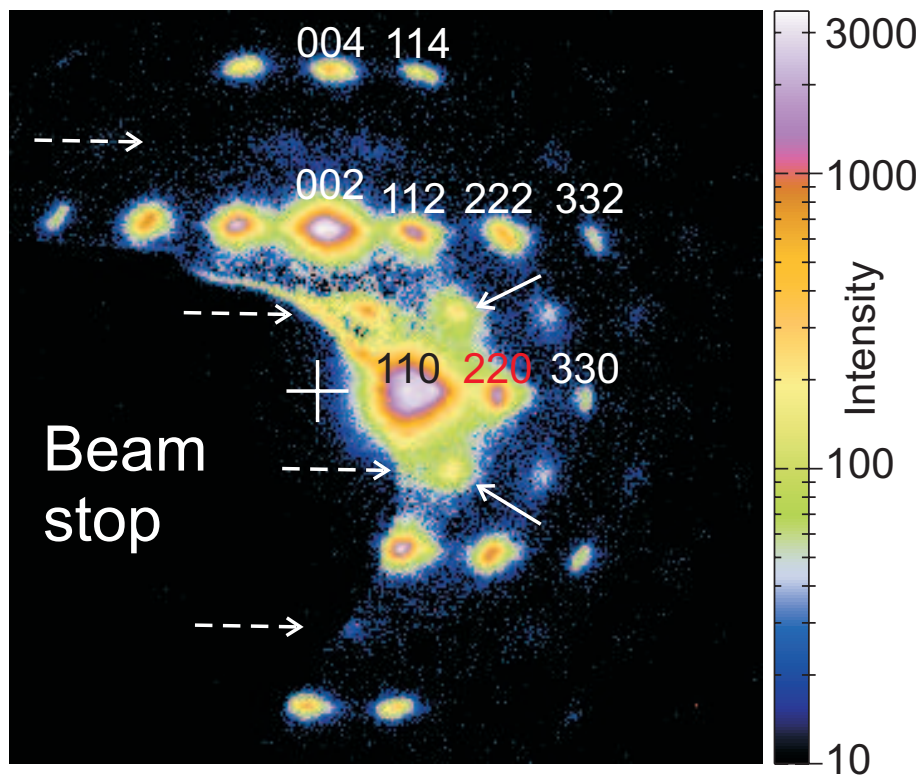


Figure 3.3: A zoom ($300 \text{ pixels} \times 300 \text{ pixels}$) of the central part of the diffraction pattern of a BCT colloidal crystal. The white cross marks the position of the direct beam, which is behind the beam stop. Note that the (110) and (002) reflections saturate the detector because of which their widths are greatly exaggerated. See text for further details.

The external electric field adds a long-range dipolar term to the interaction potential of the particles [175]. For high field strengths, the dipolar term dominates over the steric or electrostatic repulsion, favoring the formation of body-centered tetragonal (BCT) instead of close-packed structures [176]. Such BCT samples consist of ABAB-stacked, hexagonal layers that are oriented parallel to the glass substrate. However, the layers are bridge-site instead of hollow-site stacked. Using a polymerization process, this metastable BCT structure can be preserved, even after switching off the electric field (see Chapter 6).

An example of a diffraction pattern from a BCT colloidal crystal is presented in Figure 3.3. The crystal consists of (15 ± 1) hexagonally packed layers of silica spheres. The X-ray beam is normal to the hexagonal planes. The reflections are indexed using orthogonal basis vectors of length $b_1 = b_2 = ((4\pi)/(a\sqrt{6}))$ and $b_3 = (2\pi/a)$, where a is the nearest-neighbor distance. Here the \mathbf{b}_3 vector is parallel to the direction of the applied electric field. Reflections of a BCT crystal can be observed for even values of $(h + k + \ell)$. For the crystal orientation used here only the reflections with $h = k$ and even values of ℓ can be seen. The dashed arrows point to lines of reflections, which should be absent in a perfect BCT crystal because of the cancellation of contributions of 2 subsequent hexagonal layers. Their small but finite intensity can be related to the small number of layers in the crystal and lattice imperfections. The solid arrows point to two of these non-BCT reflections. This presence of these CP reflections indicate that a small portion of the crystal has changed its stacking from bridge-site to hollow-site. These reflections correspond to the (110)-class reflections in Figure 3.2a. Their intensity, however, is very much smaller than that of the (002) reflection with the same form factor and, thus, BCT is the dominating structure in the crystal.

The smallest diffraction angle of $2\theta_{(110)} = 69\mu\text{rad}$ originates from the largest real-space interplanar spacing, which corresponds to the distance between lines of close-packed particles in a hexagonal layer. From the magnitude of the diffraction vector $q_{(110)}$ in the pattern in Figure 3.3, a value for the $d_{(110)}$ distance of $(1.35 \pm 0.04) \mu\text{m}$ was found. The 3% uncertainty in the absolute value of $d_{(110)}$ mostly originates from inaccuracies in q -space calibration. It compares well with $d_{(110)} = (1.32 \pm 0.01) \mu\text{m}$ determined by confocal microscopy.

The angular resolution achieved in this experiment allowed us not only to resolve the diffraction pattern at tiny diffraction angles 2θ , but also to detect further details related to the crystal quality. For example, in the crystal used in Figure 3.3, the FWHM of reflections in the radial direction is $4.5 \cdot 10^{-4} \text{ nm}^{-1}$ to $5 \cdot 10^{-4} \text{ nm}^{-1}$, *i.e.* somewhat larger than the width of the instrument resolution function. This means that the crystal possesses a finite spatial extent of positional correlations. Moreover, the diffraction peaks are seen to be broadened in the azimuthal direction, which reveals a mosaic structure of the crystal with a small degree of misorientation between the crystallites.

3.7 Disorder in a crystal of silica spheres

Figure 3.4 displays two diffraction patterns measured from two different RHCP crystals of sterically-stabilized hard silica spheres (diameter 224 nm, dispersed in cyclohexane). The system is described in more detail in [166]. The crystals spontaneously formed in the sediment at the bottom of two different flat glass capillaries (4 mm wide, internal path length 0.2 mm). The two patterns in Figure 3.4 show Bragg reflections with remarkably different shapes. While

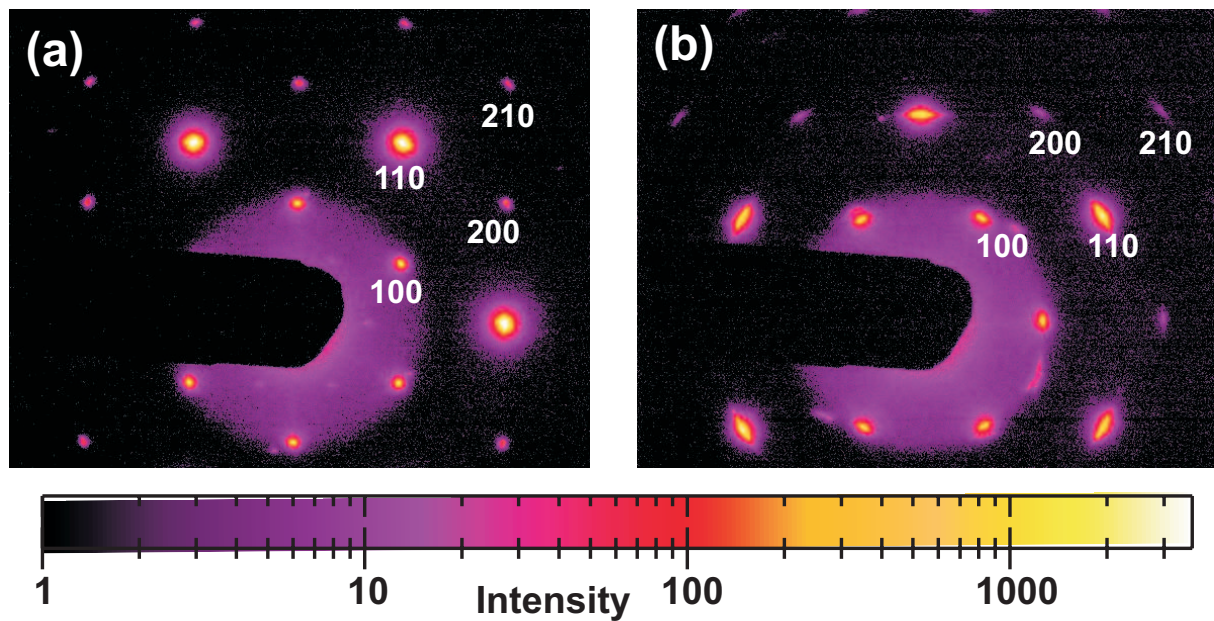


Figure 3.4: Diffraction patterns from two different crystals of silica hard spheres. Both crystals are oriented such that the X-ray beam is orthogonal to the hexagonal planes. The exposure time $\tau = 10$ s. Note that at this exposure the (100) reflection and, especially, the intense (110) reflection saturate the detector so that their width is greatly exaggerated.

panel (a) displays reflections that are (almost) circularly symmetric, panel (b) has reflections that are strongly spread in the azimuthal direction. It is obvious that the improved resolution is crucial to observe the distinction between the two crystals, which would not have been possible with the resolution used by [150–152, 177].

We have further studied the reflection width δq_{app} in the radial direction. For all reflections in Figure 3.4a, except the (110) reflection, the apparent width is found to be notably ($2\times$ to $4\times$) larger than the width of the instrument resolution function Δ that was determined from the width of the direct beam. Thus, the improved resolution allowed us to determine intrinsic widths of different reflections δq_{intr} using Equation 3.2. The result is summarized in Figure 3.5 for reflections of different order. Due to very distinct differences in the intensities of the reflections, the intrinsic width $\delta q_{(hkl)}$ for different (hkl) reflections is determined from patterns taken with different exposure times τ . For the crystal that yielded the diffraction pattern shown in Figure 3.4a, $\tau = 1, 0.01, 10$ and 60 s was used for the (100), (110), (200) and (210) reflections, respectively. For the other crystal, which produced the pattern shown in Figure 3.4b, the corresponding exposure times were respectively $\tau = 10, 1, 300$ and 300 s. As one can expect, $\delta q_{(hkl)}$ in Figure 3.4b is larger than that in Figure 3.4a. We also observe a slight increase of radial width with reflection order. Surprisingly, a difference in $\delta q_{(hkl)}$ is found between the (100), (200) and (210) reflections originating from the Bragg rods and the (110) reflection originating from the true Bragg spot. This difference in width is especially pronounced in the case of the crystal yielding the pattern presented in Figure 3.4a, where the apparent width $\delta q_{(110)}$ of the (110) reflection is yet instrument-dominated so that it is difficult to precisely determine its intrinsic width. In the following section we give another estimate of the upper limit of $\delta q_{(110)}$

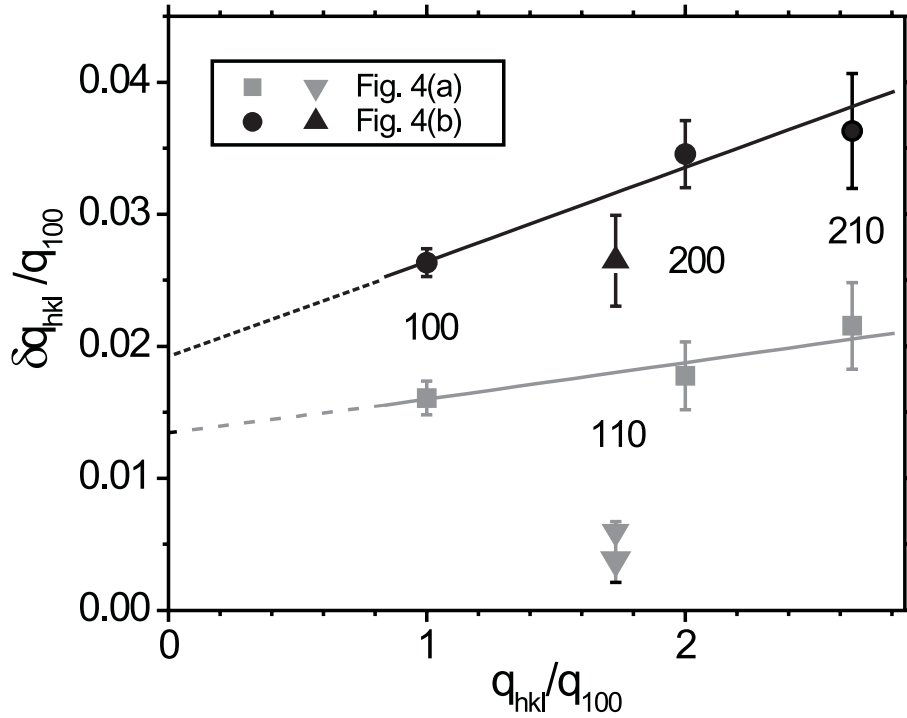


Figure 3.5: The radial intrinsic width $\delta q_{(hkl)}$ of the different-order reflections in the patterns shown in Figure 3.4 as a function of the scattering vector $q_{(hkl)}$. The error bars represent the spread of the values obtained from different reflections of the same class. The lines are linear fits to the widths of the $(hkl) = (100)$, (200) and (210) -class reflections originating from the Bragg rods induced by stacking disorder. The values of δq and $q_{(hkl)}$ on both axes are rescaled to the q -value of the lowest order reflection $q_{(100)} = 0.0310 \text{ nm}^{-1}$ and $q_{(100)} = 0.0309 \text{ nm}^{-1}$ in Figure 3.4a and Figure 3.4b, respectively. The filled symbols represent the results obtained from the analysis of the data taken with the CCD detector. The larger triangle is the estimate of the upper limit of the width of the (110) reflection of the crystal in Figure 3.4a as obtained with X-ray films (see Section 3.8).

for this crystal. The additional broadening of the (100) , (200) and (210) reflections compared to the (110) can be understood by assuming that stacking disorder is not limited to the direction perpendicular to the hexagonal planes, which means parallel to the direction of the X-ray beam in Figure 3.4, but can also be found in the lateral direction. It was shown recently that such lateral stacking disorder is not uncommon in self-assembled crystals of spherical PMMA colloids [178].

We propose that the width of reflections has two components. One component is independent of the diffraction order and can be related to the effect of the finite size of crystallites Λ in the mosaic constituting the macro-crystal. The other component, which increases with increasing q , can be induced by disorder of the second type [105]. We further assume a simple linear relation

$$\delta q_{(hkl)} = \delta q_0 + \gamma q_{(hkl)}. \quad (3.3)$$

Using a linear fit to the data, one can estimate δq_0 to be $(4.1 \pm 0.8) \cdot 10^{-4} \text{ nm}^{-1}$ and $(6.0 \pm 0.8) \cdot 10^{-4} \text{ nm}^{-1}$ for the reflections originating from the Bragg rods intersected by the Ewald sphere in the first (Figure 3.4a) and the second (Figure 3.4b) crystals, respectively. The typical

size of the crystallites can be estimated as $\Lambda = (2\pi B)/(\delta q_0)$, where B is a factor on the order of 1, which depends on the crystal shape. Using $B = 1$, $\Lambda = 16 \mu\text{m}$ and $\Lambda = 10 \mu\text{m}$ are obtained, respectively. For the slope γ , we find values of $(3 \pm 2) \cdot 10^{-3}$ and $(7 \pm 2) \cdot 10^{-3}$ in the first and the second crystals, respectively.

Unfortunately, due to the limited q -range, our current data do not allow us to distinguish the q -dependent and the q -independent components of the width of the true Bragg spots (with $\ell = 0$ and $(h - k)$ divisible by 3). A more elaborate experimental study as well as theoretical modelling of the long-range order parameters in colloidal crystals grown from concentrated dispersions is needed and will be performed in the future. However, this example already shows that the improved angular resolution allows us to access novel, more detailed information on the range of various order parameters in colloidal crystals, including disorder of the first and second types.

3.8 Measurements with X-ray films

As shown above, the data measured with the CCD detector had an angular resolution of $4.6 \mu\text{rad}$. To test the ultimate limit of the angular resolution of our setup, we also recorded the direct beam and the diffracted beams on high-resolution, X-ray-sensitive films. Unfortunately, all the images of the direct beam turned out to be severely overexposed. During the experiment, no fast beam shutter was available to ensure sufficiently short exposure times. Thus, instead of the direct beam, we present in Figure 3.6 (insert) an image of one of the (110)-class reflections of the RHCP hard-sphere colloidal crystal (see Figure 3.4a).

The image on the X-ray film was digitized using an optical microscope ($32\times$ magnification, spatial resolution of $0.5 \mu\text{m}$) equipped with a CCD camera. The result was corrected for the blackening curve of the film. A slice through the reflection in the radial direction had a FWHM width of less than $6 \mu\text{m}$. For our experimental geometry, that width corresponds to an apparent radial width of about $\delta q_{\text{app}} = 1.2 \cdot 10^{-4} \text{ nm}^{-1}$. Unfortunately, we did not have the information that was needed to determine the contributions of the instrument resolution and the intrinsic reflection width of the crystal. However, the value of $1.2 \cdot 10^{-4} \text{ nm}^{-1}$ sets an upper limit for both of them. The open triangle in Figure 3.5 presents the result of this estimate.

Thus, our results show that the SAXS scheme with refractive optics at a synchrotron source allows an angular resolution that is even higher than that in the data presented in Sections 3.5 to 3.7, where the spatial resolution of the CCD detector was the limiting factor. The higher resolution achieved in X-ray-film measurements also revealed that the (110) reflection is slightly broadened in the azimuthal direction. This broadening is practically invisible in Figure 3.4a.

3.9 Concluding remarks

In this chapter, we presented a few examples of the application of ultra-high resolution SAXS to colloidal crystals. We demonstrated that an angular resolution better than $2 \mu\text{rad}$ can be achieved using a synchrotron X-ray source and refractive optics for sample-detector distances of only a few meters. This resolution is about one order of magnitude better than the resolution of presently-realized USAXS installations exploiting Si-(111) and Si-(220) Bonse-Hart cameras [159, 160]. The setup allows for fast recording of two-dimensional diffraction data within the (sub)second acquisition times. One has to note, however, that compound refractive

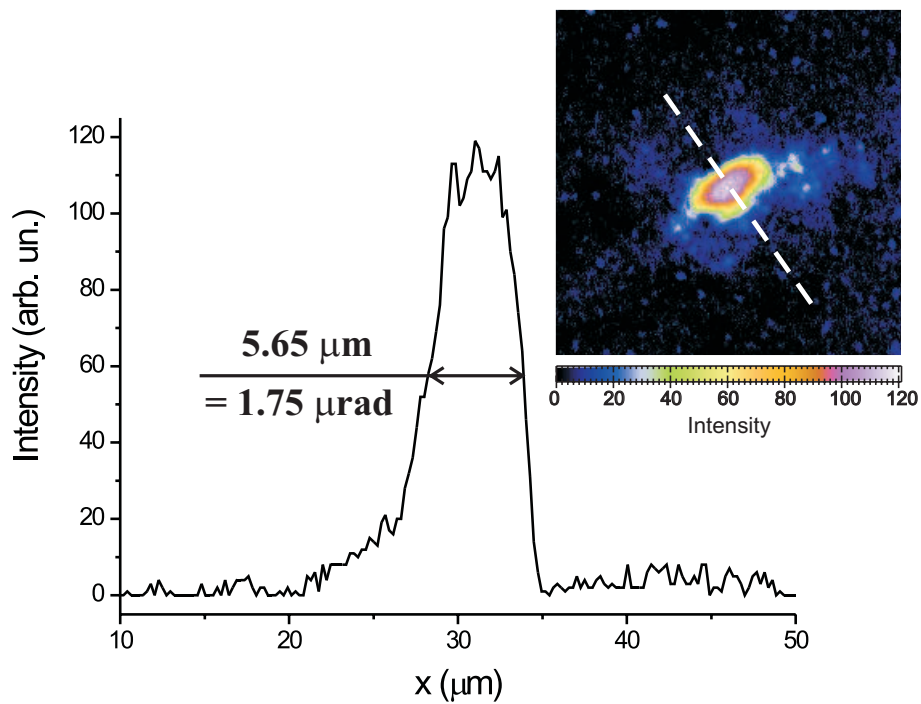


Figure 3.6: Image of one of the (110)-class reflections from the colloidal crystal shown in Figure 3.4a obtained with high-resolution X-ray film. The X-ray intensities at every pixel are calculated from the film density using a blackening curve. A $50 \mu\text{m} \times 50 \mu\text{m}$ area is presented in the insert. The profile is taken in the radial direction (dashed line in the image).

lenses have a rather high level of parasitic scattering at present, which leads to an increase of scattering background. This might create an obstacle for weakly-scattering samples and further improvement of the quality of the lenses is highly desirable.

The breakthrough in terms of angular resolution to a few microradians makes SAXS a powerful analytical tool, which allows for detailed quantitative characterization of colloidal crystals. It can provide a clear distinction between the X-ray scattering from a colloidal fluid and the X-ray diffraction from a small colloidal crystal grown at the capillary wall, the fluid and the crystal being in coexistence (Section 3.5). Microradian-resolution SAXS is able to perform detailed structural evaluation of colloidal crystals with particle separations that are even larger than 1 μm (Section 3.6). Our technique can also give access to new detailed knowledge on order parameters, including the presence of disorder of the second type (Section 3.7).

Photonic colloidal crystals are presumably not the only example where improvement of the angular resolution in two-dimensional data acquisition can play an important role. For example, it can be of importance for biological objects with large-scale organization such as that in muscles [164, 165, 167]. Microradian resolution may also be needed to further enlarge the unit-cell size accessible to protein crystallography in order to study large protein complexes such as viruses [179].

Acknowledgements

It is my pleasure to thank Federico Zontone, Henri Gleyzolle, Patrick Feder, Andrei Flueraşu and Anders Madsen for their excellent support during our X-ray scattering measurements at the ESRF in Grenoble, France. Patrick Davidson, Theyencheri Narayanan, Henk Lekkerkerker and Gert Jan Vroege are acknowledged for stimulating discussions. Marc Diot and Cyril Ponchut are acknowledged for providing the detector. The ESRF is thanked for granting us beam time. I would also like to thank Dannis 't Hart, Andrei Petukhov and Johan Stiefelhagen for critical reading of this chapter.

This work appeared as Reference [180] - A. V. Petukhov, J. H. J. Thijssen, D. C. 't Hart, A. Imhof, A. van Blaaderen, I. P. Dolbnya, A. Snigirev, A. Moussaïd and I. Snigireva, *Microradian X-ray diffraction in colloidal photonic crystals*, *Journal of Applied Crystallography* **39**(2), 137 (2006). A.V.P. initiated the project; A.V.P., J.H.J.T., D.C.'t.H., I.P.D. and A.M. were part of the experimental crew; J.H.J.T. (BCT) and A.M. (PMMA) provided samples; A.S. provided the CRL; I.S. provided X-ray film and on-site laboratory facilities; A.S. and I.S. also participated in many useful, on-site discussion; A.V.P. and J.H.J.T. performed most of the data analysis; A.V.P., A.I. and A.v.B. participated in many useful discussion and supervised the project.

Orientation, packing and stacking in convective assembly

Over the past few years, convective assembly or controlled drying has become a popular method for the fabrication of colloidal-crystal templates of silica spheres in air. Such templates can be infiltrated with high-index materials, including silicon, by chemical vapor deposition (CVD). Removal of the original silica template by a wet-chemical etch results in a 3-D photonic crystal. Although it is a popular method, the mechanism behind convective assembly remains unclear. The orientation of the hexagonal layers with respect to the meniscus of the suspending medium during convective assembly, and the stacking sequence of these layers, contain important information about this growth mechanism. Furthermore, the stacking of the hexagonal layers in, and thus the 3-D structure of, the resulting colloidal crystals affect their photonic properties. In the first part of this chapter, we present electron microscopy and X-ray diffraction data suggesting that the orientation of the hexagonal layers is such that the lines of touching particles are perpendicular to the meniscus if the crystal has approximately 5 layers or more. At the start of crystal growth, where the number of layers is smaller, the lines were found to be parallel to the meniscus in most crystallites. In the second part, we demonstrate that small-angle X-ray scattering (SAXS) is an excellent tool to obtain information about the 3-D structure of colloidal crystals grown by conventional convective assembly. It turns out that the layers parallel to the sample substrate are not exactly hexagonal and that the stacking sequence is mainly that of face-centered cubic (FCC) crystals, though stacking faults may occur.

4.1 Introduction

In Chapter 1, self-assembly of colloidal particles has been presented as an attractive route towards 3-D photonic crystals [95, 107, 108], using colloidal crystals as templates for infiltration with high-refractive-index materials [67–69, 181, 182]. One of the most popular ways of fabricating colloidal-crystal templates is convective assembly, also known as controlled drying [67, 77]. Colloidal spheres are deposited onto a flat substrate that is positioned (nearly) vertically in a colloidal dispersion, the latter having a typical colloid volume fraction of 1%. Evaporation of the solvent causes an influx of particles from the bulk suspension towards the liquid film that wets the surface of the substrate. Subsequently, capillary forces cause colloids in the vicinity of the meniscus to assemble into close-packed structures [183].

Controlled drying results in colloidal-crystal templates with a finite number of hexagonally packed layers which are parallel to the substrate. One of the major advantages of controlled drying is that the resulting close-packed structure is uniform in orientation and thickness over areas that are on the order of cm^2 [76]. The number of layers can be controlled by the particle volume fraction of the dispersion [77]. After drying of the (thin) opaline film, Van der Waals forces between the spheres keep the colloidal crystal from disintegrating, while Van der Waals forces between the spheres and the substrate keep the crystal from detaching. The mechanical stability of such crystals allows easy handling, facilitating post-fabrication processing. The controlled-drying process can even be repeated in a layer-by-layer fashion, using spheres of different size in consecutive layers, in order to arrive at binary colloidal crystals [135].

Although colloidal crystals grown by controlled drying have been successfully used as templates for infiltration with high-index-materials [67–70, 181, 182], the exact mechanism behind this self-assembly technique is still unclear [108, 184, 185]. In literature, an important observation which is usually connected to this mechanism, is the orientation of the hexagonal layers. Wostyn *et al.* [76] observed that the meniscus of the drying film directs the orientation of the layers, such that the lines of touching particles within a layer are perpendicular to the meniscus (Figure 4.1a), and claimed that it is an intrinsic property of controlled drying. Based on their observations in layer-by-layer growth of binary colloidal crystals, Velikov *et al.* [135] proposed a model which explains why the lines of touching particles are parallel to the meniscus in their experiments. Meng *et al.* [184] observed that the regions in which a growing crystal makes a transition from n to $(n + 1)$ layers have square instead of hexagonal symmetry. They claim that these transition regions play an important role in the crystallization process. Furthermore, the data they present seems to indicate that the orientation in thin crystals (~ 4 layers) is such that the lines of particles are parallel to the meniscus.

Apart from the mechanism behind controlled drying, the 3-D structure of the resulting samples is unresolved as well. It is well-known that the crystal planes parallel to the substrate have hexagonal symmetry, and that consecutive layers are hollow-site stacked, but the order in which they are stacked has not been determined unambiguously yet. In hollow-site stacked, close-packed colloidal crystals, the hexagonal layers can have three lateral positions: A, B and C (Figure 4.1b). If their sequence is ABCABC, the resulting structure is a face-centered cubic (FCC) crystal. If the sequence is ABABAB, a hexagonal close-packed (HCP) crystal is obtained, while a structure with a random sequence is usually referred to as a random hexagonal close-packed (RHCP) structure. In their experiments on controlled drying, Vlasov *et al.* observed a tendency towards FCC stacking [67]. It is true that FCC is more stable than HCP ac-

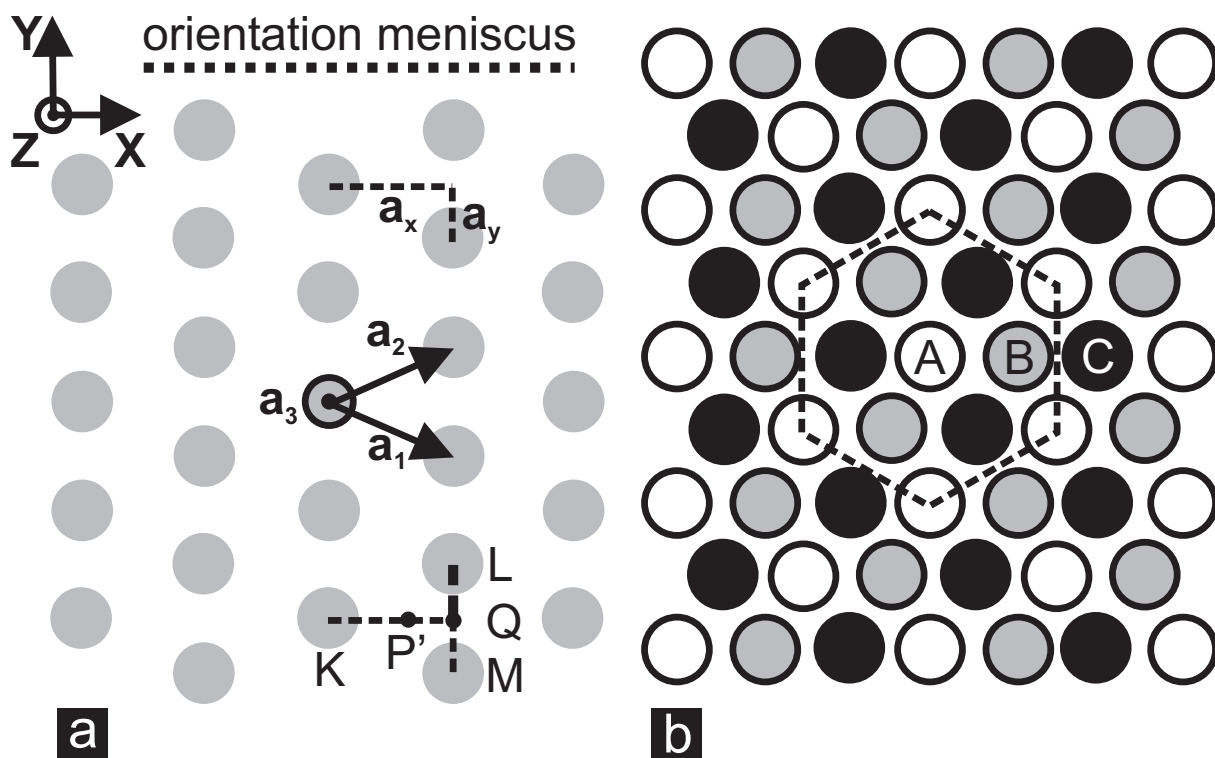


Figure 4.1: (a) Schematic representation of a deformed hexagonal layer, together with the coordinate system, the real-space basis vectors \mathbf{a}_i and the orientation of the meniscus if the lines of touching particles are oriented perpendicular to it. (b) Hollow-site stacking in controlled drying. The three different lateral position of the hexagonal layers are labelled A, B and C.

According to free-energy calculations, but the latter assume that thermodynamic equilibrium has been reached [72, 73, 186]. As the calculated free-energy difference between FCC and HCP is very small ($\sim 10^{-3} k_B T$), and the controlled-drying process is probably far from equilibrium, it is unlikely that these calculations actually apply in this case. On the other hand, preliminary results presented in Reference [187] indicate that kinetics favor FCC over RHCP stacking.

Kinetics were also considered by Norris *et al.* [108], who proposed a model which attributes the observed tendency towards FCC structures to the flow of solvent through holes in the already deposited crystal layers. Meng *et al.* confirm that there is a strong tendency towards FCC structures for controlled-drying samples with a relatively small number of layers (≤ 7) [184]. They claim that the square transition region, where a growing crystal makes a transition from n to $(n+1)$ layers, can initiate specific stacking sequences which are then propagated in subsequent growth. Using a simple model, they argue that the crystallization mechanism is an interplay between capillary forces, the physical constraint of the meniscus and the constant feedback between the deposited structure and the incoming particles. In thicker crystals, other effects could also be involved. A tendency towards FCC structures was also found in confocal microscopy measurements, though the crystals also contained stacking faults [185]. Moreover, for samples with 6 layers or more, the relative number of stacking faults appeared to be more or less constant. Finally, García-Santamaría *et al.* used spectroscopy to show that controlled-drying colloidal crystals are not really close-packed crystals [188], with measured sphere volume fractions of 71% to 73%, indicating that the structure cannot be a truly close-packed FCC structure.

As it is such a popular method, it is important that the mechanism behind controlled drying is revealed, for it may allow controllable tuning of growth parameters to improve the quality of the resulting colloidal crystals. The orientation of the hexagonal layers contains information about this mechanism. Additional clues can be obtained from the stacking of the hexagonal layers, which also affects the 3-D structure, and thus the photonic properties, of the resulting colloidal crystals [75]. In the first part of this chapter, we present electron microscopy and X-ray diffraction data suggesting that the orientation of the hexagonal layers is such that the lines of touching particles are perpendicular to the meniscus if the crystal has approximately 5 layers or more. At the start of crystal growth, where the number of layers is smaller, the lines were found to be parallel to the meniscus in most crystallites. In the second part, the 3-D structure of controlled-drying colloidal crystals is considered. As the particles have a diameter smaller than 400 nm, which allows controlled drying at room temperature, it is impossible to probe their internal 3-D structure using conventional optical techniques, such as confocal microscopy. We demonstrate that small-angle X-ray scattering (SAXS) is an excellent tool to obtain additional information about the 3-D structure of colloidal crystals grown by conventional controlled drying. As an example, the in-plane packing and the stacking of the hexagonal layers will be considered.

4.2 Theoretical model

4.2.1 Real space

Controlled drying leads to colloidal crystals consisting of (nearly) hexagonal layers that are oriented parallel to the sample substrate [67, 77, 108], as is often the case in self-assembly of

colloidal spheres [95, 107]. Therefore, we will analyze scattering data using a model in which crystals consist of a finite number N of infinitely large layers [189]. This has the advantage that finite-size effects can be taken into account and it allows easy comparison of scattering by several crystal structures, including face-centered cubic (FCC), hexagonal close-packed (HCP), random hexagonal close-packed (RHCP), body-centered tetragonal (BCT) and even simple cubic (SC). In our model, the infinite layers are spanned by two real-space lattice vectors \mathbf{a}_1 and \mathbf{a}_2 (see Figure 4.1a). We define the third real-space basis vector \mathbf{a}_3 such that it is orthogonal to the layer spanned by $(\mathbf{a}_1, \mathbf{a}_2)$ and has a length that is equal to the interlayer spacing d . Note that \mathbf{a}_3 is *not* a lattice vector, for it has to be supplemented by an additional, lateral shift vector to connect particles from layer j with those in layer $j + 1$ (see Equation 4.24).

$$\begin{aligned}\mathbf{a}_1 &= [a_x, -a_y, 0] \\ \mathbf{a}_2 &= [a_x, a_y, 0] \\ \mathbf{a}_3 &= [0, 0, d]\end{aligned}\tag{4.1}$$

Here a_y is equal to half of the distance between the colloidal particles in lines that run along the y -axis in Figure 4.1a and a_x is the distance between those lines. In truly close-packed (CP) crystals, the layers have hexagonal symmetry and all neighboring particles are touching. In that case, $a_y = (\sigma/2)$, $a_x = \sigma \cdot (\sqrt{3}/2)$ and $d_{\text{CP}} = \sigma \cdot \sqrt{2/3}$, with σ the particle diameter. For generality, we do not assume hexagonal packing. Instead, we do not specify expressions for a_x and a_y yet, we only assume that $a_x > a_y$ and that the layers are invariant under reflections in both the x -axis and the y -axis in Figure 4.1a.

Because controlled-drying colloidal crystals are known to be mechanically stable in air, we assume that the layers are hollow-site stacked (see Figure 4.1b). This means that, for example, a particle P in the second layer rests on three particles (K, L, M) of the first layer, such that its z -projection P' is in the middle of the triangle suspended by K, L and M (see Figure 4.1a). As the layer is symmetric under reflections in the x -axis, the projection P' must be on the median KQ, which is also an altitude of the isosceles triangle KLM. We define τ as the ratio of KP' and a_x (see also Figure 4.1a).

$$\begin{aligned}\text{KP}' &= \tau \cdot \text{KQ} \\ &= \tau a_x\end{aligned}\tag{4.2}$$

Note that $\tau = (2/3)$ for hexagonal layers. Because of mechanical stability, we can also safely assume that particle P is touching all particles (K, L, M) on which it is resting. This condition connects the parameter τ with the interlayer spacing d and the particle diameter σ .

$$\begin{aligned}(\text{KP}')^2 + (\text{PP}')^2 &= (\text{KP})^2 \\ (\tau a_x)^2 + d^2 &= \sigma^2\end{aligned}\tag{4.3}$$

Actually, the mechanical-stability condition also ensures that the z -projection P' of P is the

centroid of the triangle KLM, which means that τ can be expressed in terms of a_x and a_y .

$$\begin{aligned} (\text{QP}') &= (1 - \tau) \cdot a_x \\ (\text{LP}') &= (\text{MP}') = (\text{KP}') = \tau a_x \\ \tau &= \left(\frac{1}{2}\right) \cdot \left(1 + \left(\frac{a_y}{a_x}\right)^2\right) \end{aligned} \quad (4.4)$$

Note that inserting values for a_x and a_y for a hexagonal layer yields $\tau = (2/3)$. This makes perfect sense, as the triangle KLM is equilateral then.

In order to quantify possible distortions of the layers with respect to their expected hexagonal symmetry, we introduce the distortion parameter ε .

$$\alpha = \frac{a_y}{a_x} = \varepsilon \cdot \left(\frac{1}{\sqrt{3}}\right) \quad (4.5)$$

If the layers are truly hexagonal, then $\varepsilon = 1$. If the layers are (slightly) distorted, it will also affect the interlayer spacing d and the volume fraction of spheres φ . In the case of distortion, the particles in a layer are slightly pulled apart. As particles in the next layer are resting upon those particles, the layers slightly move towards one another. The interlayer spacing d can be expressed in terms of the interlayer spacing in close-packed structures d_{CP} and the interparticle spacing along the y -axis in Figure 4.1a, the latter being $2 \cdot a_y$.

$$d = d_{\text{CP}} \cdot \sqrt{\left(\frac{3}{2}\right) \cdot \left(1 - \left(\frac{1}{3}\right) \cdot \left(\frac{2a_y}{\sigma}\right)^2 \cdot \left(\frac{3}{4\varepsilon} + \frac{\varepsilon}{4}\right)\right)} \quad (4.6)$$

Although the interlayer spacing d slightly decreases, the distortion within the layers results in a decrease of the sphere volume fraction φ . Under the assumptions, the actual sphere volume fraction φ in structures consisting of hollow-site stacked, distorted hexagonal layers can be expressed in terms of the sphere volume fraction in a truly close-packed crystal $\varphi_{\text{CP}} = (\pi\sqrt{2}/6)$.

$$\varphi = \varphi_{\text{CP}} \cdot \left(\frac{\sigma}{2a_y}\right)^2 \cdot \left(\frac{1}{\sqrt{\left(\frac{3}{2\varepsilon^2}\right) \cdot \left(1 - \left(\frac{1}{3}\right) \cdot \left(\frac{2a_y}{\sigma}\right)^2 \cdot \left(\frac{3}{4\varepsilon} + \frac{\varepsilon}{4}\right)\right)}}\right) \quad (4.7)$$

4.2.2 Reciprocal space

Scattering is most easily described in reciprocal space [3, 105]. The 2-D reciprocal lattice of a single hexagonal plane is hexagonal. Similarly, using the definition of the reciprocal triad $\{\mathbf{b}'_i\}$ of the real-space basis $\{\mathbf{a}_i\}$,

$$\mathbf{b}'_i = 2\pi \cdot \frac{\mathbf{a}_j \times \mathbf{a}_k}{\mathbf{a}_i \cdot (\mathbf{a}_j \times \mathbf{a}_k)}, \quad (4.8)$$

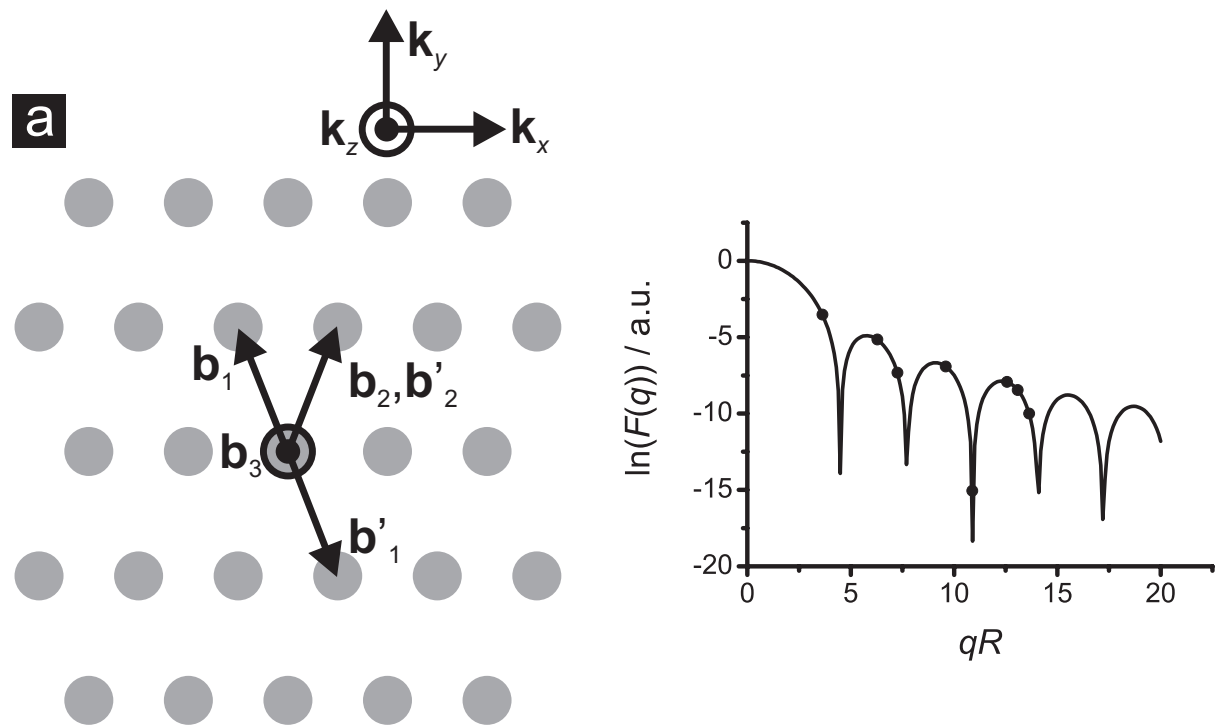


Figure 4.2: (a) Schematic representation of the 2-D reciprocal lattice of a single, deformed hexagonal plane, together with the reciprocal-space coordinate system, the calculated reciprocal-space basis $\{\mathbf{b}'_i\}$ and the conventional reciprocal-space basis $\{\mathbf{b}_i\}$. (b) Calculated graph of the form factor, in the Rayleigh-Gans-Debye approximation (see Equation 4.18), of spheres with radius R . The values of the form factor for several points in the reciprocal space of a CP structure have been plotted as black dots. These black dots correspond, respectively, to the (100), (110), (200), (210), (300), (220), (310) and (311) reflections. The Miller-indices are given in the reciprocal-space basis $\{\mathbf{b}_i\}$ (see Equation 4.10).

it can be shown that the 2-D reciprocal lattice of a distorted hexagonal plane is distorted hexagonal itself (see Figure 4.2a). We define the third reciprocal-space basis vector such that its direction is orthogonal to the plane spanned by $(\mathbf{b}'_1, \mathbf{b}'_2)$ and its length is determined by the interplanar spacing d , e.g. $b'_3 = (2\pi/d)$.

$$\begin{aligned}\mathbf{b}'_1 &= \left[\frac{\pi}{a_x}, -\frac{\pi}{a_y}, 0 \right] \\ \mathbf{b}'_2 &= \left[\frac{\pi}{a_x}, \frac{\pi}{a_y}, 0 \right] \\ \mathbf{b}'_3 &= \left[0, 0, \frac{2\pi}{d} \right]\end{aligned}\tag{4.9}$$

The 2-D reciprocal lattice of a single hexagonal plane can also be spanned by a different, more conventional choice of basis vectors $\{\mathbf{b}_i\}$ (see Figure 4.2a). Together with \mathbf{b}'_3 , they form the reciprocal-space basis vectors with which we describe scattering by our colloidal crystals.

$$\begin{aligned}\mathbf{b}_1 &= \left[-\frac{\pi}{a_x}, \frac{\pi}{a_y}, 0 \right] \\ \mathbf{b}_2 &= \left[\frac{\pi}{a_x}, \frac{\pi}{a_y}, 0 \right] \\ \mathbf{b}_3 &= \left[0, 0, \frac{2\pi}{d} \right]\end{aligned}\tag{4.10}$$

Consider an incoming wave of wave vector \mathbf{k}_0 and assume it is scattered elastically. This scattering process results in an outgoing wave of wave vector \mathbf{k} , having the same length as \mathbf{k}_0 . We define the scattering vector \mathbf{q} as the vector difference between the wave vectors of the incoming and outgoing waves.

$$\mathbf{q} = \mathbf{k} - \mathbf{k}_0\tag{4.11}$$

Furthermore, we decompose any scattering vector \mathbf{q} in the reciprocal-space basis $\{\mathbf{b}_i\}$

$$\mathbf{q} = h\mathbf{b}_1 + k\mathbf{b}_2 + \ell\mathbf{b}_3,\tag{4.12}$$

in which (h, k, ℓ) are called Miller-indices. The scattered intensity $I(\mathbf{q})$ is proportional to the square of the matrix element that describes the transition from \mathbf{k}_0 to \mathbf{k} .

$$\begin{aligned}I &\propto |\mathcal{M}_{\mathbf{k}, \mathbf{k}_0}|^2 \\ &= |\langle \mathbf{k} | V(\mathbf{r}) | \mathbf{k}_0 \rangle|^2\end{aligned}\tag{4.13}$$

Here, $V(\mathbf{r})$ is the scattering potential of all colloidal particles in the crystal. In the case of spherical particles, which all have the same orientation, the individual colloid potentials $V_c(\mathbf{r})$ are identical, isotropic and non-overlapping. In other words, the potential of all particles can be written as a sum of disjunct, identical colloid potentials $V_c(\mathbf{r})$. Thus, the matrix element $\mathcal{M}_{\mathbf{k}, \mathbf{k}_0}$ can be factorized

$$\begin{aligned}\mathcal{M}_{\mathbf{k}, \mathbf{k}_0} &= \langle \mathbf{k} | V(\mathbf{r}) | \mathbf{k}_0 \rangle \\ &= \int_{\text{crys}} e^{-i\mathbf{k}\cdot\mathbf{r}} V(\mathbf{r}) e^{i\mathbf{k}_0\cdot\mathbf{r}} d\mathbf{r} \\ &= \left[\frac{1}{V_c} \int_{\text{crys}} V_c(\mathbf{u}) e^{-i\mathbf{q}\cdot\mathbf{u}} d\mathbf{u} \right] \cdot \left[\frac{1}{n} \sum_{\mathbf{R}_i} e^{-i\mathbf{q}\cdot\mathbf{R}_i} \right],\end{aligned}\tag{4.14}$$

in which n is the number of unit cells in a macroscopic unit of volume of the crystal and v_c is the volume per unit cell.

Inserting Equation 4.14 into Equation 4.13 yields the well-known factorization of the scattered intensity in a form factor $F(\mathbf{q})$ and a structure factor $S(\mathbf{q})$

$$I(\mathbf{q}) \propto F(\mathbf{q}) \cdot S(\mathbf{q}), \quad (4.15)$$

in which

$$F(\mathbf{q}) = \left| \frac{1}{v_c} \int_{\text{crys}} V_c(\mathbf{u}) e^{-i\mathbf{q} \cdot \mathbf{u}} d\mathbf{u} \right|^2 \quad (4.16)$$

$$S(\mathbf{q}) = \left| \frac{1}{n} \sum_{\mathbf{l}} e^{-i\mathbf{q} \cdot \mathbf{R}_{\mathbf{l}}} \right|^2. \quad (4.17)$$

It is clear from Equation 4.17 that the structure factor depends solely on the positions of the individual colloids $\mathbf{R}_{\mathbf{l}}$, where \mathbf{l} sums over all unit cells. On the other hand, the form factor only depends on the functional form of the individual colloid potential V_c . In other words, the form factor contains information about the scattering from a single colloidal particle. Actually, as spheres are isotropic, the form factor only depends on the length of \mathbf{q} . In the Rayleigh-Gans-Debye (RGD) approximation, the form factor of a sphere can be calculated analytically in a straightforward manner [141].

$$F(q) = \left| 3 \cdot \left(\frac{\sin(qR) - (qR) \cos(qR)}{(qR)^3} \right) \right|^2 \quad (4.18)$$

As in Equation 4.18, the form factor is usually normalized such that $F(q=0) = 1$. Figure 4.2b displays a graph of the form factor of monodisperse spheres of radius R in the RGD-approximation.

As our colloidal crystals usually consist of a finite number N of infinite layers, we prefer to decompose the structure factor $S(\mathbf{q})$ in a term corresponding to in-plane scattering and a term corresponding to the stacking of the layers. First, the position vector $\mathbf{R}_{\mathbf{l}}$ of a colloid is written as the vector sum of the position vector \mathbf{R}_j of the origin of layer j and the in-plane vector connecting the origin of that layer with colloid i in that layer ($l_i \mathbf{a}_1 + l_i \mathbf{a}_2$).

$$\mathbf{R}_{\mathbf{l}} = \mathbf{R}_j + l_i \mathbf{a}_1 + l_i \mathbf{a}_2 \quad (4.19)$$

Inserting Equation 4.19 into Equation 4.17 results in

$$\begin{aligned} S(\mathbf{q}) &= \frac{1}{n^2} \left| \sum_{j=0}^{N-1} \sum_{l_1=0}^{M_1-1} \sum_{l_2=0}^{M_2-1} e^{-i\mathbf{q} \cdot (l_1 \mathbf{a}_1)} e^{-i\mathbf{q} \cdot (l_2 \mathbf{a}_2)} e^{-i\mathbf{q} \cdot \mathbf{R}_j} \right|^2 \\ &= \frac{1}{n^2} \left| \sum_{j=0}^{N-1} e^{-i\mathbf{q} \cdot \mathbf{R}_j} \sum_{l_1=0}^{M_1-1} e^{2\pi i h l_1} \sum_{l_2=0}^{M_2-1} e^{-2\pi i k l_2} \right|^2, \end{aligned} \quad (4.20)$$

where we have used an important property of the real-space and reciprocal-space bases, $\{\mathbf{a}_i\}$ and $\{\mathbf{b}_j\}$ respectively

$$\begin{aligned} \mathbf{a}_1 \cdot \mathbf{b}_1 &= -2\pi \\ \mathbf{a}_2 \cdot \mathbf{b}_2 &= 2\pi \\ \mathbf{a}_3 \cdot \mathbf{b}_3 &= 2\pi \\ \mathbf{a}_i \cdot \mathbf{b}_j &= 0 \quad \text{for } i \neq j. \end{aligned} \quad (4.21)$$

As the number of in-plane particles that contributes to scattering is large, $M_1 \times M_2 \sim 10^3 \times 10^3$, the summations over (l_{i_1}, l_{i_2}) will vanish if (h, k) are not integer. If (h, k) are integer, interference will be constructive and the sums can be evaluated explicitly.

$$\sum_{l_{i_1}=0}^{M_1-1} e^{2\pi i h l_{i_1}} = \sum_{l_{i_1}=0}^{M_1-1} (1) = M_1 \quad (4.22)$$

In other words, the structure factor $S(\mathbf{q})$ takes the functional form

$$S(\mathbf{q}) = \frac{1}{n^2} M_1^2 M_2^2 \left| \sum_{j=0}^{N-1} e^{-i\mathbf{q} \cdot \mathbf{R}_j} \right|^2 \quad (4.23)$$

for integer values of h and k , otherwise it is 0.

Finally, we wish to split the effect of stacking on scattering by colloidal crystals in a term corresponding to the phase shift that is induced by the interlayer spacing and a term corresponding to the phase shift that is induced by the lateral displacement of the planes with respect to each other. Therefore, we write the position vector \mathbf{R}_j of the origin of layer j as the vector sum of the spacing $j \cdot \mathbf{a}_3$ between the 0th and j th layers, and the lateral shift of the j th layer \mathbf{s}_j .

$$\mathbf{R}_j = j \cdot \mathbf{a}_3 + \mathbf{s}_j \quad (4.24)$$

That way, the structure factor can be written as

$$\begin{aligned} S(\mathbf{q}) &= \frac{1}{n^2} M_1^2 M_2^2 \left| \sum_{j=0}^{N-1} e^{-i\mathbf{q} \cdot (j \cdot \mathbf{a}_3 + \mathbf{s}_j)} \right|^2 \\ &= \frac{1}{n^2} M_1^2 M_2^2 \left| \sum_{j=0}^{N-1} e^{-i\Delta\phi_j} \right|^2, \end{aligned} \quad (4.25)$$

in which we have introduced the phase shift of the j th layer $\Delta\phi_j$.

$$\begin{aligned} \Delta\phi_j &= \mathbf{q} \cdot (j \cdot \mathbf{a}_3 + \mathbf{s}_j) \\ &= (h\mathbf{b}_1 + k\mathbf{b}_2 + \ell\mathbf{b}_3) \cdot (j \cdot \mathbf{a}_3 + \mathbf{s}_j) \\ &= 2\pi j\ell + (h\mathbf{b}_1 + k\mathbf{b}_2) \cdot \mathbf{s}_j \end{aligned} \quad (4.26)$$

In the last step of Equation 4.26, we used the explicit forms of \mathbf{a}_3 and \mathbf{b}_3 (see Equations 4.1 and 4.10). The phase shift $\Delta\phi_j$ is a useful quantity in (X-ray) scattering as constructive interference will occur if and only if both h and k are integers *and* $\Delta\phi_j$ is an integer times 2π for all j .

As an example, we derive the coherence relation for an FCC structure. In this case, the shift vector \mathbf{s}_j can be written as

$$\mathbf{s}_j = p \cdot \left(\frac{\mathbf{a}_1 + \mathbf{a}_2}{3} \right), \quad (4.27)$$

where $p = +1$ for B-layers and $p = -1$ for C-layers (see Figure 4.1). Inserting Equation 4.27 into Equation 4.26 yields the desired coherence relation

$$\Delta\phi_j = 2\pi j\ell - p \cdot \left(\frac{2\pi}{3} \right) \cdot (h - k) = 2\pi \cdot m, \quad (4.28)$$

in which m is an integer. As our colloidal particles are typically 10^3 to 10^4 times larger than the X-ray wavelength, the Ewald sphere [3, 105] is nearly flat and oriented perpendicular to the incoming X-ray beam. Equation 4.28 proves that, at normal incidence ($\ell = 0$), interference is always constructive for reflections for which $(h - k)$ is a multiple of 3. These reflections are usually referred to as the stacking-independent peaks, for interference is also constructive for these reflections in the case of HCP and RHCP. If $(h - k)$ is not a multiple of 3, interference is destructive for $\ell = 0$, but constructive for $\ell = (m \pm \frac{1}{3})$, which can be reached by specific sample rotations. These reflections depend on the stacking sequence of the hexagonal layers and can be used, in principle, to distinguish FCC, HCP and RHCP structures in X-ray scattering.

4.3 Experimental methods

4.3.1 Sample fabrication

Colloidal crystals were fabricated from dispersions of silica spheres in ethanol. The silica colloids were synthesized using a seeded-growth procedure based on the Stöber-Fink-Bohn method [91, 190, 191]. The stock dispersions were centrifuged and redispersed in technical ethanol (Lamers & Pleuger, 100%) at least three times. The particle size distribution was probed using transmission electron microscopy (TEM, typically a Philips Tecnai 12, operated at 120 kV) on 88 particles, yielding an average diameter of (353 ± 1) nm and a polydispersity (PD) of $(2.6 \pm 0.2)\%$. One of the samples, of which results are shown in this chapter, was fabricated using a colloidal dispersion of silica spheres having a slightly different size. They were synthesized in two steps, the first of which was the formation of small nano-clusters using a micro-emulsion [192]. These small silica particles were subsequently grown larger following the Stöber-Fink-Bohn method [190]. The particle size distribution was probed by TEM on 203 particles. Results from two TEM images were combined, yielding an average diameter of (336.6 ± 2.0) nm and a PD of $(1.17 \pm 0.06)\%$. The latter TEM measurements were calibrated versus a line grid (Polaron Equipment Ltd., line grating 0734, 2160 lines/mm).

Colloidal crystals were grown from the above-mentioned dispersions onto flat, glass substrates by controlled drying [77]. The stock dispersions were diluted to volume fractions of approximately 0.6% to 1%, after which 10.0 ml to 15.0 ml of dispersion was transferred to a growth bottle. Glass, 20 ml, screw-neck vials with a flat bottom were used as growth bottles. They were placed on a sedimentation-dedicated table (Figure 4.3), thus minimizing mechanical vibrations. A glass substrate was inserted vertically into the dispersion, after which it was tilted off-vertical by approximately 5° in most cases. A vertical cut through the neck of the vial ensured that the substrate would remain (nearly) vertical after insertion (Figure 4.3a). Next, in order to avoid dust falling into the growth bottle, the latter was covered with a 600 ml to 2 l glass beaker. To allow the evaporated ethanol to escape more easily, the beaker was slightly tilted by supporting one side of the beaker with an approximately 5 mm thick piece of glass or metal. Sometimes, several growth bottles were placed under the same beaker. However, we note without proof that this may lead to some amorphous deposition. During growth, the temperature in the room was kept at approximately 20°C . It was monitored twice a day, showing deviations on the order of 0.5°C .

Two kinds of glass substrates were used: Menzel-Gläser, #1 cover slip, ca. $150\ \mu\text{m}$ in thick-

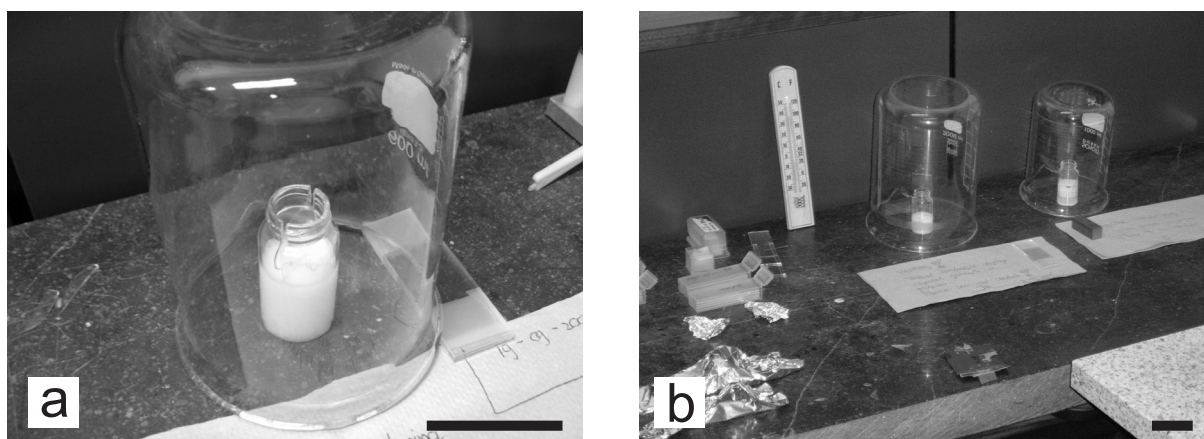


Figure 4.3: Photographs of typical setups for fabrication of colloidal crystals by controlled drying. The scale bars in both images are 5 cm.

ness and Menzel-Gläser, standard microscopy slide, ca. 1 mm thick. All glassware, bottles and slides, were cleaned prior to use with tap water, commercially available soap, deionized water (16 M Ω cm to 18 M Ω cm) and technical ethanol (Lamers & Pleuger, $\geq 96\%$). After cleaning, the growth bottles were dried in an oven at approximately (50 ± 5) °C, whereas the slides were dried with a Kimwipe tissue, after which dust was removed with flowing nitrogen. For some samples, the growth bottles and the substrates were additionally submerged in chromosulfuric acid for at least 15 minutes, after which they were copiously rinsed with deionized water and technical ethanol. However, we have not noticed any major, qualitative differences between samples fabricated with or without chromosulfuric acid cleaning.

After 5 to 10 days, samples were retrieved from the growth bottles. They were kept (nearly) vertical for at least 2 hours to allow (partial) evaporation of residual solvent. Next, the deposition on one side of the substrate was removed using a Kimwipe tissue that had been drenched in technical ethanol. Finally, colloidal-crystal samples were kept in storage boxes to avoid contamination with dust.

4.3.2 Characterization

Most macroscopic images of colloidal-crystal samples were recorded using a Fuji FinePix A340, 4.0 mega pixels digital camera. Typically, a Leica CLS 150 cold-light source illuminated the sample with white light. Optical microscopy images were taken with a Nikon D70 using a shutter time of $(1/10)$ s. This single-lens reflex (SLR) digital camera was coupled to the vertical phototube of a Leica DM IRB inverted microscope using a $2.5\times$ lens tube. A Leica HC FLUOTAR $10\times/0.3$ NA dry lens was combined with a $1.6\times$ front lens, to achieve a total magnification of $16\times$. Before the measurements, the microscope was set up for Köhler illumination.

Electron microscopy measurements were performed with a Philips XL30FEG scanning electron microscope (SEM). The vacuum in the sample chamber was kept below $8.8 \cdot 10^{-5}$ mbar. To avoid image distortions due to charging effects in the uncoated samples, the SEM was typically operated at 3.0 kV, a spot size of 2.0 nm and a working distance of 5 mm to 6 mm. Images

were recorded using a secondary-electron (SE) detector. At the start of a measurement session, the electromagnetic lenses were aligned and subsequently corrected for astigmatism.

A Bruker Vertex70 Fourier transform infrared (FTIR) spectroscope with a tungsten source and a Si-diode detector was used to obtain transmission spectra. Typical settings of the FTIR spectroscope during our measurements include a resolution of 16 cm^{-1} , averaging over 60 scans and a scanner velocity of 10 kHz. A beam aperture of 0.5 mm was selected, leading to a spot size of approximately 1 mm diameter at the sample position. All spectra were background corrected using a spectrum of a similar substrate.

X-ray diffraction experiments were performed at beamline BM26B “DUBBLE” of the European Synchrotron Radiation Facility (ESRF) in Grenoble, France (Chapter 3). The required synchrotron radiation was produced by a bending magnet source. A typical photon energy of 11 keV (wavelength $\lambda = 0.11\text{ nm}$) was selected using a Si-(111) monochromator. The setup was aligned such that an image of the source was created at the detector screen, thus increasing q -space resolution, which is necessary to measure Bragg reflections at very small angles. Furthermore, in the diffraction experiments presented in this chapter, X-rays were allowed to propagate freely towards the sample. They were focused onto the detector screen by a compound refractive lens positioned just before the sample [168, 180]. The diffraction patterns were recorded using a 12-bit charge-coupled device (CCD) camera (Photonic Science) with an X-ray phosphor screen in front, the effective pixel size being $22\text{ }\mu\text{m} \times 22\text{ }\mu\text{m}$ and the image size being $4008\text{ pixels} \times 2671\text{ pixels}$. The q -space calibration of the Photonic Science camera was performed using a silicon calibration grid with a hexagonal pattern of air holes ($1.5\text{ }\mu\text{m}$ pitch). Because of the limited dynamic range of CCD cameras, diffraction patterns were recorded several times with exposure times ranging from 10 ms up to 10 min. The variation in exposure time and sample absorption complicates the comparison of intensities of corresponding reflections in different diffraction patterns presented here. All diffraction patterns have been corrected for background scattering. Further details concerning the experimental setup are presented in Chapter 3.

4.4 Results and discussion

4.4.1 Orientation

After fabrication of a sample by controlled drying, as described in Section 4.3, one of the quickest ways to check whether the deposited structure was crystalline or not, was to look for Bragg colors by eye. When colloidal crystals are illuminated with white light, they show beautiful, ‘metallic’ iridescence for some angles of incidence (Figure 4.4a). These Bragg colors are caused by constructive interference of light that is reflected by 3-D periodic structures. As it is an interference phenomenon, the actual color observed depends on the angle of incidence, the viewing angle, the size of the constituent particles, and the refractive indices of the particles and their host medium.

Apart from revealing crystalline order, there is much more to Bragg colors from colloidal crystals than meets the eye at first. With a little bit of experience, additional information can be extracted from these colors. First of all, being caused by interference, Bragg colors have a metallic appearance. In other words, they look much brighter than colors that are caused by

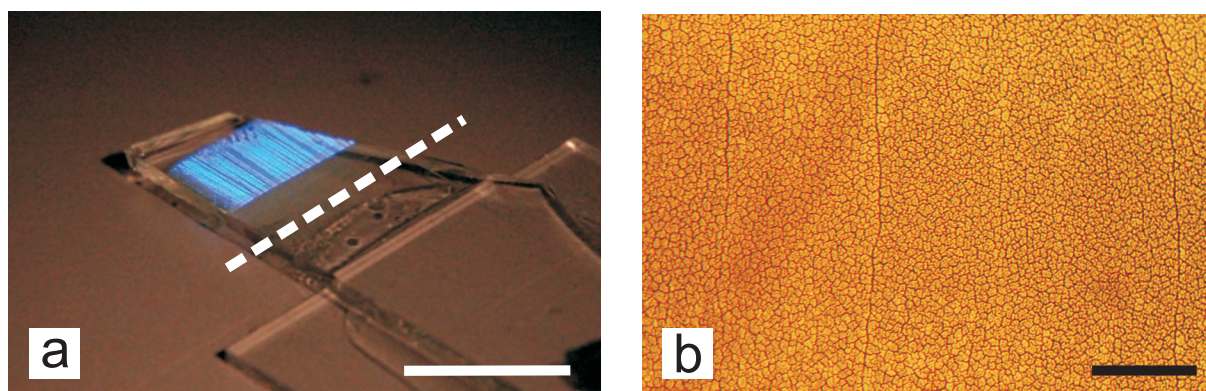


Figure 4.4: Panel (a) is a photograph of a colloidal crystal grown by convective assembly. It consists of 337 nm diameter silica spheres in air and displays beautiful Bragg colors in white-light illumination. The alternation of bright and dark stripes is clearly visible in this picture. Panel (b) is an optical micrograph of a similar colloidal crystal of 353 nm diameter silica spheres, showing different domains and long vertical cracks. In panel (a), the orientation of the meniscus during sample growth is indicated by the white dashed line, in panel (b) it is indicated by the scale bar. The scale bar in panel (a) is 1 cm, the one in panel (b) is 0.2 mm.

scattering & absorption, paint being an example of the latter. If the crystal is covered with an amorphous layer, for example, the Bragg colors coming from the sample will look a little dull. Secondly, in samples with a modest index contrast, silica spheres in air for example, interference needs to build up over several crystal layers. Thus, if the samples consists of only 1 or 2 layers, the colors will not look as bright as from a sample with 10 or more layers.

A striking feature of Bragg colors from colloidal crystals grown by controlled drying is the alternation of bright and dark stripes (Figure 4.4a). If samples are slightly tilted, the dark stripes become bright stripes and vice versa. The stripes are oriented perpendicular to the meniscus. Even close to the vertical edge of the sample, where the meniscus curves upwards during growth due to capillary forces (Figure 4.1a), the stripes stay perpendicular to the meniscus, causing them to slightly deviate from the vertical direction. In optical microscopy (Figure 4.4b), long cracks are visible that run vertically along the sample. It is tempting to interpret these cracks as the boundaries of the stripes. The stripes could then correspond to crystal areas having different stacking sequences [193]. Although we have not investigated this link in detail, we note here that we have seen color differences in optical microscopy using a $15\times / 0.4$ NA Cassegrain objective on a Bruker Hyperion 2000 microscope, but we have not observed any qualitative differences between bright and dark stripes in SEM and FTIR spectroscopy. All the same, the stripes seem to indicate the presence of a preferential direction in colloidal crystals grown by controlled drying.

Another fast method to obtain some mesoscopic information on colloidal crystals is optical microscopy. Although the resolution in optical microscopy is not sufficient for observing individual colloidal particles with a diameter around 400 nm, it does provide valuable sample characteristics such as the number of cracks, typical domain sizes and the number of layers. Furthermore, it allows the identification of markers which can be used for positioning purposes in SEM (Figure 4.5). From optical microscopy, it is already clear that in controlled drying, the

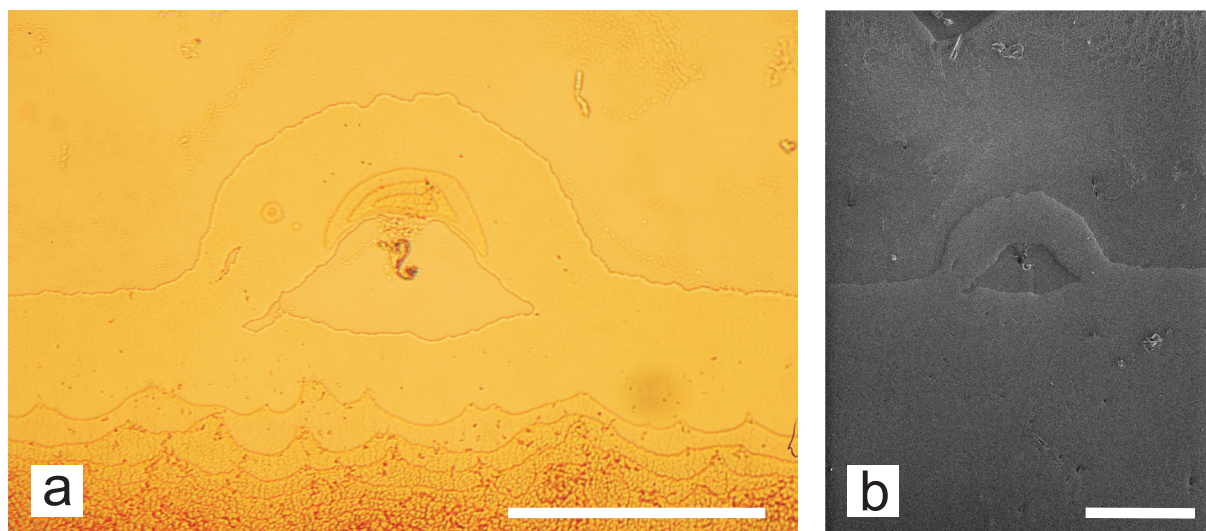


Figure 4.5: Optical microscopy and SEM top views of a colloidal crystal of 353 nm diameter silica spheres in air, grown by controlled drying. The images show a clear, unintentional marker for positioning purposes in electron microscopy. In both images, the meniscus was oriented horizontally during crystal growth. The scale bars in both panels are 0.2 mm.

number of layers of the colloidal crystal at the start is 1. As the meniscus sweeps the substrate, the number of layers increases one by one.

Unfortunately, optical microscopy does not have the resolution that is required to probe the orientation of the hexagonal layers in real space. Using positioning markers, the same spot on the sample was studied using SEM, in which the required resolution could easily be obtained. Similar observations were made in other controlled-drying crystals that we studied. In SEM, it was very clear that crystal growth indeed started with only 1 layer (Figure 4.6a). The edge of the first crystal layer was not straight, rather jagged, which could have been caused by the solvent not wetting the substrate properly. The lines of touching particles, which were clearly parallel to the meniscus in the first layer, even followed the jagged shape of the meniscus. This implies that surface tension is the dominating mechanism orienting the hexagonal layer at the start of crystal growth.

Moving downwards, away from the meniscus, the orientation of the hexagonal layers still seemed to have a preference for aligning the lines of particles parallel to the meniscus (Figures 4.6c and 4.6d), although domains in which the lines of particles are oriented perpendicular to the meniscus were also observed. As far as $\sim 500 \mu\text{m}$ downwards, the lines of particles were still oriented parallel to the meniscus in at least a substantial number of domains (Figure 4.6b).

As was observed in optical microscopy, the number of layers increased one by one. At the transition from n to $(n+1)$ layers, a thin region with square instead of hexagonal symmetry was observed (Figure 4.6c and 4.6d), as was reported by Meng *et al.* [184]. At such a transition, the orientation of a domain was either conserved or it switched. As square symmetry has lines of particles both perpendicular and parallel to the meniscus, this transition region could be the manifestation of a mechanism for crystal domains to switch from one orientation to the other. Note that *if* the crystal is hollow-site stacked, as expected, the orientation of a crystal domain has to be the same from the top to the bottom layer, otherwise the hexagonal layers will not fit

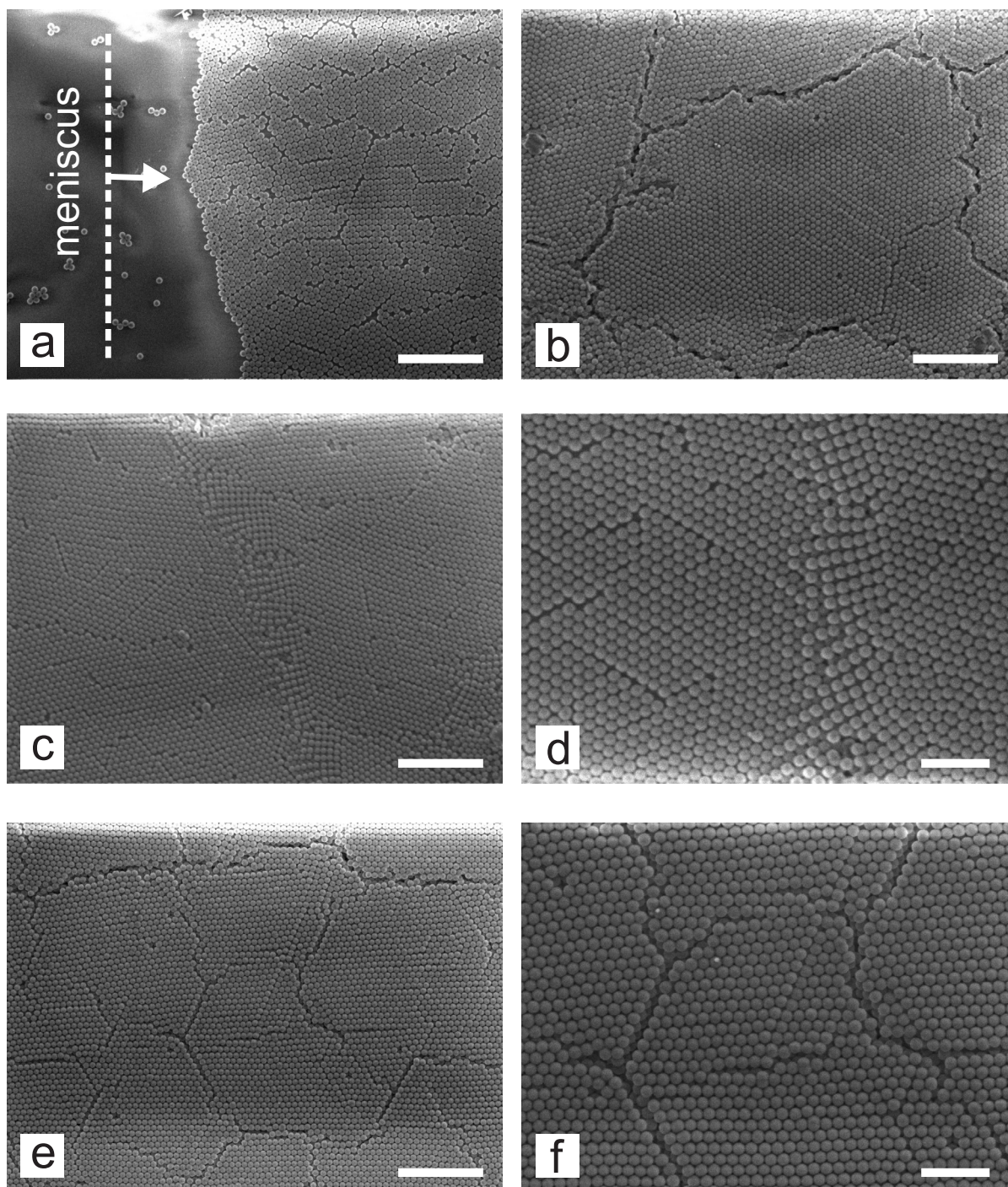


Figure 4.6: SEM top views of colloidal crystals grown by controlled drying at different distances below the start of crystal growth: (a) at the start of crystal growth, (b) at $\sim 475 \mu\text{m}$, (c,d) at $\sim 100 \mu\text{m}$, (e,f) at $\sim 1.15 \text{ cm}$. The crystal consists of 353 nm diameter silica spheres. From panel (a) to panel (f), the orientation of the hexagonal layers changes from parallel to perpendicular to the meniscus. During convective assembly, the meniscus was oriented vertically in all panels, as indicated by the white, dashed line. The movement of the meniscus during controlled drying is indicated by the white arrow. The white scale bars in panels (a,b,c,e) are $5 \mu\text{m}$, the ones in panels (d,f) are $2 \mu\text{m}$.

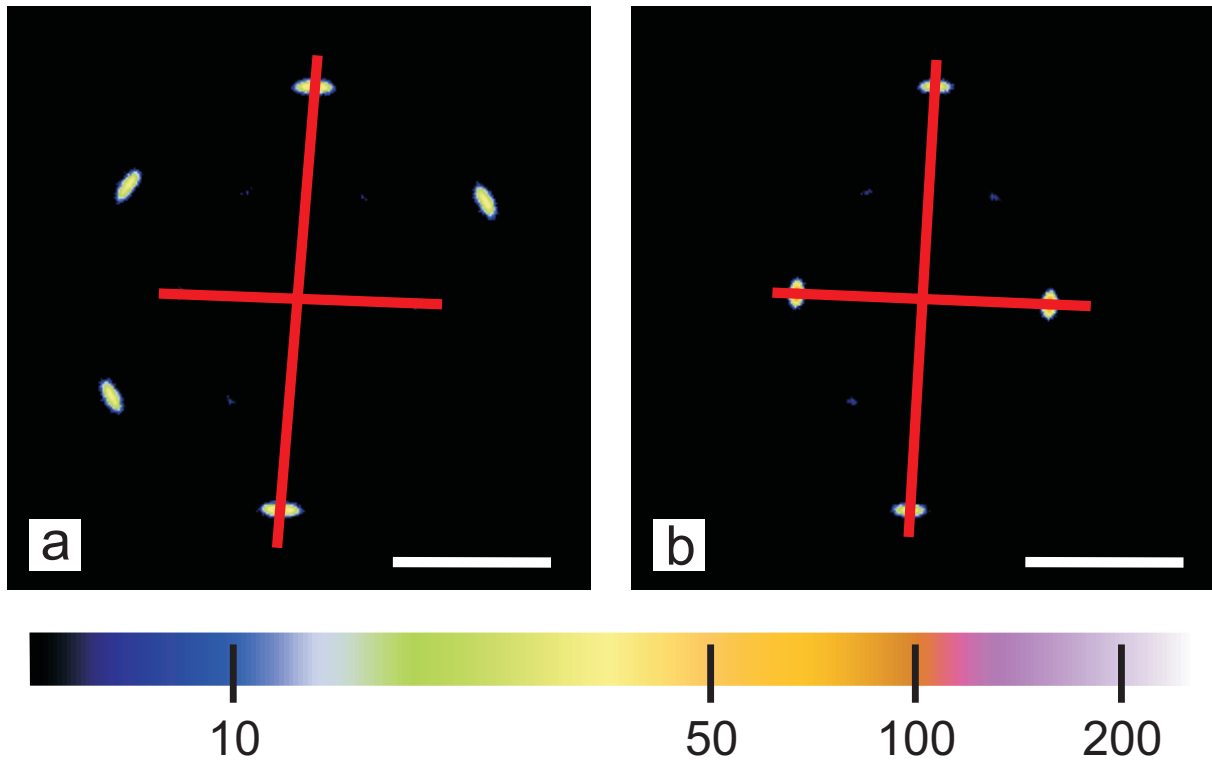


Figure 4.7: X-ray diffraction patterns of a colloidal crystal grown by controlled drying at angles of incidence of approximately (a) 0° and (b) -21.5° . The colloidal crystal consisted of 337 nm diameter silica spheres in air. The $(\bar{1}\bar{1}0)$ and (110) reflections are visible in both panels, as they are on the axis of rotation. Both white scale bars are $25 \mu\text{m}^{-1}$. The numbers below the intensity scale bar are detector pixel values. Line profiles for measuring distances in reciprocal space were taken along the red lines.

onto each other in the direction perpendicular to the substrate.

Far from the meniscus, on the order of 1 cm downwards, all domains were oriented with their lines of particles perpendicular to the meniscus, apparently without any exception (Figure 4.6e and 4.6f). Unfortunately, we did not probe intermediate distances in SEM, but we did by X-ray diffraction. A major advantage of X-ray diffraction over SEM is that it shows the orientation of the hexagonal layers over the entire cross-section of the beam in a single shot. With a typical size of the X-ray source of about $380 \mu\text{m} \times 260 \mu\text{m}$, primary slits with a $300 \mu\text{m} \times 500 \mu\text{m}$ gap at 27.6 m from the source and the sample at 48.7 m, the X-ray beam should form a spot on the sample of approximately $0.8 \text{ mm} \times 0.6 \text{ mm}$. This estimate of the cross-section of the X-ray beam corresponds pretty well with the size of the brown spot ($\sim 1 \text{ mm}$ diameter) that was left in the glass substrate after prolonged exposure to X-rays. Such brown spots are probably due to the formation of color centers within the glass substrate during exposure to X-rays [3, 4].

We analyzed the diffraction data in terms of a deformed hexagonal lattice (Section 4.2). The reason for this is that all our crystals, as is often the case in colloidal self-assembly, consist of stackings of (nearly) hexagonally packed layers that orient parallel to the substrate. Figure 4.7 presents typical X-ray diffraction patterns of a colloidal crystal, grown by controlled drying, at angles of incidence of 0° and -21.5° relative to the substrate normal. The X-ray beam was positioned 4.5 to 5.5 mm below the start of crystal growth. The meniscus would have been

parallel to the horizontal axis in this case. In both diffraction patterns, the (110) and $(\bar{1}\bar{1}0)$ reflections are on the vertical axis, which means the reciprocal-space basis vectors \mathbf{b}_1 and \mathbf{b}_2 are not on the vertical axis. This, in turn, means that one of the two real-space basis vectors, \mathbf{a}_1 or \mathbf{a}_2 , was on the vertical axis, implying that the lines of touching particles ran perpendicular to the meniscus in this sample. The orientation of the hexagonal layers in several controlled-drying colloidal crystals was determined by X-ray diffraction and we have not encountered any sample in which the lines of particles were oriented parallel to the meniscus.

4.4.2 Packing

Normal-incidence, X-ray diffraction patterns of colloidal crystals grown by controlled drying do not only reveal the orientation of the hexagonal layers over $\sim\text{mm}^2$ areas, they also contain valuable information about the (3-D) structure of these crystals. For example, it has been observed in spectroscopic measurements that the volume fraction of colloidal crystals grown by controlled drying is 71% to 73%, which is smaller than the close-packing value of $\sim 74\%$ [188]. A possible explanation claims that the ‘missing’ volume corresponds to cracks and other defects, which are always present in such colloidal crystals [76]. Another explanation could be that the hexagonal layers in controlled-drying colloidal crystals are not exactly hexagonal. Whether or not these layers are really hexagonal can be extracted from diffraction patterns such as shown in Figure 4.7. Taking line profiles through $(1\bar{1}0)$ & $(\bar{1}10)$ and $(\bar{1}\bar{1}0)$ & (110) , as indicated in Figure 4.7 by red/dark-gray lines, the deformation coefficient α or ε (see Equation 4.5) can be calculated using

$$\alpha = \frac{a_y}{a_x} = \varepsilon \cdot \left(\frac{1}{\sqrt{3}} \right) = \frac{\Delta q_x}{\Delta q_y}. \quad (4.29)$$

The values for Δq_x and Δq_y can be obtained from the line profiles (Figure 4.8) using

$$\begin{aligned} \Delta q_x &= \left\| (\bar{1}10) - (1\bar{1}0) \right\| \\ \Delta q_y &= \left\| (110) - (\bar{1}\bar{1}0) \right\|. \end{aligned} \quad (4.30)$$

Note that the line profiles for Δq_x and Δq_y should be perpendicular to one another, but they are actually at an angle of approximately 88° in both measurements. At this moment, we do not have an explanation for this observation, but $\cos(2^\circ)$ is so close to 1 that the tilt hardly affects the results presented here. Although it requires a correction for the angle of rotation, we prefer to extract the Δq values from diffraction patterns at an angle of incidence of -21.5° , because the reflections in the line profiles of these patterns are either allowed, or they are on the axis of rotation. This means the signal-to-noise ratio in these line profiles is much better than in those taken from normal-incidence diffraction patterns, where the $(1\bar{1}0)$ and $(\bar{1}10)$ reflections are not allowed. The $(1\bar{1}0)$ and $(\bar{1}10)$ reflections should actually reach their maximum at $\ell = \pm\frac{1}{3}$ [105], which corresponds to an angle of incidence of -19.5° . However, the angle of -21.5° is much closer to the experimental value of -21.8° , which was determined using a rocking curve (Figure 4.10, discussed later on).

From the line profiles in Figure 4.8, a value for ε of (0.961 ± 0.007) was extracted. Values for the deformation parameter ε were extracted from diffraction patterns of several other samples as well. The measured deformation in those samples was approximately as large as,

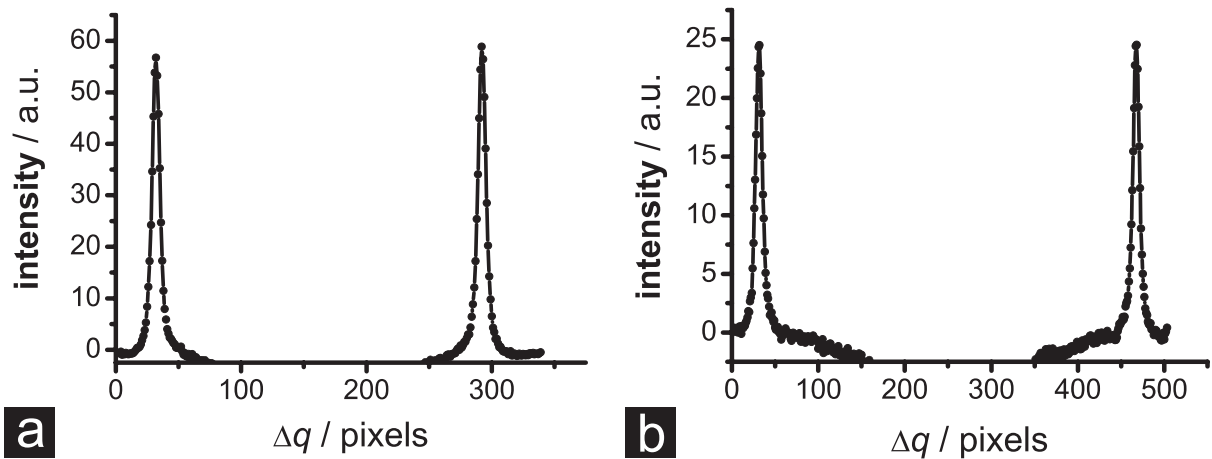


Figure 4.8: Line profiles along the dark-gray lines through the (a) $(1\bar{1}0)$ & $(\bar{1}10)$ reflections & the (b) $(\bar{1}\bar{1}0)$ and (110) reflections in the diffraction pattern shown in Figure 4.7b, which was taken at an angle of incidence of -21.5° . The colloidal crystal in the X-ray beam consisted of 337 nm diameter silica spheres and was grown by controlled drying. The peak profiles were obtained by averaging the intensity over a band approximately as wide as the reflections in Figure 4.7. As we are currently only interested in ratios of distances in reciprocal space, the unit of that distance need not be converted from pixels to μm^{-1} . The numbers on the vertical axes of the graphs are detector pixel values.

or larger than, the deformation presented here. As ε equals 1 for a hexagonal layer, this result indicates that the hexagonal layers in colloidal crystals grown by controlled drying are slightly expanded parallel to the meniscus. To check whether the measured deformation was not due to a detector artefact, a value for ε was also extracted from a normal-incidence, X-ray diffraction pattern of the same sample at an orthogonal orientation. The pattern was recorded at the same position on the detector and yielded $\varepsilon = (0.953 \pm 0.008)$. As these two values are so close, we conclude that the measured deformation of approximately 4% in colloidal crystals grown by controlled drying is accurate within 1 percentage point.

In order to check the deformation of controlled-drying colloidal crystals in real space, scanning electron microscopy (SEM) top views at orthogonal orientations were recorded (Figure 4.9). For the sample of which diffraction patterns were shown in Figure 4.7, an estimate for ε was obtained from Figures 4.9a and 4.9b by measuring at least 28 spacings for both a_x and a_y , yielding $\varepsilon = 0.98$ and $\varepsilon = 0.97$, respectively. Although better statistics are required to draw definite conclusions, these SEM measurements do not contradict the X-ray result. More importantly, the SEM images provide a possible explanation for the deformation. Upon careful inspection of the images, one can observe that the lines of touching particles, which are oriented perpendicular to the meniscus, are not straight lines. Instead, they appear to wiggle around an average straight line. In X-ray scattering, which provides macroscopically-averaged data, this wiggling looks like a distorted hexagonal plane, resulting in a value of ε lower than 1.

The in-plane deformation that was observed both in X-ray diffraction and in SEM allows the interlayer spacing to be slightly smaller than in the case of close-packing (Equation 4.6). For the above-mentioned sample, assuming that particles were touching along the lines perpendicular to the meniscus, the interlayer spacing obtained from Equation 4.6 is $(0.9948 \pm 0.0010) \cdot d_{\text{CP}}$, using $\varepsilon = (0.961 \pm 0.007)$ as measured in X-ray diffraction. Because the hexagonal layers

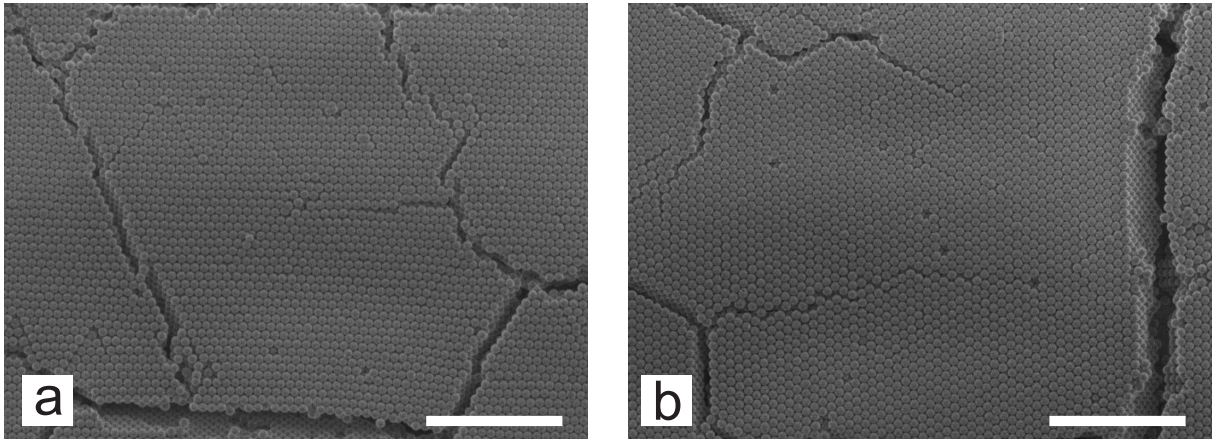


Figure 4.9: SEM top views, at orthogonal orientations of the SEM sample stage, of a colloidal crystal grown by controlled drying. The colloidal crystal consists of 337 nm diameter silica spheres in air (see also figure 4.7). The white scale bars are 5 micron.

are slightly deformed and the interlayer spacing is slightly decreased, the volume fraction of spheres in these crystals changes as well (Equation 4.7), yielding (0.715 ± 0.004) . Such a value for the sphere volume fraction is significantly lower than the maximum packing fraction of $(\pi\sqrt{2}/6) \approx 0.740$ for close-packed crystals and is in reasonable agreement with the 71% to 73% obtained from spectroscopic measurements [188]. This indicates that colloidal crystals grown by controlled drying are not truly close-packed, which was independently observed in FTIR spectroscopy [188].

4.4.3 Stacking

After determining the in-plane packing in controlled-drying colloidal crystals, the stacking of the nearly hexagonal layers is still left to be determined. In order to probe the stacking of colloidal crystals, one of the stacking-dependent reflections should be considered. For close-packed colloidal crystals, it was shown in Section 4.2.2 that interference is always constructive at normal incidence for reflections for which $(h - k)$ is a multiple of 3, independent of the stacking sequence of the hexagonal layers. However, interference turned out to be destructive for reflections for which $(h - k)$ is not a multiple of 3. For those reflections, the stacking-induced phase difference can be compensated at non-zero values of ℓ , which can be reached by specific sample rotations. In the case of an FCC structure (ABC-stacking), the phase difference is compensated at $\ell = \pm \frac{1}{3}$. For HCP stacking, the phase difference cannot be fully compensated at any value of ℓ , whereas it is compensated at half-integer values of ℓ for random stacking (RHCP).

Figure 4.10a shows the rocking curve for the $(1\bar{1}\ell)$ reflection, which is one of the stacking-dependent reflections, from a colloidal crystal grown by controlled drying. Actually, it is the same sample of which diffraction patterns at two different angles of incidence are shown in Figure 4.7. In our setup (Chapter 3), the angle of incidence can be varied by rotating the sample around the vertical axis. After measuring the X-ray diffraction pattern at various angles of rotation γ , a rocking curve is obtained by plotting the total intensity of the $(1\bar{1}0)$ reflection

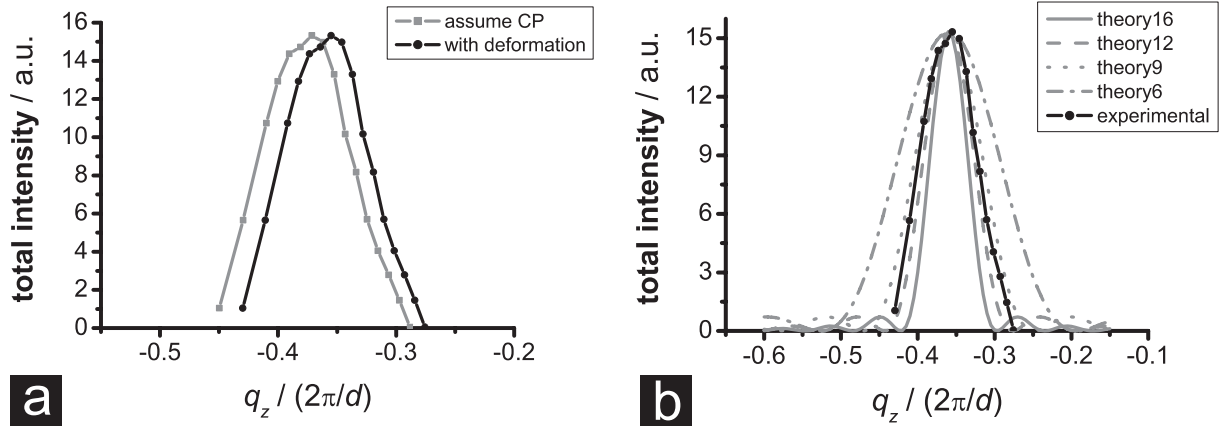


Figure 4.10: Rocking curves for the $(1\bar{1}\ell)$ reflection from a colloidal crystal of 337 nm diameter silica spheres in air, grown by controlled drying. Panel (a) shows the shift of the position of the maximum of the experimental rocking curve upon correction for the deformation of the hexagonal layers. Panel (b) shows the corrected experimental curve (black), together with theoretical curves that were calculated for different numbers of layers N . Calculations for different N were scaled to the intensity maximum of the experimental rocking curve. The numbers along the vertical axis in both panels are rescaled total detector pixel values ($/1000$) over a fixed area around the $(1\bar{1}\ell)$ reflection.

versus the angle γ . Usually, the angle is converted to a value of ℓ , after which $I(\ell)$ is plotted. The conversion from γ to ℓ requires a value for the deformation coefficient ε and for the interlayer spacing d .

$$l = \left(\frac{2\varepsilon d}{\sigma\sqrt{3}} \cdot \tan \gamma \right) \quad (4.31)$$

The two rocking curves in Figure 4.10a differ only in whether or not the approximately 4% deformation of the hexagonal layers was taken into account. Correcting for the deformation clearly causes the maximum of the measured rocking curve to shift towards the theoretical value of $l = -\frac{1}{3}$ for FCC crystals. The deformation also enters the phase condition for constructive interference (see Section 4.2.2). For our crystals, consisting of deformed hexagonal layers, the lateral shift vector can be written as

$$\mathbf{s}_j = j \cdot [\tau a_x, 0, 0] . \quad (4.32)$$

If this shift vector is inserted into Equation 4.26, the resulting coherence relation is

$$\Delta\phi_j = 2\pi j\ell - 2\pi \cdot \left(\frac{j\tau}{2} \right) \cdot (h - k) . \quad (4.33)$$

The required value for τ can be calculated from the measured value of $\varepsilon = (0.961 \pm 0.007)$ using Equation 4.2, yielding $\tau = 0.654 < (2/3)$. The deformation ε thus causes τ to decrease with respect to non-deformed CP crystals, which means ℓ has to increase in absolute value to compensate for the deformation-induced phase difference. Qualitatively, the shift in the position of the rocking-curve maximum confirms the deformation of the hexagonal layers in controlled-drying samples.

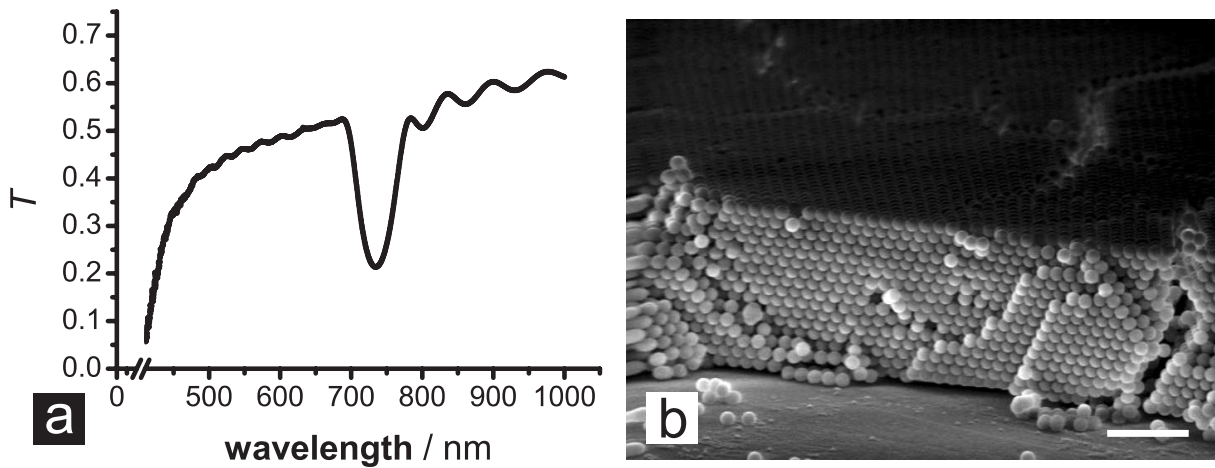


Figure 4.11: FTIR transmission spectrum (a) and SEM side view (b) of one and the same crystal of silica spheres in air, grown by controlled drying. The transmission spectrum was taken at the same position on the sample as the X-ray diffraction patterns and rocking curves in Figures 4.7 and 4.10. The scale bar in panel (b) is $2 \mu\text{m}$.

In addition, the width of a rocking curve contains important information about the stacking of the hexagonal layers. Stacking faults will broaden the nodes in reciprocal space along ℓ [105]. In other words, stacking faults cause points in reciprocal space to be elongated along ℓ . Unfortunately, a finite number of layers will also cause broadening of the points, along the same direction [105]. If the number of layers is small, it might be difficult to distinguish between broadening due to finite-size effects and broadening due to stacking faults. Figure 4.10b shows the experimental rocking curve of the $(1\bar{1}0)$ reflection from the above-mentioned sample. The deformation of the nearly hexagonal layers has been taken into account. Finite-size effects along the stacking directions can be taken into account by fitting the experimental rocking curve to

$$I(\ell) \propto \left(\frac{\sin(\pi N \ell)}{\pi \ell} \right)^2, \quad (4.34)$$

in which N is the number of ‘hexagonal’ layers of the colloidal crystal [105]. Using Equation 4.34, theoretical curves for several numbers of layers have been plotted along with the experimental rocking curve, using the position and the height of the experimental curve as input for the calculated curves (see Figure 4.10b). It is quite clear that a curve for 9 to 12 layers fits the experimental curve best.

However, the sample may have consisted of more than approximately 10 layers, if stacking faults broadened the reflection. A conclusive answer could only be obtained after independent determination of the number of layers in a different measurement. Figure 4.11a shows a transmission spectrum of the same colloidal crystal, taken with a beam spot of approximately 1 mm in diameter, i.e. similar to the X-ray beam. Using the brown spot on the glass substrate (color centers) as a marker, the spectrum was taken at the very same spot that was probed using X-rays. From such a spectrum, the number of layers can be extracted using Fabry-Pérot fringes (450 nm to 650 nm in Figure 4.11a) [77]. The spacing of the fringes yielded an optical thickness $t_{\text{op}} = \bar{n} \cdot t$ of the colloidal crystal of $(6.25 \pm 0.08) \mu\text{m}$. The optical thickness of the crystal

can be converted to the number of layers N using the position of the first-order (111) Bragg reflection and Bragg's law (Equation 4.35), without using the average refractive index \bar{n} of the crystal (Equation 4.36).

$$2\bar{n}d_{(111)}^{(1)} = \lambda_{(111)}^{(1)} \quad (4.35)$$

This leads to

$$N - 1 = \frac{t}{d} = \frac{t_{\text{op}}}{\bar{n}} \cdot \frac{2\bar{n}}{\lambda_{(111)}^{(1)}} = 2 \left(\frac{t_{\text{op}}}{\lambda_{(111)}^{(1)}} \right). \quad (4.36)$$

FTIR measurements indicated that the number of interlayer spacings was (17.0 ± 0.2) . This number has to be corrected for finite-size effects, half of the top and bottom layers 'sticking out' of the sample, leading to a number of layers of $N = 17$. SEM side views of the same sample, though taken at a different spot of the sample, indicated a layer number of 15, which is in good agreement with the FTIR result.

The experimental rocking curve in Figure 4.10 is clearly wider than the theoretical curve for 16 layers. As the sample consisted of 17 layers at the position that was probed using X-ray diffraction, our measurements seem to indicate that the sample did not have a single stacking sequence. However, the experimental rocking curve is much narrower than the theoretical curve for 6 layers (Figure 4.10b) and the position of the maximum is much closer to $\ell = -\frac{1}{3}$ than to $l = -\frac{1}{2}$, which clearly excludes random stacking. In the case of hexagonal close-packing, maxima of different heights can be expected at integer and half-integer values of l , which is not the case here either. Therefore, the ABCABC stacking sequence of FCC is the most probable stacking sequence, although 1 or more stacking faults could have been present, thus explaining peak broadening.

Strangely enough, we have not observed stacking faults in SEM (Figure 4.11b). Although stacking sequences are hard to determine in SEM side views, which is why we have not extensively studied it in SEM, stacking faults should have been discernable. It may be that the peak broadening in our samples was *not* caused by stacking faults, but by the deformation of the hexagonal layers. Inserting the experimentally obtained value for τ in Equation 4.33 yields the following coherence relation

$$\Delta\phi_j = 2\pi j\ell - 2\pi \cdot (j \cdot (0.327) \cdot (h - k)) . \quad (4.37)$$

At normal incidence ($\ell = 0$), the phase shift of layer j was caused solely by its lateral shift with respect to the first layer ($j = 0$). In CP crystals, the term in between brackets is an integer for all values of j if $(h - k)$ is a multiple of 3, because $(\tau/2) = (1/3)$. In our deformed crystals, however, $\tau/2 = (0.327) \neq (1/3)$. This means that the term in between brackets in Equation 4.37 is, in general, not an integer if $(h - k)$ is a multiple of 3. For small values of j , the deformation-induced phase shift will still be close to an integer times 2π , thus allowing constructive interference. However, if $j = 12$ for example, the phase shift is approximately $(11.8 \cdot 2\pi)$, which significantly deviates from an integer multiple of 2π . In other words, interference between the first A-layer ($j = 0$) and consecutive A-layers (j a multiple of 3) is no longer completely constructive in our deformed colloidal crystals at normal incidence. In our case, this deformation-induced phase shift becomes substantial after 9 to 12 layers.

Actually, rewriting Equation 4.33

$$\Delta\phi_j = 2\pi j \left(\ell - \left(\frac{\tau}{2} \right) \cdot (h - k) \right) \quad (4.38)$$

shows that interference is constructive for all values of j if

$$\ell = \left(\frac{\tau}{2}\right) \cdot (h - k) , \quad (4.39)$$

which means the maximum of the experimental rocking curve for the $(1\bar{1}0)$ reflection in Figure 4.10 should be reached for $\ell \approx -0.346 < -\frac{1}{3}$. At angles close to $\ell = -0.346$, interference is no longer completely constructive. This is also true for non-deformed crystals, but a non-uniform deformation of the hexagonal layers may cause additional peak broadening. A more detailed analysis of both the theoretical model and the X-ray diffraction data will be required to resolve whether peak broadening in controlled-drying colloidal crystals is due to stacking faults or (non-uniform) in-plane deformation.

4.5 Conclusions and outlook

In this chapter, we have considered orientation, packing and stacking of ‘hexagonal’ layers in colloidal crystals grown by controlled drying of silica particles with a diameter around ~ 350 nm. We find in SEM that the lines of touching particles in the hexagonal layers are parallel to the meniscus close to the start of crystal growth, where the number of layers is still small (< 5). This result agrees with observations by Meng *et al.* [184]. At larger distances from the start of the crystal (~ 1 cm), where the number of layers is larger, the orientation of the hexagonal layers has switched, such that lines of touching particles are *perpendicular* to the meniscus. X-ray diffraction measurements confirm the perpendicular orientation and show that it already starts at a distance of no more than 3 mm from the start of the crystal. These observations seem to indicate that for small numbers of layers, for which lines of touching particles line up parallel to the meniscus, surface tension is the dominating mechanism orienting the hexagonal layers in controlled drying. However, as the number of layers gets larger, shear forces take over and orient the layers such that lines of touching particles are perpendicular to the meniscus.

A more detailed analysis of X-ray diffraction patterns, taken at normal and off-normal incidence, shows that the hexagonal layers in controlled-drying colloidal crystals are not exactly hexagonal, but are expanded along the meniscus by $(4 \pm 1)\%$. Although better statistics are required, real-space measurement in scanning electron microscopy (SEM) confirm the deformation. This means that such crystals are not truly close-packed, but have a sphere volume fraction of approximately 71.5%, assuming optimal stacking of the deformed layers. This value for the volume fraction agrees quite well with values obtained from FTIR spectroscopy [188].

A shift in the position of the maximum of the rocking curve for the $(1\bar{1}0)$ reflection in such a controlled-drying sample further confirms the deformation of the hexagonal layers. The position and width of the rocking curve indicate that the crystal was ABCABC stacked, which means its 3-D structure was close to (slightly deformed) face-centered cubic (FCC). Broadening of the rocking curve of the $(1\bar{1}0)$ reflection indicates that this 17-layer crystal contained at least 1 stacking fault, which would not contradict the results from experiments by Wei *et al.* [185]. We argue, however, that the broadening of the rocking curve may also have been caused by non-uniform deformation, causing additional phase shifts. In order to draw definite conclusions on the 3-D structure of colloidal crystals grown by controlled drying, better statistics are required and both the theoretical model (Section 4.2) and the X-ray diffraction data need to be studied

more extensively. Nevertheless, we have demonstrated that small-angle X-ray scattering is a valuable characterization technique for 3-D colloidal crystals.

Acknowledgements

The research that has been presented in this chapter could not have been performed without the help and support of many different people. First of all, Christina Graf and Anouk Wetzels are gratefully acknowledged for particle syntheses; Angela Kylner for cleaning up some of the dispersions. Over the years, growth bottles and substrates were cut by various people at the glassware workshop of the department of Chemistry, Utrecht University. Many thanks to Dannis 't Hart, Carlos van Kats and Carmen Zoldesi for all the transmission electron microscopy (TEM) images that they have made in my interest. Pim van Maurik is acknowledged for scanning electron microscopy (SEM) training, support and maintenance. I would also like to express my gratitude towards Dannis 't Hart, Arnout Imhof and Andrei Petukhov for being part of the April 2006 SAXS crew. Wim Bras, Daniel Brau, Dirk Detollenaere, Sergey Nikitenko, Giuseppe Portale, Nikolas Vilayphiou and Harry van der Wal are gratefully acknowledged for the excellent support both before and during our X-ray diffraction experiments at beamline BM26B "DUBBLE" of the European Synchrotron Radiation Facility (ESRF) in Grenoble, France. Anatoly Snigirev is acknowledged for providing the X-ray lens and some calibration grids. I would also like to thank Dr. Florencio García-Santamaría and Prof. Paul Braun for useful discussions on the sphere volume fraction of controlled-drying colloidal crystals. Rianne van Eerd, Dannis 't Hart and Andrei Petukhov are acknowledged for critical reading of the manuscript. Last, but definitely not least, I would like to express my sincere gratitude towards Andrei Petukhov for many pleasant and useful discussions on the analysis of X-ray diffraction data.

Towards binary colloidal crystals for photonic applications

In this chapter, binary colloidal crystals of organic spheres (polystyrene, PMMA) and/or inorganic spheres (silica) are introduced as promising templates for the fabrication of strongly photonic crystals via the infiltration of high-index materials. Unfortunately, organic templates cannot be directly infiltrated by chemical vapor deposition (CVD), for its reaction temperature of approximately 350 °C is far above the glass transition temperature of polystyrene (PS) and PMMA. Silica templates can be infiltrated by CVD directly, but binary colloidal crystals of silica spheres have a layer of colloidal fluid on top. Because of its isotropic scattering, this layer has to be removed before further processing. In test experiments, we demonstrate that atomic layer deposition (ALD) of alumina can be used to infiltrate even organic templates. After burning of the original template, the refractive-index contrast can be further enhanced by infiltration with silicon using CVD. This results in silicon being deposited onto both sides of the alumina frame - in the air-sphere cavities and in the interstitial voids. Unfortunately, our calculations show that an FCC crystal of air spheres with such a silicon-alumina-silicon coating does not have a band gap, contrary to FCC crystals of air spheres in silicon. Preliminary etching experiments show that successive treatments with different plasmas can be used to etch polymer-embedded, colloidal-crystal templates of silica spheres. A first trial with peeling off crystal layers using adhesive tape shows that this may be a much easier, faster and cheaper technique for 'etching' such templates.

5.1 Introduction

Photonic crystals (PCs) are 3-D structures in which the refractive index varies periodically throughout space, such that strong interactions with electromagnetic radiation can occur [7–9, 194]. If the refractive-index contrast is large enough (~ 2 in Reference [114]), and a suitable periodic arrangement is chosen, PCs can exhibit a photonic band gap, which is the optical analogue of electronic band gaps in semiconductors [16–18]. Photonic band-gap materials are interesting both from a fundamental and a technological point of view. As PCs allow modification of the (local) density of states of photons [195–197], they are ideal laboratories to study the interaction of electromagnetic radiation with matter under extreme conditions [120]. Their strong interaction with light may also lead to supreme control over the emission and propagation of light [19–25], giving way to important applications in, for example, infrared telecommunications [26–28].

A promising route towards 3-D PCs is the self-assembly of colloidal particles [95, 107, 108]. Monodisperse microspheres can spontaneously form 3-D periodic arrangements, which are analogous to thermodynamic crystal phases [57, 198, 199]. If the refractive index of the particles is different than that of the surrounding medium, such colloidal crystals are PCs by definition, though the index contrast in such self-assembled structures is typically too low to open up a photonic band gap [65]. Compared to other PC fabrication methods, colloidal self-assembly is rather inexpensive. An additional advantage is that structure, size and composition of the individual building blocks can be modified in order to tune their optical properties. Advances in chemical synthesis have resulted in, for example, anisotropic particles [83–86] core-shell morphologies [87–89], metallodielectric colloids [90], and the incorporation of luminescent materials, such as fluorescent dyes [91, 92], rare-earth ions [93] and even quantum dots [94]. Furthermore, the interparticle potential can be affected by external fields [95], including patterned walls in colloidal epitaxy [78, 79], geometric confinement [200], electric fields [175], optical fields [96, 97] and shear flows [81, 82].

The symmetry of self-assembled colloidal crystals is determined by thermodynamics. This resulted, until recently, in a limited number of available crystal structures. However, as control over interparticle interactions is improving rapidly, the number of observed crystal structures is increasing significantly [201–204]. Unfortunately, only a few of those structures can be used as templates for further processing in order to increase the refractive-index contrast - the latter is required to open up a photonic band gap. There are, of course, other fabrication methods for PCs, including lithography, direct-writing assembly and multibeam holography. Although they have restrictions of their own, these techniques offer greater flexibility in crystal structure. Still, increasing the refractive-index contrast remains a challenge. Currently, one of the few routes towards photonic band-gap materials that have been realized experimentally is convective assembly [67, 77, 108], which is also known as ‘controlled drying’. The latter yields single-crystals with, at best, the face-centered cubic (FCC) crystal structure (see Chapter 4). As these templates can be grown with silica spheres, they can be inverted by infiltration with silicon using chemical vapor deposition (CVD) [182]. Subsequent removal of the silica spheres by a wet-chemical etch yields an FCC crystal of air spheres in silicon [67, 68]. Photonic band-structure calculations have predicted that such a structure has a photonic band gap [65, 66, 116], but its width relative to the midgap frequency is only $\sim 5\%$. Moreover, the gap is situated between high-lying bands, 8 and 9 in this case, which means the gap is not very stable against

disorder [74, 205].

The lack of flexibility in crystal structure is a pity, for it has already been known for quite a while that crystal symmetry has a huge effect on the optical properties of PCs. The currently known clear champion structures, both for opening up a band gap at the lowest refractive-index contrast (around 2) and the largest gap-to-midgap ratio, are dielectric diamond [32, 36, 37] and pyrochlore [38, 206, 207]. Both of these structures also give rise to gaps at low-lying bands. However, both diamond and pyrochlore are difficult to fabricate by self-assembly, because the volume fraction of spheres in those structures is relatively low. All the same, several methods to realize structures with diamond or pyrochlore symmetry by self-organization of colloids have been proposed [206, 208]. However, they require complicated and/or non-spherically-symmetric potentials that are yet to be realized experimentally [132, 133]. Recently, a new self-assembly route towards PCs with the structure of diamond and/or pyrochlore, having a band gap in the visible, was proposed. It involves the fabrication of these structures through the self-assembly of one of the Laves phases, MgCu_2 , using a binary mixture of colloidal spheres [114]. Although the proposed scheme has not yet been implemented experimentally, it only requires techniques that have been demonstrated before: the preparation of two species of colloidal spheres, surface patterning and the removal of one of the species.

Although it would not lead to diamond and/or pyrochlore structures, the use of binary mixtures of colloids for the fabrication of photonic band-gap materials has been proposed before. Biswas *et al.* already showed that binary colloidal crystals, such as the AB_2 structure [209], might be interesting PC templates. Their calculations show that the resulting PCs can have band gaps with relative widths that exceed those of inverse FCC at the same refractive index contrast [65]. Such AB_2 structures can form spontaneously in dispersions of poly(methyl methacrylate) (PMMA) spheres if the ratio of the volume fractions of particle species A and B, and the total volume fraction, are chosen carefully. However, the underlying homogeneous nucleation results in crystallites with varying orientation, which is not favorable for photonic applications. Velikov *et al.* developed a layer-by-layer fabrication method for AB_2 structures [135], resulting in binary crystals with a single orientation. Unfortunately, as it is a layer-by-layer growth technique, fabricating crystals with a large number of layers is laborious and time-consuming.

In a recent article, Leunissen *et al.* showed that a host of different binary crystals can be grown by self-assembly of oppositely-charged colloidal PMMA particles [201]. Due to homogeneous nucleation, these crystals also have varying orientations with respect to the sample wall. However, for approximately $2 \mu\text{m}$ diameter particles, crystallites as large as $100 \times 100 \mu\text{m}^2$, having a single orientation, were observed. As a thickness of 10 lattice constants is sufficient for most applications [75, 210], single-crystals of approximately 50×50 particles will be more than satisfactory. In the same article, the authors demonstrate that binary crystals with the structure of sodium chloride (NaCl) can be grown by self-assembly of oppositely-charged silica colloids with a size ratio of approximately 0.31 [201, 202]. In a particle system with the same size ratio, NaCl colloidal crystals can also be realized in an external electric field [211]. To predict their optical properties, we performed photonic band-structure calculations with the MIT Photonic Bands package (MPB, see Chapter 2) for NaCl structures of air spheres in silicon. As can be seen in Figure 5.1a, NaCl crystals can have a gap between bands 8 and 9 with a relative width of approximately 9%. Note that this is 4 percentage points wider than the gap between bands 8 and 9 in an FCC structure of air spheres in silicon. Although the NaCl crystal basis is slightly more complicated than that of FCC, the former having 2 instead of 1 particle in a unit cell, MPB

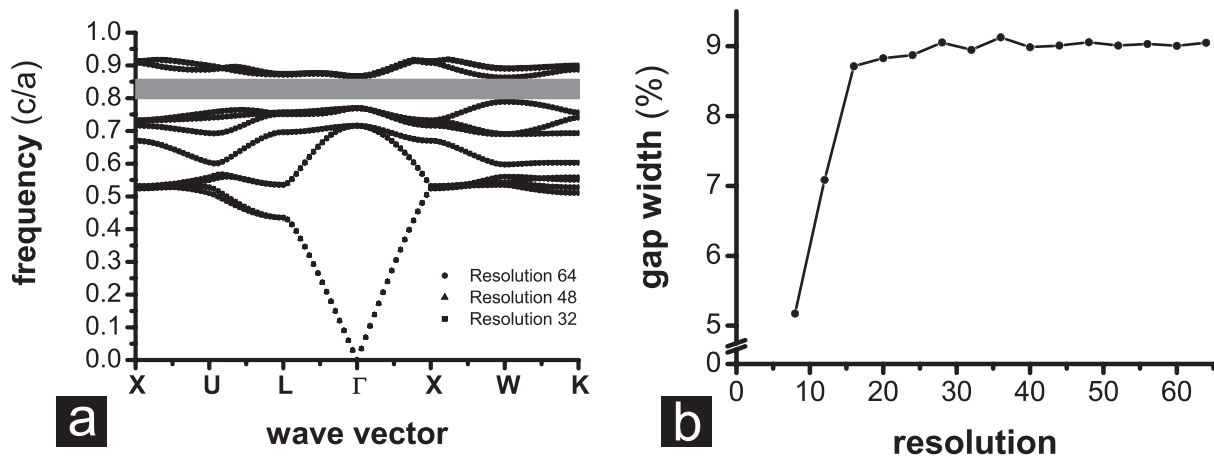


Figure 5.1: MPB photonic band-structure calculations for an NaCl structure of air spheres ($\epsilon = 1$) in silicon ($\epsilon = 12.25$). The large air spheres of the NaCl structure are touching, the size ratio of the small and large spheres is approximately 0.29. Panel (a) shows the calculated photonic band diagram for such a structure at three different values of the calculational resolution (see Chapter 2). There is a gap between bands 8 and 9 with a relative width of approximately 9%. From panel (b), it is clear that the calculations converge for resolutions larger than 16.

calculations converge for a calculational resolution of 16 or larger (see Section 2.4.2), which is similar to convergence in MPB calculations for FCC structures.

Although the fabrication of binary colloidal crystals was demonstrated in experiments, it is not straightforward to use them as templates for strongly photonic crystals. First of all, binary crystals of PMMA spheres cannot be infiltrated with high-index materials by chemical vapor deposition directly. The CVD process takes place at a temperature of approximately 350 °C, which excludes the use of organic templates consisting of PMMA or polystyrene (PS), for these materials have a glass transition temperature around 100 °C [212, 213]. In other words, such organic templates would melt during the CVD process. In principle, CVD can be used to infiltrate the above-mentioned sodium-chloride crystals with silicon, for they consist of silica spheres. Unfortunately, they also have a layer of colloidal fluid on top, typically having a thickness that is equal to of a couple of interlayer spacings of the crystal on which it rests. The isotropic scattering of light by the fluid layer will strongly deteriorate the optical properties of resulting photonic crystals. The same problem arises in other self-assembly procedures for photonic band-gap materials, including sedimentation.

In this chapter, we first show that colloidal crystals of approximately 377 nm diameter PS spheres can be infiltrated with silicon by CVD after atomic layer deposition (ALD) of a 15 nm to 25 nm thick layer of alumina. ALD is a deposition technique in which sequential application of reactants, coupled with substrate temperature optimization, leads to layer-by-layer growth of materials such as alumina ($\text{Al}_2\text{O}_3(\text{s})$) or titania ($\text{TiO}_2(\text{s})$) at temperatures that can be lower than 100 °C [70, 71]. As PS and PMMA have similar glass transition temperatures, these results are relevant for PMMA crystals as well. Our experiments with ALD on sediments of approximately 750 nm diameter PMMA spheres underline this relevance. Note that these experiments are also important for the fabrication of inverse (FCC) crystals in general. Due to the relatively high density of silica, growing crystals of > 400 nm diameter silica colloids by controlled drying is

difficult. Controlled drying of micron-sized spheres is more feasible if PS colloids are used, for its density is approximately half that of silica. Finally, we show that removing layers of colloidal fluid from the top of colloidal crystals may be possible by plasma etching, though it will be a laborious and time-consuming procedure. Though accuracy may be an issue, i.e. it may be difficult to remove exactly one crystal layer at a time, preliminary experiments on removal of crystal layers using adhesive tape show that this may be a much easier, faster and cheaper technique for ‘etching’ colloidal-crystal templates.

5.2 Experimental methods

5.2.1 Sample fabrication

In this chapter, we show results on colloidal crystals or sediments grown by controlled drying of polystyrene (PS), poly(methyl methacrylate) (PMMA) or silica particles. The fabrication of PS and PMMA colloidal crystals is described below, the fabrication of silica colloidal crystals is described in Section 4.3.1.

The PS colloidal-crystal templates were fabricated from dispersions of PS spheres in ethanol. These colloids had been synthesized by emulsion polymerization with a cationic initiator [212], which finally resulted in positively charged polystyrene spheres [214] in absolute ethanol. After sedimentation of the particles to the bottom of the storage bottle, the supernatant was removed with a pipette, after which the bottle was refilled up to the original level with ethanol pro analysi (Merck). Static light scattering (SLS) measurements on these PS particles in diluted dispersions showed that they had an average diameter of 377 nm with a polydispersity (PD) of approximately 4%.

Colloidal crystals were grown from the above-mentioned dispersions onto flat, glass substrates by convective assembly [77], also known as ‘controlled drying’, as has been described in Section 4.3 too. The stock dispersion was diluted to a volume fraction of approximately 0.9%, after which 10.0 ml of dispersion was transferred to a growth bottle. Glass, 20 ml, screw-neck vials with a flat bottom were used as growth bottles. They were placed on a table that was dedicated to sedimentation experiments (Figure 4.3), thus minimizing mechanical vibrations. A glass substrate was inserted vertically into the dispersion, after which it was tilted off-vertical by approximately 5°. A vertical cut through the neck of the vial ensured that the substrate would remain (nearly) vertical after insertion (Figure 4.3a). Next, in order to avoid dust falling into the growth bottle, the latter was covered with a 2 l glass beaker. To allow the evaporated ethanol to escape, the beaker was slightly tilted by supporting one side of the beaker with an approximately 5 mm thick piece of glass or metal. During growth, the temperature in the room was kept at (21 ± 1) °C.

Menzel-Gläser, standard microscopy slides, ca. 1 mm thick were used as glass substrates. All glassware, bottles and slides, were cleaned prior to use with tap water, commercially available soap, deionized water (16 MΩcm to 18 MΩcm) and technical-grade ethanol (Lamers & Pleuger, $\geq 96\%$). After cleaning, the growth bottles were dried in an oven at (50 ± 5) °C, whereas the slides were dried with a Kimwipe tissue, after which dust was removed with flowing nitrogen. After 2 to 7 days, the samples were retrieved from the growth bottles. They were kept (nearly) vertical for at least 2 hours to allow evaporation of residual ethanol. Next,

the deposition on one side of the substrate was removed using a Kimwipe tissue that had been drenched in technical-grade ethanol. Finally, colloidal crystal samples were kept in storage boxes to avoid contamination with dust.

In a similar way, PMMA sediments were fabricated from dispersions of spherical PMMA colloids in hexane. The stock dispersion consisted of PMMA particles in a mixture of hexane and dodecane. Part of the stock dispersion was transferred to hexane (Biosolve), by centrifugation and redispersion, and subsequently diluted to a volume fraction of approximately 1%. The PMMA spheres had an average diameter of approximately 750 nm and a PD of ca. 5% [215]. Sediments were formed by controlled drying, as described for PS spheres above, within 24 hours.

5.2.2 Atomic layer deposition and silicon infiltration

PS crystals and PMMA sediments were infiltrated with alumina ($\text{Al}_2\text{O}_3(\text{s})$) by atomic layer deposition (ALD, Cambridge Nanotech, Inc., Savannah 100) at the University of Illinois at Urbana-Champaign (IL, USA). Two precursor gases were used: de-ionized water ($\text{H}_2\text{O}(\text{g})$) and trimethylaluminum ($\text{TMAI}(\text{g})$). In a typical ALD run, water/TMAI vapor pulses of 0.05/0.1 s and exposure times of 0.0/0.0 s were used. In between consecutive pulses, the sample chamber was pumped vacuum for 10 s. In total, 90 cycles to 150 cycles were performed at gas flows of 20 sccm, a pressure of approximately 0.3 Torr and a temperature of 80 °C. These settings resulted in a 12 nm to 26 nm thick layer of alumina being deposited onto the spheres, the thickness of the layer depending on the number of cycles used. The actual thickness of the deposited layer was determined by ellipsometry on a clean silicon substrate that was in the sample chamber during the same run.

After infiltration with alumina by ALD, the PS spheres of the colloidal-crystal template were removed by heating. Samples were placed in a glass tube, which was subsequently inserted in a Lindberg/Blue tube furnace. Samples were heated up to 300 °C within 5 minutes and they were subsequently kept at 300 °C for 30 minutes. Next, the samples were heated from 300 °C to 375 °C within 5 minutes, at which temperature they were kept for several hours. After burning away the PS spheres, the samples were infiltrated using chemical vapor deposition (CVD) in a set-up in the group of Prof. Paul Braun at the University of Illinois at Urbana-Champaign (IL, USA), which was built there by Dr. Florencio-García Santamaría. For CVD, samples were heated up to 360 °C with a ramp rate of 8 °C/min. The pressure during the reaction was on the order of 10^{-6} mbar. During the CVD process, which took approximately 2 hours, the disilane precursor gas reacted at the alumina surface to form silicon ($\text{Si}(\text{s})$).

5.2.3 Silica etching

Plasma etching was performed using a Plasmalab 80+ ICP (Oxford Instruments) at the AMOLF NanoCenter in Amsterdam, The Netherlands. To etch silica, a mixture of $\text{CHF}_3(\text{g})$ and $\text{Ar}(\text{g})$ was used, with gas flows of 25.0 sccm and 25.0 sccm respectively. The forward power that was delivered to the plasma was set at 300 W. The pressure was set to 30 mTorr; the sample was not subjected to additional heating. To etch approximately 1 layer of a colloidal crystal of 336 nm diameter silica spheres, a reaction duration of approximately 14 minutes was used. As the plasma is pulled from the ionization chamber towards the sample by an anode, instead of

the sample being inside the chamber itself, we refer to this kind of plasma etch as a ‘directional plasma etch’.

Removing layers from colloidal crystals of silica spheres in air on a glass substrate using adhesive tape, which will be referred to as ‘tape etching’ from this point onwards, was performed with Scotch Magic (3M). The tape was gently laid down on top of the colloidal crystal, after which it was gently tapped with one finger over the entire area of the sample. Next, the tape was removed from the sample in a single pull.

5.2.4 Sample characterization

Most macroscopic images of the colloidal crystal samples were recorded using a Fuji FinePix A340, 4.0 mega pixels digital camera. The flashlight of the camera acted as a source for white light illumination.

Most scanning electron microscopy (SEM) images were taken with a Hitachi S-4700 SEM. It was typically operated at 2.0 kV, except if samples were coated with an approximately 5 nm thick layer of a gold/palladium alloy to reduce charging effects; in that case, it was operated at 10 kV. For the colloidal crystals of silica spheres, SEM images were taken with a Philips XL30FEG SEM. The vacuum in the sample chamber was kept below $9 \cdot 10^{-5}$ mbar at all times. To avoid image distortions due to charging effects in the uncoated samples, this SEM was typically operated at 3.0 kV, a spot size of 2.0 nm and a working distance of 5 mm to 7 mm. Images were recorded using the secondary-electron (SE) detector. At the start of a measurement session, the electromagnetic lenses were aligned and subsequently corrected for astigmatism. The SEM images in Figure 5.12 were recorded, after coating them with an approximately 30 nm thick layer of carbon, with a JEOL JSM-6460 SEM that was operated at 30 kV.

All transmission and reflection spectra that are presented in this chapter have been recorded with a Fourier transform infrared (FTIR) spectroscope. A Bruker Vertex 70 FTIR spectroscope was coupled to a Bruker Hyperion 2000 microscope; the sample was placed on the microscope sample stage. For these measurements, a microscope aperture of 0.6 mm was used in combination with a $4\times/0.10$ NA objective/condenser [216], yielding a typical spot size of $150 \mu\text{m}$ at the sample. A near-infrared (NIR) source was used for all spectra, the transmitted or reflected signals were measured with Si-diode detector in the visible and a InSb-detector in the NIR. Transmission measurements were taken after the microscope was set up for Köhler illumination with the sample in place. Reflection measurements were calibrated versus a silver mirror.

5.3 Results and discussion

5.3.1 Infiltrating crystals of organic colloids

Immediately after retrieval of the controlled drying PS samples from the growth bottles, it was clear that the deposited PS particles had formed crystalline structures. In white light illumination, the samples showed beautiful Bragg colors, which became slightly brighter after removing the deposition from the back side of the substrate (see Figure 5.2a). Just like for controlled drying colloidal crystals of silica spheres, the Bragg colors in PS crystals show an alternation of

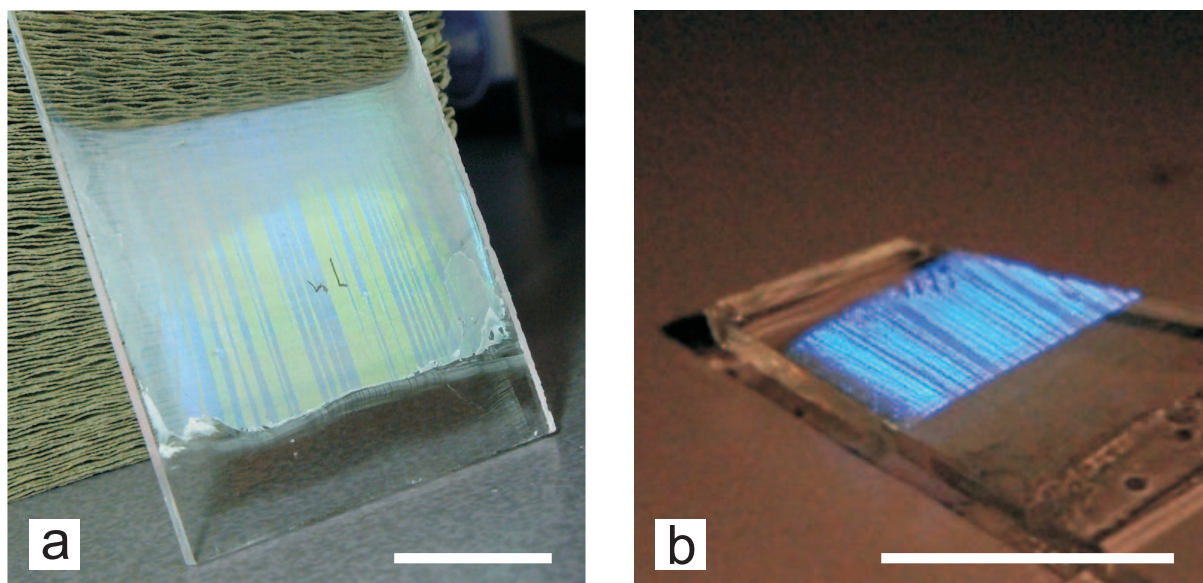


Figure 5.2: Panel (a) is a digital photograph of a colloidal crystal of PS spheres that was grown by controlled drying onto a glass substrate. It consists of 377 nm diameter PS spheres in air and displays beautiful Bragg colors in white light illumination (flashlight). The alternation of bright and dark stripes is clearly visible in this picture. A bright and a dark stripe have been labelled by intentional scratches. Panel (b) is a digital photograph of a similar crystal of 337 nm diameter silica spheres (see Figure 4.4). Both scale bars are 10 mm.

dark and bright stripes. In Section 4.4, we suggested that these stripes have different colors because they correspond to sample areas with different stackings [193], though we have not investigated this issue thoroughly. Using scratches as intentional markers (see Figure 5.2a), we did compare differently colored areas in SEM and by FTIR spectroscopy, but we have found no qualitative differences.

Note that the formation of cm^2 colloidal crystals of these PS spheres is quite remarkable in itself. To our knowledge, controlled drying has not been attempted before with positively charged colloidal particles. Although it is difficult to observe in printed photographs, Bragg colors from our PS samples (Figure 5.2a) are slightly hazier than Bragg colors from our silica samples (Figure 5.2b). It could mean that part of the PS deposition is amorphous, though most of the deposition must be crystalline, because the PS samples would have a white appearance otherwise. For example, due to the positive charge on the PS particles and the negative charge on the glass substrate, the bottom layer of these PS crystals may be non-crystalline, adding a hazy appearance to the Bragg colors. We note without proof that indications for a non-crystalline bottom layer were obtained from SEM images. Furthermore, comparing FTIR measurements for a controlled drying colloidal crystal of silica spheres (Figure 4.11a) with similar measurements for the PS sample in Figure 5.2a (see Figure 5.7), it is striking that the Bragg dip is only 20% T for the PS sample, whereas it is close to 30% T for the silica sample. Though the number of layers is larger in the silica sample, the refractive-index contrast is larger in the PS sample. In short, FTIR measurements do not contradict the hypothesis of a non-crystalline bottom layer in our PS colloidal crystals.

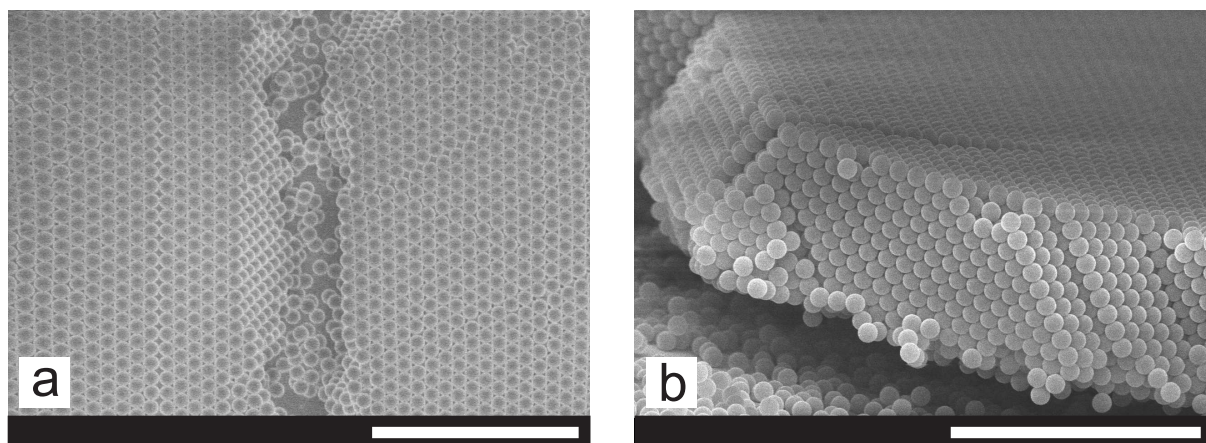


Figure 5.3: SEM images of a colloidal crystal of 377 nm diameter PS spheres on a glass substrate: (a) top view and (b) side view. The crystal was grown by controlled drying and it consists of approximately 12 hexagonal layers parallel to the sample substrate. Note that there appear to be no stacking faults. For image (B), an approximately 5 nm thick layer of a gold/palladium alloy was deposited onto the side of the crystal. Both scale bars are 5 μm .

SEM images of the PS samples confirm that the deposition is mostly crystalline (see Figure 5.3a). Many cracks are present in the PS samples, dividing the crystal in single-crystalline domains with an area on the order of $20\ \mu\text{m} \times 20\ \mu\text{m}$. All these domains have the same orientation, as is the case in controlled drying samples of silica particles. For the latter, the orientational correlation of the domains is explained by assuming that a single-crystal is formed at first. Cracks are then formed upon drying of the solvent. Side views of PS colloidal crystals in SEM indicate that these crystals had approximately 12 layers. These layers are parallel to the substrate, more or less hexagonal and hollow-site stacked. Although it is difficult to determine the exact stacking sequence in SEM, there appear to be no stacking faults in these crystals. Bear in mind that the interaction potential of our PS particles, specifically the Debye-Hückel screening length, may have been different than that of our silica particles.

Several colloidal crystals of PS spheres were partly infiltrated with alumina by ALD to test whether (binary) colloidal crystals of organic particles can be inverted. After ALD, the PS samples were studied by SEM. It is clear from Figure 5.4a that the colloidal particles are still spherical, which means PS can stand ALD at $80\ ^\circ\text{C}$. In Figure 5.4b, the particles seem to be non-spherical, but this is an SEM imaging artefact caused by drift of the SEM stage. It is also clear from Figure 5.4 that the particles in the crystal are overlapping, as the deposited alumina partly fills up the voids in between the spheres. At the contact point of two spheres in a crystal, no alumina can be deposited, causing a dimple/hole in the ALD layer if the two spheres are pulled apart after ALD (Figure 5.4b). After deposition of a thin layer of alumina, the mechanical stability of the alumina frame was tested by burning the original PS spheres. For 377 nm diameter spheres, a layer of alumina of only 12 nm thick results in a self-supporting frame, as can be seen in Figure 5.5a.* Figure 5.5b is a similar image of the same sample,

*Growth of binary colloidal crystals from dispersions of PMMA particles was demonstrated with colloidal spheres having a diameter of approximately $2\ \mu\text{m}$ [201]. In principle, mechanical stability of alumina frames that were fabricated using PS templates of 377 nm diameter spheres is no guarantee for mechanical stability of

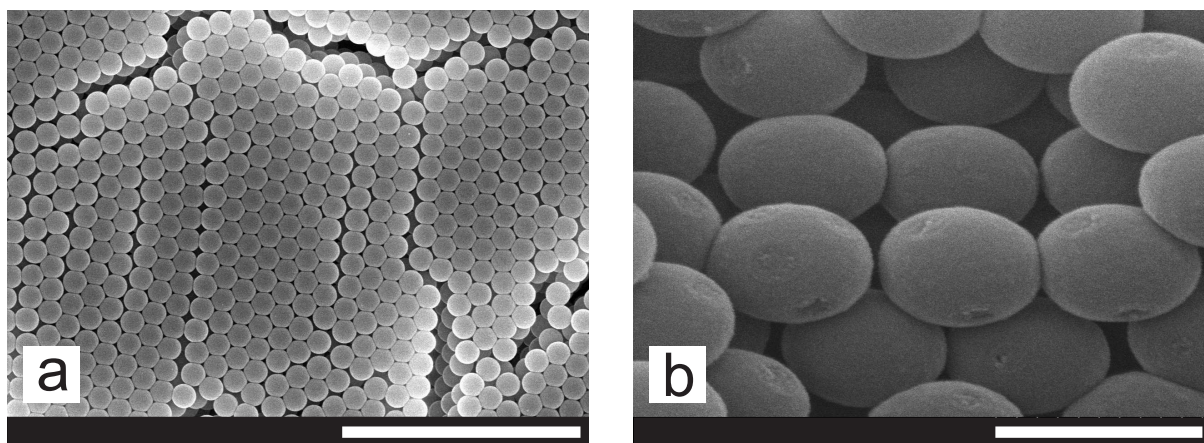


Figure 5.4: SEM (a) top view and (b) side view of a colloidal crystal of 377 nm diameter PS spheres on a glass substrate after ALD of a 12 nm thick, conformal layer of alumina. Note the dimples on the spheres in panel (b) at the points where the spheres touched before ALD. The particles in image (B) seem to be non-spherical, but this is an imaging artefact that is due to drift of the SEM stage. The scale bar in panel (a) is 4 micron, the one in panel (b) is 500 nm, the particles in both images were 377 nm diameter.

at a higher magnification, clearly proving that the PS spheres have been removed by the heat treatment. At the contact point of two spheres in a crystal, no alumina can be deposited, causing connecting holes between air spheres in the crystal upon removal of the PS colloids (see also the dimples in Figure 5.4b). The figure also shows that the alumina frame consists of overlapping shells, that were formed around the PS spheres, thus proving that the PS spheres did not melt during ALD. Furthermore, Figure 5.5a shows that the entire crystal, down to the substrate, has been infiltrated with alumina.

The PS samples were characterized by FTIR spectroscopy as well. At the various stages of the fabrication process, FTIR spectra of the samples were obtained and the position of the first-order (111) Bragg peak was monitored (see Figure 5.6). The spectrum of the PS colloidal-crystal template itself features a first-order (111) Bragg dip of approximately $20\%T$ at 848 nm. Using a volume-averaged refractive index, assuming a refractive index $n_{\text{PS}} = 1.59$ for the PS particles, this wavelength corresponds to an interlayer spacing of 295 nm, which agrees quite well with the interlayer spacing in a close-packed crystal of 377 nm diameter spheres. Analysis of the Fabry-Pérot fringe spacing yields a crystal thickness of 11 interlayer spacings, which means (12 ± 1) layers after correcting for finite-size scattering effects. After ALD of a 26 nm thick layer of alumina, the spectrum no longer features a first-order (111) Bragg dip, though it still shows Fabry-Pérot fringes. As the deposited alumina has nearly the same refractive index ($n_{\text{alumina}} \approx 1.6$) as the PS spheres ($n_{\text{PS}} = 1.59$), the crystal has effectively been refractive-index matched, thus nearly eliminating coherent scattering. However, the refractive-index contrast over the crystal-air and substrate-crystal interfaces is still appreciable, explaining the presence of the Fabry-Pérot fringes.

If the deposited layer of alumina is thinner, the structure is not completely refractive-index-

alumina frames if they are fabricated using PS frames of micron-sized spheres. However, experiments by Xindi Yu at the University of Illinois at Urbana-Champaign (IL, USA) have shown that a 15 nm layer of alumina also yields mechanically stable frames if a PS template of 1 μm diameter spheres is used.

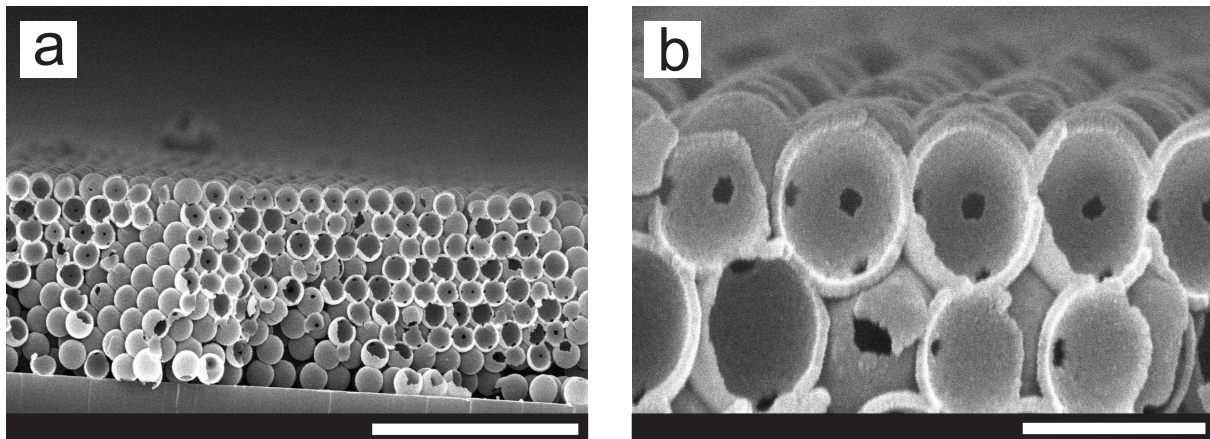


Figure 5.5: SEM side view of (a) a 9-layer colloidal crystal of air spheres in alumina. The colloidal-crystal template, consisting of 377 nm diameter PS spheres, was burnt after ALD of a 12 nm alumina layer. Panel (b) is a similar image of the same sample at a higher magnification. Note the holes in the alumina layer that connect the air spheres (see also the dimples in Figure 5.4b). Approximately 5 nm of a gold/palladium alloy was deposited onto the side of the crystal. The scale bar in panel (a) is 3 μm , the one in panel (b) is 500 nm.

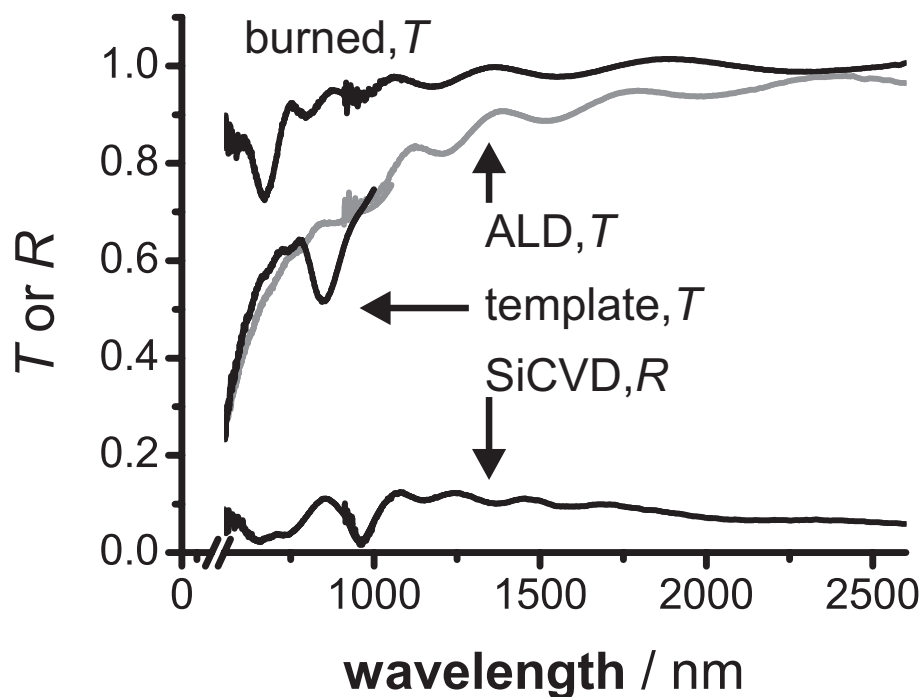


Figure 5.6: FTIR spectra of a colloidal crystal of, originally, 377 nm diameter PS spheres on a glass substrate at different stages of the fabrication process: PS template, (gray) after ALD of a 26 nm thick layer of alumina, after removal of the PS spheres by heating and after infiltration with silicon by CVD. Note that most graphs represent transmission (T) measurements, but some represent reflection (R) measurements.

matched, allowing detection of the Bragg dip after ALD before burning the PS (see Figure 5.7). From the shift of the first-order Bragg diffraction upon ALD, we can extract an estimate of the thickness of the alumina layer that was deposited on the PS spheres in the colloidal crystal. Figure 5.6 shows an FTIR spectrum of a crystal of PS spheres before ALD (black line). The average refractive index $\bar{n} = (1.44 \pm 0.01)$ of the crystal was calculated by averaging the refractive indices of the composite materials by volume ($n_{\text{PS}} = 1.59$ and $n_{\text{air}} = 1$). From the position of the first-order Bragg diffraction at (857.3 ± 1.1) nm, an interlayer spacing $d_{(111)} = (297.7 \pm 2.1)$ nm was extracted using Bragg's law

$$2\bar{n}d_{(hkl)} = m \cdot \lambda_{(hkl)}^{(m)}. \quad (5.1)$$

ALD of a $\Delta t_{\text{ALD}} = 12$ nm alumina layer, as determined by ellipsometry measurements on a cleaned silicon substrate that was in the sample chamber during the same ALD run, caused the first-order Bragg diffraction to shift to (903.7 ± 1.2) nm. Inserting this wavelength into Bragg's law (Equation 5.1), together with the measured value of $d_{(111)}$, resulted in a value for the average refractive index of the interstitial voids $\bar{n}_{\text{voids}} = (1.31 \pm 0.05)$. Averaging the refractive indices of alumina ($n_{\text{alumina}} = 1.59$) and air by volume yielded the ratio of the volume of alumina and the volume of the interstitial voids: $\phi_{\text{ALD}} = (0.53 \pm 0.09)$. Note that deposition of a 12 nm layer of alumina fills up 53% of interstitial space! An estimate of the thickness of the alumina layer Δt_{ALD} can be extracted from ϕ_{ALD} by solving equation

$$\begin{aligned} \phi_{\text{ALD}} &= \left(\frac{\pi\sqrt{2}}{6}\right) \cdot \left([1+x]^3 - 1\right) \\ &\quad - \left(\frac{\pi}{\sqrt{2}}\right) \cdot \left(2[1+x]^3 - 3[1+x]^2 + 1\right) \\ \text{with } x &= \frac{\Delta t_{\text{ALD}}}{R}, \end{aligned} \quad (5.2)$$

which is based on a geometric model of the structure after ALD. The model only assumes that PS spheres and their alumina layers are concentric and that the overlap volume of two alumina layers consists of alumina. Using the graph of $\phi_{\text{ALD}}(x)$ (Figure 5.8), the thickness of the alumina layer according to FTIR spectroscopy was (14 ± 3) nm. Note that this value is in reasonable agreement with the thickness of 12 nm from ellipsometry.

After burning the original PS colloidal-crystal template, the structure is no longer refractive-index matched, not even for thick alumina frames, causing the Bragg dip to reappear in Figure 5.6. The Bragg dip, however, has blue-shifted compared to the case of the PS colloidal-crystal template, for the filling fraction of alumina in the inverse structure is much smaller than the filling fraction of polystyrene in the template.

After infiltration of silicon by CVD, transmission measurements are no longer possible in the visible and near-infrared (NIR), as silicon strongly absorbs light with a wavelength smaller than approximately $1 \mu\text{m}$. That is why the reflection (R) signal in Figure 5.6 drops almost to 0 below a wavelength of $1 \mu\text{m}$, rising again around 850 nm due to Bragg reflections from the first couple of crystal layers that can be probed by unabsorbed light. The red-shift of the Bragg peak is, of course, caused by the enhanced average refractive index after silicon CVD.

As was explained in the introduction, our test experiments on infiltrating PS colloidal crystals using ALD should ensure successful infiltration of PMMA colloidal crystals as well, for the glass transition temperatures of both materials are similar. Of course, ALD on colloidal crystals of PMMA spheres would have been an even better test, as the binary colloidal-crystal

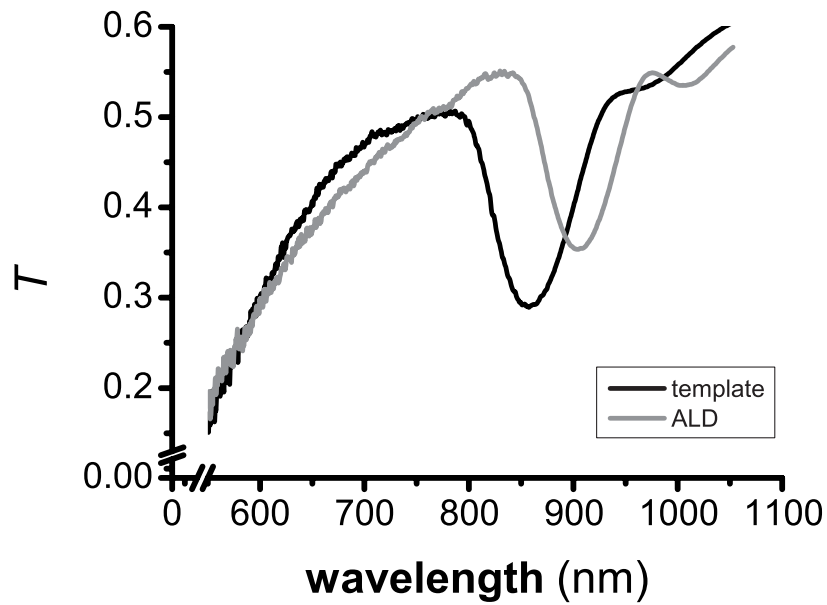


Figure 5.7: FTIR spectra of a colloidal crystal of, originally, 377 nm diameter PS spheres on a glass substrate both before (black) and after (gray) ALD of a 12 nm layer of alumina.

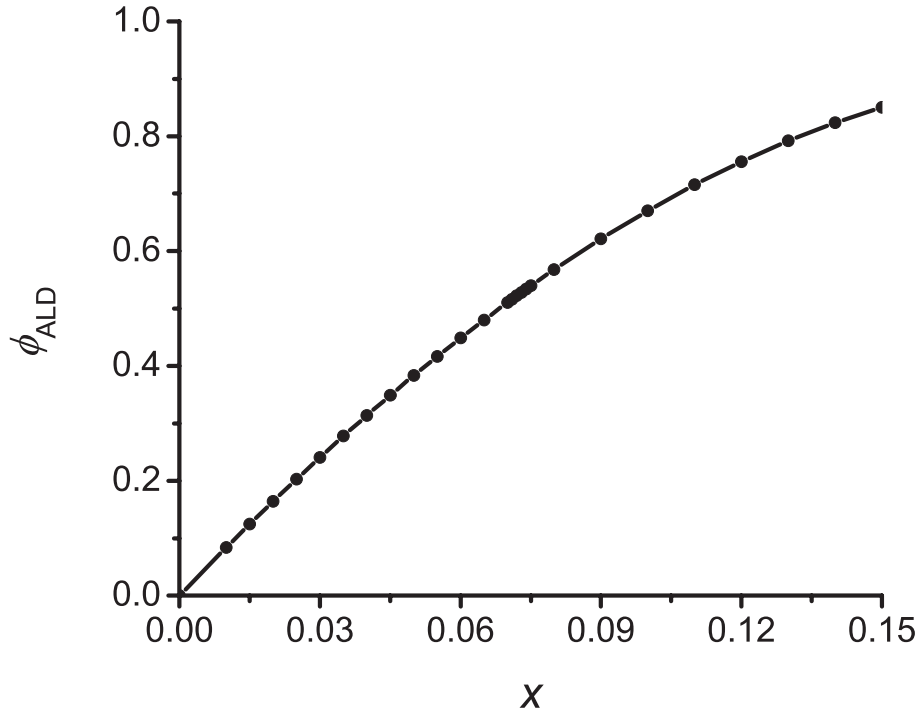


Figure 5.8: Calculated graph of the volume fraction of deposited material in the interstitial voids ϕ_{ALD} of a CP crystal of spheres as a function of the thickness Δt_{ALD} of the deposited layer relative to the radius R of the spheres ($x = \Delta t_{\text{ALD}}/R$). For the functional form of this graph, see Equation 5.2.

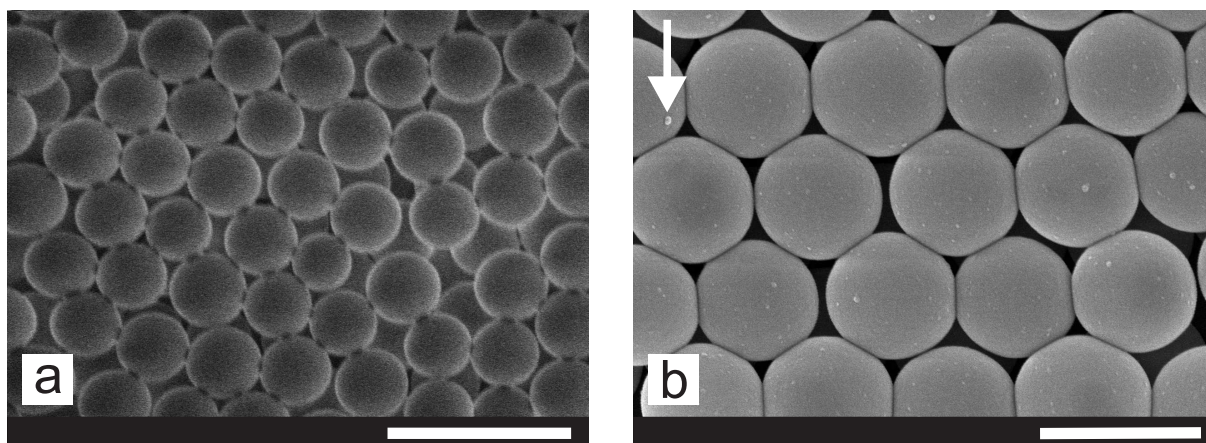


Figure 5.9: SEM top views of sediments of approximately 750 nm diameter PMMA spheres on a glass substrate (a) before and (b) after ALD of a 12 nm thick alumina layer. Note the contamination with small ($\lesssim 25$ nm) particles on top of the colloidal particles (see white arrow). The sample in panel (b) was coated with approximately 5 nm of a gold/palladium alloy. The scale bar in panel (a) is 2 μm , the one in panel (b) is 1 μm .

templates were also fabricated using PMMA spheres [201]. Unfortunately, we have not been able to grow colloidal crystals of PMMA spheres by controlled drying. The hexane in which the PMMA particles are dispersed probably does not wet the surface of the glass substrate well enough. All the same, infiltrating colloidal crystals of PMMA spheres with alumina by ALD *will* reveal whether PMMA melts during ALD or not. Figure 5.9 shows SEM images of sediments of approximately 750 nm diameter PMMA spheres on a glass substrate, both before and after ALD. It is clear in Figure 5.9b that alumina has been deposited in the sediment, for some of the spheres are apparently overlapping. These were probably touching PMMA spheres that are now overlapping due to the additional alumina layer that was deposited onto them. Most importantly, the PMMA particles are still spherical, which means that PMMA does not melt during ALD.

5.3.2 Future challenges

Two problems were encountered during our ALD experiments. First of all, as shown in Figure 5.9b, small ($\lesssim 25$ nm) particles could sometimes be found on the colloidal crystals after ALD of an alumina layer. The size and number of these ‘dust-like’ particles seems to depend on the specific values of the ALD parameters and on the way the sample chamber is pumped/vented before/after the ALD process. Moreover, these dust-like particles seem to appear only in SEM top views of our samples, not in side views. This suggests that these particles are formed in the sample chamber during ALD and are subsequently deposited onto the sample. Suspending the sample upside-down will probably not alleviate this problem, as the dust-like particles are so small that they will be dragged along in gas flows. Fine-tuning the ALD process parameters will probably be the only way to avoid the formation of these dust-like particles. However, no effect of these particles on, for example, FTIR spectra has been observed, which is due to the fact that they are much smaller than the typical wavelength of light.

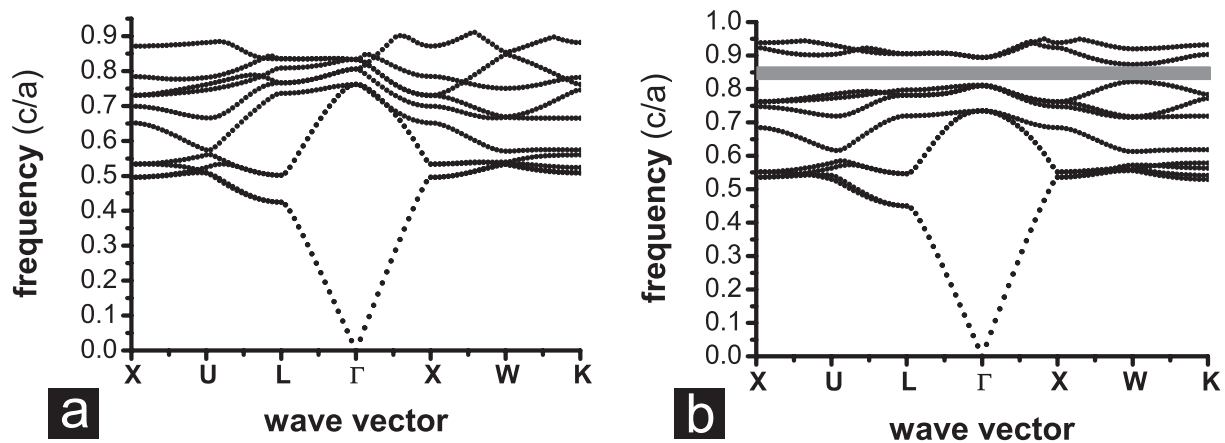


Figure 5.10: Calculated (MPB) photonic band diagrams for (a) an FCC crystal after ALD of alumina, removal of the original PS template and partial silicon infiltration, and (b) an FCC crystal after silicon infiltration and removal of the original silica template. If 350 nm diameter spheres are used for the template, the inner silicon layer, alumina layer and outer silicon layer in (a) all have a thickness of 15 nm (see text for further details). For panel (b), if 350 nm diameter spheres are used in the colloidal crystal template, the silicon layer would have a thickness of 30 nm. Note that there is a gap between bands 8 and 9 in panel (b) but not in panel (a).

Secondly, after ALD of alumina and removal of the original PS or PMMA template, the refractive-index contrast can be enhanced even further by infiltration with silicon by CVD. However, the inside volume of the air spheres left behind by the burnt PS or PMMA spheres is then available for the disilane CVD precursor gas as well, causing deposition of silicon on the outside *and* on the inside of the air-sphere cavities. Unfortunately, MPB calculations have shown that the presence of the alumina layer and the inner silicon layer closes the gap between bands 8 and 9 for inverse FCC structures (see Figure 5.10), basically because light no longer ‘sees’ the structure as bicontinuous.

5.3.3 Etching crystals of silica colloids

As was mentioned in the introduction, it is also possible to grow binary crystals from a bi-disperse dispersion of silica spheres having a specific size ratio [201]. Although a silica template can be infiltrated with silicon without an intermediate ALD step, the growth of these binary, sodium chloride (NaCl) colloidal crystals is often accompanied by a layer of colloidal fluid on top of the crystals. Because of its isotropic scattering, it is essential for photonic applications that such a layer of colloidal fluid is removed. In this section, we present preliminary measurements on attempts to remove crystal layers of colloidal crystals of silica spheres with two different etching techniques: plasma and tape etching.

Before etching, the colloidal silica crystals looked like typical crystals grown by controlled drying (see Chapter 4). Thus, no layer of colloidal fluid was present in this case. After etching using a CHF_3/Ar -plasma, the exposed crystal surface looks severely damaged, especially if it is compared with a part of the crystal that was not exposed to the plasma during etching (see Figure 5.11a). Not only SEM reveals the damage, it is also clear from the corresponding optical

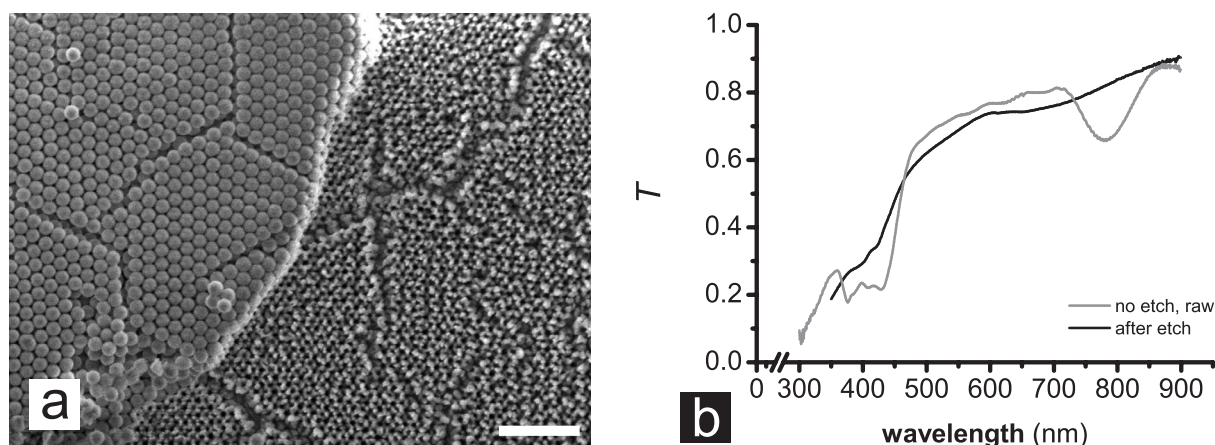


Figure 5.11: (a) SEM top view of a colloidal crystal of 347 nm diameter silica spheres on a glass substrate after plasma etching. The sample consisted of approximately 11 hexagonal layers parallel to the sample substrate, approximately 1.5 of which were removed by etching. In the lower right part of the image, the top of the crystal after etching is visible. The upper left part of the image is probably a piece of crystal that broke off and turned over after plasma etching. During the etching process, the colloids in this layer would then be shielded from the plasma by the layers above, explaining why they appear to be undamaged. The scale bar is $2\ \mu\text{m}$. (b) Optical transmission spectra of the same colloidal crystal (gray) before and (black) after plasma etching. Because of the damage that the top layer suffered during etching the first-order (111) Bragg dip has disappeared. Some features of the second-order peak are still visible.

spectra that crystals etched with a plasma undergo severe morphological changes (see Figure 5.11b). All the same, some of the features of the second-order (111) Bragg dip are visible, possibly because they correspond to scattering by layers that are not parallel to the exposed (111) plane(s).

We think that a directional plasma etch will not be successful in removing layers of colloidal crystals, if no mechanism is introduced to terminate etching after 1 or 2 (crystal) layers [67, 80], because the surface of the crystal is not a flat, homogeneous slab of dielectric material. During etching, some parts of the crystal layer below the top layer can still be shielded from the plasma by what is left of the spheres on top, while other parts are already being etched. If so, plasma etching of colloidal crystals could work if etching of the second layer is prevented while the top layer is being etched.

Although shielding of the layer below the top layer during plasma etching of the top layer itself might sound complicated, it can actually be realized quite easily. For example, the polymer that is used to immobilize colloidal particles in body-centered tetragonal (BCT) crystals (see Chapter 6) turns out not to be affected by the plasma that was used for silica etching (see Figure 5.12). If, after UV-polymerization, the silica spheres of the top layer stick out of the polymer network in which the colloids have been fixed, these spheres can be etched by a plasma etch without the polymer network being destroyed (Figure 5.12). The polymer itself, in turn, can be etched using an oxygen plasma that does not affect the silica particles.

As the plasma is drawn towards the sample by an anode just above the sample itself, etching is directional in this particular plasma etcher. This means that only the polymer between the

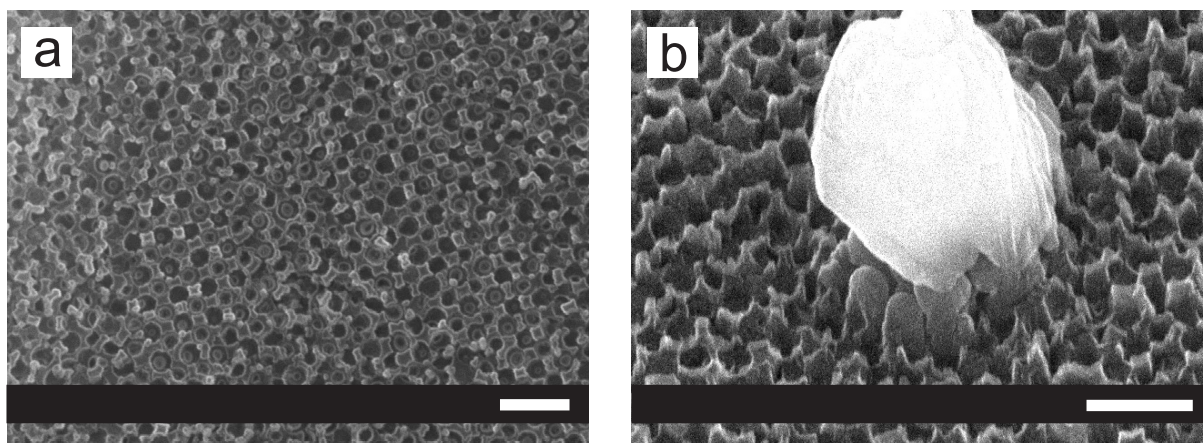


Figure 5.12: SEM top views of a colloidal crystal of 336 nm diameter silica spheres in a polymer network on a glass substrate after plasma etching. It is clear from panels (a) and (b) that the polymer is hardly affected by the plasma, therefore acting as an etching stop. The plasma has removed the spheres in the top layer of the sample, leaving behind the polymer sockets of those spheres. Objects on top of the sample, such as dust particles, can block the plasma, as was clearly the case in panel (b). Both scale bars are 1 μm . Images courtesy of Yu Ling Wu.

spheres of the top 2 or 3 layers is etched during a plasma etch, as the polymer in the layers below is shielded by the silica particles of the top few layers. Combined with this shadow effect, the two different plasmas for silica and polymer, CHF_3/Ar and O_2 respectively, can be used to etch away the fluid layer on top of colloidal-crystal templates of silica spheres. If the polymer overfills the crystal, a plasma etch can be used to etch away the superfluous polymer, thus exposing the top silica spheres. These silica spheres will eventually stop the etching of polymer due to the shadow effect. Subsequently, the top part of the silica template can be removed by a silica plasma etch, which will be stopped because of shielding by the polymer. Next, the exposed polymer can be removed again by a polymer plasma etch and so on. Note that, because the polymer is removed from more than 1 layer at the same time, this scheme may result in the loss of 1 or 2 crystal layers of silica spheres if the polymer is used as a stop for the silica etch.

Although this scheme may succeed in etching the top fluid layer, it is a laborious route, especially if the fluid layer of colloids is thick. In that case, multiple polymer and silica plasma etches are required. With typical reaction times of 15 minutes for etching 1 crystal layer of silica spheres, etching thick depositions of silica will take quite some time, even more so because the plasma chamber needs to be cleaned with an additional oxygen etch when switching between the two different gas mixtures for silica and polymer etches. Therefore, a faster etching method would be more than welcome. In two recent papers [217, 218], Zhang *et al.* mention that crystal layers can be peeled off colloidal crystals using adhesive tape. Although we only tried it once, the results are promising, as can be seen in Figure 5.13. We have not checked yet in spectroscopy how many layers were actually peeled off by tape etching, but the SEM images seem to indicate that at most 2 layers were removed. In some places, it seems as if no layers were removed, in other areas 1 or 2 layers were removed.

This patchy removal is probably due to specifics of the tape etching procedure. In our test

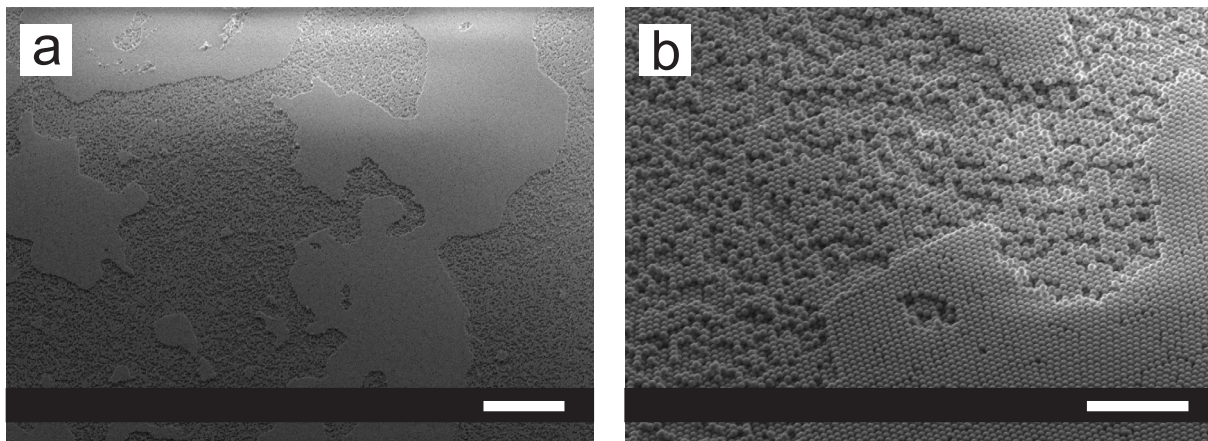


Figure 5.13: Scanning electron microscopy (SEM) top views, at a tilt angle of approximately 45° of a colloidal crystal of 347 nm diameter silica spheres on a glass substrate after removal of 1 or several of the top layers using adhesive tape. Before tape etching, the sample consisted of approximately 13 hexagonal layers parallel to the sample substrate. Panels (a) and (b) differ only in the magnification used during imaging. The white scale bar in panel (a) is $20\ \mu\text{m}$, the one in panel (b) is $5\ \mu\text{m}$.

experiments, we gently laid down the adhesive tape on top of the colloidal crystal, after which it was gently tapped with a single finger over the entire area of the sample. Next, the tape was removed from the sample in a single pull. Some colloids were definitely removed from the sample, as a white deposition could be discerned on the tape by eye. However, the tapping probably caused the tape to adhere with different strengths to different areas of the colloidal crystal. After laying down the tape on top of the sample, it may be better just to give it one single stroke with the thumb to let the tape adhere to the colloidal particles more homogeneously. It may require some tuning, but we think crystal layers can be removed by tape etching one by one. Whether it will also work for fluid layers on top of colloidal crystals remains to be checked experimentally. Fortunately, tape etching is fast and cheap, so multiple tests can be performed quite quickly.

5.4 Conclusions and outlook

In this chapter, we have investigated methods to invert colloidal crystals that should be compatible with (binary) colloidal crystals consisting of organic particles. The latter have recently been described in literature as candidates for the fabrication of strongly photonic crystals. Unfortunately, these relatively new templates also lead to new challenges in the post-fabrication towards 3-D materials with a photonic band gap. Some of the colloidal-crystal templates have to be grown from dispersions of polystyrene (PS) or poly(methyl methacrylate) (PMMA) spheres. The refractive-index contrast in such organic templates cannot be enhanced by chemical vapor deposition (CVD) of silicon directly, because that infiltration method requires temperatures of approximately $350\ ^\circ\text{C}$, which is far above the glass transition temperatures of PS and PMMA ($\sim 100\ ^\circ\text{C}$). Other binary templates can be grown from dispersion of silica colloids, therefore allowing infiltration with high-index materials by CVD, but these templates often have a layer

of colloidal fluid on top. Because of its isotropic scattering, this fluid layer has to be removed before further processing can take place.

For the colloidal-crystal templates of PS or PMMA spheres, we have shown that atomic layer deposition (ALD) is a promising infiltration technique. The original template can be burnt after ALD of an approximately 15 nm thick layer of alumina, yielding a self-supporting alumina frame. Subsequently, the mechanically stable alumina frame can be used for further processing, such as infiltration with silicon by CVD. All the same, two problems are left to be tackled. First of all, silicon will also be deposited on the inside of the air-sphere cavities left behind by the burnt template spheres, causing the remaining air spheres to be smaller than at close-packing. MPB calculations have shown, for example, that this will close the photonic band gap in inverse FCC structures. Furthermore, dust-like particles with a size of approximately 10 nm are deposited onto the samples during ALD, which might be circumvented by fine-tuning the ALD process parameters. We expect, however, that such small particles will not have a major influence on the optical properties of these photonic crystals.

Furthermore, we attempted to remove crystal layers of templates consisting of silica colloids by plasma etching. The plasma causes significant damage to the top of the crystal, leaving behind a surface that seriously deteriorates its optical properties. If the silica template is embedded in a polymer matrix, successive treatments with plasmas that etch either the polymer or the silica can in principle be used to etch the template in a layer(s)-by-layer(s) fashion. However, this is a laborious and time-consuming route, partly because the plasma chamber has to be cleaned with an oxygen etch in between successive plasma treatments. Although the experiments were preliminary in nature, etching colloidal crystals of silica spheres with adhesive tape seems promising. It may require some tuning of the experimental procedure, but it is a much faster and cheaper method. After some additional tuning, it may work just as well for other types of particles, including PS and PMMA. As tape etching is of no use after infiltration with silicon or germanium, for example, the possibility of ultramicrotomy should be considered [142, 219–221].

Acknowledgements

Carlos van Kats is gratefully acknowledged for providing the PMMA spheres. I would also like to thank Prof. Paul Braun for letting me work in his group at the University of Illinois at Urbana-Champaign (IL, USA) for several weeks. My sincere gratitude has been earned by Erik Nelson (ALD, CVD, SEM), Xindi Yu (ALD, SEM, FTIR, ellipsometry) and Dr. Florencio García Santamaría (ALD, FTIR, CVD), owing to their assistance during my experiments in Illinois. Chris Rétif and Yu Ling Wu are acknowledged for assistance during the plasma-etching experiments. Finally, I would like to thank Dannis 't Hart and Teun Vissers for critical reading of this chapter.

Electric-field-induced photonic colloidal crystals

Photonic crystals are materials with a refractive index that varies periodically in space. Because of their strong interaction with light, they can provide unprecedented control over the emission and propagation of light. A promising route towards three-dimensional (3-D) photonic crystals is self-assembly of colloidal particles. In this chapter, we show that large crystals can be grown by sedimentation of colloidal particles in an external, high-frequency electric field. The method results in body-centered tetragonal (BCT) crystals that do not have a layer of colloidal fluid on top. In addition, the electric field can be used as an external control to switch between close-packed (CP) and BCT crystal structures within seconds. Since the BCT crystal structure is not close-packed, we also developed two procedures to invert it without loss of structure. Both methods involve immobilization of the colloidal particles by means of polymerization of the surrounding solvent mixture, either by diffusion-polymerization or by photo-induced polymerization. We even infiltrated the BCT crystals with silicon using chemical vapor deposition (CVD), though this leads to some damage at the bottom of the crystal. Finally, we show that light scattering can be used to monitor the 3-D structure of colloidal crystals over macroscopic areas in real time.

6.1 Introduction

Materials with a periodic modulation of refractive index on the (sub)micron scale interact strongly with light and can exhibit a photonic band gap, the optical analogue of the electronic band gap in semiconductors [7, 8, 16–18]. Colloidal suspensions of monodisperse microspheres that self-organize into periodic structures having the lowest free energy, analogously to atomic crystals, are promising as three-dimensional (3-D) photonic materials [8, 68, 81, 108, 114, 222–224]. Most photonic applications require periodic structures with a lower filling fraction of the component with the highest refractive index. This can be achieved by preparing ‘wet’ colloidal crystals with a high particle volume fraction and inverting the lattice by drying the crystal, re-infiltrating it with a high-index material and ultimately removing the solid spheres by etching or burning [223].

Colloidal crystals with a high volume fraction can be made by allowing colloids in suspension to sediment in gravity and densify. When colloids interact with each other as hard spheres, or as slightly charged spheres having a hard-core plus a repulsive interparticle interaction, the resulting equilibrium structure is a face-centered cubic (FCC) crystal. However, for hard spheres, the difference in free energy between FCC and hexagonal close-packed (HCP) structures is very small [225]. In experiments, this often gives rise to random-hexagonal close packing (RHCP), an uncontrolled mixture of FCC and HCP crystal stackings [154, 226, 227]. The latter is undesirable, because the photonic properties of, for example, FCC crystals deteriorate upon the introduction of stacking faults [75].

In addition, self-assembled colloidal sediments always contain, for entropic reasons, a layer of colloidal fluid on top and are thus never completely crystalline [227, 228]. The colloidal-fluid layer typically has a thickness that is equal to of a couple of interlayer spacings of the crystal on which it rests. Alternatively, the popular method of convective assembly [67, 77] uses capillary forces to grow large and complete crystals, but generally produces twinned crystals [76]. For these reasons, preparing large single-domain crystals is challenging and necessitates the use of external fields, such as structured surfaces in colloidal epitaxy [78] or flow fields [81]. External *electric* fields have been used in various ways: direct-current (DC) electrophoresis to accelerate gravitational settling [229], low-frequency electrohydrodynamics to create close-packed structures in systems of charged colloids [230, 231] and dielectrophoresis to create two-dimensional crystals [232].

Recently an external, high-frequency (1 MHz) electric field was used to switch between close-packed (CP) and body-centered tetragonal (BCT) crystal structures in a colloidal suspension of fluorescently labelled, silica microspheres in a refractive-index-matching solvent mixture [137]. The use of a high-frequency electric field has the advantage that it polarizes the dielectric core of the colloidal particle and not its double-layer. The dipole moments that are thus induced in the particles add a dipolar term to the interaction potential of the particle. If the field strength is large enough, the mutual dipolar interaction will dominate over the steric or electrostatic repulsion, thus favoring the formation of BCT over FCC structures [137, 138, 175, 176]. As the dipole moments are induced in the dielectric core of the particles, the method works for both charged and uncharged particles.

To increase the interaction of light with photonic crystals fabricated from colloidal-crystal templates, the refractive-index contrast in such structures needs to be increased. If the index contrast is high enough and the template has the right structure, a photonic band gap could be

opened up this way. In a purely dielectric FCC crystal, an index contrast at optical frequencies of $\delta_n = (n_{\max}/n_{\min}) > 2.9$ and an “inverse lattice” ($n_{\text{medium}} > n_{\text{spheres}}$) configuration are required to open a photonic band gap [31, 65, 66]. According to Tao *et al.*, a band gap is also possible for purely dielectric, inverse BCT crystals for $\delta_n > 3.96$ [139], although our calculations indicate that there is no band gap for such BCT structures (Section 2.5). Note that restrictions on crystal symmetry dictated by such contrast requirements are possibly less strict for metallodielectric structures [32]. Even if no band gap can be opened up, there exist applications, including photonic sensors [222], where a stop gap is all that is required. For most applications, a thickness of 10 lattice constants is sufficient [75, 210], but a macroscopic lateral extent is beneficial.

In this chapter, we demonstrate that external, high-frequency electric fields can be used to grow colloidal crystals with a body-centered tetragonal (BCT) crystal structure for the fabrication of photonic materials. The homogeneity of the electric field, in combination with a procedure that involves annealing out defects by repeated sedimentation while ramping the field, results in large, $\sim \text{mm}^2$ colloidal crystals. Because the BCT structure is not close-packed, we also developed a procedure to invert it without loss of structure, which involves immobilization of the colloidal particles by means of diffusion-polymerization. More specifically, the colloids are dispersed in a solvent that contains a low volume fraction of monomer. Dispersed particles are immobilized when the monomer gets cross-linked. The procedure is rather lengthy, for it takes 7 to 12 days for dissolved monomer components to diffuse from the edges to the center of the sample cell. Immobilized crystals can be inverted without loss of structure by infiltration with a UV-curable monomer. Alternatively, after solvent evaporation, immobilized crystals can be infiltrated with silicon by chemical vapor deposition (CVD), though this leads to some damage at the bottom of the crystal.

In addition, we present here a fast and robust fabrication method for colloidal BCT crystals that is based on photo-induced polymerization of a solvent mixture containing monomer [100]. Not only does photo-induced polymerization allow immobilization of the colloids at almost every stage of the fabrication of colloidal-crystal templates, it also reduces the time that is required to grow one crystal sample from 7 to 12 days to approximately 4 hours! We also show results on infiltrating such BCT structures with silicon by CVD.

In this chapter, we mainly rely on confocal and electron microscopy for the characterization of colloidal crystals at various stages of their fabrication. However, in Section 6.5, we show that light-scattering experiments can provide complementary, 3-D structural information. For example, the external electric field can be used in our experimental system to switch between CP and BCT crystal structures within seconds. This means we can switch Bragg reflections “on” and “off” within seconds! We show that scattering is an excellent tool to monitor such macroscopic, structural changes in real time.

6.2 Experimental methods

6.2.1 Sample fabrication involving diffusion-polymerization

Colloidal suspensions were composed of core-shell silica particles (3% polydispersity) in a refractive-index-matching, liquid mixture of water and dimethyl sulfoxide (88.4 wt-% DMSO). The spheres had a 193 nm radius silica core that was fluorescently labelled. It was surrounded

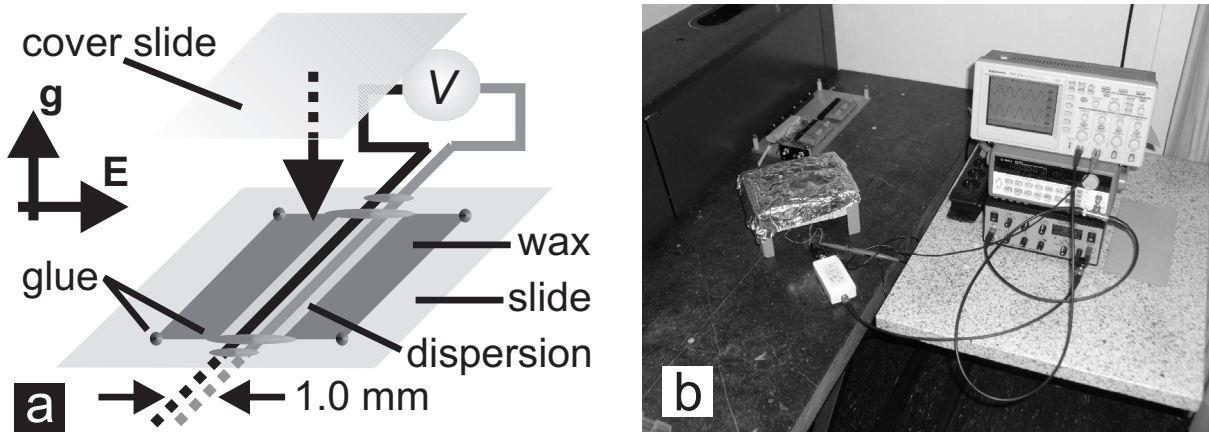


Figure 6.1: (a) Schematic picture of the sample cell geometry in which colloidal BCT crystals were grown by sedimentation in a high-frequency, external electric field. Note that, for reasons of image clarity, gravity is pointing upwards in panel (a). Panel (b) is a photograph of the electronic setup that was used to generate the external electric field. To avoid premature, photo-induced polymerization, the sample itself was covered with a box.

by a non-fluorescent shell of thickness 492 nm (transmission electron microscopy, TEM). The total radius was 702 nm (static light scattering, SLS). In the absence of an electric field and added salt, the particles did not strictly interact as hard spheres, for the interparticle spacing a was $1.0 \cdot \sigma$ to $1.06 \cdot \sigma$, where $\sigma = 2R$ is the total diameter of the particles. However, under the conditions of this experiment, but without an electric field, the behavior found for this system was consistent with the behavior of hard spheres [227]. The core-shell architecture allows three-dimensional (3-D) position determination without ambiguity, even for touching spheres, via fluorescent confocal microscopy [89, 99].

From the above-mentioned dispersions, colloidal crystals were fabricated by the following procedure. Two lengths of 50 μm diameter electrode wire (Goodfellow T2 Thermocouple Alloy Ni95/(Al+Mn+Si)5) were placed parallel atop a clean 25 mm \times 75 mm \times 1 mm microscope slide, 1.1 mm or 1.25 mm apart, and glued under tension using Bison Epoxy Rapide (the gluing points were outside the sample area). Contacts were made to insulated electric wires using silver epoxy or tin solder. A clean cover slide was placed atop the wires, which thus also served as sample spacers, and glued down at the 4 corners. The edges parallel to the wires were sealed with high-density wax (White Microcrystalline Wax 863, Frank B. Ross Co. Inc.): half a pellet (roughly 3 mm diameter) was placed on each edge and made to carefully fill the sample up to the closest wire by melting the wax using a hotplate. Next, a drop of colloidal suspension was placed at one of the open ends of the sample. Capillary forces caused the dispersion to fill the sample cell, after which the open ends were glued with a two-component adhesive - Bison Epoxy Rapide. The epoxy resin of this adhesive is based on bisphenol A - epichlorohydrin with an average molecular weight < 700 g/mol [233]. The main ingredient of the hardener is N(3-dimethylaminopropyl)-1,3-propylenediamine. This sample ensured a controlled geometry for the slow dissolution and subsequent (re)polymerization of the epoxy.

Large single-domain, field-aligned crystals were made as follows. The electric field was applied between the two electrode wires (for a description of the electronic setup, see Section

6.2.2). During colloidal sedimentation, the voltage was ramped up to its final value in 5 steps. Prior to each increase in field strength, the sample was turned over for 10 s, during which the field was turned off. The final value of the peak-to-peak (pp) voltage that was applied across the electrode wires was approximately $250 V_{pp}$. This repeated sedimentation, while not an optimized procedure, was seen in this work to successfully anneal out defects in the structure. Moreover, it increased both crystallite size and the orientational correlation between different crystallites. After the final field strength was reached, it took 7 to 12 days for the dissolved epoxy to reach the middle of the sample cell and (re)polymerize, thus immobilizing the particles.

6.2.2 Sample fabrication involving photo-induced polymerization

The dispersions used in these preparations consisted of core-shell silica spheres [91, 190, 191] with a total diameter of $1.1 \mu\text{m}$ and a polydispersity of 3%, as determined by static light scattering (SLS). The approximately 400 nm diameter silica cores of all the particles were labelled with fluorescein isothiocyanate (FITC). The particles were dispersed in a 10.1 vol-% solution of trimethylolpropane ethoxylate triacrylate (Aldrich, average molecular weight = 428 g/mol) in dimethyl sulfoxide (DMSO, Aldrich, > 99.6%). Next, 10 μl of a 1.0 vol-% solution of photo-initiator 2-hydroxy-2-methyl-propiophenone (Aldrich, 97%) in DMSO was added to 50 μl of the dispersion. The resulting dispersion was used for crystal growth. The final number of crystal layers parallel to the sample substrate depends on the crystal structure, the diameter of the particles, the field strength, the sample geometry and so on. We note that, if the sample cell that is described below was used, a particle volume fraction of approximately 16% resulted in BCT crystals of 20 to 25 crystal layers for $1.1 \mu\text{m}$ diameter spheres.

Body-centered tetragonal (BCT) crystals were fabricated from the above-mentioned dispersions by sedimentation onto a glass cover slide (Menzel-Gläser, #1 cover slip, ca. $150 \mu\text{m}$ thick) in an alternating-current (AC) electric field (see below) perpendicular to gravity [109, 175]. Crystals were grown in a sample cell that is similar to the one described in Section 6.2.1 (see Figure 6.1a), although the spacing between the electric spacer wires was 1.0 mm to 1.2 mm. During sedimentation of the colloids onto the sample substrate, the peak-to-peak voltage across the wires was typically $(100 \pm 2) V_{pp}$. After 15 minutes to 30 minutes, the voltage was increased to $(200 \pm 2) V_{pp}$. The stepwise increase of the voltage was continued until a voltage of $350 V_{pp}$ to $400 V_{pp}$ was reached. Colloidal particles in the sample were subsequently immobilized by illumination with UV-light (UVP, UVGL-58, 365 nm, 6 W) for 2 minutes at a distance on the order of a centimeter.

The electronic setup that was used for the generation of external electric fields has undergone several improvements during the research described in this chapter. Figure 6.1b shows a photograph of a typical example of the final electronic setup. The setup that was used in the fabrication of the colloidal BCT crystal presented in Figure 6.7 is provided below. A Hewlett Packard function/arbitrary-waveform generator (33120A, 15 MHz) was used to generate an AC, sinusoidal voltage signal with a frequency of (1.000 ± 0.005) MHz. This source signal was amplified by a wideband amplifier (Krohn-Hite Corporation, model 7602M). Any DC signals coming from the amplifier were short-circuited by a home-made DC-filter. Using this combination of amplifier and DC-filter, the peak-to-peak voltage across the wires was amplified up to a maximum of $400 V_{pp}$. In the fabrication of colloidal BCT crystals involving diffusion-

polymerization, the DC-filter was not used yet. Peak-to-peak voltages and frequencies of sample signals were measured using a digital, real-time oscilloscope (Tektronix TDS224) via a 10x probe (Tektronix P2100). A second input of the oscilloscope was used to probe the signal coming from the function generator, which was used for the triggering of the oscilloscope.

6.2.3 Infiltrating crystals with silicon

After fabrication of a colloidal BCT crystal in solution, the solvent (mixture) was allowed to evaporate, after which the sample was opened up, removing the cover slide with the colloidal crystal from the 1 mm thick microscopy slide. Before infiltration, the crystals were typically heated up in an oven to 425 °C to 500 °C, at an average rate of 100 °C/h at most. They were kept at the final temperature for at least 3 h in order to remove the polymer network, which was found to inhibit infiltration of the crystal layers below the top layer in some cases. Infiltration of the resulting colloidal-crystal templates was performed using chemical vapor deposition (CVD) [234]. Disilane (Si_2H_6) was used as the precursor gas. In the CVD run for the sample in Figure 6.14, for example, gas flows of 10 sccm for the disilane gas and 100 sccm for the hydrogen gas were used. The temperature at the sample was approximately 450 °C, the pressure was 0.020 mbar, and the reaction duration was 300 min. The CVD process resulted in the deposition of amorphous silicon, which has a refractive index that is slightly larger than that of crystalline silicon (3.59 instead of 3.5 [235]).

6.2.4 Sample characterization

Confocal microscopy measurements were performed using a Leica TCS SP2 or TCS NT confocal scan head mounted on a Leica DM IRB inverted microscope. After solvent evaporation, crystal samples were index matched by infiltration with a mixture of water and DMSO (80 vol-% DMSO) or a mixture of water and glycerol (87 vol-% glycerol). Typically, a Leica PL APO 100x (1.4 NA) oil-immersion objective was used, in combination with Cargille immersion oil (type B). The FITC in the cores of the particles was excited using the 488 nm line of an Ar laser. Dry and infiltrated crystals were (additionally) characterized, uncoated, using a Philips XL30FEG scanning electron microscope (SEM), operating at an accelerating voltage of 2 keV to 5 keV and a working distance of approximately 5 mm to 7 mm.

Some confocal microscopy measurements were calibrated by imaging a calibration slide in the same measurement session. The slide that was used for calibrating measurements in the confocal xy -plane, which is the plane perpendicular to the optical axis of the microscope, contains crossed micrometer scales that are oriented orthogonally (Ted Pella Inc, product number 2280-16, 1 mm in 0.010 mm divisions). The relative calibration of the two crossed micrometer scales was checked in a laser diffraction experiment, indicating that the two orthogonal scales do not differ by more than $(0.5 \pm 0.35)\%$. In other words, if calibrated distances, measured along the x and y -axis in our confocal microscopes, differed by more than 1%, the difference was significant.

In a typical laser diffraction experiment, a green HeNe laser (Melles Griot, maximum output 5 mW at 543.5 nm) acted as the source. After reflection off a mirror, the beam was passed through an aperture in a screen to catch the back-reflected diffraction pattern of the sample. To avoid stray light, care was taken to make the diameter of the pinhole slightly larger than the

beam diameter of approximately 1 mm. Using the zero-order reflection of the laser beam, the sample was aligned perpendicular to the primary beam. The transmitted and diffracted light were collected at the backside of the sample by a white sheet of paper, acting as the detector screen. Because the sheet of paper is not very thick, of the order of 0.1 mm, Bragg reflections could easily be observed at the backside of the sheet. A Nikon D70 single-lens reflex (SLR) digital camera with a Nikkor AF-S 18 mm to 70 mm lens was used to capture images of the diffraction pattern using various shutter times. If the transmitted, primary beam was allowed to hit the detector screen, the spot was usually so bright that other Bragg reflections were no longer visible in the digital image. Therefore, the primary beam was blocked by a circular, black piece of paper that was taped to the front side of the detector screen. Both the detector screen and the digital camera were aligned perpendicular to the primary beam by eye. To image the internal structure of a single Bragg reflection, a particular diffracted beam was reflected directly onto the charge-coupled device (CCD) detector of the digital camera using a mirror at the backside of the sample.

Transmission spectra were measured with a Varian Cary 5, double-grating, UV-Vis-NIR spectrophotometer. For these measurements, machine parameters included a step size of 0.5 nm and a spectral bandwidth of 2 nm. The spectrum in Figure 6.11 was taken with a similar, empty sample cell in the reference beam. The cross-sections of both the sample and the reference beam were reduced to approximately 1 mm diameter using one aperture per beam. All spectra were measured against 0%*T* and 100%*T* baselines, which were taken in the same experimental session. The baselines were measured without the samples but with the pinholes in both the sample and the reference beams.

6.3 Results and discussion – diffusion-polymerization

Figure 6.3A is a region of a two-dimensional (2-D), confocal *xy*-scan of the bottom hexagonal plane of an approximately 7-layer, body-centered tetragonal (BCT) crystal grown as described in Section 6.2.1. Adjacent spheres were nearly touching, but only their fluorescent cores are visible. Figure 6.3B is a projection of all hexagonal planes in the crystal showing the characteristic 2-layer bridge-site stacking. A model projection (Figure 6.3B, inset) shows 2 adjacent $(110)_{\text{conv}}$ hexagonal-packed planes of gray or white spheres, respectively, of a BCT crystal (see also Figure 6.2). The spheres in both layers are nearly touching, but they have been drawn smaller for clarity. The symmetry of the observed projection corresponds well with the model.* A slice in the *xz* plane (Figure 6.3C) shows the stacking of the BCT $(110)_{\text{conv}}$ planes.

The crystalline order over macroscopic areas of the colloidal BCT crystals is demonstrated in Figure 6.3D, which shows a He-Ne laser diffraction image. The 1 mm diameter beam was positioned in between the electrode wires. The BCT structure shows a rectangular symmetry that is distinct from the high 6-fold symmetry seen in diffraction patterns of FCC or HCP structures. An additional, striking feature of the diffraction pattern is the presence of vertical stripes that connect, for example, the (10ℓ) & (01ℓ) and $(1\bar{1}\ell)$ & $(\bar{1}1\ell)$ reflections. They are probably

*When we used low-ionic-strength 16 MΩcm water, analysis by 3-D particle position determination showed that the crystal was slightly non-tetragonal and in actual fact face-centered orthorhombic (FCO), whereas the crystals were perfectly tetragonal when 2 MΩcm water was used. As the deviation from the tetragonal case was rather small, we will continue calling our crystals BCT in this chapter.

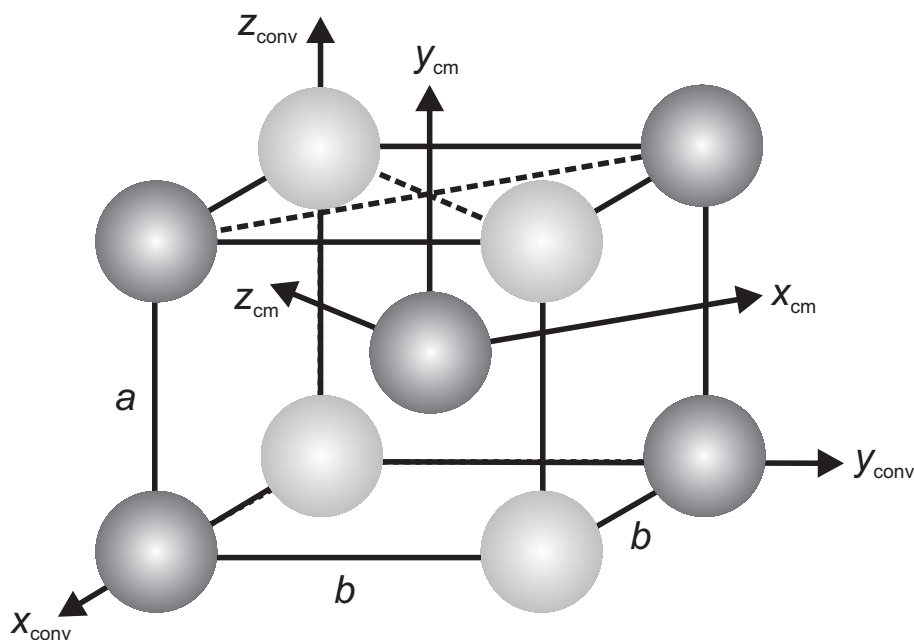


Figure 6.2: Schematic picture of the conventional unit cell for the BCT structure in real space. The conventional laboratory frame is labelled $(x_{\text{conv}}, y_{\text{conv}}, z_{\text{conv}})$, the coordinate frame in confocal microscopy is labelled $(x_{\text{cm}}, y_{\text{cm}}, z_{\text{cm}})$. For $b/a = (\sqrt{6}/2)$, the $(110)_{\text{conv}}$ plane, which is indicated by the dark gray spheres, has hexagonal symmetry. The spheres have not been drawn to scale for clarity.

caused by the fact that the lines of touching particles in a hexagonal $(110)_{\text{conv}}$ plane, along the y -direction in Figure 6.3A, are not exactly straight - they are slightly wiggling. Furthermore, the four reflections of the $(2\bar{1}\ell)$ -family seem to be slightly too far from the direct beam, the latter was blocked by a beam stop, which is due to refraction of the diffracted beams at the sample-air interface and to the curvature of the Ewald sphere (Section 6.5). Diffraction images taken as a function of position in the sample exhibited an orientational correlation that spanned the extent of the sample (2.4 cm) and that was much larger than the extent of one single crystallite. Large-area crystalline order was also clear from the nearly uniform Bragg color coming from such BCT crystals under white-light illumination (Figure 6.4). Only a small part of the crystal had a slightly different orientation, which resulted in a blue instead of a red Bragg color.

The BCT crystal structure is not close-packed and cannot be preserved simply by drying because of its vulnerability to capillary forces. We immobilized the “wet crystals” by means of a diffusion-polymerization process to create a low-volume-fraction polymer gel that was strong enough to keep the particles in place while drying. First, we utilized the slow solubility of a two-component adhesive (applied at the sample edges) in the solvent mixture of water and dimethyl sulfoxide. The epoxy dissolved and polymerized in the solution over a period of 7 to 12 days. This process was limited by diffusion of the monomer components of the epoxy. The remarkable feature of this “pre-polymerization” step is that a polymer network is created slowly, such that possible strain that builds up during diffusion-polymerization does not destroy the BCT crystal. Yet, the resulting polymer network is strong enough to allow drying and refilling with liquids or a polymer. Next, we carefully cleaved the cell into two halves. One half was used to produce the scanning electron micrograph of the pre-polymerized and dried BCT

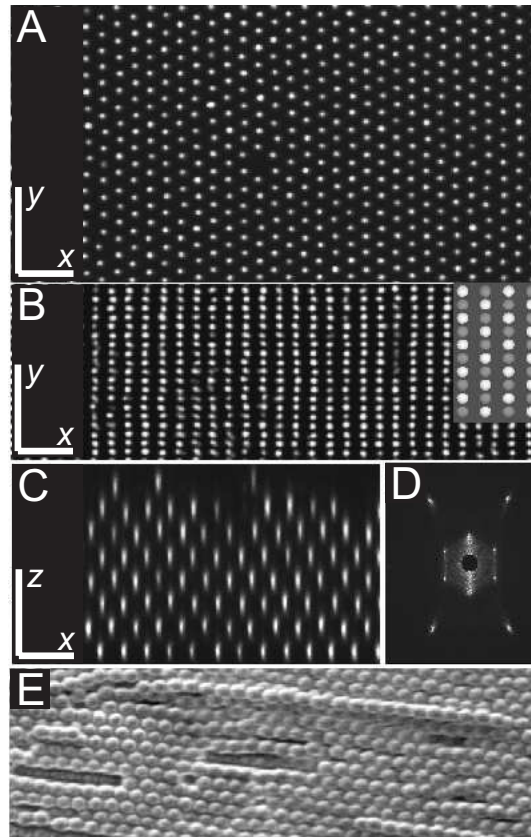


Figure 6.3: A 7-layer, electric-field-induced BCT crystal. (A) A $42 \mu\text{m} \times 22 \mu\text{m}$ (including the label area) xy_{cm} optical slice, with the electric field along y_{cm} and gravity along z_{cm} , of an in-focus hexagonal $(110)_{\text{conv}}$ plane. Neighboring spheres are nearly touching, but only the fluorescent cores are visible. (B) A projection of all the hexagonal planes in the BCT crystal. When the images of 2 adjacent hexagonal close-packed layers are overlaid, the projection exhibits rectangular symmetry, while those of close-packed crystals (not shown here) exhibit the higher 6-fold symmetry. The inset shows 2 model hexagonal planes that have been overlaid, with gray and white spheres corresponding to different hexagonal layers, and the circles drawn smaller; at actual size adjacent gray spheres (and white spheres) would be touching. (C) An xz_{cm} scan shows the 2-layer periodicity in stacking. Thus, the projection of the entire crystal along the z_{cm} direction in a BCT crystal is identical in symmetry to the 2-layer projection. (D) A laser diffraction picture (beam diameter 1 mm) of a pre-polymerized BCT crystal shows the characteristic rectangular symmetry. (E) An electron micrograph of a BCT crystal that has been immobilized by the diffusion-polymerization procedure shows clearly that the BCT order is preserved in dry form. The coordinate labels in this figure refer to the confocal coordinate frame (Figure 6.2).

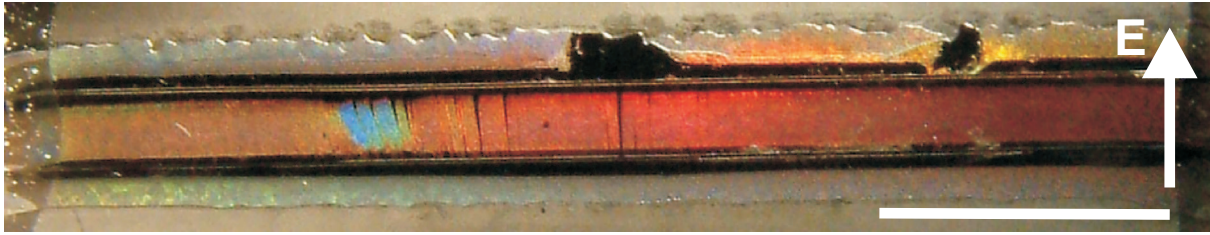


Figure 6.4: Photograph of Bragg colors coming from an approximately 7-layer, colloidal BCT crystal under white light illumination. The crystal consists of $1.4 \mu\text{m}$ diameter silica spheres. After fabrication in solution, the colloids were immobilized using the diffusion-polymerization procedure. The blue colored area corresponds to a crystallite that had a slightly different orientation with respect to the electric field vector than the red colored area. The white scale bar is 0.5 cm.

crystal (Figure 6.3E) - one sees successive $(110)_{\text{conv}}$ lattice planes of a BCT crystal.

To demonstrate that we could turn our dried BCT crystals into ones with an ‘inverse’ contrast, we filled the other half of the dried, pre-polymerized cell with a UV-curable epoxy (Norland Optical Adhesive NOA 73, viscosity 130 cP). Filling and subsequent polymerization did not perturb the structures. Figure 6.5A shows single-domain BCT order in a projection, through the sample bulk, of images in which consecutive hexagonal planes were in focus. The sample was cured in ultraviolet light while on the microscope stage. We verified the absence of particle motion during this process. Figure 6.5B shows an image (time-averaged over 930 s) of an immobile, and hence well-resolved, in-focus hexagonal layer after the UV cure. Finally, we removed the top plate of the sample and imaged (Figure 6.5C) the immobilized structure of an incomplete layer with a scanning electron microscope (SEM). This layer was originally complete and in the sample bulk, but it was torn apart while taking apart the sample. Spheres in polymer-inverted BCT crystals touch along the field direction (Figure 6.5C). No polymer network can be formed at the contact point of two such spheres. After removal, they will leave behind two connected air spheres. Thus, all the spheres could have been dissolved by hydrofluoric acid, as in the creation of air-sphere FCC crystals [67], for the acid could have penetrated the entire crystal via the connecting holes.

Unfortunately, BCT crystals of air spheres in a polymer network have a relative modest dielectric contrast ($\epsilon_m/\epsilon_p \approx 1.5$) [236]. To obtain strongly photonic materials, the BCT template should be infiltrated with a material having a high refractive index, such as silicon or germanium. As is shown in Figure 6.3E, the pre-polymerization immobilizes colloidal spheres in BCT crystals in a polymer matrix that is strong enough to preserve the BCT structure upon solvent evaporation. We attempted to infiltrate these non-close-packed colloidal-crystal templates with amorphous silicon. Samples were first heated up to 425°C in air to burn away the polymer in the interstitial space. After this heat treatment, samples were infiltrated with amorphous silicon by chemical vapor deposition (CVD).

Figure 6.6 clearly shows that the infiltration of BCT crystals was successful. The interstitial space in between the spheres has partly been filled with silicon, because of which the colloidal building blocks of the crystal seem to be hexagonal instead of spherical. After infiltration, the sample was broken in two pieces. Figure 6.6B is an SEM image of the side of one of the pieces of the cleaved BCT crystal. The crystal has clearly been infiltrated with silicon all the way

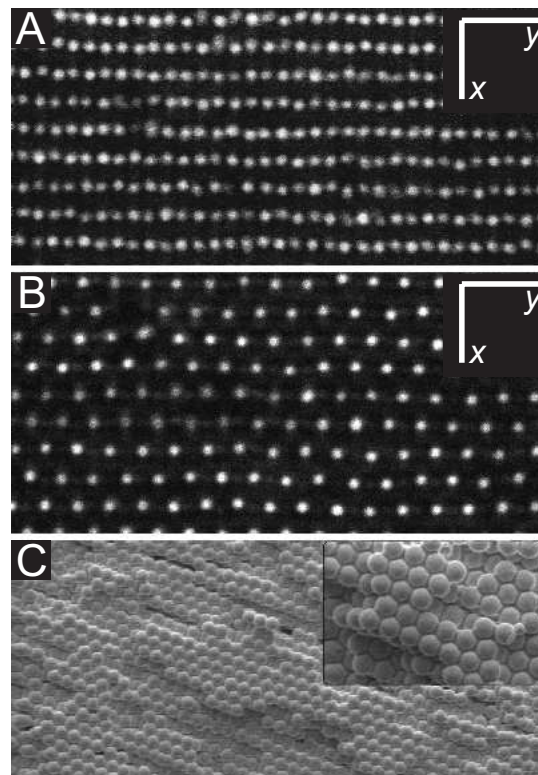


Figure 6.5: (A) After refilling the dried BCT sample with UV-curable epoxy, the resulting structure is still BCT, as evidenced by the projection of all the hexagonal layers in the crystal. (B) The time-average of a single hexagonal plane over 930 s shows that the spheres are indeed stationary. (C) Scanning electron microscopy (SEM) images (magnified region in inset) show the characteristic BCT stacking with adjacent hexagonal layers shifted by half a lattice spacing in the direction of the bead-chains. The coordinate labels in this figure refer to the confocal coordinate frame (Figure 6.2).

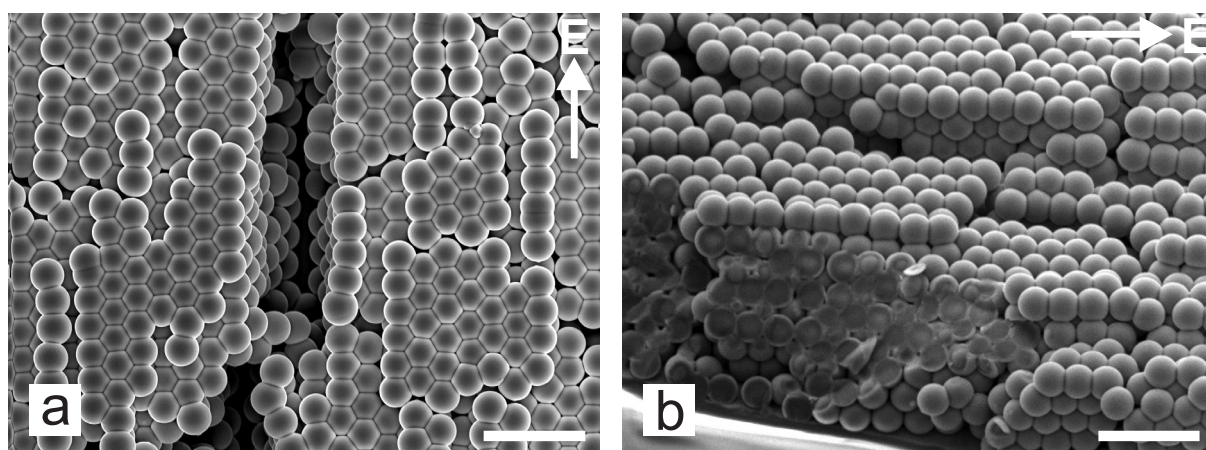


Figure 6.6: SEM images of a colloidal BCT crystal of $1.4\ \mu\text{m}$ diameter silica spheres on a #1 glass cover slide, after infiltration of the crystal with silicon. The top view through a crack (a) shows that the crystal consists of approximately 7 layers. The incomplete, 8th layer on top provides some information on the stacking of the top layers, which is mostly (BCT) bridge-site stacking. Although care has to be taken with images of crystal cracks, it seems as if the bottom 2 layers of the crystal are shifted out of register, being (CP) hollow-site stacked. After cleaving, side-views can be imaged in SEM, at a tilt angle of 45° in panel (b). The spheres have been covered with a layer of silicon, all the way down to the substrate, which is especially clear for spheres that have been cut in two and at places where part of the silicon layer has broken off. The white scale bars in both panels are $5\ \mu\text{m}$.

down to the substrate. A striking feature of infiltrated crystals is that spheres are often cut in half upon cleaving of the sample. Although we have not performed a thorough investigation, we think it may be analogous to the cutting of glass using scissors. If one tries to cut glass in air, it will splinter, whereas cutting is possible if the piece of glass is suspended in water. In infiltrated colloidal crystals, the silicon absorbs vibrations, causing the silica spheres to be cut in two instead of breaking off.

6.4 Results and discussion – photo-induced polymerization

The diffusion-polymerization procedure that is described in the previous section (6.3) turned out to be slightly less robust than we thought at first. Attempts to reproduce the results with $1.1\ \mu\text{m}$ instead of $1.4\ \mu\text{m}$ diameter silica spheres failed. Because of the smaller sphere size, stronger electric fields were required to grow BCT crystals. Unfortunately, the colloidal particles could then no longer be immobilized in the BCT structure within 2 weeks using the diffusion-polymerization procedure. Sometimes, only a small part of the sample would polymerize, sometimes it would only polymerize after switching off the field (resulting in CP instead of BCT crystals). Although we have not thoroughly investigated this issue, we think the diffusion-polymerization may depend on spurious direct-current (DC) signals coming from the amplifier in our electric setup. After all, a typical sample capacitance on the order of $100\ \text{pF}$, which is mainly caused by the coaxial cables connecting the sample to the amplifier, is a heavy load for the amplifier at $1\ \text{MHz}$. Increasing the field strength to compensate for the smaller

sphere size may have changed the amplitude of these spurious DC signals, thus causing the pre-polymerization to fail, possibly because of hydrolysis reaction products. To eliminate the dependence on spurious DC signals, the electronic setup for the fabrication procedure involving photo-induced polymerization was extended with a DC-filter that basically short-circuited DC signals.

Not only did we require a more robust fabrication method for colloidal BCT crystals, we also wanted to reduce the fabrication time, for 7 to 12 days is rather impractical. Photo-induced polymerization seemed to match our purposes perfectly, both because of the speed of the polymerization reaction and the ability to initiate polymerization at nearly any stage of the fabrication process. The idea is that colloids are dispersed in an organic monomer (TMPTA), which is polymerized upon release of radicals by a photo-initiator. The initiator itself is excited by illumination with UV-light. Colloidal crystals can be immobilized using pure monomer as a solvent, as reported by Jiang *et al.* [80]. However, we were not able to grow BCT crystals of 1.1 μm diameter silica spheres in TMPTA with our electronic setup. Probably, the dielectric constant of TMPTA at 1 MHz is very close to the dielectric constant of silica ($\epsilon \approx 4.4$ [237]). If the spheres are nearly matched to the solvent at 1 MHz, the induced dipole moments will be very small, causing CP crystals to be energetically more favorable than BCT crystals [138].

Because of the low dielectric constant of TMPTA at 1 MHz, we decided to switch to solvent mixtures of dimethyl sulfoxide (DMSO) and TMPTA. DMSO is a good solvent for many organic substances and it has a relatively high dielectric constant at 1 MHz ($\epsilon \sim 45$ [238]). Therefore, DMSO is the perfect solvent for TMPTA in BCT crystal-growth experiments. An additional advantage of using solvent mixtures of DMSO and TMPTA (approximately 90:10 vol-%) is that the solvent becomes slightly less photo-sensitive, significantly reducing the chance of polymerization by illumination with room light (fluorescent tubes). Preferably, the volume fraction of DMSO is as high as possible, thus maximizing the dielectric contrast with the colloidal particles. We note, however, that if solvent mixtures with less than 10 vol-% of TMPTA are used, they might not be able to immobilize the colloids.

6.4.1 Characterization by confocal microscopy

Although particles could be immobilized by illuminating the samples for only 2 minutes with UV-light, which means the polymerization took place within 2 minutes instead of the 7 to 12 days for diffusion-polymerization, we were able to grow BCT crystals that looked, at first sight, similar to those grown by means of the diffusion-polymerization procedure. As was explained in the previous section (6.3), our colloidal BCT crystals consist of ABAB, bridge-site stacked, hexagonal layers that are parallel to the sample substrate. The substrate itself is perpendicular to gravity during crystal growth and subsequent polymerization of the solvent. As expected, the confocal image of the bottom layer of such a crystal in Figure 6.7a has hexagonal symmetry, which is even more obvious from the fast-Fourier transform (FFT) of the image (see Figure 6.7). Note that up to 4 orders are visible in all directions in the FFT, which is 1 order more than in a typical FFT of a layer of a convective-assembly colloidal crystal, though these are usually extracted from SEM instead of confocal microscopy images [77]. Keep in mind that the decrease in intensity in higher orders is not only due to crystal imperfections, it is partly due to the form factor of the (fluorescent) spheres as well.

One of the advantages of real-space imaging over scattering data is that microscopic infor-

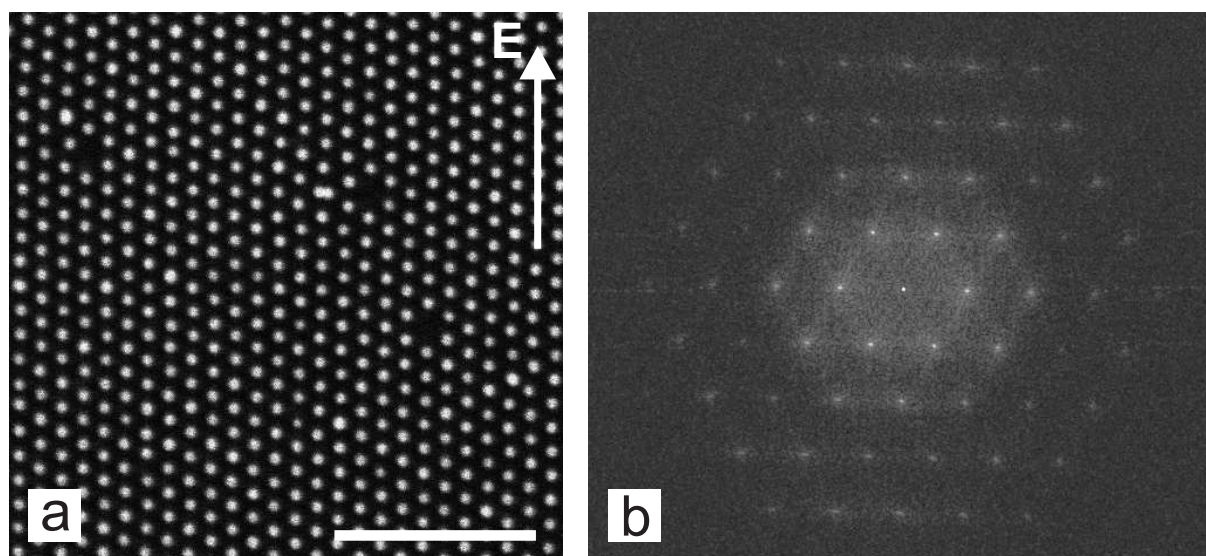


Figure 6.7: Average of 4 confocal xy -images (a) of the bottom layer of a colloidal BCT crystal, after immobilization by means of photo-induced polymerization. The crystal had approximately 25 layers and consisted of core-shell silica spheres with a diameter of $1.1 \mu\text{m}$, but only the 400 nm diameter cores were fluorescently labelled. The bottom layer displays hexagonal symmetry, which is also very clear from the fast-Fourier transform (FFT, panel (b)) of the confocal xy -image of which panel (a) is just a part. The white scale bar in panel (a) is $10 \mu\text{m}$.

mation is obtained. For example, although Figure 6.7a clearly shows hexagonal ordering in our colloidal BCT crystals, it also reveals the presence of vacancies and dumbbell particles, which is very difficult to deduce from reciprocal-space data. The image also proves that dumbbells do not necessarily disturb crystalline order in their direct neighborhood. This is contrary to our experience with convective assembly, where dumbbells almost always lead to line defects. The difference is probably due to the fact that BCT crystals are grown and immobilized in solution, where the interparticle spacing is approximately 6% to 10% larger than the particle diameter. In convective assembly, on the other hand, crystals grow upon solvent evaporation, leading to structures in which the particles are truly touching. In that case, polydispersity and dumbbells have a much larger effect on local crystal quality.

Colloidal BCT crystals grown via the diffusion-polymerization procedure have been shown to consist of slightly deformed hexagonal layers (see Chapter 7) [100]. Small-angle X-ray scattering (SAXS) and confocal microscopy measurements agreed that the hexagonal layers are compressed along the direction of the external electric field. To further compare the two fabrication methods, the compression of the bottom layer of a BCT crystal fabricated using photo-induced polymerization, part of which is shown in Figure 6.7a, was determined by calibrated confocal microscopy measurements. From the raw measurements, a compression of $(1.3 \pm 0.2)\%$ was extracted by counting more than 30 lattice spacings both parallel and perpendicular to the field direction. From the tracked coordinates of the particles in a 3-D confocal scan spanning 20 layers, a compression of 2.0% was determined [239]. Right after the confocal measurements, the xy -plane of the confocal microscope was calibrated using crossed micrometer scales. According to these calibration measurements, the confocal microscope underesti-

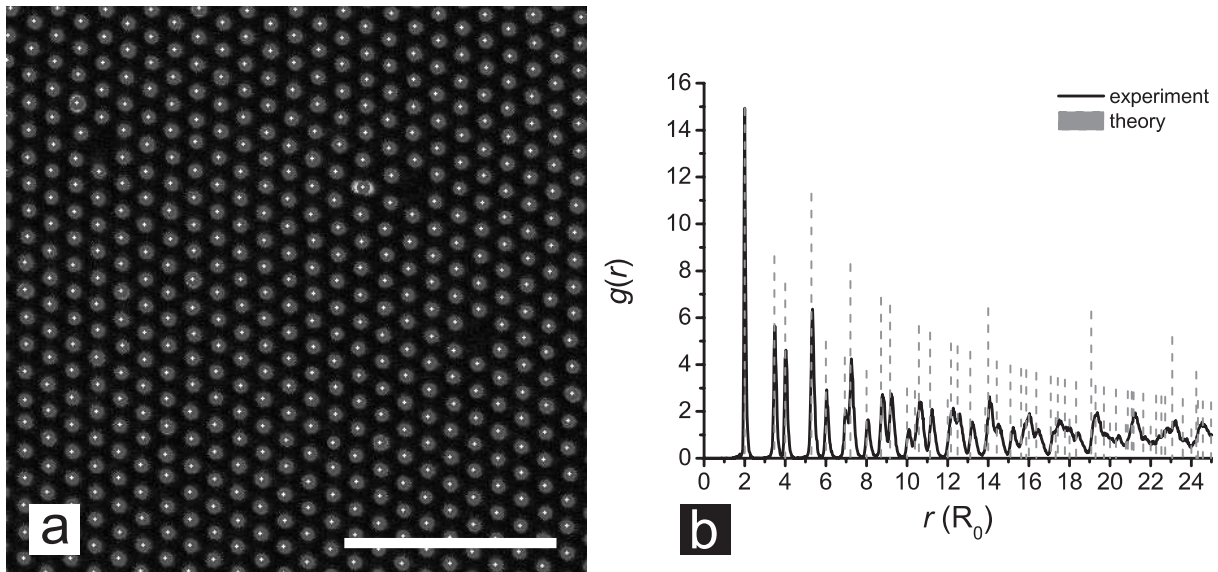


Figure 6.8: (a) Tracked coordinates of the particles in figure 6.7a. Panel (b) shows the radial distribution function $g(r)$ of the hexagonal bottom layer of this BCT crystal. It was calculated from tracked coordinates of the particles (~ 2682) in the confocal xy -image of which panel (a) is just a part. The radial distance r is given in units of half the lattice spacing (R_0). In this case, R_0 was determined by setting the position of the first peak in $g(r)$ at $2R_0$. The experimental $g(r)$ is compared with the theoretical $g(r)$ for an ideal hexagonal crystal layer. The first peak of the theoretical $g(r)$ was normalized to the height of the first peak of the experimental $g(r)$, but it has been drawn slightly higher for clarity. The white scale bar in panel (a) is $10 \mu\text{m}$.

mated the compression by a factor of 1.015, resulting in a final compression along the direction of the external electric field of, respectively, 2.8% and 3.2%.

The (nearly) hexagonal ordering in the bottom layer, part of which is shown in figures 6.7a and 6.8b, can be quantified using order parameters, such as the radial distribution function $g(r)$ [101]. In principle, the radial distribution function only applies to systems that are isotropic and homogeneous, such as colloidal fluids. Crystals are not truly isotropic and homogeneous systems, but $g(r)$ is still a sensible, physical quantity for crystals. After all, $g(r)$ is a measure of the probability to find a particle at a distance r from another particle. In an ideal crystal, this probability is 0 for some values of r , whereas it is non-zero only for specific lattice spacings. In other words, the $g(r)$ of an ideal crystal consists of a number of delta peaks at very specific distances, corresponding to lattice spacings. The height of the delta peaks decreases upon increasing r , as the number of combinations of lattice vectors yielding a specific value of r increases slower than the area for increasing values of r . For very large distances, the $g(r)$ of a physical crystal converges to 1, because the value of $g(r)$ is normalized to the value in an ideal gas.

Figure 6.8a shows part of a confocal xy -image of the bottom layer of a colloidal BCT crystal - it is actually the same part of the image that is shown in Figure 6.7a. Using image-analysis procedures, written in Interactive Data Language (IDL), the coordinates of all ~ 2682 particles in the original image were tracked. Figure 6.7a was overlaid with the coordinates of the tracked particles, each coordinate being represented by a circle, resulting in Figure 6.8a. From

the coordinates of all ~ 2682 particles, the radial distribution function $g(r)$ in Figure 6.8b was calculated. The agreement with the calculated $g(r)$ for an ideal hexagonal crystal layer is excellent. First of all, the positions of the peaks match almost perfectly up to $20R_0$, which is $10\times$ the lattice parameter. Not only the positions, the relative heights of the peaks also match really well, although the decrease in peak height with increasing r seems to be somewhat steeper for the physical crystal than it is for the ideal hexagonal layer. The most important feature of the experimental $g(r)$ curve is that it really drops to 0 in between lattice spacings, even if the lattice spacings are quite close in distance (such as the second and third peak). The curve drops to 0 for up to 6 lattice spacings, whereas the $g(r)$ for convective-assembly crystals usually drops to 0 only between the first and second peak [240]. The main difference between the experimental and the calculated curve is, of course, that the peaks of the experimental $g(r)$ are broader than the delta peaks of the calculated one. There are at least two reasons for this peak broadening. First of all, Brownian motion of the colloidal particles gets frozen-in upon polymerization, because of which they regularly deviated from their ideal lattice position during confocal microscopy. Secondly, dispersions that were used for crystal growth were never truly monodisperse. We think, however, that polydispersity does not contribute as much to peak broadening as Brownian motion in our BCT crystals. After all, the latter consisted of fairly monodisperse, electrostatically stabilized silica particles with an additional dipolar interaction. In suspension, the colloids in a crystal typically had a lattice parameter that was approximately 6% to 10% larger than the diameter of the particles. For nearly monodisperse systems, it has been shown that polydispersity does not destroy long-range order in colloidal crystals, but that need not be true for polydisperse systems.

In Section 6.3, we explained how projections of hexagonal layers along the optical axis of the confocal microscope (the z -axis) can be used in combination with vertical xz -slices to determine the 3-D structure of colloidal crystals. Figure 6.9c is a projection of the bottom 7 layers of the same crystal that was presented in Figure 6.7, revealing bridge-site stacking of the hexagonal layers. In combination with the ABAB stacking sequence that is observed in the confocal xz -slice in Figure 6.9a, we conclude that the crystal indeed had a BCT structure. However, it was not a perfect BCT crystal. A projection of layers 8 to 15 looks very similar to Figure 6.9c, but the projection of all 15 layers clearly indicates that some parts of the two crystal blocks were shifted with respect to one another. In specific directions, a grazing view of Figure 6.9a the reason for this shift becomes clear - there were wedge defects in the crystal. One of them is located between layers 7 and 8 in Figure 6.9a. A wedge defect is formed when 2 layers move slightly apart along z , allowing a third layer to shift in between them like a wedge. In this sample, such defects caused the crystal layers parallel to the sample substrate to ‘wobble’, which was even worse for layers 15 to 25. In total, the crystal had approximately 25 layers. Apart from the wedge defects, the xz -scan also shows 3 vacancy defects.

The vertical xz -slice in Figure 6.9a not only reveals the stacking sequence of the crystal, it also indicates that the particles were really stationary after polymerization of the surrounding solvent mixture. The image is actually the average of a series of 10 xz -slices, taken in a time span of approximately 13 s. If the particles had still displayed Brownian motion, with a typical self-diffusion time on the order of 10 s, they would have moved significant distances in between scans, appearing blurred in the average image. Except for a lower noise level, the averaged image looks the same as a single xz -scan, proving that the particles were truly stationary. The particles do look elongated along the z -direction, but this is due to the point-spread function of

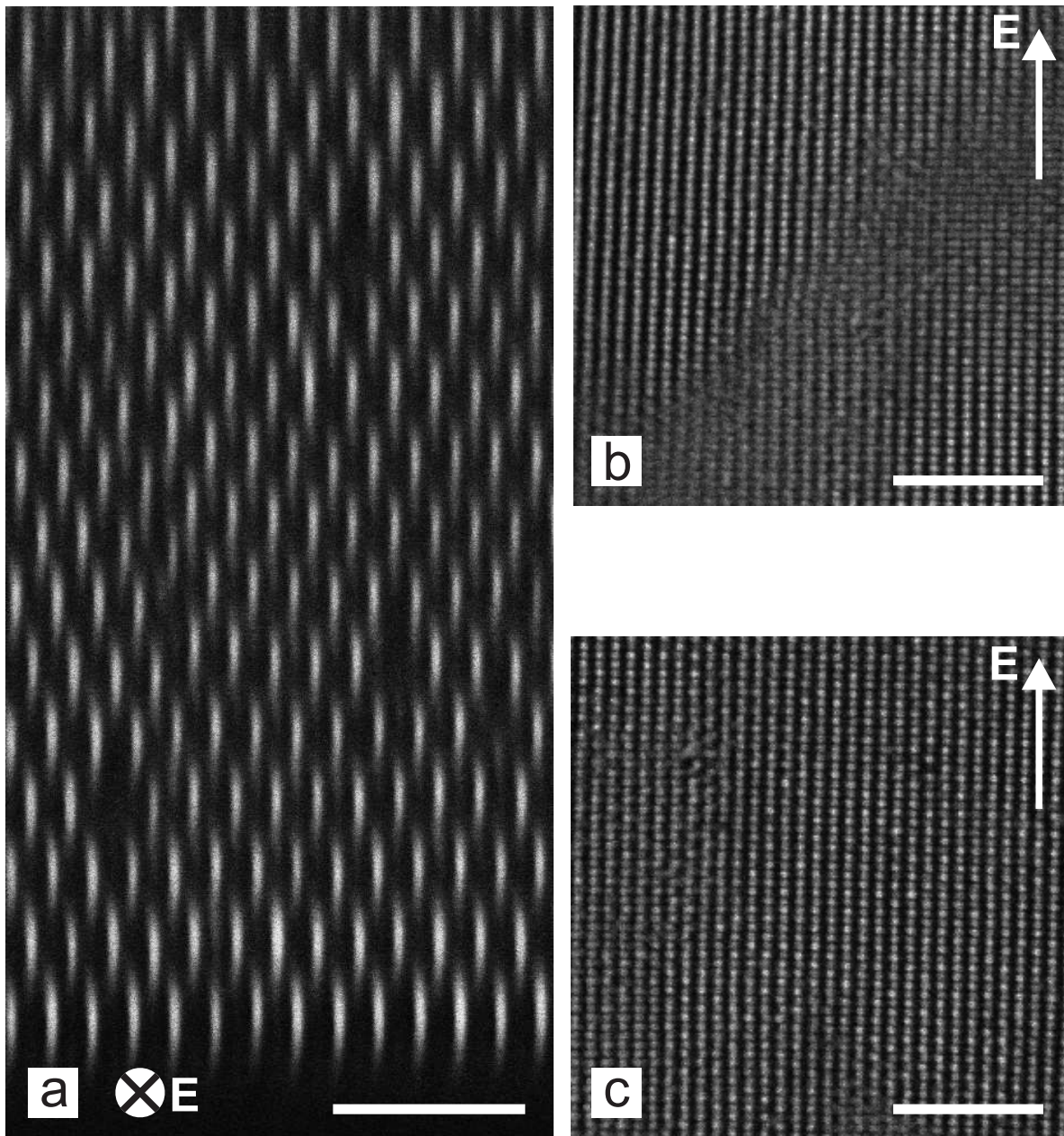


Figure 6.9: (a) Average of a confocal xzt -scan, spanning 10 frames, of an approximately 25-layer, colloidal BCT crystal after photo-induced polymerization. The crystal consisted of core-shell silica spheres with a diameter of $1.1\ \mu\text{m}$, but only the $0.4\ \mu\text{m}$ diameter cores were fluorescently labelled. The z -axis of the confocal microscope was not correctly calibrated during this particular measurements, which resulted in distances along the z -axis being severely overestimated ($\sim 3\times$). Even if the z -axis would have been calibrated correctly, the fluorescent cores would have been elongated due to the point spread function of the confocal microscope. Panels (b) and (c) show projections along the optical axis of the confocal microscope, which is parallel to the BCT $[110]_{\text{conv}}$ direction, of a 3-D scan spanning (b) the bottom 15 layers and (c) the bottom 7 layers. The lines of particles in the projections indicate (BCT) bridge-site stacking, with an ABAB stacking sequence (a). The white scale bars in all panels are $10\ \mu\text{m}$.

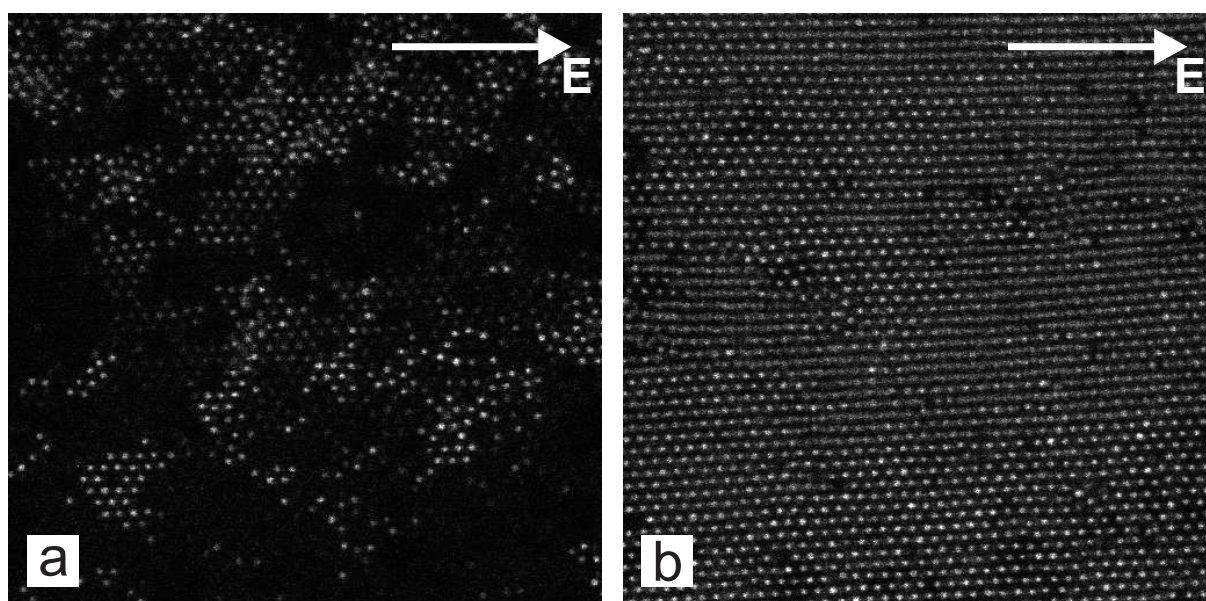


Figure 6.10: Confocal xy -images of a colloidal BCT crystal after solvent evaporation and refilling with a refractive-index-matching liquid. The crystal was the same as presented in Figure 6.7: a 25-layer crystal consisting of $1.1 \mu\text{m}$ diameter silica spheres. Panel (a) shows the bottom part of the crystal, closest to the sample substrate, indicating that solvent evaporation seriously damages the bottom part of such BCT crystals. Panel (b) shows a similar xy -scan, after moving the sample stage downwards over a distance of approximately 2 particle diameters. Although, the crystal seems tilted with respect to the confocal xy -plane, the layers are clearly hexagonal and they are still bridge-site stacked.

the confocal microscope. Whether or not the particles were stationary was checked by taking a series of 300 xz -frames, at an interval of 1 s, spanning 5 minutes in total. It showed that the particles were stationary over time intervals that were many times longer than the typical self-diffusion time of a single colloid.

6.4.2 Inverting BCT crystals

In order to increase the refractive-index contrast within immobilized colloidal BCT crystals, the samples needed to be dried, opened up and infiltrated with a high-index material such as silicon. As was shown in Section 6.3, BCT crystals grown by the fabrication procedure involving diffusion-polymerization could be dried without (much) structural damage. Unfortunately, this turned out not to be the case for BCT crystals that were fabricated by means of photo-induced polymerization. As can be seen in Figure 6.10a, the bottom layer of the crystal was severely damaged after drying and refilling of the sample. Amazingly enough, from the second or third layer upwards, the structure appeared to be fine and still displayed BCT bridge-site stacking (Figure 6.10b). We think the polymer network shrinks upon evaporation of the solvent. The crystal will shrink accordingly, retaining its BCT structure, except at the bottom, where the particles of the bottom layer also stick to the glass substrate. We note here, without proof, that we tried coating the glass substrates with stearyl alcohol, which should make the particles adhere less strongly to the substrate. Unfortunately, this did not seem to work. Another solution might

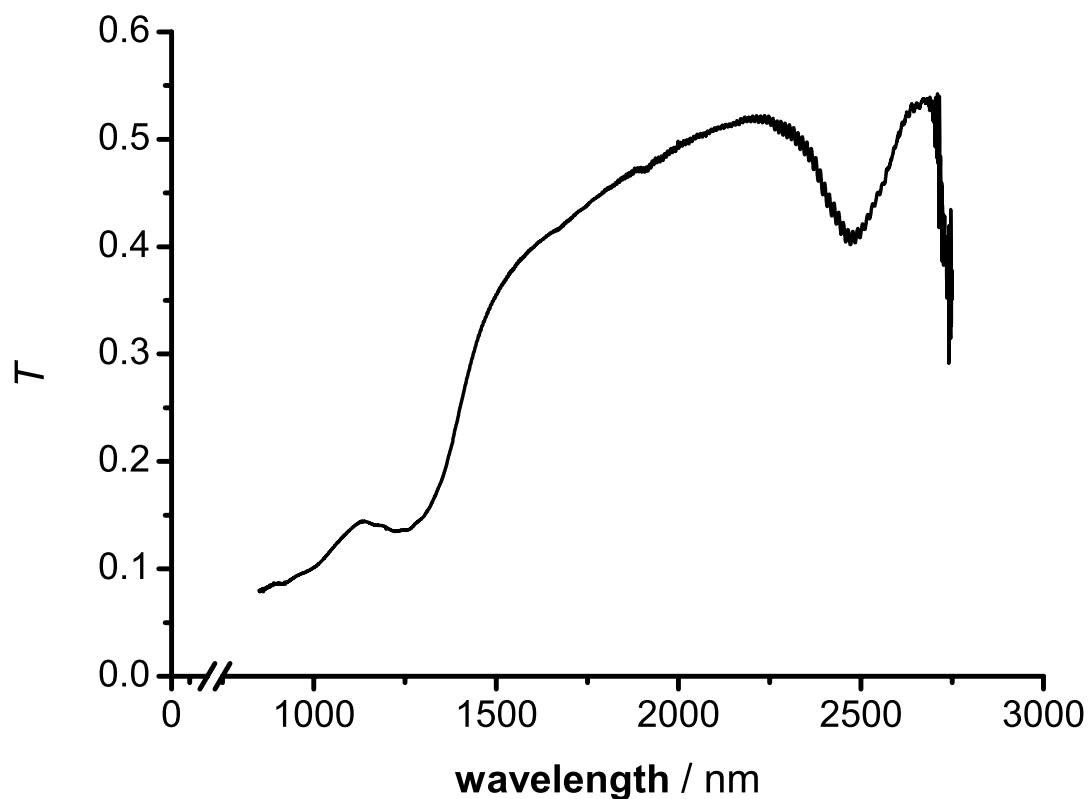


Figure 6.11: Transmission spectrum of an approximately 22-layer, colloidal BCT crystal of $1.1 \mu\text{m}$ diameter silica spheres after solvent evaporation. There is a $10\%T$ Bragg dip at 2475 nm , the second order dip of which is at approximately 1238 nm . The sharp decrease in transmission around 2700 nm is due to absorption by water in the air.

be to change the concentration of monomer in the solvent mixture, thus producing a less tenuous polymer network, which may decrease shrinkage of the network upon solvent evaporation.

As demonstrated in the previous sections, we can check whether our silica crystals are BCT or CP after solvent evaporation by infiltrating them with a refractive-index-matching liquid mixture, thus enabling confocal microscopy measurements. However, infiltration with a liquid might affect the 3-D structure of the crystals. Another way to distinguish between BCT and CP crystals is by measuring the distance between consecutive hexagonal layers. A very sensitive technique to measure such interplanar spacings in colloidal crystals is optical spectroscopy, which does not require infiltration with an index-matching liquid. On the contrary, as spectroscopy measures differences in refractive index at visible and near-infrared wavelengths, it is difficult to measure interplanar spacings in index-matched colloidal crystals. Fortunately, after solvent evaporation, the refractive-index contrast in our crystals, which is the contrast between the silica spheres and the tenuous polymer network, is large enough for Bragg diffraction to be observable in transmission spectroscopy.

Figure 6.11 shows a transmission spectrum of a colloidal crystal of 1.1 μm diameter silica spheres in a porous polymer network. The crystal was fabricated by means of photo-induced polymerization (Section 6.2.2). The volume fraction of polymer in the interstitial space was approximately 7%. The spectrum has a first-order Bragg dip around (2476 ± 3) nm that corresponds to the interplanar spacing between consecutive hexagonal layers. Furthermore, second-order Bragg diffraction is located around half that wavelength, around 1238 nm. Bragg's law can be used to extract the interplanar spacing from the wavelengths at which Bragg diffraction occurs, but a value of the average refractive index of the colloidal crystal is required. That value can be estimated or calculated if the sphere packing fraction of the crystal is known (see Section 2.6). However, BCT and CP structures have different average refractive indices at optimal packing. Moreover, parameters such as the interparticle distance may have changed upon solvent evaporation, which affects the volume fraction of spheres in the crystal and thus complicates the determination of the interlayer spacing.

To analyze the spectroscopic data, the following values for the refractive indices of the various composite materials were used: 1.46 for silica [146], 1.47 for the polymer [236] and 1.00 for air. Furthermore, we assumed additivity of volumes, refractive-index averaging by volume and interstitial volume to be filled with a homogeneous mixture of air and polymer ($\sim 7.5\%$ TMPTA). If, in addition, optimal BCT packing is assumed, the value of the interplanar spacing extracted from the transmission spectrum in Figure 6.11 is 913 nm, while basic geometry yields 906 nm. These two numbers compare much better to one another than the equivalent values for CP structures, 900 nm and 854 nm respectively. We also considered two alternative models: one in which the interparticle spacing is larger than the diameter of the spheres and one in which the hexagonal layers are touching, but the interparticle distance within hexagonal layers is larger than the particle diameter. In both alternative models, there is no interparticle spacing for which the spectroscopic and geometric results agree better for CP structures than for BCT structures, indicating that the crystal was probably still BCT. Note that it would be hard to extract absolute values for the interplanar spacing in confocal microscopy as well. Because of the mismatch in refractive index between cover slide and dispersion, distances measured along the optical axis of confocal-microscope objectives require calibration [147].

Neglecting the presence of the polymer increases the difference between the spectroscopic and geometric values for the interplanar spacing, from $(913 \text{ nm} - 906 \text{ nm}) = 7 \text{ nm}$ to $(936 \text{ nm} - 906 \text{ nm}) = 30 \text{ nm}$ if optimal BCT packing is assumed. Thus, optical spectroscopy indicates that the colloids in the BCT crystal were still suspended in a tenuous polymer matrix after solvent evaporation. SEM images (Figure 6.12a) confirm the presence of a tenuous polymer network surrounding the colloidal particles. Later on in the inversion procedure, it turned out that the polymer network needs to be removed to allow infiltration with silicon. We attempted to burn the polymer by slowly heating the sample up to 500 $^{\circ}\text{C}$. As can be seen in Figure 6.12b, the polymer had indeed been removed from the structure by the heat treatment and the crystal still displayed an ABAB stacking sequence. Unfortunately, it is difficult to judge from such an image at a 45 $^{\circ}$ tilt whether the hexagonal layers were still bridge-site stacked.

As mentioned above, removing the polymer network before infiltration with silicon turned out to be quite important. Figure 6.13 clearly shows that infiltrating BCT crystals that were immobilized by photo-induced polymerization, but that had not undergone a heat treatment, was not always successful. In the bulk of the crystal, some silicon was deposited, but most of it was deposited within the top few layers. In the bulk, it is clear that part of the polymer was

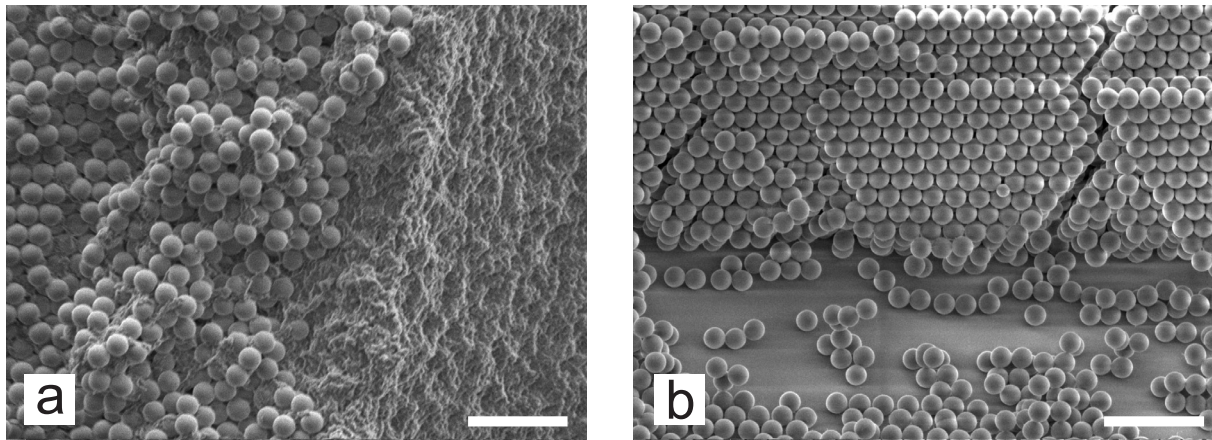


Figure 6.12: (a) SEM image of a piece that broke off a colloidal BCT crystal of $1.1 \mu\text{m}$ diameter silica spheres after photo-induced polymerization and drying of the solvent. The fluffy polymer fills up the interstitial space in between the colloidal particles in the crystal, providing a backbone for the meta-stable BCT structure. Heating up the sample to $500 \text{ }^\circ\text{C}$ for 3 hours removes the polymer from the interstitial space. After heating, the sample is still crystalline and displays ABAB-stacking, as shown in the SEM side-view at a 45° tilt (b). The white scale bars in both panels are $5 \mu\text{m}$.

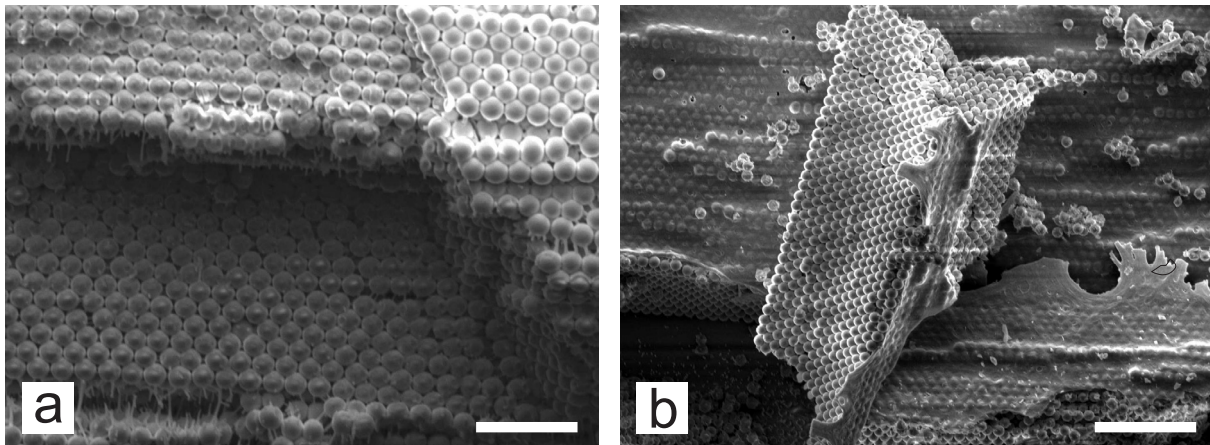


Figure 6.13: SEM images of a colloidal BCT crystal of $1.1 \mu\text{m}$ diameter silica spheres. After photo-induced polymerization, the solvent was dried and the sample was infiltrated with silicon without a preceding heat treatment. Panel (a) shows a top view of an area where a piece of the crystal broke off after silicon infiltration. Panel (b) shows such a broken-off piece. The white scale bar in panel (a) is $5 \mu\text{m}$, the one in panel (b) is $10 \mu\text{m}$.

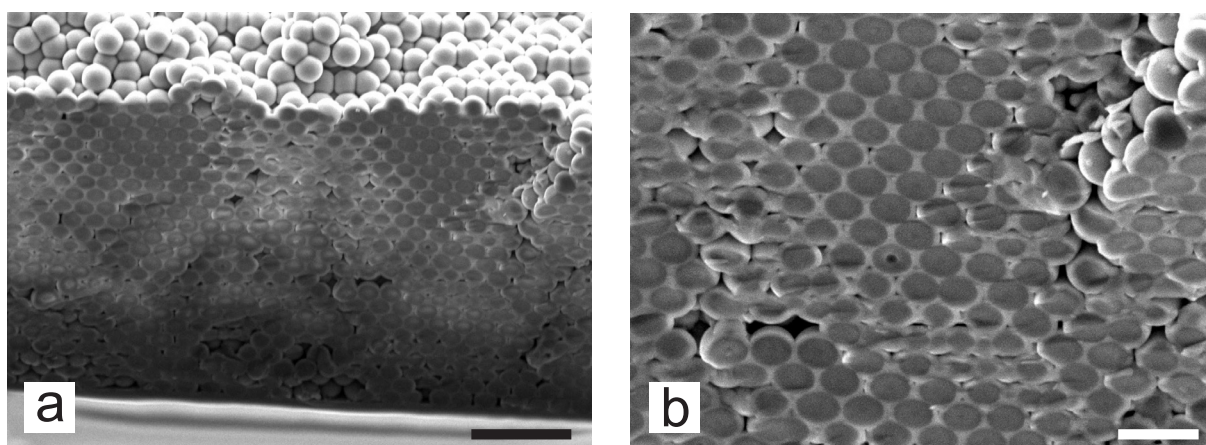


Figure 6.14: SEM side-views, at a tilt angle of 45° of an approximately 22-layer, colloidal BCT crystal after solvent evaporation, heat treatment and silicon infiltration. The crystal had approximately 22 layers, consisted of $1.1 \mu\text{m}$ diameter silica spheres and was cleaved after silicon infiltration. The image in panel (b) is a zoom of the image in panel (a). The black scale bar in panel (a) is $5 \mu\text{m}$, the white scale bar in panel (a) is $2 \mu\text{m}$.

removed by the heating during chemical vapor deposition (CVD), but some of it survived long enough for silicon ‘wires’ to be formed. At the top of the crystal, an entire silicon sheet was formed (Figure 6.13)b, probably prohibiting further silicon growth in the bulk of the crystal. After removal of the polymer by a heat treatment at approximately 500°C for 3 hours (Figure 6.12b), infiltration by chemical vapor deposition (CVD) with a high-index material such as silicon was no longer a problem (Figure 6.14). Characterization of silicon-infiltrated colloidal crystals by small-angle X-ray scattering (SAXS) is described in Chapter 7.

6.5 Results and discussion – diffraction and switching

Apart from microscopy measurements, we performed light-scattering experiments on colloidal BCT crystals, for reciprocal-space data can provide complementary, macroscopically-averaged structural information. Figure 6.15a shows a normal-incidence, laser diffraction pattern of an approximately 7-layer, colloidal BCT crystal. The number of layers in this crystal, in the middle of the sample cell, was determined by confocal microscopy. Although laser diffraction requires refractive-index matching, just like confocal microscopy, it yields information about the 3-D structure of the sample over an area as large as the cross-section of the laser beam ($\sim 1 \text{ mm}$ diameter). It is immediately clear from the diffraction pattern that the sample does not have a CP structure. Instead of the hexagonal symmetry of CP samples, the pattern clearly contains rectangular features, due to the tetragonal symmetry of BCT crystals.

Such laser diffraction patterns are slightly more difficult to interpret than X-ray diffraction patterns, as the Ewald sphere is not flat in this case [3, 105] and the diffraction angles need to be corrected for refraction at the sample-air interface. However, by explicitly summing the contributions to the structure factor of the subsequent layers of the colloidal crystal, taking into account the form factor of the colloidal spheres as well, relative intensities of the various re-

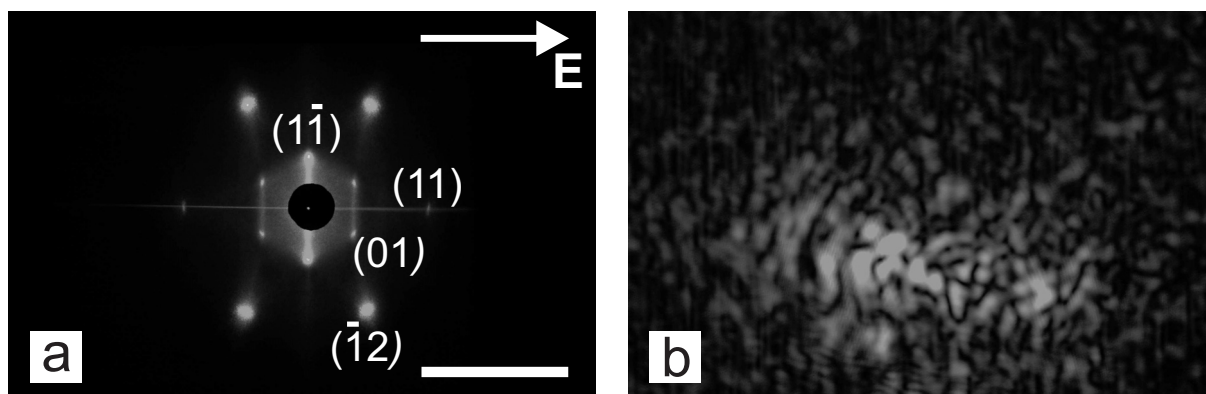


Figure 6.15: (a) Normal-incidence, laser diffraction pattern in transmission of an approximately 7-layer, colloidal BCT crystal after immobilization by means of diffusion-polymerization. The crystal consisted of $1.4 \mu\text{m}$ diameter silica spheres in a refractive-index-matching solvent mixture. During the diffusion-polymerization process, the peak-to-peak voltage over the sample was switched many times between $0 V_{\text{pp}}$ and $375 V_{\text{pp}}$ (see supplementary information online, *switching.avi*). Because the value of the third Miller-index varies from one family of Bragg reflections to another, the reflections have only been labelled with the first two Miller indices (e.g. (10) corresponds to \mathbf{b}_1 and (01) to \mathbf{b}_2). Panel (b) is a recording of one of the reflections of a BCT crystal of $1.1 \mu\text{m}$ diameter silica spheres in a solvent mixture that nearly matches the refractive index of the silica. The speckles in this Bragg reflection are clearly visible. The white scale bar in panel (a) is 5 cm.

flections can be evaluated. Calculations were performed in *Mathematica 5.2* for a 6-layer BCT crystal of $1.4 \mu\text{m}$ diameter silica spheres. The interparticle spacing was set to $1.5 \mu\text{m}$, as particles in crystals of electrostatically stabilized colloidal spheres are usually not touching. Qualitatively, the calculations predicted the positions of the Bragg reflections in the experimental diffraction pattern correctly (compare figures 6.15a and 6.16a). For example, in the calculated diffraction pattern (Figure 6.16a), which does not take into account refraction at the sample-air interface, the line connecting the $(2\bar{1})$ & $(\bar{1}2)$ reflections does not coincide with the line connecting the (10) & (01) reflections. This means that, in the experimental pattern, the lines are not overlapping because of refraction *and* because of the curvature of the Ewald-sphere, which is projected onto a flat screen. Compared to the calculated diffraction pattern, there are Bragg reflections missing from the experimental pattern, but this is due to total internal reflection at the sample-air interface.

In addition to the positions of the Bragg reflections, the calculations also yielded their relative intensities, showing that the $I_{(\bar{1}2)}$, $I_{(1\bar{1})}$, $I_{(01)}$ and $I_{(11)}$ reflections are prominent. For the 6-layer BCT crystal that was described in the previous paragraph, it was predicted that $I_{(\bar{1}2)} > I_{(1\bar{1})} > I_{(01)} > I_{(11)}$, which is roughly what can be observed in Figure 6.15. However, we note that calculated relative intensities were very sensitive to the number of layers and that the order of some of the reflections in the list could be changed by assuming a different number of layers. Moreover, it is unlikely that the number of layers in the sample was constant over the entire cross-section of the incident laser beam, so a direct comparison between calculated relative intensities and experimental diffraction patterns was not performed.

Looking at the graph of the structure factor $S(\ell)$ in Figure 6.16b partly explains why the

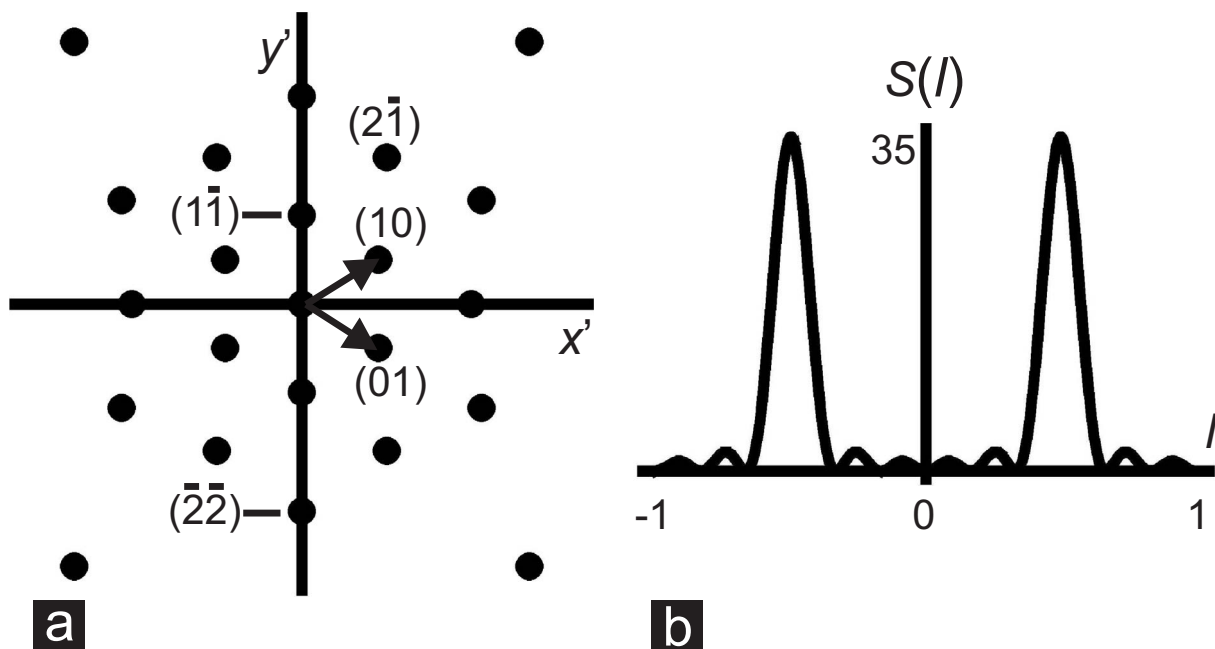


Figure 6.16: (a) Calculated diffraction pattern of a 6-layer BCT crystal of $1.4 \mu\text{m}$ diameter silica spheres in a refractive-index-matching solvent. The interparticle distance was assumed to be $1.5 \mu\text{m}$, which is slightly larger than the particle diameter. The pattern of the transmitted beams, as recorded on a flat screen, was calculated for a laser beam with a wavelength in vacuum of 543.5 nm at normal incidence. Although reflections may have different intensities, they have all been represented by black dots. Because the value of the third Miller-index varies from one family of Bragg reflections to another, the reflections have only been labelled with the first two Miller indices (e.g. (10) corresponds to \mathbf{b}_1 and (01) to \mathbf{b}_2). Panel (b) shows the structure factor $S(\ell)$ of the $(1\bar{2}\ell)$ reflection as a function of the third Miller index ℓ .

calculated ($\bar{1}2$) reflections are so strong. The value of ℓ corresponding to the ($\bar{1}2$) family of reflections is approximately -0.46, which means the ($\bar{1}2$) reflection is very close to one of the points in reciprocal space, namely ($\bar{1}2\frac{1}{2}$). Note that we used a non-primitive, reciprocal-space unit cell with a hexagonal basis, which means some, or all, Miller-indices can take fractional values. In our case, the third Miller-index ℓ can take integer and half-integer values [189], though h and k still have to be integers (see Section 4.2.2). It is also clear from Figure 6.16b that points in reciprocal space are still quite elongated along ℓ for a crystal of 6 layers. This explains why Bragg reflections that are forbidden in infinite BCT crystals may still be observable in an experimental diffraction pattern.

Not only can useful information be extracted from the positions and relative intensities of Bragg reflections in laser diffraction, the internal structure of a single Bragg reflection can be used to determine whether the polymerization was successful in immobilizing the colloidal particles or not. Figure 6.15b is a recording of one of the reflections of the (01) family (see Figure 6.15a). In a perfect, stationary crystal, such reflections would have a smooth appearance. The grainy appearance of this reflection revealed the non-ideality of the crystal itself. Due to Brownian motion, or polydispersity, the particles in a colloidal crystal (regularly) deviate from their ideal lattice sites, leading to speckle formation within Bragg reflections. As long as the particles display Brownian motion, interference on a specific spot of the Bragg reflection can change from destructive to constructive or the other way around, which means that the intensity of speckles will fluctuate in time (see supplemental information online, *fluc_speckles.avi*). Upon immobilization of the colloidal particles by means of photo-induced polymerization of the surrounding solvent mixture, the particles are no longer able to perform Brownian motion. As a significant part of the colloids are not at their ideal lattice positions during immobilization, there are still speckle patterns within the Bragg reflections. However, as the colloids are now stationary, the intensity of the speckles no longer fluctuates. The grainy appearance of the Bragg reflections then only reveals ‘frozen-in’ Brownian motion (see supplemental information online, *stat_speckles.avi*).

As a final example, we used Bragg diffraction to monitor structural changes in colloidal crystals. Before polymerization, the particles in our experimental system are still free to move about. At high field strengths, they form BCT crystals, while the structure is CP at low field strengths. Switching between BCT and CP occurs on a time-scale on the order of seconds (see supplemental information online, *switching.avi*). This is most obvious in scattering experiments, where the structural change immediately causes a Bragg color change (figures 6.17a and 6.17d) and a change in the diffraction pattern (figures 6.17b and 6.17c). Bear in mind that switching between a CP and a BCT structure is a martensitic transition [137], which means that entire crystal layers are shifted within seconds! It would not have been possible to monitor this dramatic structural change in real time over such a large area of the sample using confocal microscopy. This is because nearly all microscopy techniques suffer from the disadvantage that they either have a large field of view or a high resolution, but seldom a combination of both in a single measurement. In addition, most confocal microscopes rely on a scanning mechanism for imaging. A single 3-D scan takes much too long to allow monitoring of the 3-D structure of the sample in real time. Although it may be difficult to determine which parts of the sample actually contribute to scattering, 2-D reciprocal data, such as diffraction patterns, essentially contain information on the 3-D structure of the sample in a single image. Therefore, scattering can be used to monitor 3-D structural changes over macroscopically large areas in real time.

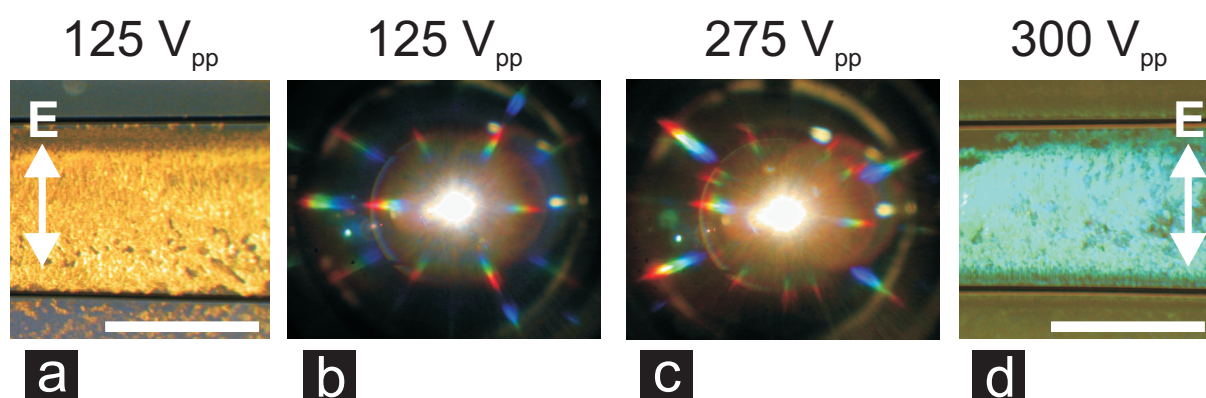


Figure 6.17: The difference between CP and BCT crystals can be observed using Bragg diffraction. Images (a) and (d) show the same sample area under off-normal, white light illumination at peak-to-peak voltages of (a) $125 V_{pp}$ and (d) $300 V_{pp}$. The sample consists of approximately 20 hexagonal layers of $1.1 \mu\text{m}$ diameter silica spheres in a refractive-index-matching mixture of water and dimethyl-sulfoxide (DMSO). The change in crystal structure is reflected in a color change, caused by the difference in spacing between the equivalent of the BCT $(100)_{\text{conv}}$ planes in the CP and BCT structure. The change in crystal structure is also obvious from Bertrand, diffraction images of similar samples for (b) $125 V_{pp}$ and (c) $275 V_{pp}$. Instead of the usual hexagonal symmetry, the Bertrand image for the CP structure (b) displays triangular symmetry, which is probably due to a slight misalignment of the condenser. The misalignment would also explain the slight deformation in the BCT Bertrand image. The white scale bars in panels (a) and (d) are 1.1 mm to 1.2 mm.

6.6 Conclusions and outlook

In this chapter, we have demonstrated a fabrication method for generating large-area colloidal crystals with a body-centered tetragonal (BCT) crystal structure. The samples are completely crystalline and show orientational order on the scale of millimeters. A recipe was developed to immobilize the colloidal particles by means of diffusion-polymerization. Subsequently, the crystals can be dried in air without inflicting serious damage to the crystal structure, thus allowing inversion of the index contrast using a UV-curable monomer. Even better, the colloidal-crystal templates can be infiltrated with silicon by chemical vapor deposition (CVD). Unfortunately, upon heating and/or infiltration with silicon, part of the crystal relaxes to hollow-site stacking (CP) instead of bridge-site stacking (BCT).

The fabrication method involving diffusion-polymerization turned out to be less robust as we thought at first. Probably due to complications in the electronic setup, the results presented in the first part of this chapter could not be reproduced with smaller spheres ($1.1 \mu\text{m}$ diameter instead of $1.4 \mu\text{m}$). For this reason, and to reduce the time that is required for the fabrication of a sample, we developed a faster fabrication method for colloidal BCT crystals that is based on photo-induced polymerization. Using this method, fabrication of a crystal sample only takes approximately 4 hours instead of 7 to 12 days! Unfortunately, the bottom part of these immobilized crystals, by which we mean the first couple of layers counting from the sample substrate, is damaged upon solvent evaporation - the remainder of the crystal remains BCT. After solvent evaporation and a heat treatment, the remaining colloidal-crystal templates can be infiltrated with amorphous silicon by CVD. The heat treatment is necessary, for if the polymer is not burnt

away before infiltration, the top layer of the crystal can clog, thus hindering the infiltration of the crystal layers below.

Apart from allowing a different structure than the usual CP one, the electric field allows switching between CP and BCT structures on a time-scale on the order of seconds. We have shown that light scattering in general, and laser diffraction in particular, allow monitoring of such structural changes over macroscopic areas in real time. This might be interesting for macroscopic devices in which Bragg reflections need to be switched on and off within seconds. Furthermore, speckles in single Bragg reflections observed in laser scattering experiments can be used to quickly determine whether or not photo-induced polymerization has successfully immobilized the colloidal particles in the crystal.

Although the switching might be interesting for specialized applications, and much information about defects in colloidal crystals might be extracted from speckles in Bragg reflections, the main challenge for the near future is the fast, electric-field-induced fabrication of large-area, colloidal BCT crystals that can withstand drying, heat treatments and infiltration with silicon by chemical vapor deposition (CVD) [68]. Chemical modification of the surface of the planar substrate is the most probable route to success, though we note here without proof that preliminary trials with stearyl alcohol did not yield favorable results. Another option would be to remove the damaged crystal layers by etching (Chapter 5), polishing, or slicing.

Acknowledgements

Jacob Hoogenboom, Dannis 't Hart and Yu Ling Wu are acknowledged for particle synthesis. I would like to express my sincere gratitude towards Hans Wisman for all his patience and his help with the electronics. Yu Ling Wu is gratefully acknowledged for many useful discussions on photo-induced polymerization. I would also like to thank Karine van der Werf and Ruud Schropp for silicon infiltration with CVD. Pim van Maurik is acknowledged for his help with scanning electron microscopy (SEM), Dirk Vossen for some of the SEM images. Many thanks to Ed van Vliet and Cees van Walree for the technical support that was required for the spectroscopic measurements. Andrei Petukhov and Arnout Imhof are gratefully acknowledged for many useful discussions on laser diffraction and small-angle X-ray scattering (SAXS). Finally, I would like to thank Rianne van Eerd and Michiel Hermes for critical reading of this chapter.

Part of the work that is described in this chapter, in particular the work on the fabrication of colloidal BCT crystals using diffusion-polymerization, has been published as Reference [109] - A. Yethiraj, J. H. J. Thijssen, A. Wouterse and A. van Blaaderen, *Large-area electric-field-induced colloidal single crystals for photonic applications*, *Advanced Materials* **16**(7), 596 (2004). A.Y., J.H.J.T. and A.W. were responsible for sample preparation and characterization by confocal microscopy; J.H.J.T. performed laser diffraction on some of the samples; A.Y., J.H.J.T. and A.W. performed the data analysis; A.v.B. initiated and supervised the project.

Characterization of photonic colloidal crystals by microradian X-ray diffraction

Three-dimensional (3-D) photonic crystals, or periodic materials that do not allow the propagation of photons with a wavelength in the band gap in all directions, can provide unprecedented control over the emission and propagation of light. A promising route towards photonic crystals (PCs) is colloidal self-assembly. However, the route from colloidal crystals to strongly photonic crystals is a multi-step fabrication process that can significantly affect the final 3-D structure of the PC. Therefore, it is important to structurally characterize such PCs at every stage of their fabrication. Because of the relatively weak interaction of X-rays with matter, X-ray scattering is an excellent tool to probe the internal 3-D structure of PCs, even if the refractive-index contrast is large in the visible region. However, the dramatic difference between the X-ray wavelength (ca. 0.1 nm) and the colloid diameter (ca. 1 μm) leads to tiny diffraction angles on the order of 10^{-4} rad. We demonstrated in Chapter 3 that the required angular resolution can be obtained at a third-generation synchrotron. In this chapter, we show that this angular resolution allows the characterization of the internal 3-D structure of photonic crystals, with lattice spacings on the order of a micrometer, at various stages of their fabrication. Furthermore, for the first time, we have performed a comparison of both real-space and reciprocal-space 3-D structural data of equivalent colloidal crystals fabricated from one system of particles.

7.1 Introduction

Photonic crystals (PCs) can provide unprecedented control over both the emission and the propagation of light, allowing important applications in, for example, infrared telecommunications [7, 8, 19]. However, fabrication and characterization of PCs is challenging owing to the large refractive-index contrast that is needed to open up a photonic band gap [31]. Here we demonstrate that microradian X-ray diffraction can be used to characterize various (inverse) PCs with lattice spacings as large as $1.3 \mu\text{m}$ at different stages of their fabrication. We have even fabricated non-close-packed (non-CP) PC structures by self-assembly of colloidal micro-spheres in an external electric field. Inverse PCs have been obtained by infiltration of the colloidal-crystal templates with amorphous silicon. The size of the colloidal particles allows us to characterize the internal 3-D structure of these crystal templates in both real and reciprocal space.

PCs are structures in which the refractive index varies periodically in space on a length scale comparable to the wavelength of light [7]. If the refractive-index contrast is large enough, PCs can have a photonic band gap, which is the photonic analogue of the electronic band gap in semiconductors [16–18]. A promising route towards relatively cheap PCs with many crystal layers is colloidal self-assembly. Monodisperse colloids can self-assemble into 3-D periodic arrangements, analogous to thermodynamic crystal phases [57]. These colloidal crystals are then used as templates for infiltration with a high-index material, such as silicon, after which the original template is removed by a wet chemical etch [67, 68].

The multi-step fabrication process can significantly affect the final 3-D structure of the PC. Therefore, it is important to structurally characterize the PCs at every stage of their fabrication. The colloidal-crystal templates can be characterized in three dimensions using optical techniques, such as confocal microscopy, after refractive-index matching using a suitable liquid [78, 99]. However, index matching is not an option for (silicon) infiltrated PCs. Moreover, even for dry crystals, which can be index matched at visible wavelengths, it would still be very useful to have a 3-D characterization technique that does not involve index matching. The infiltration of the crystal with a liquid and subsequent removal of this liquid might affect the 3-D structure. Because of the relatively weak interaction of X-rays with matter, X-ray scattering is an excellent tool to probe the internal structure of these PCs, as has been demonstrated for sub-micrometer lattice spacings [150, 241]. The challenge for X-rays stems from the dramatic difference between the X-ray wavelength (ca. 0.1 nm) and the colloid diameter (ca. $1 \mu\text{m}$), leading to tiny diffraction angles on the order of 10^{-4} rad. However, it has recently been demonstrated that the required microradian angular resolution is attainable [168, 180] (see also Chapter 3). In this chapter, we demonstrate that microradian X-ray diffraction yields clear information on the order in and 3-D structure of PCs, i.g. by analyzing the positions and heights of Bragg reflections.

7.2 Experimental methods

7.2.1 Sample preparation

All dispersions consisted of core-shell silica spheres [91, 190, 191] with a total diameter of $1.1 \mu\text{m}$ or $1.4 \mu\text{m}$ and a polydispersity of 3%, as determined by static light scattering (SLS). The approximately 400 nm diameter silica cores of all the particles were labelled with fluorescein

isothiocyanate (FITC). The body-centered tetragonal (BCT) crystals were fabricated from dispersions of such spheres in a mixture of water and dimethyl sulfoxide (87 vol-% DMSO) by sedimentation onto a glass cover slide (Menzel-Gläser, #1 cover slip, ca. 150 μm thick) in an AC electric field perpendicular to gravity [109, 175].* The electric field was generated by applying a sinusoidal voltage signal with a frequency of (1.000 ± 0.005) MHz and a peak-to-peak voltage of 200 V_{pp} to 400 V_{pp} to parallel electrodes with a diameter of 50 μm and a mutual spacing of approximately 1.0 mm to 1.25 mm. As the sample cell volume was fixed, the number of layers in these samples was determined by the volume fraction of silica spheres in the colloidal dispersion (e.g., 16.5 vol-% yields ca. 15 layers).

The particles were immobilized by a polymerization process, which is the result of the interaction between the solvent and the glue that was used to seal the sample cells (Bison Epoxy Rapide) [109]. This allows the electric field to be switched off without the crystal losing its then metastable BCT structure. However, the sample used for Figure 7.4i was fabricated using a different polymerization process. In this case, the 1.1 μm diameter silica particles were dispersed in a 10.1 vol-% solution of trimethylolpropane ethoxylate triacrylate (Aldrich, average molecular weight = 428 g/mol) in DMSO (Aldrich, > 99.6%). Next, 10 μl of a 1.0 vol-% solution of photo-initiator 2-hydroxy-2-methyl-propiophenone (Aldrich, 97%) in DMSO was added to 50 μl of the dispersion. The resulting dispersion was used for BCT crystal growth [109]. The particles in the crystal were subsequently immobilized by illumination with UV-light (UVP, UVGL-58, 365 nm, 6 W) for 2 minutes at a distance on the order of a centimeter. Close-packed (CP) crystals of similar spheres were obtained by vertical controlled drying [67, 77].

Some samples were infiltrated with silicon by chemical vapor deposition (CVD) [234]. Disilane (Si_2H_6) was used as the precursor gas. In a typical CVD run, gas flows of 10 sccm for the disilane gas and 100 sccm for the hydrogen gas were used. The temperature at the sample was approximately 450 $^\circ\text{C}$, the pressure was 0.020 mbar and the reaction duration was 300 min. At these conditions, the CVD process results in the deposition of amorphous silicon, which has a refractive index that is slightly larger than that of crystalline silicon (3.59 instead of 3.5 [235]). Before infiltration, the BCT crystals were heated up to at least 425 $^\circ\text{C}$, at an average rate of 100 $^\circ\text{C}/\text{h}$ at most. They were kept at the final temperature for at least 3 h in order to remove the polymer network, which was found to inhibit infiltration of the crystal layers below the top layer in some cases.

7.2.2 Sample characterization

The silica templates were characterized by confocal microscopy and scanning electron microscopy (SEM). Confocal microscopy measurements were performed using a Leica TCS SP2 and TCS NT confocal scan head mounted on a Leica DM IRB inverted microscope. The crystal samples were index matched by infiltration with a mixture of water and DMSO (80 vol-% DMSO) or a mixture of water and glycerol (Merck, 87 vol-% glycerol). A Leica PL APO 100 \times (1.4 NA) oil-immersion objective was used, in combination with Cargille immersion oil (type B). The FITC was excited using the 488 nm line of an Ar laser. Dry and infiltrated crystals were (additionally) characterized using a Philips XL30FEG scanning electron microscope (SEM), operating at an accelerating voltage of 2 keV to 5 keV and a working distance of approximately

*For a more detailed description of the fabrication of colloidal BCT crystals, see Chapter 6.

5 mm.

Diffraction experiments were performed at the beamlines BM26B “DUBBLE” and ID10A “TROÏKA” of the European Synchrotron Radiation Facility (ESRF) in Grenoble, France. The synchrotron X-ray radiation was produced by either a bending magnet source (“DUBBLE”) or an undulator source (“TROÏKA”).[†] A typical photon energy of 11 keV (wavelength $k = 0.11$ nm) was selected using a Si-(111) monochromator. The setup was aligned such that an image of the source was created at the detector screen, thus increasing the q -space resolution, which is necessary to measure Bragg reflections at very small angles. Furthermore, in most experiments, X-rays were allowed to propagate freely towards the sample, after which the transmitted and diffracted beams were focused by a compound refractive lens positioned just after the sample [168, 180].

At “DUBBLE”, the diffraction patterns were recorded using a 16-bit charge-coupled device (CCD) camera (Photonic Science, Xios II) with a pixel size of $22.7 \mu\text{m} \times 22.7 \mu\text{m}$ and an image size of 1270 pixels \times 1160 pixels. The q -space calibration of the Photonic Science camera was performed at “DUBBLE” using dry rat-tail collagen, yielding an inherent uncertainty in absolute q -space distances of 3%. At “TROÏKA”, a 12-bit CCD camera (Sensicam, PCO CCD Imaging) was used, with a pixel size of $6.7 \mu\text{m} \times 6.7 \mu\text{m}$ and an image size of 1280 pixels \times 1024 pixels. The Sensicam camera was calibrated using a CP reference crystal, which had been measured at “DUBBLE” as well. Because of the limited dynamic range of CCD cameras, diffraction patterns were recorded several times with exposure times ranging from 1 s up to 10 minutes. The variation in exposure time and sample absorption complicates the comparison of the intensities of corresponding reflections in different diffraction patterns presented here. All diffraction patterns have been corrected for background scattering. The peak profiles in Figures 7.2 and 7.4 were obtained by averaging the intensity over a band of 5 detector pixels to 7 detector pixels wide. Distances in reciprocal space were measured between the maxima of allowed Bragg reflections, whose positions were determined by fitting Gaussian curves to their line profiles.

7.3 Results and discussion

We analyzed the diffraction data in terms of a hexagonal lattice. The reason for this is that all our crystals, as is often the case in colloidal self-assembly, consist of stackings of hexagonally packed layers, which orient parallel to the substrate. In BCT crystals these layers are ABAB bridge-site stacked, yielding lines of particles in a real-space z -projection (see Figure 7.1a). The conventional BCT unit cell, the direction of the electric field \mathbf{E} , the laboratory xyz -frame and the real-space lattice vectors \mathbf{a}_1 , \mathbf{a}_2 , \mathbf{a}_3 are given in Figure 7.1b. The CP structures, on the other hand, consist of hollow-site stacked layers with three possible lateral positions: A, B and C (see Figure 7.1c). The 2-D reciprocal lattice of a single hexagonal plane is hexagonal and can be generated by two basis vectors, \mathbf{b}_1 and \mathbf{b}_2 (Figure 7.1d). The 3-D reciprocal lattice depends on the stacking of the layers. Any scattering vector can be decomposed into $\mathbf{q} = h\mathbf{b}_1 + k\mathbf{b}_2 + \ell\mathbf{b}_3$, where \mathbf{b}_3 is taken along the z -direction with a length $b_3 = (2\pi/d)$ determined by the interplanar spacing d . This non-primitive, reciprocal-space unit cell facilitates easy comparison between

[†]For further details concerning the microradian X-ray diffraction setup, see Chapter 3.

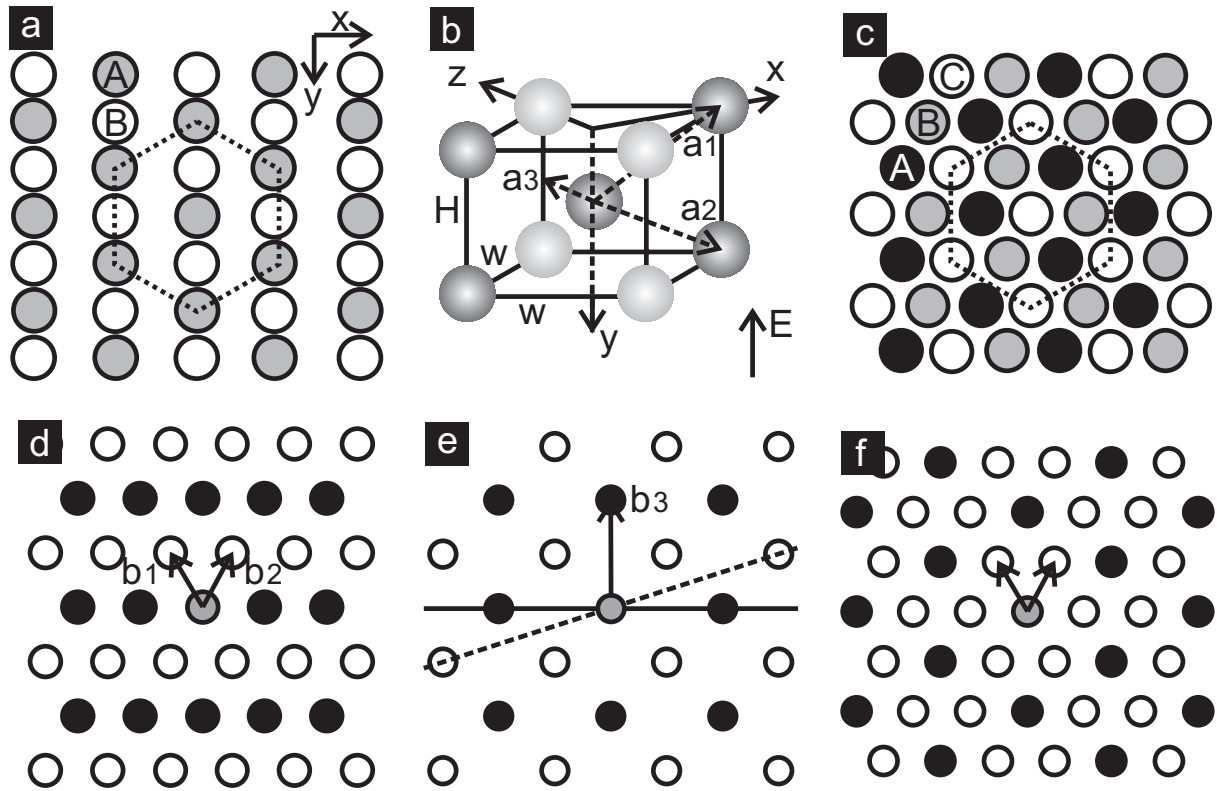


Figure 7.1: (a) Projection of the BCT structure along the z -axis, which is perpendicular to the hexagonal planes (see panel (b)), revealing BCT ABAB bridge-site stacking. (b) Conventional unit cell for the BCT real-space structure. The hexagonal plane (xy) is indicated by the dark-gray spheres. The real-space basis vectors are labelled \mathbf{a}_1 , \mathbf{a}_2 and \mathbf{a}_3 . (c) Projection of an FCC (face-centered cubic) structure along the z -axis, revealing ABCABC hollow-site stacking. In panels (a - c), the spheres have not been drawn to scale for clarity. (d, e) Cross sections through the BCT reciprocal lattice along the hexagonal (xy) plane (d) and the xz -plane (e). The black dots correspond to integer ℓ and the white dots to half-integer ℓ . The reciprocal basis vectors are labelled \mathbf{b}_1 , \mathbf{b}_2 and \mathbf{b}_3 . Furthermore, the Ewald planes for an angle of incidence of 0° (solid line) and 18.43° (dashed line) are shown in panel (e). (f) Hexagonal (xy) plane of the reciprocal lattice of a CP crystal. At normal incidence ($\ell = 0$), only the stacking-independent lattice points in reciprocal space (black dots) are probed.

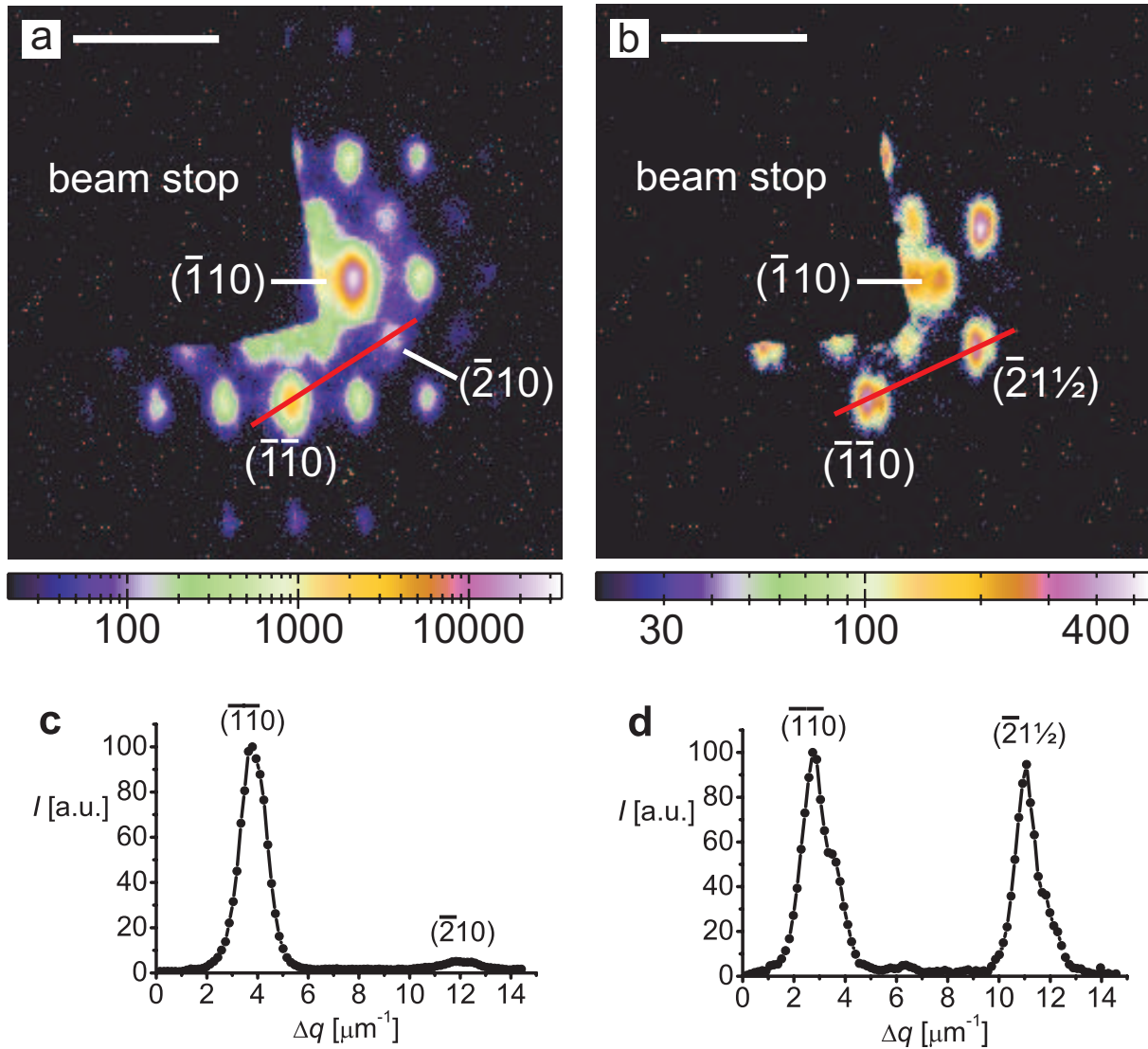


Figure 7.2: (a) Diffraction pattern at normal incidence of a 7-layer BCT crystal of $1.4 \mu\text{m}$ diameter silica spheres. (b) Diffraction pattern of the same crystal at an angle of incidence of 18.44° . The $(\bar{1}\bar{1}0)$ reflection has not disappeared, as it is on the axis of rotation (y -axis, see Figure 7.1e). The white scale bar in both images is $10 \mu\text{m}^{-1}$. The numbers below the intensity scale bar are detector pixel values. (c, d) Line profiles through the $(\bar{1}\bar{1}0)$ and $(\bar{2}10)$ or $(\bar{2}1\frac{1}{2})$ reflections, as indicated in panels (a) and (b) by a red line. Both reflections are at the same distance from the direct beam, which means the value of the form factor is equal for both reflections. In both graphs, the maximum intensity (I) of the highest peak was scaled to 100.

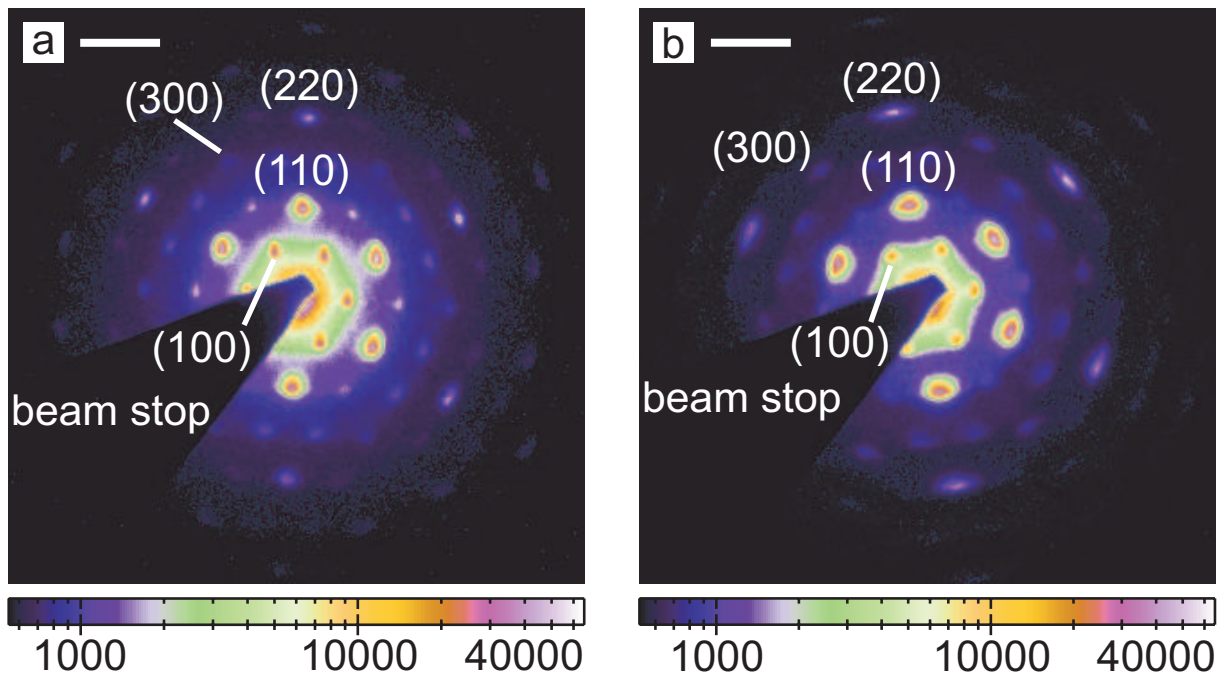


Figure 7.3: (a) Diffraction pattern at normal incidence of an approximately 6-layer CP crystal of $1.1 \mu\text{m}$ diameter silica spheres in air. The stacking-independent reflections (see Figure 7.1f) are much stronger than the other reflections. (b) Normal-incidence diffraction pattern of a CP crystal with approximately 20 layers after partial infiltration with amorphous silicon. The white scale bar in both images is $10 \mu\text{m}^{-1}$. The numbers below the intensity scale bar are detector pixel values.

the scattering by CP and BCT structures. Note that the third Miller index ℓ can take fractional values [189], whereas h and k still have to be integers [3, 105].

For any given crystal orientation, only lattice points in reciprocal space that are intersected by the Ewald sphere are probed. As our colloidal particles are typically 10^4 times larger than the X-ray wavelength, the Ewald sphere [3, 105] is nearly flat and oriented perpendicular to the incoming X-ray beam. At normal incidence ($\ell = 0$), interference is constructive for BCT structures if $(h + k)$ is even and destructive if $(h + k)$ is odd (see Figure 7.1d). For odd $(h + k)$, the stacking-induced phase difference between the layers is compensated at half-integer values of ℓ , which can be reached by specific sample rotations (see Figure 7.1e). For a CP crystal at normal incidence ($\ell = 0$), interference is always constructive for $(h - k)$ divisible by 3 (see Figure 7.1f and Section 4.2.2).

Figure 7.2a presents the normal-incidence ($\ell = 0$), X-ray diffraction pattern of a 7-layer BCT crystal. As expected, reflections for which $(h + k)$ is even are much stronger than those for which $(h + k)$ is odd (see Figure 7.2c). It is convenient to compare reflections at the same distance from the direct beam. In that case, no form-factor correction is necessary to compare peak intensities. Forbidden reflections are still slightly visible, since destructive interference is not complete in BCT if the number of layers is odd. This becomes especially apparent if the number of layers is small. Note that the microradian resolution of the setup allows us to resolve even those Bragg reflections that are very close to the direct beam, such as the $(\bar{1}10)$ reflection at a diffraction angle of only $72 \mu\text{rad}$. To further clarify its structure, the BCT crystal was rotated to vary the angle of incidence of the X-ray beam. Single-scattering theory predicts that the $(\bar{2}1\ell)$ reflection, which is forbidden for $\ell = 0$, should show up if the sample is rotated over an angle of 18.43° around the vertical y -axis. Indeed, the $(\bar{2}1\frac{1}{2})$ reflection is observed and seen to be nearly as strong as the $(\bar{1}\bar{1}0)$ reflection (Figure 7.2d). The $(\bar{1}\bar{1}0)$ reflection is still visible in Figure 7.2b because it is on the axis of rotation (see Figure 7.1e).

One of the major advantages of X-rays is that the internal 3-D structure of samples with a large index contrast in the visible region can still be probed. Figure 7.3a shows a normal-incidence ($\ell = 0$) X-ray diffraction pattern of an approximately 6-layer CP crystal of silica spheres in air. The reflections for which $(h - k)$ is divisible by 3, like the six reflections of the (110) family and the six reflections of the (220) family, are much stronger than the other reflections, as expected (see Figure 7.1f). Note that $(h - k)$ is also divisible by 3 for the six reflections of the (300) family, but these appear close to the third minimum of the sphere form factor (see Section 4.2.2), reducing their intensity significantly. The appearance of forbidden reflections, like the six reflections of the (100) family, can be attributed to the finite number of layers and/or possible stacking disorder [153]. The refractive-index contrast can be enhanced even further by infiltration of the crystal with amorphous silicon. Figure 7.3b shows a similar diffraction pattern of an approximately 20-layer CP crystal, which was partially infiltrated with amorphous silicon (estimated layer thickness 21 nm). As in Figure 7.3a, the dominant features are the six reflections of the (110) family and the six reflections of the (220) family (see Figure 7.1f), demonstrating that CP crystals can be silicon-infiltrated by chemical vapor deposition (CVD) without causing any significant damage. The forbidden reflections are less pronounced than in Figure 7.3a, which is due to the larger number of layers.

Finally, Figure 7.4 demonstrates that X-ray diffraction can be used to characterize even non-CP PCs at various stages of their fabrication. Figure 7.4a shows a normal-incidence X-ray diffraction pattern of an approximately 15-layer BCT crystal of $1.4 \mu\text{m}$ diameter silica spheres

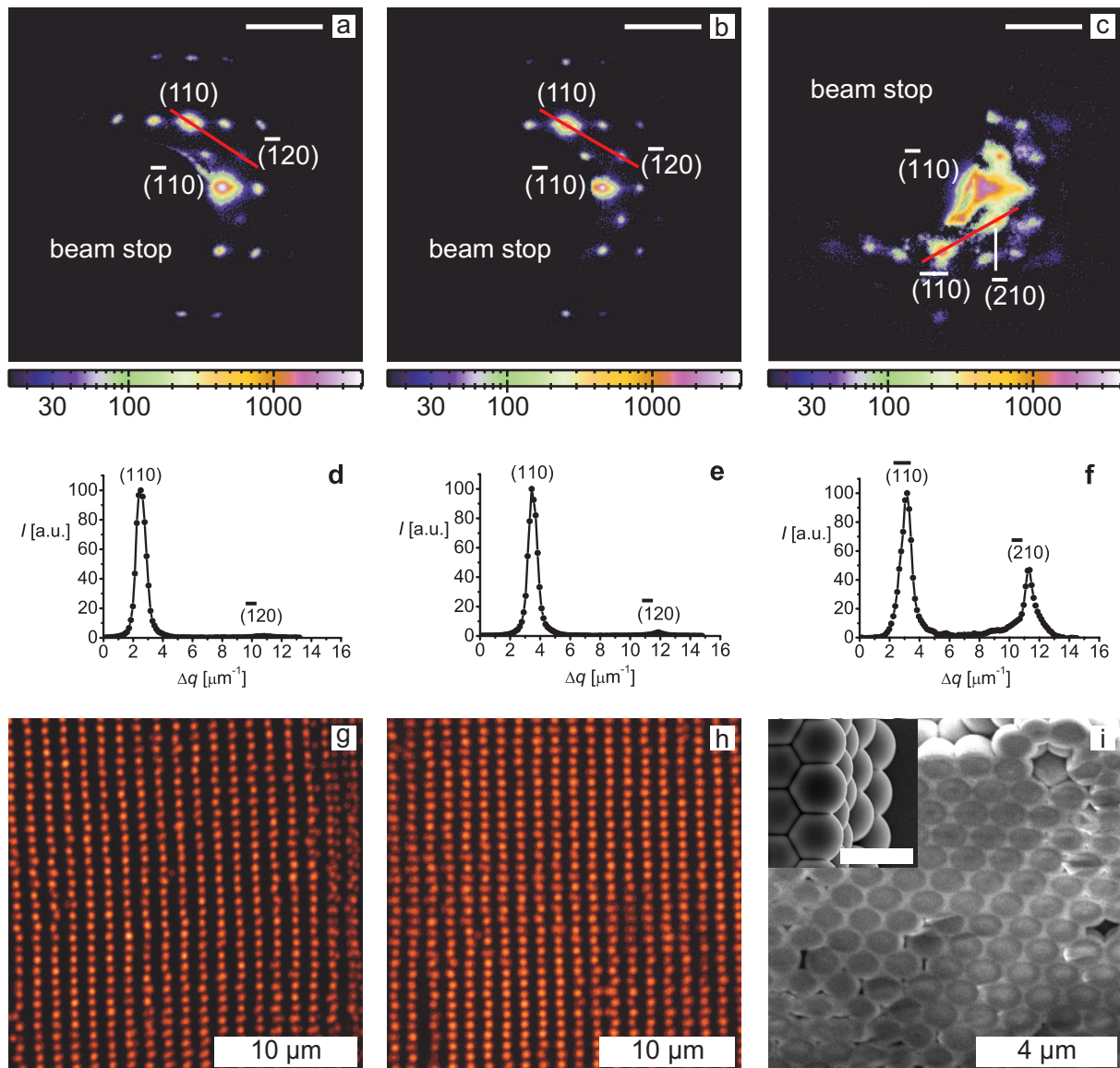


Figure 7.4: (a - c) Normal-incidence, X-ray diffraction patterns of a BCT crystal consisting of $1.4 \mu\text{m}$ diameter silica spheres; (a) in a water-DMSO mixture, (b) after solvent evaporation and (c) after infiltration with amorphous silicon. The number of layers is approximately 15, 15 and 7, respectively. The white scale bar in all images is $10 \mu\text{m}^{-1}$. The numbers below the intensity scale bar are detector pixel values. The reflections in this figure appear to be much narrower than those in Figures 7.2 and 7.3. This is because an undulator source instead of a bending-magnet source was used. (d - f) Line profiles taken along the red lines in the diffraction images. (g, h) Projections along the z -axis of 3-D confocal microscopy scans spanning 6 hexagonal layers of a BCT crystal of $1.4 \mu\text{m}$ diameter silica spheres, both before (g) and after (h) solvent evaporation and refilling. (i) SEM image showing the yz -plane, at a tilt angle of 45° , of a silicon-infiltrated BCT crystal. The inset shows a top view (xy) of a similar crystal at larger magnification. The scale bar in the inset is $2 \mu\text{m}$.

in a mixture of water and DMSO. We can check that the structure is BCT in real space by looking at a z -projection of a confocal 3-D scan spanning 6 crystal layers, clearly revealing BCT bridge-site stacking (see Figure 7.4g). After solvent evaporation and subsequent refilling for index matching, confocal microscopy measurements did not indicate that the crystals suffer any serious damage upon solvent evaporation (see Figure 7.4h). This was confirmed by X-ray measurements (see Figure 7.4b), although the intensity of the forbidden reflection ($\bar{1}20$) seems slightly larger. The latter suggests that only a very small part of the crystal, if any at all, has a CP structure (see figures 7.1f and 7.3). Owing to the large capillary forces applied during solvent evaporation, slippage of a layer from the bridge sites to the hollow sites can cause part of a crystal to relax from BCT to CP.

Once the crystals have been infiltrated with amorphous silicon, it becomes impossible to characterize their 3-D structure quantitatively in real space. Figure 7.4i shows a scanning electron microscopy (SEM) image of an infiltrated BCT crystal that was cleaved after infiltration. The space in between the spheres has been filled with silicon and the hexagonal layers are still ABAB stacked. The crystal seems to have taken quite some damage, but this might have been caused by the cleaving as well. One of the advantages of X-ray diffraction is that it can probe the 3-D structure in situ. Furthermore, it yields macroscopically-averaged structural data, whereas SEM only provides information on a small part of the surface. Figure 7.4c shows the diffraction pattern of a similar, 7-layer crystal. Although the BCT fingerprint is still visible in the diffraction pattern, the forbidden ($\bar{2}10$) reflection is nearly as strong as the allowed ($\bar{1}\bar{1}0$) reflection, which means large parts of the crystal are no longer bridge-site but hollow-site stacked. The inset of Figure 7.4i indeed shows that the bottom 2 layers are hollow-site stacked, which is probably due to adhesion of the particles of the bottom layer to the glass substrate.

From a projection such as Figure 7.4g, we can determine in real space the ratio α of the distance between the lines of particles and the distance between the particles in a line. This ratio α can also be determined in reciprocal space by comparing distances along the ($\bar{1}10$) and (110) directions. For a perfect BCT crystal with touching spheres, α would equal $\sqrt{3}$. From the X-ray diffraction pattern shown in Figure 7.4a, a value for α of $(1.023 \pm 0.002) \cdot \sqrt{3}$ can be extracted, whereas confocal microscopy on the same sample yields $(1.017 \pm 0.005) \cdot \sqrt{3}$. The values for α agree quite well and they both indicate that the hexagonal planes are compressed along the direction of the external electric field [109].

7.4 Conclusions

We have demonstrated that X-ray scattering is an excellent probe of the internal 3-D structure of CP and non-CP colloidal PCs with lattice spacings on the order of a micrometer. For example, using this advanced scattering technique, we have found that the 3-D structure of non-CP colloidal crystals can be significantly altered in going from dried to silicon-infiltrated crystals. Furthermore, for the first time, we have performed a comparison of both real-space and reciprocal-space 3-D structural data of equivalent colloidal crystals fabricated from one system of particles. Up until now, we have only considered the position and the intensity of the diffraction peaks. The microradian resolution of our X-ray diffraction setup also allows accurate determination of the width of the Bragg reflections. Thus, important information on the presence of defects and long-range order can be obtained as well, even for samples that scatter

strongly in the visible.

Acknowledgements

We thank Jacob Hoogenboom for particle synthesis and Yu Ling Wu for useful discussions on UV-polymerization. Furthermore, we would like to thank Igor Dolbnya, Florian Meneau, Abdellatif Moussaïd, Erik-Jan de Jong, Dirk Detollenaere, Jeroen Jacobs, Federico Zontone, Henri Gleyzolle, Patrick Feder, Andrei Fluerasu, Marc Diot, Cyril Ponchut, Anatoly Snigirev, Anders Madsen and Wim Bras for the excellent support they provided both before and during our X-ray diffraction measurements. I would also like to thank Andrei Petukhov and Johan Stiefelhagen for critical reading of this chapter.

This work has appeared as Reference [100] - J. H. J. Thijssen, A. V. Petukhov, D. C. 't Hart, A. Imhof, C. H. M. van der Werf, R. E. I. Schropp and A. van Blaaderen, *Characterization of photonic colloidal single crystals by microradian X-ray diffraction*, *Advanced Materials* **18**(13), 1662 (2006). J.H.J.T. and D.C.'t.H. fabricated colloidal crystals; C.H.M.vd.W. and R.E.I.S. were responsible for infiltration of colloidal crystals with silicon; J.H.J.T. performed the real-space characterization; J.H.J.T., A.V.P., D.C.'t.H., A.I. and A.v.B. were part of the experimental crews during X-ray scattering experiments; J.H.J.T. and A.V.P. performed the data analysis; A.V.P., A.I. and A.v.B. initiated and supervised the project.

Summary

In this thesis, we present (mostly) experimental work on the characterization of photonic colloidal crystals in real and reciprocal space. In Chapter 1, the main concepts of this research subject are introduced in an intuitive manner. First, the notion and the possible applications of photonic crystals are introduced in analogy with electronic semiconductors. Photonic crystals are defined as structures in which the refractive index n varies periodically in space in one, two or three dimensions. The periodicity is typically on the order of the wavelength of (visible) light. One of the most important properties of photonic crystals is the possibility of their having a photonic band gap - a frequency range, or ‘color’ range, for which no propagating electromagnetic modes exist within the crystal, regardless of propagation direction or polarization. In a one-dimensional (1-D) model, the basic physics behind photonic band gaps is clarified using (dielectric) mirrors as crystal planes.

After a short overview of some other possible fabrication methods, self-assembly of colloidal particles is introduced as a promising route towards three-dimensional (3-D) photonic crystals having areas on the order of mm^2 and a large number of layers ($\gtrsim 25$). Colloids are mesoscopic particles of which at least one dimension has a size between a few nanometers (~ 0.000001 mm) and a few micrometers (~ 0.001 mm). They are approximately $1,000\times$ larger than the molecules of which the suspending medium consists, but they are still small enough to perform Brownian motion on a length scale that is comparable to their size. Consequently, colloidal particles dispersed in a solvent are excellent condensed-matter model systems, for they display phase behavior that is analogous to that of atoms and molecules, but they are more accessible in experiments.

In the last part of the Introduction, characterization of crystalline structures consisting of submicrometer particles is discussed. Although far from trivial, real-space imaging is only touched upon briefly, as the notion of real space is intuitively clear. A large part of this thesis, however, is about characterization by scattering or diffraction. We demonstrate that diffraction is most easily described in reciprocal space and we ‘derive’ reciprocal-space basis vectors intuitively from the general real-space structure of crystals.

As the fabrication of 3-D photonic band-gap materials remains a major challenge, calculations that predict their optical properties play an important role in guiding the fabrication process. In Chapter 2, we start with a review of how to deal with photonic crystals within the framework of classical electrodynamics. Next, it is shown that the optical properties of photonic band-gap materials can be described effectively by band diagrams, of which we show some examples in subsequent sections. First of all, we calculated photonic band structures of binary Laves phases, especially MgCu_2 . By removal of one of the two species of colloids from the MgCu_2 structure, either diamond or pyrochlore structures can be fabricated. Combined with thermodynamic stability simulations by Antti-Pekka Hynninen, our results have led to a proposed route towards photonic colloidal crystals with a band gap in the visible region. The

issue of convergence of (MPB) plane-wave calculations in such strongly photonic crystals is also discussed. Next, we present photonic band diagrams of (inverse) body-centered tetragonal (BCT) crystals. In contradiction to results in literature, we found that there is no photonic band gap for inverse BCT crystals. Finally, we demonstrate that photonic band-structure calculations can be used in the analysis of optical spectra of photonic colloidal crystals.

The fabrication of photonic crystals using self-assembled colloidal crystals as templates for infiltration with high-refractive-index materials is a multistep fabrication procedure in which each step can significantly affect the 3-D structure of the resulting photonic crystal. Because of their relatively weak interaction with matter, X-rays are an excellent probe of the internal structure of photonic crystals at the various stages of their fabrication. The major challenge for X-rays stems from the dramatic difference between typical X-ray wavelengths of 0.1 nm and typical colloid diameters of 1 μm , leading to tiny diffraction angles on the order of 10^{-4} rad. In Chapter 3, we demonstrate that an angular resolution of about $2 \cdot 10^{-6}$ rad is readily achievable at a third-generation synchrotron source using compound refractive optics. The scheme allows for fast acquisition of two-dimensional X-ray diffraction data and can be realized at sample-detector separations of only a few meters. As a result, diffraction measurements in colloidal crystals with interplanar spacings larger than a micrometer are made possible. Moreover, the range of various order parameters can be determined, for even the width of Bragg peaks can be probed.

As it is a popular method for growing photonic-crystal templates, colloidal crystals grown from dispersions of silica spheres by controlled drying, also known as convective assembly, are quantitatively characterized using microradian X-ray diffraction in Chapter 4. We present X-ray diffraction patterns and electron microscopy images suggesting that the orientation of the hexagonal layers is such that the lines of touching particles are perpendicular to the meniscus if the crystal has approximately 5 layers or more. At the start of crystal growth, where the number of layers is smaller, the lines were found to be parallel to the meniscus in most crystallites. Furthermore, quantitative analysis of X-ray diffraction patterns showed that the layers parallel to the sample substrate were not exactly hexagonal and that the stacking sequence was mainly that of face-centered cubic (FCC) crystals, though stacking faults may have been present.

In Chapter 5, binary colloidal crystals of organic spheres (polystyrene, PMMA) and/or inorganic spheres (silica) are introduced as promising templates for the fabrication of strongly photonic crystals. Unfortunately, the refractive-index contrast in organic templates cannot be directly enhanced using standard infiltration techniques such as chemical vapor deposition (CVD). For example, the reaction temperature of silicon CVD is approximately 350 $^{\circ}\text{C}$, which is far above the glass transition temperature of polystyrene (PS) and PMMA. Silica templates can be infiltrated by CVD directly, but binary colloidal crystals of silica spheres often have a layer of colloidal fluid on top. In test experiments, we used atomic layer deposition (ALD) of alumina to infiltrate even organic templates. After burning of the original template, the refractive-index contrast was further enhanced by infiltration with silicon using CVD. Preliminary etching experiments demonstrated that it may be possible to use successive treatments with different plasmas to etch polymer-embedded, colloidal-crystal templates of silica spheres. However, a first trial with peeling off crystal layers using adhesive tape showed that this may be a much easier, faster and cheaper technique for ‘etching’ such templates.

Apart from their experimental accessibility, an additional advantage of colloidal dispersions as condensed-matter model systems is the ability to tune the interaction between colloids us-

ing chemical synthesis or external fields. In Chapter 6, we exploit the long-range term that is added to the interparticle interaction potential of colloids because of the dipole moments that are induced in colloidal particles by applying external, high-frequency electric fields. Sedimentation of micrometer-sized, silica spheres in an electric field perpendicular to gravity yielded large-area colloidal crystals. The growth procedure resulted in body-centered tetragonal (BCT) crystals that had areas on the order of mm^2 , but did not have a layer of colloidal fluid on top. In addition, the electric field was used as an external control to switch between close-packed (CP) and BCT crystal structures within seconds. We demonstrate that light scattering can be used to monitor such 3-D structural changes in colloidal crystals over macroscopic areas in real time.

Since the BCT crystal structure is not close-packed, and thus mechanically less stable than CP structures, we also developed two procedures to invert it without loss of structure. Both methods involve immobilization of the colloidal particles by means of polymerization of the surrounding solvent mixture, either by diffusion-polymerization or by photo-induced polymerization. We even infiltrated BCT crystals with silicon using CVD, though this led to some damage at the bottom of the crystals. Characterization of colloidal BCT and CP crystals of micrometer-sized silica spheres by small-angle X-ray scattering (SAXS) is described in Chapter 7. We demonstrate that microradian X-ray diffraction can be used to determine the internal 3-D structure of and long-range order in photonic colloidal crystals at the various stages of their fabrication. Excellent agreement was found with real-space images that were obtained from confocal and electron microscopy.

Samenvatting

In dit proefschrift presenteren we (hoofdzakelijk) experimenteel werk aan de karakterisering van fotonische colloïdale kristallen in de reële en in de reciproke ruimte. De belangrijkste begrippen uit dit onderzoeksgebied worden op intuïtieve wijze uitgelegd. Eerst worden de ideeën en de mogelijke toepassingen van fotonische kristallen uiteengezet in een vergelijking met elektronische halfgeleiders. Fotonische kristallen worden gedefinieerd als structuren waarin de brekingsindex n op een regelmatige wijze varieert in één, twee of drie dimensies. De lengteschaal van die periodiciteit komt overeen met de golflengte van (zichtbaar) licht. Een van de belangrijkste eigenschappen van fotonische kristallen is de mogelijke aanwezigheid van een bandscheiding in hun fotonische bandenstructuur - een verzameling frequenties, of 'kleuren', waarmee licht zich niet kan voortplanten door het kristal, onafhankelijk van de voortplantingsrichting of de polarisatie. De essentiële natuurkunde achter fotonische bandscheidingen wordt behandeld in een model waarin (diëlektrische) spiegels op een ééndimensionaal (1D) kristalrooster gezet worden.

Na een kort overzicht van enkele andere fabricagemethoden wordt zelfassemblage van colloïdale deeltjes opgevoerd als een veelbelovende manier om driedimensionale (3D) fotonische kristallen te maken met een oppervlak in de orde van mm^2 en een relatief groot aantal lagen ($\gtrsim 25$). Colloïden zijn mesoscopische deeltjes waarvan tenminste één afmeting tussen een paar nanometer (~ 0.000001 mm) en een paar micrometer (~ 0.001 mm) ligt. Ze zijn daarmee ongeveer $1.000\times$ groter dan de moleculen waaruit hun oplosmiddel bestaat, maar ze zijn nog wel klein genoeg om Brownse bewegingen te ondergaan op de lengteschaal van hun eigen omvang. Dientengevolge zijn colloïdale dispersies uitstekende modelsystemen voor gecondenseerde materie in het algemeen, want ze vertonen fasegedrag dat analoog is aan dat van atomen en moleculen, maar ze zijn veel makkelijker te observeren in experimenten.

In het laatste gedeelte van hoofdstuk 1 wordt de karakterisering besproken van kristallijne structuren die bestaan uit deeltjes met een afmeting in de orde van een micrometer. Ook al is het ook geen sinecure, de karakterisering met behulp van microscopie wordt slechts aangestipt, aangezien de kwalitatieve interpretatie van microscoopafbeeldingen intuïtief al duidelijk is. Een groot gedeelte van dit proefschrift gaat echter over karakterisering met behulp van verstrooiingstechnieken. We leggen uit dat verstrooiing het gemakkelijkst beschreven kan worden in de reciproke ruimte en we leiden uitdrukkingen voor basisvectoren van de reciproke ruimte af vanuit de structuur van kristallen zoals die in een microscoop waargenomen kan worden.

Aangezien de fabricage van fotonische materialen wetenschappers nog steeds voor geweldige uitdagingen plaatst, spelen berekeningen waarmee de optische eigenschappen van fotonische kristallen voorspeld kunnen worden een belangrijke rol in het sturen van dergelijke fabricageprocessen. In hoofdstuk 2 beginnen we dan ook met een overzicht van de manier waarop fotonische kristallen behandeld kunnen worden binnen het theoretisch kader van de klassieke elektrodynamica. Vervolgens leggen we uit waarom de optische eigenschappen van fotonische

materialen doeltreffend samengevat kunnen worden in een fotonisch bandendiagram, waarvan we er in de daaropvolgende paragrafen een aantal laten zien. Ten eerste hebben we de fotonische bandenstructuur uitgerekend van binaire kristallen met een Laves-structuur, in het bijzonder MgCu_2 . Door één van de twee soorten bollen uit MgCu_2 te verwijderen kan een kristal gemaakt worden met de structuur van diamant of van pyrochloor. In combinatie met simulaties aan de thermodynamische stabiliteit van zulke binaire kristallen hebben onze berekeningen geleid tot een plan waarmee wellicht fotonische kristallen met een bandscheiding voor zichtbaar licht gemaakt kunnen worden. Het computerprogramma waarmee wij fotonische bandendiagrammen uitrekenen (MIT's MPB) heeft moeite met enkele sterk fotonische structuren, waaronder diamant en pyrochloor. De nauwkeurigheid van onze berekeningen voor diamant wordt uitgebreid besproken, wat van belang is voor de gebruikers van dit wijdverspreide programma. Ten tweede presenteren we fotonische bandendiagrammen voor (inverse) kristallen met de lichaamsgecentreerd tetragonale structuur (Eng: body-centered tetragonal, BCT). In tegenstelling tot resultaten in de vakliteratuur vonden wij dat er geen fotonische bandscheiding is voor inverse BCT kristallen. Tenslotte bespreken we in hoofdstuk 2 de analyse van spectroscopische metingen in het zichtbaar met behulp van berekende fotonische bandenstructuren.

De fabricage van fotonische kristallen door middel van het opvullen van de ruimtes tussen de bollen in een zelfgeorganiseerd kristal van colloïden met materialen die een hoge brekingsindex hebben, is een proces met vele stappen. In elk van die stappen kan de 3D structuur van het uiteindelijke fotonische kristal sterk aangetast worden. Vanwege de zwakke interactie met materie is röntgenstraling bij uitstek geschikt voor de karakterisering van fotonische kristallen in de verschillende stadia van hun fabricageproces. De grote uitdaging bij het gebruik van röntgenstraling komt voort uit het enorme verschil tussen de golflengte van röntgenstralen (ongeveer 0.1 nm) en de diameter van de colloïden in het kristal (ongeveer 1 μm), wat leidt tot zeer kleine verstrooiingshoeken in de orde van 10^{-4} rad. In hoofdstuk 3 laten we zien dat hoeken tot wel $2 \cdot 10^{-6}$ rad gemeten kunnen worden in een verstrooiingsopstelling waarin een synchrotron van de derde generatie als bron dient. De opstelling maakt het mogelijk om in korte tijd tweedimensionale diffractiepatronen op te nemen, waarbij de afstand tussen het monster en de detector slechts enkele meters bedraagt. Dientengevolge kunnen röntgendiffractiepatronen opgenomen worden van kristallen met roosterafstanden in de orde van een micrometer. Aangezien zelfs de breedte van de diffractiepieken nauwkeurig bepaald kan worden, is het mogelijk om te bepalen of monsters geordend zijn over afstanden die groot zijn in vergelijking met de omvang van de colloïden in het kristal.

Een populaire methode om colloïdale kristallen mee te groeien voor de fabricatie van fotonische materialen is 'beheerste verdamping'. In hoofdstuk 4 laten we zien dat röntgenverstrooiing gebruikt kan worden om zulke kristallen kwantitatief te karakteriseren. Uit röntgendiffractiepatronen en elektronenmicroscopieplaatjes blijkt dat de oriëntatie van de hexagonale lagen in deze kristallen zodanig is dat de rijen van elkaar rakende deeltjes loodrecht staan op de oriëntatie van de meniscus, en dus niet parallel aan de meniscus, mits het aantal lagen groter is dan ongeveer 5. Daar waar het kristal begonnen is met groeien, daar zien we dat de rijen van elkaar rakende deeltjes zich juist wel parallel langs de meniscus richten. Nauwkeurige analyse van de röntgendiffractiedata laat zien dat de lagen die parallel aan de monsterdrager liggen niet precies hexagonaal zijn en dat de stapelvolgorde van die lagen dezelfde is als die van vlakgecentreerd kubische (Eng: face-centered cubic, FCC) kristallen, al kunnen er stapelfouten in voorkomen.

In hoofdstuk 5 leggen we eerst uit dat binaire colloïdale kristallen bestaande uit organische bollen (polystyreen, PMMA) en/of anorganische bollen (silica) gebruikt zouden kunnen worden voor de fabricatie van sterk fotonische kristallen. Helaas kan het brekingsindexcontrast in kristallen van organische bollen niet vergroot worden door zomaar de lege ruimtes op te vullen met behulp van standaardtechnieken als CVD (Eng: chemical vapor deposition). CVD is een proces waarbij een reactant in de gasfase aan een oppervlak reageert tot een vaste stof, bijvoorbeeld silicium. De afzetting van silicium met behulp van CVD vindt plaats bij een temperatuur van ongeveer 350 °C en dat is veel hoger dan de temperatuur waarbij materialen als polystyreen (PS) en PMMA gaan vloeien. Binaire kristallen van silica bollen kunnen wel opgevuld worden met silicium met behulp van CVD, maar er ligt vaak een laag colloïdale vloeistof bovenop zulke kristallen. In enkele proefexperimenten hebben we kristallen van organische bollen (gedeeltelijk) opgevuld met anorganisch materiaal door gebruik te maken van een techniek die in het Engels bekend staat onder de afkorting ALD (Eng: atomic layer deposition). ALD is een afzettechniek waarbij het monster keer op keer blootgesteld wordt aan dezelfde serie van gassen, waardoor er per serie één laagje atomen van een bepaald materiaal afgezet wordt, bijvoorbeeld aluminiumoxide ($\text{Al}_2\text{O}_3(\text{s})$). Na ALD hebben we het oorspronkelijke kristal van PS of PMMA bollen verbrand, waarna we het brekingsindexcontrast in het overgebleven raamwerk verhoogd hebben door de lege ruimtes met behulp van CVD (gedeeltelijk) op te vullen met silicium. Experimenten in de voorbereidende fase tonen aan dat het mogelijk moet zijn om colloïdale kristallen te etsen door ze bloot te stellen aan plasma's. De kristallen moeten dan wel vastgezet worden in een laag polymeer en er moet gebruik gemaakt worden van verschillende plasma's om afwisselend polymeer en silica te etsen. We hebben ook een keer geprobeerd om kristallagen te verwijderen door ze met plakband van het kristal af te trekken, wat nog wel eens een veel makellijkere, snellere en goedkopere manier van 'etsen' zou kunnen zijn.

Naast hun experimentele toegankelijkheid hebben colloïdale dispersies als modelsysteem nog een voordeel boven moleculaire systemen. Bij colloïden kunnen de interacties tussen de deeltjes namelijk naar wens afgestemd worden door hun chemische synthese aan te passen of door ze te onderwerpen aan externe velden. In hoofdstuk 6 gebruiken we een extern, hoogfrequent elektrisch veld om een dipoolmoment in colloïden te induceren. Hierdoor wordt aan hun interactiepotentiaal een term toegevoegd die een lange dracht heeft. Door silica bollen met een diameter van ongeveer 1 μm te laten bezinken in een elektrisch veld dat loodrecht op de zwaartekracht staat, zijn kristallen met een groot oppervlak gegroeid. Deze procedure leverde colloïdale lichaams-gecentreerd tetragonale (BCT) kristallen op die een oppervlak in de orde van mm^2 hadden en er lag geen laag colloïdale vloeistof bovenop. Daarnaast is het elektrisch veld gebruikt als een externe schakelaar waarmee binnen enkele secondes geschakeld kon worden tussen BCT kristallen en dichtstgepakte (Eng: close-packed, CP) structuren. We tonen aan dat lichtverstrooiing bij uitstek geschikt is om zulke veranderingen in de 3D structuur van colloïdale kristallen met macroscopisch grote oppervlakken live te volgen.

Aangezien BCT kristallen niet dichtgepakt zijn, en daarom mechanisch minder stabiel zijn dan CP kristallen, hebben we ook twee procedures ontwikkeld waarmee BCT structuren geïntegreerd kunnen worden zonder dat hun ordening verwoest wordt. In beide procedures worden de colloïdale deeltjes vastgezet door het hen omringende oplosmiddel te polymeriseren. In het ene geval wordt de polymerisatie gedreven door diffusie, in het andere geval door lichtgevoelige stoffen in het oplosmiddel. Het is ons zelfs gelukt om de lege ruimtes tussen de bollen in een BCT kristal op te vullen met silicium, al beschadigde de benodigde CVD wel de onderkant van

de kristallen. Hoofdstuk 7 beschrijft de karakterisatie van BCT en CP kristallen van silica bollen met een diameter van ongeveer een micrometer met behulp van röntgenverstrooiing. We laten zien dat het mogelijk is om met röntgendiffractie bij kleine hoeken (Eng: small-angle X-ray scattering, SAXS) de 3D structuur van colloïdale kristallen te bepalen en de afstand waarover die kristallen gemiddeld genomen geordend zijn. Het bleek zelfs mogelijk te zijn om dat voor fotonische colloïdale kristallen te doen die zich in verschillende stadia van hun fabricage bevonden. De uitkomsten van deze röntgendiffractiemetingen bleken uitstekend overeen te komen met plaatjes die reeds gemaakt waren met confocale microscopie en elektronenmicroscopie.

Acknowledgements

It is not up to us to decide who we meet, only how to treat the people that we do actually meet. I have been fortunate enough to meet many people over the last four years and though all of them have contributed to my development one way or the other, I would like to take this opportunity to put some of them in the spotlight.

First and foremost, I would like to thank my advisor, Alfons van Blaaderen, and my co-advisor, Arnout Imhof. It has been a pleasure to perform my PhD research in the Soft Condensed Matter (SCM) group that you run together with Marjolein Dijkstra in Utrecht. Alfons, thanks for allowing me to work in such an inspiring group, for introducing me to the wonderful world of colloids and for offering me the possibility to perform experiments abroad. Arnout, your enthusiasm for scattering has been truly inspirational. I have always been amazed that you could listen to my theoretical ramblings for the umpteenth time and I can only hope that you have enjoyed those discussions as much as I have.

Besides an advisor and a co-advisor, I was lucky enough to have Andrei Petukhov as my mentor in scattering. Andrei, you once told me that I have two legs - one in real space and one in reciprocal space. That may be so, but you are the one who taught me how to walk in reciprocal space. I will not forget our joint X-ray scattering measurements in Grenoble at 5.00 AM in the morning, neither the lively discussions that we had about the interpretation of the resulting diffraction patterns. Besides research, I also enjoy teaching. Therefore, Marjolein and Toine Arts are acknowledged for sparking my enthusiasm for thermal physics. As a teaching assistant in your problem classes, I have learned a great deal about thermodynamics and about teaching physics. At this point, I also wish to thank Dannis, Minko, Brian, Ronen, Lucas and Anke for enduring me as daily supervisor during their research projects in the SCM group. I really enjoyed working together with you and I would be pleased if you have learned as much from me as I have learned from all of you.

Although I did not check it, I would not be surprised if the people that I have spent most of my time with during the last four years are my roomies! Carmen, Christina (Chrissy) and Teun, thanks a million for keeping up with me as a roommate, for saving the plants in our office and for providing appropriate music at each and every moment of the day. Respect! Together with my roommates, my other colleagues in the SCM group provided a very pleasant atmosphere to work in. María ensured that there was always a friendly face around. Mirjam showed me that it never hurts to 'just try' an experiment and she was always willing to give me a pat on the back. Patrick Johnson taught me how to fathom the basic physics of a scientific problem. Dirk's enthusiasm has always been catching and his questions have always kept me keen. Astrid, they should make a "Will & Grace" episode about the importance of tools for tweezers. Joan, I really enjoyed our discussions on optical experiments. Colleagues like Dannis have always been able to lift my spirits, either during X-ray diffraction experiments in Grenoble ("het is eigenlijk best binnen te houden deze keer") or at parties ("biertje?"). I enjoyed supervising students, organizing the

DO!-days 2005 and visiting the *Zomerconcerten* together with Yu Ling. Esther, thanks for your continual feedback and your constructive criticism - I have truly enjoyed working together with you. Finally, coffee breaks, lunches, volleyball tournaments, hallway discussions and the like would not have been the same without Ahmet, Alejandro, Andrea, Andrew, Antti-Pekka, Didi, Eduardo (we'll meet again), Johan, Krassimir, Laura, Matthias, Matthieu, Michiel, Paddy, Peter, Rao, René, Slava, Zhoucheng and all the others that I have already mentioned or will mention later on or accidentally forgot.

Apart from the people in the SCM group, I have had the privilege of meeting many others in the scientific community. Bonny, Dirk, Karel, Mark, Maurice, Roel, Stefano, Volkert and all the others from the FCC group to start with. I do not know who came up with the idea to have SCMFCC or FCCSCM group meetings, but I think it was a bull's-eye. Hans (Gerritsen), Dave and Gijs are acknowledged for their interest. I am grateful towards Paul Braun for allowing me to work on atomic layer deposition (ALD) in his group at the University of Illinois at Urbana-Champaign (USA). Furthermore, I would like to thank him (PB), John Busbee and Amy Lynch for their kind hospitality and for all their assistance concerning housing. I would also like to thank all the members of the Braun and Wiltzius Research Groups at UIUC, especially my room mates Erik, Xindi, Abby and Martin, for making my stay in Illinois so enjoyable.

No colloidal crystal is grown without colloids. Therefore, my sincere gratitude has been earned by Dannis, Jacob, Christina (Tina), Anouk Wetzels, Carlos, Arnout, Carmen and Andrew for providing such high-quality particles and for making all the TEM images that I needed to characterize them - I have been truly spoiled over the last few years. Apart from colloids, solid technical support has been indispensable in my research. Hans Wisman has taught me most of what I know about electronics. He was always there for me when I ran into trouble with one of the setups, with my computer or with the network. Pim van Maurik & Hans Meeldijk are acknowledged for SEM and TEM support, Ed Vlietstra & Kees van Walree for help with the double-grating spectrophotometer, Karine van der Werf & Ruud Schropp for silicon CVD, Henk Mos for assistance in the case of all kinds of computer and network problems, Erik-Jan de Jong for making the tantalum beam stop and Gerard van Lingen for general technical support. Last, but not least, many thanks to Henk den Hartog, Dick van der Weijden and Barry Selles. You were always there as soon as possible to help us out with our confocal microscopes. No matter how challenging our requests, you never failed in finding a suitable solution. You guys taught me the ins and outs of confocal microscopes!

At last, there are many people in my environment that are not directly connected with my research. All the same, they have contributed significantly to this thesis. Johan, Maaïke, Bram, Jop, Rudy, Stephanie, Auke and Michiel, thanks for regularly pulling me back into the real world. Kitty and Margret, your continual interest and friendship through all the years have been very important to me. It has also been of great help to me that I could frequently work off my emotions on a tennis ball. Fortunately, Marloes, Adriaan, Lisa, Ellen, Erwin and Barbara were always there to return it. Sjors, it must be great to have nothing on your mind but food. It goes without saying that I am both happy and honored that Jorina and my brother Jacco have agreed to act as *paranimfen*. Together with pa, ma, tante Corrie, oom Ulco and Tineke, they have always provided an environment that felt like home. Mom, dad, it is great to know that I can always count on your support. Last, but definitely not least, Rianne - it takes two to tango!

Curriculum vitae

On April 19th 1980, I was born in a small village called Wamel, which is situated between the rivers Maas and Waal in the Province of Gelderland, the Netherlands. I was named after my mother and father, resulting in Job Hendrikus Jacobus Thijssen. First, I attended primary school at *basisschool De Laak* in Wamel and subsequently secondary school at the *Pax Christi College* in Druten, where I obtained my high-school degree in 1998.

From 1998 onwards, I studied physics at Utrecht University, where I received my first-year graduation with distinction. My B.Sc. project was performed at the Dutch institute for high-energy and subatomic physics (NIKHEF) under the supervision of Dr. Stan Bentvelsen, resulting in a B.Sc. thesis entitled *Uncertainty in Leading Order Higgs Production through Gluon Fusion at LHC*. My M.Sc. research project in Prof. Dr. Alfons van Blaaderen's Soft Condensed Matter group yielded two theses - *Extraordinary optical transmission through sub-wavelength hole arrays* and *Towards metallodielectric photonic crystals*. In 2003, I started my PhD research in the same group, the results of which are described in this thesis. An important part of the experimental work was performed at the European Synchrotron Radiation Facility (ESRF) in Grenoble, France. Furthermore, experiments on atomic layer deposition (ALD) were performed as a visitor in Prof. Paul Braun's group at the University of Illinois at Urbana-Champaign (USA). Part of my PhD research has been published in scientific journals and was presented as contributed oral presentations at international conferences. Besides research, I enjoyed being a teaching assistant for undergraduate students in problem classes on thermal physics. I also supervised several B.Sc. and M.Sc. students during their research projects in the Soft Condensed Matter group.

Besides my scientific activities, I was a member (2004-2006) and chairman (2005-2006) of the PhD committee of the (former) Debye Institute. Furthermore, I chaired the organizing committee of a biannual winter school (2 days) for graduate students in that Institute. My spare time is spent on tennis, ballroom dancing, reading, cooking and listening to loads of music.



Publications

This thesis is partly based on the following publications. Parts of Chapters 2, 4 and 5 are in preparation for publication.

- A.-P. Hynninen, J. H. J. Thijssen, E. C. M. Vermolen, M. Dijkstra and A. van Blaaderen, *Self-assembly route for photonic crystals with a bandgap in the visible region*, Nature Materials **6**(3), 202 (2007) - Chapter 2.
- J. H. J. Thijssen, A. V. Petukhov, D. C. 't Hart, A. Imhof, C. H. M. van der Werf, R. E. I. Schropp and A. van Blaaderen, *Characterization of photonic colloidal single crystals by microradian X-ray diffraction*, Advanced Materials **18**(13), 1662 (2006) - Chapter 7.
- A. V. Petukhov, J. H. J. Thijssen, D. C. 't Hart, A. Imhof, A. van Blaaderen, I. P. Dolbnya, A. Snigirev, A. Moussaïd and I. Snigireva, *Microradian X-ray diffraction in colloidal photonic crystals*, Journal of Applied Crystallography **39**(2), 137 (2006) - Chapter 3.
- A. Yethiraj, J. H. J. Thijssen, A. Wouterse and A. van Blaaderen, *Large-area electric-field-induced colloidal single crystals for photonic applications*, Advanced Materials **16**(7), 596 (2004) - Chapter 6.

Other publications:

- A. V. Petukhov, J. H. J. Thijssen, D. C. 't Hart, A. Imhof, A. van Blaaderen, I. P. Dolbnya, A. Snigirev, A. Moussaïd and I. Snigireva, *Microradian X-ray Diffraction in Colloidal Photonic Crystals and Liquid Crystals*, ESRF Highlights, 57 (2005).
- A. V. Petukhov, J. H. J. Thijssen, A. Imhof, A. van Blaaderen, I. P. Dolbnya, A. Snigirev, I. Snigireva and M. Drakopoulos, *3D structure and (dis-)order in photonic crystals by microradian synchrotron X-ray diffraction*, ESRF Newsletter **38**, 19 (2003).

References

- [1] <http://en.wikipedia.org/wiki/Wiki>, 2007.
- [2] http://nobelprize.org/nobel_prizes/physics/laureates/1956/index.html, 2007.
- [3] J. Ziman, *Principles of the Theory of Solids*, Cambridge University Press, New York (USA), 1995.
- [4] W. A. Harrison, *Solid State Theory - International Student Edition*, McGraw-Hill Book Company, New York, 1970.
- [5] C. Kittel, *Introduction to Solid State Physics*, John Wiley & Sons Inc., New York, 7th edition, 1996.
- [6] J. Pendry, *Applied physics - Playing tricks with light*, *Science* **285**, 1687 (1999).
- [7] J. D. Joannopoulos, R. D. Meade, and J. N. Winn, *Photonic Crystals: Molding the Flow of Light*, Princeton University Press, Princeton (New Jersey), 1995.
- [8] C. M. Soukoulis, editor, *Photonic Crystals and Light Localization in the 21st Century*, volume 563 of *NATO Science Series (C): Mathematical and Physical Sciences*, Kluwer Academic Publishers, Dordrecht, 2001.
- [9] E. Yablonovitch, *Photonic crystals: Semiconductors of light*, *Scientific American* **285**, 46 (2001).
- [10] J. D. Jackson, *Classical Electrodynamics*, John Wiley & Sons Inc., New York (USA), 3rd edition, 1999.
- [11] D. J. Griffiths, *Introduction to electrodynamics*, Prentice-Hall Inc., Upper Saddle River (New Jersey), 2nd edition, 1989.
- [12] M. Minnaert, *De natuurkunde van 't vrije veld*, B.V. W.J. Thieme & Cie, Zutphen (Netherlands), 5th edition, 1974.
- [13] B. Bransden and C. Joachain, *Quantum Mechanics*, Pearson Education Limited, Harlow (England), 2nd edition, 2000.
- [14] D. R. Lide, editor, *Handbook of Chemistry and Physics*, special student edition, CRC Press Inc., Boca Raton (USA), 72nd edition, 1991-1992.
- [15] L. Jones and P. Atkins, *Chemistry - Molecules, Matter, and Change*, W.H. Freeman and Company, New York, 4th edition, 2000.
- [16] V. Bykov, *Spontaneous emission from a medium with a band spectrum*, *Soviet Journal of Quantum Electronics* **4**, 861 (1975).
- [17] E. Yablonovitch, *Inhibited Spontaneous Emission in Solid-State Physics and Electronics*, *Physical Review Letters* **58**, 2059 (1987).
- [18] S. John, *Strong localization of photons in certain disordered dielectric superlattices*, *Physical Review Letters* **58**, 2486 (1987).
- [19] P. Lodahl, A. F. van Driel, I. S. Nikolaev, A. Irman, K. Overgaag, D. L. Vanmaekelbergh, and W. L. Vos, *Controlling the dynamics of spontaneous emission from quantum dots by photonic crystals*, *Nature* **430**, 654 (2004).

- [20] R. Sprik, B. A. van Tiggelen, and A. Lagendijk, *Optical emission in periodic dielectrics*, Europhysics Letters **35**, 265 (1996).
- [21] E. P. Petrov, V. N. Bogomolov, I. Kalosha, and S. V. Gaponenko, *Spontaneous emission of organic molecules embedded in a photonic crystal*, Physical Review Letters **81**, 77 (1998).
- [22] S. Noda, A. Chutinan, and M. Imada, *Trapping and emission of photons by a single defect in a photonic bandgap structure*, Nature **407**, 608 (2000).
- [23] M. J. A. de Dood, A. Polman, and J. G. Fleming, *Modified spontaneous emission from erbium-doped photonic layer-by-layer crystals*, Physical Review B **67** (2003).
- [24] D. Englund, D. Fattal, E. Waks, G. Solomon, B. Zhang, T. Nakaoka, Y. Arakawa, Y. Yamamoto, and J. Vuckovic, *Controlling the spontaneous emission rate of single quantum dots in a two-dimensional photonic crystal*, Physical Review Letters **95** (2005).
- [25] I. S. Nikolaev, P. Lodahl, and W. L. Vos, *Quantitative analysis of directional spontaneous emission spectra from light sources in photonic crystals*, Physical Review A **71** (2005).
- [26] J. C. Knight, J. Broeng, T. A. Birks, and P. S. J. Russel, *Photonic band gap guidance in optical fibers*, Science **282**, 1476 (1998).
- [27] J. C. Knight, *Photonic crystal fibres*, Nature **424**, 847 (2003).
- [28] P. Russell, *Photonic crystal fibers*, Science **299**, 358 (2003).
- [29] K. Riley, M. Hobson, and S. Bence, *Mathematical methods for physics and engineering*, Cambridge University Press, Cambridge (UK), 2nd edition, 2002.
- [30] A. Yariv and P. Yeh, *Optical Waves in Crystals*, John Wiley & Sons, New York.
- [31] H. S. Sözüer, J. W. Haus, and R. Inguva, *Photonic Bands - Convergence Problems with the Plane-Wave Method*, Physical Review B **45**, 13962 (1992).
- [32] A. Moroz, *Metallo-dielectric diamond and zinc-blende photonic crystals*, Physical Review B **66**, 115109 (2002).
- [33] S. Simeonov, U. Bass, and A. R. McGurn, *Photonic band structure of zinc blende type periodic dielectric media*, Physica B **228**, 245 (1996).
- [34] K. M. Ho, C. T. Chan, and C. M. Soukoulis, *Existence of a Photonic Gap in Periodic Dielectric Structures*, Physical Review Letters **65**, 3152 (1990).
- [35] E. Yablonovitch, T. J. Gmitter, and K. M. Leung, *Photonic Band-Structure - the Face-Centered-Cubic Case Employing Nonspherical Atoms*, Physical Review Letters **67**, 2295 (1991).
- [36] M. Maldovan, C. K. Ullal, W. C. Carter, and E. L. Thomas, *Exploring for 3D photonic bandgap structures in the 11 f.c.c. space groups*, Nature Materials **2**, 664 (2003).
- [37] M. Maldovan and E. L. Thomas, *Diamond-structured photonic crystals*, Nature Materials **3**, 593 (2004).
- [38] A. J. Garcia-Adeva, *Band structure of photonic crystals with the symmetry of a pyrochlore lattice*, Physical Review B **73**, 073107 (2006).
- [39] C. C. Cheng, V. ArbetEngels, A. Scherer, and E. Yablonovitch, *Nanofabricated three dimensional photonic crystals operating at optical wavelengths*, Physica Scripta **T68**, 17 (1996).
- [40] S. Noda, N. Yamamoto, and A. Sasaki, *New realization method for three-dimensional photonic crystal in optical wavelength region*, Japanese Journal of Applied Physics **35**, L909 (1996).
- [41] S. Y. Lin, J. G. Fleming, D. L. Hetherington, B. K. Smith, R. Biswas, K. M. Ho, M. M. Sigalas, W. Zubrzycki, S. R. Kurtz, and J. Bur, *A three-dimensional photonic crystal operating at infrared wavelengths*, Nature **394**, 251 (1998).
- [42] J. G. Fleming and S. Y. Lin, *Three-dimensional photonic crystal with a stop band from 1.35 to 1.95 μm* , Optics Letters **24**, 49 (1999).

- [43] S. Noda, K. Tomoda, N. Yamamoto, and A. Chutinan, *Full Three-Dimensional Photonic Bandgap Crystals at Near-Infrared Wavelengths*, *Science* **289**, 604 (2000).
- [44] K. M. Ho, C. T. Chan, C. M. Soukoulis, R. Biswas, and M. Sigalas, *Photonic Band-Gaps in 3-Dimensions - New Layer-by-Layer Periodic Structures*, *Solid State Communications* **89**, 413 (1994).
- [45] G. M. Gratson, M. J. Xu, and J. A. Lewis, *Microperiodic structures - Direct writing of three-dimensional webs*, *Nature* **428**, 386 (2004).
- [46] S. Yang, M. Megens, J. Aizenberg, P. Wiltzius, P. M. Chaikin, and W. B. Russel, *Creating periodic three-dimensional structures by multibeam interference of visible laser*, *Chemistry of Materials* **14**, 2831 (2002).
- [47] S. Jeon, V. Malyarchuk, J. A. Rogers, and G. P. Wiederrecht, *Fabricating three dimensional nanostructures using two photon lithography in a single exposure step*, *Optics Express* **14**, 2300 (2006).
- [48] M. Campbell, D. N. Sharp, M. T. Harrison, R. G. Denning, and A. J. Turberfield, *Fabrication of photonic crystals for the visible spectrum by holographic lithography*, *Nature* **404**, 53 (2000).
- [49] J. M. Shaw, J. D. Gelorme, N. C. LaBianca, W. E. Conley, and S. J. Holmes, *Negative photoresists for optical lithography*, *Ibm Journal of Research and Development* **41**, 81 (1997).
- [50] N. Tétreault, G. von Freymann, M. Deubel, M. Hermatschweiler, F. Perez-Willard, S. John, M. Wegener, and G. A. Ozin, *New route to three-dimensional photonic bandgap materials: Silicon double inversion of polymer templates*, *Advanced Materials* **18**, 457 (2006).
- [51] W. Russel, D. Saville, and W. Schowalter, *Colloidal Dispersions*, Cambridge University Press, Cambridge (UK), 1999.
- [52] E. Lankwarden, *Scheikunde*, Leidraad voor het land- en tuinbouwonderwijs (serie B), N.V. Uitgevers-Maatschappij W.E.J. Tjeenk Willink, Zwolle (Netherlands), 1932.
- [53] T. Graham, *Liquid Diffusion Applied to Analysis*, *Philosophical Transactions of the Royal Society of London* **151**, 183 (1861).
- [54] E. Verwey and J. Overbeek, *Theory of the stability of lyophobic colloids*, Dover Publications Inc., Mineola, 1999.
- [55] R. Brown, *A brief account of microscopical observations made in the months of June, July and August, 1827, on the particles contained in the pollen of plants; and on the general existence of active molecules in organic and inorganic bodies*, *Phil. Mag.* **4**, 161 (1828).
- [56] A. Einstein, *Über die von der molekularkinetischen Theorie der Wärme geforderte Bewegung von in ruhenden Flüssigkeiten suspendierten Teilchen*, *Annalen der Physik* **17**, 548 (1905).
- [57] P. N. Pusey and W. van Meegen, *Phase behaviour of concentrated suspensions of nearly hard colloidal spheres*, *Nature* **320**, 340 (1986).
- [58] W. Poon, *Colloids as big atoms*, *Science* **304**, 830 (2004).
- [59] http://nobelprize.org/nobel_prizes/physics/laureates/1926/index.html, 2007.
- [60] B. Comiskey, J. D. Albert, H. Yoshizawa, and J. Jacobson, *An electrophoretic ink for all-printed reflective electronic displays*, *Nature* **394**, 253 (1998).
- [61] T. Bert and H. De Smet, *The microscopic physics of electronic paper revealed*, *Displays* **24**, 103 (2003).
- [62] P. Pusey, *The effect of polydispersity on the crystallization of hard spherical colloids*, *Journal de physique* **48**, 709 (1987).
- [63] C. Kittel and H. Kroemer, *Thermal Physics*, W.H. Freeman and Company, New York, 2nd edition, 1998.

- [64] D. Frenkel, *De tweede jeugd van de entropie*, in *RADAR 95: De stand der zaken in de wetenschap*, edited by H. Tennekes, H. Cassee, and E. Nijssen, pages 145–162, Aramith Uitgevers, Bloemendaal (Netherlands), 1994.
- [65] R. Biswas, M. M. Sigalas, G. Subramania, and K.-M. Ho, *Photonic band gaps in colloidal systems*, *Physical Review B* **57**, 3701 (1998).
- [66] A. Moroz and C. Sommers, *Photonic band gaps of three-dimensional face-centred cubic lattices*, *Journal of Physics-Condensed Matter* **11**, 997 (1999).
- [67] Y. A. Vlasov, X.-Z. Bo, J. C. Sturm, and D. J. Norris, *On-chip natural assembly of silicon photonic bandgap crystals*, *Nature* **414**, 289 (2001).
- [68] A. Blanco, E. Chomski, S. Grabtchak, M. Ibisate, S. John, S. W. Leonard, C. López, F. Meseguer, H. Míguez, J. P. Mondia, G. A. Ozin, O. Toader, and H. M. van Driel, *Large-scale synthesis of a silicon photonic crystal with a complete three-dimensional bandgap near 1.5 micrometres*, *Nature* **405**, 437 (2000).
- [69] H. Míguez, E. Chomski, F. García-Santamaría, M. Ibisate, S. John, C. López, F. Meseguer, J. P. Mondia, G. A. Ozin, O. Toader, and H. M. v. Driel, *Photonic Bandgap Engineering in Germanium Inverse Opals by Chemical Vapor Deposition*, *Advanced Materials* **13**, 1634 (2001).
- [70] J. S. King, C. W. Neff, C. J. Summers, W. Park, S. Blomquist, E. Forsythe, and D. Morton, *High-filling-fraction inverted ZnS opals fabricated by atomic layer deposition*, *Applied Physics Letters* **83**, 2566 (2003).
- [71] J. S. King, D. Heineman, E. Graugnard, and C. J. Summers, *Atomic layer deposition in porous structures: 3D photonic crystals*, *Applied Surface Science* **244**, 511 (2005).
- [72] L. V. Woodcock, *Entropy difference between the face-centred cubic and hexagonal close-packed crystal structures*, *Nature* **385**, 141 (1997).
- [73] P. G. Bolhuis, D. Frenkel, S. C. Mau, and D. A. Huse, *Entropy difference between crystal phases*, *Nature* **388**, 235 (1997).
- [74] Z.-Y. Li and Z.-Q. Zhang, *Fragility of photonic band gaps in inverse-opal photonic crystals*, *Physical Review B* **62**, 1516 (2000).
- [75] Z. L. Wang, C. T. Chan, W. Y. Zhang, Z. Chen, N. B. Ming, and P. Sheng, *Optical properties of inverted opal photonic band gap crystals with stacking disorder*, *Physical Review E* **67**, 016612 (2003), Part 2.
- [76] K. Wostyn, Y. X. Zhao, B. Yee, K. Clays, A. Persoons, G. de Schaetzen, and L. Hellemans, *Optical properties and orientation of arrays of polystyrene spheres deposited using convective self-assembly*, *Journal of Chemical Physics* **118**, 10752 (2003).
- [77] P. Jiang, J. F. Bertone, K. S. Hwang, and V. L. Colvin, *Single-crystal colloidal multilayers of controlled thickness*, *Chemistry of Materials* **11**, 2132 (1999).
- [78] A. van Blaaderen, R. Ruel, and P. Wiltzius, *Template-directed colloidal crystallization*, *Nature* **385**, 321 (1997).
- [79] J. P. Hoogenboom, A. K. van Langen-Suurling, J. Romijn, and A. van Blaaderen, *Epitaxial growth of a colloidal hard-sphere hcp crystal and the effects of epitaxial mismatch on crystal structure*, *Physical Review E* **69** (2004), Part 1.
- [80] P. Jiang and M. J. McFarland, *Large-scale fabrication of wafer-size colloidal crystals, macroporous polymers and nanocomposites by spin-coating*, *Journal of the American Chemical Society* **126**, 13778 (2004).
- [81] R. M. Amos, J. G. Rarity, P. R. Tapster, T. J. Shepherd, and S. C. Kitson, *Fabrication of large-area face-centered-cubic hard-sphere colloidal crystals by shear alignment*, *Physical Review E* **61**, 2929 (2000).

- [82] T. Sawada, Y. Suzuki, A. Toyotama, and N. Iyi, *Quick fabrication of gigantic single-crystalline colloidal crystals for photonic crystal applications*, Japanese Journal of Applied Physics Part 2-Letters **40**, L1226 (2001).
- [83] F. M. van der Kooij and H. N. W. Lekkerkerker, *Formation of nematic liquid crystals in suspensions of hard colloidal platelets*, Journal of Physical Chemistry B **102**, 7829 (1998).
- [84] P. A. Buining, C. Pathmamanoharan, J. B. H. Jansen, and H. N. W. Lekkerkerker, *Preparation of Colloidal Boehmite Needles by Hydrothermal Treatment of Aluminum Alkoxide Precursors*, Journal of the American Ceramic Society **74**, 1303 (1991).
- [85] V. N. Manoharan, M. T. Elsesser, and D. J. Pine, *Dense packing and symmetry in small clusters of microspheres*, Science **301**, 483 (2003).
- [86] P. M. Johnson, C. M. van Kats, and A. van Blaaderen, *Synthesis of colloidal silica dumbbells*, Langmuir **21**, 11510 (2005).
- [87] K. P. Velikov and A. van Blaaderen, *Synthesis and characterization of monodisperse core-shell colloidal spheres of zinc sulfide and silica*, Langmuir **17**, 4779 (2001).
- [88] A. van Blaaderen, A. Imhof, W. Hage, and A. Vrij, *3-Dimensional Imaging of Submicrometer Colloidal Particles in Concentrated Suspensions Using Confocal Scanning Laser Microscopy*, Langmuir **8**, 1514 (1992).
- [89] A. van Blaaderen, *Imaging Individual Particles in Concentrated Colloidal Dispersions by Confocal Scanning Light-Microscopy*, Advanced Materials **5**, 52 (1993).
- [90] C. Graf and A. van Blaaderen, *Metallodielectric colloidal core-shell particles for photonic applications*, Langmuir **18**, 524 (2002).
- [91] A. van Blaaderen and A. Vrij, *Synthesis and Characterization of Colloidal Dispersions of Fluorescent, Monodisperse Silica Spheres*, Langmuir **8**, 2921 (1992).
- [92] N. A. M. Verhaegh and A. Vanblaaderen, *Dispersions of Rhodamine-Labeled Silica Spheres - Synthesis, Characterization, and Fluorescence Confocal Scanning Laser Microscopy*, Langmuir **10**, 1427 (1994).
- [93] M. J. A. de Dood, B. Berkhout, C. M. van Kats, A. Polman, and A. van Blaaderen, *Acid-based synthesis of monodisperse rare-earth-doped colloidal SiO₂ spheres*, Chemistry of Materials **14**, 2849 (2002).
- [94] C. Graf, S. Dembski, A. Hofmann, and E. Ruhl, *A general method for the controlled embedding of nanoparticles in silica colloids*, Langmuir **22**, 5604 (2006).
- [95] A. van Blaaderen, *Colloids under external control*, MRS Bulletin **29**, 85 (2004).
- [96] D. G. Grier, *A revolution in optical manipulation*, Nature **424**, 810 (2003).
- [97] D. L. J. Vossen, A. van der Horst, M. Dogterom, and A. van Blaaderen, *Optical tweezers and confocal microscopy for simultaneous three-dimensional manipulation and imaging in concentrated colloidal dispersions*, Review of Scientific Instruments **75**, 2960 (2004).
- [98] R. J. Hunter, *Foundations of Colloid Science*, Oxford University Press, Oxford, 2nd edition, 2002.
- [99] A. van Blaaderen and P. Wiltzius, *Real-Space Structure of Colloidal Hard-Sphere Glasses*, Science **270**, 1177 (1995).
- [100] J. H. J. Thijssen, A. V. Petukhov, D. C. 't Hart, A. Imhof, C. H. M. van der Werf, R. E. I. Schropp, and A. van Blaaderen, *Characterization of photonic colloidal single crystals by microradian X-ray diffraction*, Advanced Materials **18**, 1662 (2006).
- [101] K. J. Strandburg, editor, *Bond-Orientational Order in Condensed Matter Systems*, Springer-Verlag, New York, 1992.
- [102] J. C. Crocker and D. G. Grier, *Methods of digital video microscopy for colloidal studies*, Journal of Colloid and Interface Science **179**, 298 (1996).

- [103] P. Vukusic and J. R. Sambles, *Photonic structures in biology*, Nature **424**, 852 (2003).
- [104] J. E. Marsden and A. J. Tromba, *Vector calculus*, W.H. Freeman and Company, New York, 4th edition, 1996.
- [105] A. Guinier, *X-Ray Diffraction In Crystals, Imperfect Crystals, and Amorphous Bodies*, Dover Publications Inc., New York (USA), 1994.
- [106] S. Y. Lin, J. G. Fleming, and E. Chow, *Two- and three-dimensional photonic crystals built with VLSI tools*, MRS Bulletin **26**, 627 (2001).
- [107] C. López, *Materials aspects of photonic crystals*, Advanced Materials **15**, 1679 (2003).
- [108] D. J. Norris, E. G. Arlinghaus, L. Meng, R. Heiny, and L. E. Scriven, *Opaline Photonic Crystals: How Does Self-Assembly Work?*, Advanced Materials **16**, 1393 (2004).
- [109] A. Yethiraj, J. H. J. Thijssen, A. Wouterse, and A. van Blaaderen, *Large-area electric-field-induced colloidal single crystals for photonic applications*, Advanced Materials **16**, 596 (2004).
- [110] A. Mihi, M. Ocaña, and H. Míguez, *Oriented colloidal-crystal thin films by spin-coating microspheres dispersed in volatile media*, Advanced Materials **18**, 2244 (2006).
- [111] M. Deubel, G. Von Freymann, M. Wegener, S. Pereira, K. Busch, and C. M. Soukoulis, *Direct laser writing of three-dimensional photonic-crystal templates for telecommunications*, Nature Materials **3**, 444 (2004).
- [112] F. García-Santamaría, H. T. Miyazaki, A. Urquia, M. Ibisate, M. Belmonte, N. Shinya, F. Meseguer, and C. López, *Nanorobotic manipulation of microspheres for on-chip diamond architectures*, Advanced Materials **14**, 1144 (2002).
- [113] S. Eiden-Assmann, J. Widoniak, and G. Maret, *Synthesis and characterization of porous and nonporous monodisperse colloidal TiO₂ particles*, Chemistry of Materials **16**, 6 (2004).
- [114] A.-P. Hynninen, J. H. J. Thijssen, E. C. M. Vermolen, M. Dijkstra, and A. van Blaaderen, *Self-assembly route for photonic crystals with a bandgap in the visible region*, Nature Materials **6**, 202 (2007).
- [115] H. Míguez, F. Meseguer, C. López, A. Blanco, J. S. Moya, J. Requena, A. Mifsud, and V. Fornes, *Control of the photonic crystal properties of fcc-packed submicrometer SiO₂ spheres by sintering*, Advanced Materials **10**, 480 (1998).
- [116] K. Busch and S. John, *Photonic band gap formation in certain self-organizing systems*, Physical Review E **58**, 3896 (1998).
- [117] L. F. Shen, Z. Ye, and S. He, *Design of two-dimensional photonic crystals with large absolute band gaps using a genetic algorithm*, Physical Review B **68**, 035109 (2003).
- [118] Z. Ye, L. F. Shen, and S. L. He, *Design for 2D anisotropic photonic crystal with large absolute band gaps by using a genetic algorithm*, European Physical Journal B **37**, 417 (2004).
- [119] A. Gondarenko, S. Preble, J. Robinson, L. Chen, H. Lipson, and M. Lipson, *Spontaneous emergence of periodic patterns in a biologically inspired simulation of photonic structures*, Physical Review Letters **96**, 143904 (2006).
- [120] E. J. Reed, M. Soljacic, and J. D. Joannopoulos, *Reversed Doppler effect in photonic crystals*, Physical Review Letters **91**, 133901 (2003).
- [121] W. Friedrich, P. Knipping, and M. von Laue, *Interference Phenomena with Rontgen Rays*, Sitzb. kais. Akad. Wiss. , 303 (1912).
- [122] J. Sakurai, *Modern Quantum Mechanics*, Addison-Wesley Publishing Company Inc., Reading, Massachusetts, revised edition, 1994.
- [123] L. P. Bouckaert, R. Smoluchowski, and E. Wigner, *Theory of Brillouin Zones and Symmetry Properties of Wave Functions in Crystals*, Physical Review **50**, 58 (1936).

- [124] C. Bradley and A. Cracknell, *The Mathematical Theory of Symmetry in Solids*, Clarendon Press, Oxford, 1972.
- [125] http://ab-initio.mit.edu/wiki/index.php/Main_Page, 2006.
- [126] S. Johnson and J. Joannopoulos, *Block-iterative frequency-domain methods for Maxwell's equations in a planewave basis*, *Optics Express* **8**, 173 (2001).
- [127] <http://dir.gmane.org/gmane.comp.science.photonic-bands>, 2006.
- [128] <http://www1.phys.uu.nl/helpdesk/linux/venus/default.htm>, 2006.
- [129] X. Wang, X.-G. Zhang, Q. Yu, and B. N. Harmon, *Multiple-scattering theory for electromagnetic waves*, *Physical Review B* **47**, 4161 (1993).
- [130] A. Moroz, *Density-of-states calculations and multiple-scattering theory for photons*, *Physical Review B* **51**, 2068 (1995).
- [131] <http://www.wave-scattering.com/>, 2006.
- [132] Z. L. Zhang, A. S. Keys, T. Chen, and S. C. Glotzer, *Self-assembly of patchy particles into diamond structures through molecular mimicry*, *Langmuir* **21**, 11547 (2005).
- [133] A. V. Tkachenko, *Morphological diversity of DNA-colloidal self-assembly*, *Physical Review Letters* **89**, 148303 (2002).
- [134] V. N. Manoharan and D. J. Pine, *Building materials by packing spheres*, *MRS Bulletin* **29**, 91 (2004).
- [135] K. P. Velikov, C. G. Christova, R. P. A. Dullens, and A. van Blaaderen, *Layer-by-Layer Growth of Binary Colloidal Crystals*, *Science* **296**, 106 (2002).
- [136] <http://cst-www.nrl.navy.mil/lattice/struk/laves.html>, 2006.
- [137] A. Yethiraj, A. Wouterse, B. Groh, and A. van Blaaderen, *Nature of an electric-field-induced colloidal martensitic transition*, *Physical Review Letters* **92**, 058301 (2004).
- [138] A.-P. Hynninen and M. Dijkstra, *Phase behavior of dipolar hard and soft spheres*, *Physical Review E* **72**, 051402 (2005), Part 1.
- [139] R. Tao and D. Xiao, *Three-dimensional dielectric photonic crystals of body-centered-tetragonal lattice structure*, *Applied Physics Letters* **80**, 4702 (2002).
- [140] A. A. Chabanov, Y. Jun, and D. J. Norris, *Avoiding cracks in self-assembled photonic band-gap crystals*, *Applied Physics Letters* **84**, 3573 (2004).
- [141] C. F. Bohren and D. R. Huffman, *Absorption and Scattering of Light by Small Particles*, Wiley Science Paperback Series, John Wiley & Sons, Inc., New York, 1998.
- [142] A. Labrosse and A. Burneau, *Characterization of porosity of ammonia catalysed alkoxysilane silica*, *Journal of Non-Crystalline Solids* **221**, 107 (1997).
- [143] A. Walcarius, C. Despas, and J. Bessiere, *Molecular sieving with amorphous monodisperse silica beads*, *Microporous and Mesoporous Materials* **23**, 309 (1998).
- [144] M. Megens, C. M. van Kats, P. Bösecke, and W. L. Vos, *In situ characterization of colloidal spheres by synchrotron small-angle x-ray scattering*, *Langmuir* **13**, 6120 (1997).
- [145] A. Imhof, A. van Blaaderen, G. Maret, J. Mellema, and J. K. G. Dhont, *A Comparison between the Ion-Time Self-Diffusion and Low Shear Viscosity of Concentrated Dispersions of Charged Colloidal Silica Spheres*, *Journal of Chemical Physics* **100**, 2170 (1994).
- [146] D. L. J. Vossen, *Optical tweezers in concentrated colloidal dispersions*, Phd thesis, Utrecht University, 2004.
- [147] A. C. Dogariu and R. Rajagopalan, *Optical traps as force transducers: The effects of focusing the trapping beam through a dielectric interface*, *Langmuir* **16**, 2770 (2000).

- [148] A. Moroz, *Three-dimensional complete photonic-band-gap structures in the visible*, Physical Review Letters **83**, 5274 (1999).
- [149] R. Rengarajan, D. Mittleman, C. Rich, and V. Colvin, *Effect of disorder on the optical properties of colloidal crystals*, Physical Review E **71**, 016615 (2005), Part 2.
- [150] W. L. Vos, M. Megens, C. M. van Kats, and P. Bösecke, *X-ray diffraction of photonic colloidal single crystals*, Langmuir **13**, 6004 (1997).
- [151] H. Versmold, S. Musa, and A. Bierbaum, *Concentrated colloidal dispersions: On the relation of rheology with small angle x-ray and neutron scattering*, Journal of Chemical Physics **116**, 2658 (2002).
- [152] A. V. Petukhov, D. G. A. L. Aarts, I. P. Dolbnya, E. H. A. de Hoog, K. Kassapidou, G. J. Vroege, W. Bras, and H. N. W. Lekkerkerker, *High-resolution small-angle x-ray diffraction study of long-range order in hard-sphere colloidal crystals*, Physical Review Letters **88**, 208301 (2002).
- [153] A. V. Petukhov, I. P. Dolbnya, D. G. A. L. Aarts, G. J. Vroege, and H. N. W. Lekkerkerker, *Bragg rods and multiple x-ray scattering in random-stacking colloidal crystals*, Physical Review Letters **90**, 028304 (2003).
- [154] P. N. Pusey, W. van Meegen, P. Bartlett, B. J. Ackerson, J. G. Rarity, and S. M. Underwood, *Structure of Crystals of Hard Colloidal Spheres*, Physical Review Letters **63**, 2753 (1989).
- [155] J. X. Zhu, M. Li, R. Rogers, W. Meyer, R. H. Ottewill, W. B. Russell, and P. M. Chaikin, *Crystallization of hard-sphere colloids in microgravity*, Nature **387**, 883 (1997).
- [156] J. L. Harland and W. van Meegen, *Crystallization kinetics of suspensions of hard colloidal spheres*, Physical Review E **55**, 3054 (1997), Part B.
- [157] W. K. Kegel and J. K. G. Dhont, *"Aging" of the structure of crystals of hard colloidal spheres*, Journal of Chemical Physics **112**, 3431 (2000).
- [158] A. V. Petukhov, D. van der Beek, R. P. A. Dullens, I. P. Dolbnya, G. J. Vroege, and H. N. W. Lekkerkerker, *Observation of a hexatic columnar liquid crystal of polydisperse colloidal disks*, Physical Review Letters **95**, 077801 (2005).
- [159] T. Narayanan, O. Diat, and P. Bösecke, *SAXS and USAXS on the high brilliance beamline at the ESRF*, Nuclear Instruments and Methods in Physics Research Section a-Accelerators Spectrometers Detectors and Associated Equipment **467**, 1005 (2001), Part 2.
- [160] J. Ilavsky, A. J. Allen, G. G. Long, and P. R. Jemian, *Effective pinhole-collimated ultrasmall-angle x-ray scattering instrument for measuring anisotropic microstructures*, Review of Scientific Instruments **73**, 1660 (2002).
- [161] U. Bonse and M. Hart, *Small Angle X-Ray Scattering by Spherical Particles of Polystyrene and Polyvinyltoluene*, Zeitschrift für Physik **189**, 151 (1966).
- [162] A. Freund, *Synchrotron X-Ray Beam Optics*, in *Complementarity between Neutron and Synchrotron X-Ray Scattering*, edited by A. Furrer, page 329, World Scientific Publishing Company, 1998.
- [163] T. Harada, H. Matsuoka, T. Ikeda, and H. Yamaoka, *The mystery of colloidal crystal formation - novel aspects obtained by ultra-small-angle X-ray scattering*, Colloids and Surfaces a-Physicochemical and Engineering Aspects **174**, 79 (2000).
- [164] M. Linari, G. Piazzesi, I. Dobbie, N. Koubassova, M. Reconditi, T. Narayanan, O. Diat, M. Irving, and V. Lombardi, *Interference fine structure and sarcomere length dependence of the axial x-ray pattern from active single muscle fibers*, Proceedings of the National Academy of Sciences of the United States of America **97**, 7226 (2000).
- [165] M. Reconditi, M. Linari, L. Lucii, A. Stewart, Y. B. Sun, P. Bösecke, T. Narayanan, R. F. Fischetti, T. Irving, G. Piazzesi, M. Irving, and V. Lombardi, *The myosin motor in muscle generates a smaller and slower working stroke at higher load*, Nature **428**, 578 (2004).

- [166] A. V. Petukhov, I. P. Dolbnya, D. Aarts, and G. J. Vroege, *Destruction of long-range order recorded with in situ small-angle x-ray diffraction in drying colloidal crystals*, Physical Review E **69**, 031405 (2004), Part 1.
- [167] N. Yagi and K. Inoue, *Ultra-small-angle X-ray diffraction and scattering experiments using medium-length beamlines at SPring-8*, Journal of Applied Crystallography **36**, 783 (2003).
- [168] M. Drakopoulos, A. Snigirev, I. Snigireva, and J. Schilling, *X-ray high-resolution diffraction using refractive lenses*, Applied Physics Letters **86**, 014102 (2005).
- [169] V. N. Astratov, A. M. Adawi, S. Fricker, M. S. Skolnick, D. M. Whittaker, and P. N. Pusey, *Interplay of order and disorder in the optical properties of opal photonic crystals*, Physical Review B **66**, 165215 (2002).
- [170] M. Megens and W. L. Vos, *Particle excursions in colloidal crystals*, Physical Review Letters **86**, 4855 (2001).
- [171] S. K. Sinha, M. Tolan, and A. Gibaud, *Effects of partial coherence on the scattering of x rays by matter*, Physical Review B **57**, 2740 (1998).
- [172] A. Snigirev, V. Kohn, I. Snigireva, and B. Lengeler, *A compound refractive lens for focusing high-energy X-rays*, Nature **384**, 49 (1996).
- [173] V. Kohn, I. Snigireva, and A. Snigirev, *Diffraction theory of imaging with X-ray compound refractive lens*, Optics Communications **216**, 247 (2003).
- [174] F. van der Veen and F. Pfeiffer, *Coherent x-ray scattering*, Journal of Physics-Condensed Matter **16**, 5003 (2004).
- [175] A. Yethiraj and A. van Blaaderen, *A colloidal model system with an interaction tunable from hard sphere to soft and dipolar*, Nature **421**, 513 (2003).
- [176] U. Dassanayake, S. Fraden, and A. van Blaaderen, *Structure of electrorheological fluids*, Journal of Chemical Physics **112**, 3851 (2000).
- [177] F. M. van der Kooij, K. Kassapidou, and H. N. W. Lekkerkerker, *Liquid crystal phase transitions in suspensions of polydisperse plate-like particles*, Nature **406**, 868 (2000).
- [178] J. Meijer, *Stacking disorder in hard sphere crystals*, Bachelor thesis, Utrecht University, 2006.
- [179] J. M. Grimes and D. I. Stuart, *Large unit cells and cellular mechanics*, Nature Structural Biology **5**, 630 (1998), Suppl. S.
- [180] A. V. Petukhov, J. H. J. Thijssen, D. C. 't Hart, A. Imhof, A. van Blaaderen, I. P. Dolbnya, A. Snigirev, A. Moussaïd, and I. Snigireva, *Microradian X-ray diffraction in colloidal photonic crystals*, Journal of Applied Crystallography **39**, 137 (2006).
- [181] F. Meseguer, A. Blanco, H. Míguez, F. García-Santamaría, M. Ibisate, and C. López, *Synthesis of inverse opals*, Colloids and Surfaces a-Physicochemical and Engineering Aspects **202**, 281 (2002).
- [182] N. Tétreault, H. Míguez, and G. A. Ozin, *Silicon inverse opal - A platform for photonic bandgap research*, Advanced Materials **16**, 1471 (2004).
- [183] A. S. Dimitrov and K. Nagayama, *Continuous convective assembling of fine particles into two-dimensional arrays on solid surfaces*, Langmuir **12**, 1303 (1996).
- [184] L. L. Meng, H. Wei, A. Nagel, B. J. Wiley, L. E. Scriven, and D. J. Norris, *The role of thickness transitions in convective assembly*, Nano Letters **6**, 2249 (2006).
- [185] H. Wei, L. Meng, Y. Jun, and D. J. Norris, *Quantifying stacking faults and vacancies in thin convectively assembled colloidal crystals*, Applied Physics Letters **89**, 241913 (2006).
- [186] S. C. Mau and D. A. Huse, *Stacking entropy of hard-sphere crystals*, Physical Review E **59**, 4396 (1999).

- [187] S. Auer and D. Frenkel, *Crystallization of weakly charged colloidal spheres: a numerical study*, Journal of Physics-Condensed Matter **14**, 7667 (2002).
- [188] F. García-Santamaría and P. V. Braun, *Are artificial opals close-packed fcc structures?*, 2006, oral presentation (MRS Spring).
- [189] W. Loose and B. J. Ackerson, *Model-Calculations for the Analysis of Scattering Data from Layered Structures*, Journal of Chemical Physics **101**, 7211 (1994).
- [190] W. Stöber, A. Fink, and E. Bohn, *Controlled Growth of Monodisperse Silica Spheres in the Micron Size Range*, Journal of Colloid and Interface Science **26**, 62 (1968).
- [191] H. Giesche, *Synthesis of Monodispersed Silica Powders II. Controlled Growth Reaction and Continuous Production Process*, Journal of the European Ceramic Society **14**, 205 (1994).
- [192] K. Osseasare and F. J. Arriagada, *Preparation of SiO₂ Nanoparticles in a Nonionic Reverse Micellar System*, Colloids and Surfaces **50**, 321 (1990).
- [193] H. J. Schöpe, A. B. Fontecha, H. König, J. M. Hueso, and R. Biehl, *Fast microscopic method for large scale determination of structure, morphology, and quality of thin colloidal crystals*, Langmuir **22**, 1828 (2006).
- [194] K. Busch, S. Lölkes, R. B. Wehrspohn, and H. Föll, editors, *Photonic Crystals: Advances in Design, Fabrication, and Characterization*, Wiley-VCH, Weinheim (Germany), 2004.
- [195] Z. Y. Li, L. L. Lin, and Z. Q. Zhang, *Spontaneous emission from photonic crystals: Full vectorial calculations*, Physical Review Letters **84**, 4341 (2000).
- [196] R. Z. Wang, X. H. Wang, B. Y. Gu, and G. Z. Yang, *Local density of states in three-dimensional photonic crystals: Calculation and enhancement effects*, Physical Review B **67** (2003).
- [197] R. C. McPhedran, L. C. Botten, J. McOrist, A. A. Asatryan, C. M. de Sterke, and N. A. Nicorovici, *Density of states functions for photonic crystals*, Physical Review E **69** (2004), Part 2.
- [198] B. J. Alder and T. E. Wainwright, *Phase Transition for a Hard Sphere System*, The Journal of Chemical Physics **27**, 1208 (1957).
- [199] W. W. Wood and J. D. Jacobson, *Preliminary Results from a Recalculation of the Monte Carlo Equation of State of Hard Spheres*, The Journal of Chemical Physics **27**, 1207 (1957).
- [200] Y. D. Yin, Y. Lu, B. Gates, and Y. N. Xia, *Template-assisted self-assembly: A practical route to complex aggregates of monodispersed colloids with well-defined sizes, shapes, and structures*, Journal of the American Chemical Society **123**, 8718 (2001).
- [201] M. E. Leunissen, C. G. Christova, A.-P. Hynninen, C. P. Royall, A. I. Campbell, A. Imhof, M. Dijkstra, R. van Roij, and A. van Blaaderen, *Ionic colloidal crystals of oppositely charged particles*, Nature **437**, 235 (2005).
- [202] A. P. Hynninen, C. G. Christova, R. van Roij, A. van Blaaderen, and M. Dijkstra, *Prediction and observation of crystal structures of oppositely charged colloids*, Physical Review Letters **96**, 138308 (2006).
- [203] A. P. Hynninen, M. E. Leunissen, A. van Blaaderen, and M. Dijkstra, *CuAu structure in the restricted primitive model and oppositely charged colloids*, Physical Review Letters **96**, 018303 (2006).
- [204] E. V. Shevchenko, D. V. Talapin, N. A. Kotov, S. O'Brien, and C. B. Murray, *Structural diversity in binary nanoparticle superlattices*, Nature **439**, 55 (2006).
- [205] R. Biswas, M. M. Sigalas, G. Subramania, C. M. Soukoulis, and K. M. Ho, *Photonic band gaps of porous solids*, Physical Review B **61**, 4549 (2000).
- [206] A. J. Garcia-Adeva, *Band gap atlas for photonic crystals having the symmetry of the kagome and pyrochlore lattices*, New Journal of Physics **8** (2006).

- [207] T. T. Ngo, C. M. Liddell, M. Ghebrebrhan, and J. D. Joannopoulos, *Tetrastack: Colloidal diamond-inspired structure with omnidirectional photonic band gap for low refractive index contrast*, Applied Physics Letters **88**, 241920 (2006).
- [208] F. Garcia-Santamaria, C. López, F. Meseguer, F. López-Tejeira, J. Sanchez-Dehesa, and H. T. Miyazaki, *Opal-like photonic crystal with diamond lattice*, Applied Physics Letters **79**, 2309 (2001).
- [209] P. Bartlett, R. H. Ottewill, and P. N. Pusey, *Superlattice Formation in Binary-Mixtures of Hard-Sphere Colloids*, Physical Review Letters **68**, 3801 (1992).
- [210] J. F. Bertone, P. Jiang, K. S. Hwang, D. M. Mittleman, and V. L. Colvin, *Thickness dependence of the optical properties of ordered silica-air and air-polymer photonic crystals*, Physical Review Letters **83**, 300 (1999).
- [211] C. Christova, *Binary colloidal crystals*, Phd thesis, Utrecht University, 2005.
- [212] J. Goodwin, R. Ottewil, and R. Pelton, *Studies on the preparation and characterization of monodisperse polystyrene latices V.: The preparation of cationic latices*, Colloid and Polymer Science **257**, 61 (1979).
- [213] E. Kumacheva, O. Kalinina, and L. Lilge, *Three-dimensional arrays in polymer nanocomposites*, Advanced Materials **11**, 231 (1999).
- [214] A. Imhof, 2006, internal communication.
- [215] C. M. van Kats, 2006, internal communication.
- [216] Y. J. Lee, S. A. Pruzinsky, and P. V. Braun, *Diffraction response of colloidal crystals: effect of numerical aperture*, Optics Letters **30**, 153 (2005).
- [217] G. Zhang, D. Y. Wang, and H. Mohwald, *Decoration of microspheres with gold nanodots-giving colloidal spheres valences*, Angewandte Chemie-International Edition **44**, 7767 (2005).
- [218] G. Zhang, D. Y. Wang, and H. Mohwald, *Patterning microsphere surfaces by templating colloidal crystals*, Nano Letters **5**, 143 (2005).
- [219] O. Becker and K. Bange, *Ultramicrotomy - an Alternative Cross-Section Preparation for Oxidic Thin-Films on Glass*, Ultramicroscopy **52**, 73 (1993).
- [220] H. Hofmeister, S. Thiel, M. Dubiel, and E. Schurig, *Synthesis of nanosized silver particles in ion-exchanged glass by electron beam irradiation*, Applied Physics Letters **70**, 1694 (1997).
- [221] J. I. Amalvy, M. J. Percy, S. P. Armes, and H. Wiese, *Synthesis and characterization of novel film-forming vinyl polymer/silica colloidal nanocomposites*, Langmuir **17**, 4770 (2001).
- [222] J. H. Holtz and S. A. Asher, *Polymerized colloidal crystal hydrogel films as intelligent chemical sensing materials*, Nature **389**, 829 (1997).
- [223] J. E. G. J. Wijnhoven and W. L. Vos, *Preparation of Photonic Crystals Made of Air Spheres in Titania*, Science **281**, 802 (1998).
- [224] G. Subramania, K. Constant, R. Biswas, M. M. Sigalas, and K. M. Ho, *Optical photonic crystals fabricated from colloidal systems*, Applied Physics Letters **74**, 3933 (1999).
- [225] S. Pronk and D. Frenkel, *Can stacking faults in hard-sphere crystals anneal out spontaneously?*, Journal of Chemical Physics **110**, 4589 (1999).
- [226] Y. A. Vlasov, V. N. Astratov, A. V. Baryshev, A. A. Kaplyanskii, O. Z. Karimov, and M. F. Limonov, *Manifestation of intrinsic defects in optical properties of self-organized opal photonic crystals*, Physical Review E **61**, 5784 (2000).
- [227] J. P. Hoogenboom, D. Derks, P. Vergeer, and A. van Blaaderen, *Stacking faults in colloidal crystals grown by sedimentation*, Journal of Chemical Physics **117**, 11320 (2002).
- [228] P. V. Braun and P. Wiltzius, *Microporous materials - Electrochemically grown photonic crystals*, Nature **402**, 603 (1999).

- [229] A. L. Rogach, N. A. Kotov, D. S. Koktysh, J. W. Ostrander, and G. A. Ragoisha, *Electrophoretic deposition of latex-based 3D colloidal photonic crystals: A technique for rapid production of high-quality opals*, *Chemistry of Materials* **12**, 2721 (2000).
- [230] T. Y. Gong, D. T. Wu, and D. W. M. Marr, *Electric field-reversible three-dimensional colloidal crystals*, *Langmuir* **19**, 5967 (2003).
- [231] W. D. Ristenpart, I. A. Aksay, and D. A. Saville, *Electrically guided assembly of planar superlattices in binary colloidal suspensions*, *Physical Review Letters* **90**, 128303 (2003).
- [232] S. O. Lumsdon, E. W. Kaler, J. P. Williams, and O. D. Velev, *Dielectrophoretic assembly of oriented and switchable two-dimensional photonic crystals*, *Applied Physics Letters* **82**, 949 (2003).
- [233] [http : //www.bison.nl/NL/nl/index.do](http://www.bison.nl/NL/nl/index.do), 2006.
- [234] A. Madan, P. Rava, R. E. I. Schropp, and B. von Roedern, *A New Modular Multichamber Plasma-Enhanced Chemical-Vapor-Deposition System*, *Applied Surface Science* **70-1**, 716 (1993).
- [235] J. Kalkman, E. de Bres, A. Polman, Y. Jun, D. J. Norris, D. C. 't Hart, J. P. Hoogenboom, and A. van Blaaderen, *Selective excitation of erbium in silicon-infiltrated silica colloidal photonic crystals*, *Journal of Applied Physics* **95**, 2297 (2004).
- [236] [http : //www.sigmaaldrich.com/](http://www.sigmaaldrich.com/), 2006.
- [237] G. Kaye and T. Laby, *Tables of Physical and Chemical constants*, Longman Scientific and Technical, New York, 15th edition, 1986.
- [238] [http : //www.mpbio.com/landing.php](http://www.mpbio.com/landing.php), 2006.
- [239] M. Hermes, 2006, internal communication.
- [240] M. van der Maas, *Defects in Colloidal Crystals - A Quantitative Real-Space Analysis*, Bachelor thesis, Utrecht University, 2006.
- [241] M. Megens, C. M. van Kats, P. Bösecke, and W. L. Vos, *Synchrotron small-angle X-ray scattering of colloids and photonic colloidal crystals*, *Journal of Applied Crystallography* **30**, 637 (1997).